

VLF PROPAGATION AND NOISE IN THE IONOSPHERE OBSERVED BY SOUNDING ROCKETS

By: L. E. ORSAK L. H. RORDEN G. B. CARPENTER B. P. FICKLIN

Prepared for:

OFFICE OF RESEARCH GRANTS AND CONTRACTS
CODE SC
NATIONAL AERONAUTICS AND SPACE ADMINISTRATION
WASHINGTON, D.C.

CONTRACT NASr-49(01)

STANFORD RESEARCH INSTITUTE

MENLO PARK, CALIFORNIA

***SRI**

GPO PRICE \$ _____

CSFTI PRICE(S) \$ _____

Hard copy (HC) 1.00

Microfiche (MF) 1.25

ff 653 July 65

N 65-35579

FACILITY FORM 602

(ACCESSION NUMBER)

217

(PAGES)

CR-67374

(NASA CR OR TMX OR AD NUMBER)

(THRU)

1

(CODE)

13

(CATEGORY)



January 1965

Final Report

VLF PROPAGATION AND NOISE IN THE IONOSPHERE OBSERVED BY SOUNDING ROCKETS

Prepared for:

OFFICE OF RESEARCH GRANTS AND CONTRACTS
CODE SC
NATIONAL AERONAUTICS AND SPACE ADMINISTRATION
WASHINGTON, D.C.

CONTRACT NASr-49(01)

By: L. E. ORSAK L. H. RORDEN G. B. CARPENTER B. P. FICKLIN

SRI Project 3749

Approved: W. R. VINCENT, MANAGER
COMMUNICATION LABORATORY

D. R. SCHEUCH, EXECUTIVE DIRECTOR
ELECTRONICS AND RADIO SCIENCES

Copy No. 30

ABSTRACT

Two instrumented payloads were designed, constructed, and flown aboard two Aerobee rockets launched from Wallops Island, Virginia. The first flight was at local noon and the second shot was two hours before local midnight. Three magnetic antennas (loops) were flown: one approximately vertical and one horizontal for measurements in the frequency range 0.2 to 100 kc, and one vertical for measurements in the frequency range 1250 to 1600 kc. One horizontal electric dipole was flown for measurements on the NSS (22.3 kc) Navy transmitter and for measurements of the complex antenna terminal impedance. On one flight, a low-frequency (≈ 100 cps) swept-bias conductance probe was flown.

Narrow-band sweeping receivers covered the frequency range 0.2 to 100 kc and 1250 to 1600 kc, giving contiguous spectral data on man-made as well as naturally occurring signals. Profiles of attenuation as a function of altitude were obtained on many signals, man-made as well as natural. Interesting natural noise phenomena were observed. A broadband receiver (0.3 to 12.5 kc) obtained data on many whistler-type signals, including a new type called the subprotonospheric whistler.

The sweeping receivers covering the range 0.2 to 100 kc and the broadband receiver constituted the essential components of the experiment flown by Stanford University and Stanford Research Institute on the NASA EOGO satellite. The rocket flights were a successful test of the engineering and scientific design of the satellite experiment.

The complex (resistive and reactive components) impedance of an electric dipole was measured at 1.54 and 120 kc. Data were obtained at nighttime only because of equipment failure on the daytime flight. Detailed impedance data were obtained through a very thin sporadic-E ionization layer and at the lower edge of the F layer. Sensitivity to 10^3 elec/cc was observed.

Measurements of both phase and amplitude were made at 22.3 kc (NSS) using the vertical and horizontal loop antennas and the horizontal dipole. Amplitude of the electric and magnetic field strengths (and therefore an indication of power density) were obtained as well as data on wave normal direction and polarization. The phase measurement produced an integrated electron density profile that matched very well with ionosonde data and in form with the conductance probe data, and extended the measurement of electron density down to approximately 100 elec/cc.

Dynamic conductance as a function of dc bias was obtained at 112 cps on a small probe. By observing conductance as a function of dc bias, the electron temperature and rocket potential were measured. An estimate of ion drift velocity may be made from the observations, and lends support to the hypothesis that a static electric field exists in the mid-latitude F region.

CONTENTS

ABSTRACT	iii
LIST OF ILLUSTRATIONS	ix
LIST OF TABLES	xiii
ACKNOWLEDGMENTS	xv
1 INTRODUCTION	1
2 OBJECTIVES	3
3 GENERAL EXPERIMENT AND FLIGHT OPERATIONS	5
3.1 Aerobee 4.58 UI	5
3.2 Aerobee 4.59 UI	7
4 INSTRUMENTATION	9
5 MECHANICAL DESCRIPTION OF PAYLOAD	19
6 GROUND SUPPORT EQUIPMENT	23
6.1 Checkout Sets	23
6.2 Ground Receiver	24
7 DATA RECORDING AND DATA REDUCTION	25
7.1 General	25
7.2 Radar and Photography	25
7.3 Ionosonde	28
7.4 Broadband Spectrum Analysis	28
7.5 Panoramic Data Display, Sweeping Receivers	28
8 FLIGHT TRAJECTORY AND DISCUSSION	31
8.1 Trajectory	31
8.2 Aspect	31
8.2.1 General	31
8.2.2 Sun-Earth Sensor, Aerobee 4.58 UI	31

CONTENTS (Continued)

8.2.3	Moon Sensor, Aerobee 4.59 UI	35
8.2.4	Magnetometer	38
9	DATA ANALYSIS AND DISCUSSION	45
9.1	Narrow-Band Sweeping Receivers	45
9.1.1	Instrumentation	45
9.1.1.1	Circuit Description of Band 1 Receiver.	47
9.1.1.2	Circuit Description of Band 2 Receiver.	48
9.1.1.3	Circuit Description of Band 3 Receiver.	50
9.1.1.4	Circuit Description of Band 4 Receiver.	50
9.1.1.5	In-Flight Calibrator	52
9.1.2	Data and Discussion	53
9.1.2.1	General	53
9.1.2.2	Band 1 Receiver, Aerobee 4.58 UI	53
9.1.2.3	Band 2 Receiver, Aerobee 4.58 UI	54
9.1.2.4	Band 3 Receiver, Aerobee 4.58 UI	58
9.1.2.5	Band 4 Receiver, Aerobee 4.58 UI	72
9.1.2.6	Aerobee 4.59 UI Sweeping Receivers	85
9.1.2.7	Band 1 Receiver, Aerobee 4.59 UI	91
9.1.2.8	Band 2 Receiver, Aerobee 4.59 UI	92
9.1.2.9	Band 3 Receiver, Aerobee 4.59 UI	93
9.1.2.10	Band 4 Receiver, Aerobee 4.59 UI	102
9.2	Broadband Receiver	115
9.2.1	Instrumentation	115
9.2.2	Data and Discussion	115
9.2.2.1	Spectral Data	116
9.2.2.2	Amplitude Data	123
9.2.2.3	Results Obtained by Stanford University	129
9.3	Impedance Probe	132
9.3.1	Instrumentation	132
9.3.2	Data and Discussion	134

CONTENTS (Concluded)

9.4	NSS Receivers	142
9.4.1	Instrumentation	142
9.4.2	Doppler Measurements	145
9.4.2.1	Procedure	145
9.4.2.2	Daytime Electron Density Profiles	151
9.4.2.3	Nighttime Electron Density Profiles	156
9.4.3	Amplitude Measurements	158
9.4.3.1	Daytime Results	161
9.4.3.2	Nighttime Results	167
9.5	Conductance Probe	175
9.5.1	Purpose	175
9.5.2	Instrumentation	175
9.5.3	Theory of Operation	177
9.5.4	Results	182
9.6	Temperature and Voltage Monitor	187
10	SUMMARY	189
	REFERENCES.	193
	Appendix A -- CURRENT TO AN INFINITELY LONG CYLINDER	195
	Appendix B -- CURRENT TO A MOVING CYLINDER	201

ILLUSTRATIONS

Fig. 4.1	Aerobee 4.58 UI Instrumentation (Block Diagram)	11
Fig. 4.2	Aerobee 4.59 UI Instrumentation (Block Diagram)	13
Fig. 5.1	Aerobee 4.59 UI Payload	20
Fig. 7.1	Aerobee 4.58 UI Oscillograph Chart Recordings	26
Fig. 7.2	Aerobee 4.59 UI Oscillograph Chart Recordings	27
Fig. 8.1	Aerobee 4.58 UI Trajectory	32
Fig. 8.2	Aerobee 4.59 UI Trajectory	33
Fig. 8.3	Flight Geometry	34
Fig. 8.4	Magnetometer and Moon Sensor Output	39
Fig. 8.5	Attitude of Rocket Spin Axis	41
Fig. 8.6	Rocket Spin Rate and Total Velocity	42
Fig. 9.1	Narrow-Band Sweeping and Broadband Receivers (Simplified Block Diagram).	46
Fig. 9.2	Typical Logarithmic Compressor Response	49
Fig. 9.3	Aerobee 4.58 UI Band 1 Data with Calibrations	55
Fig. 9.4	Aerobee 4.58 UI Band 2 Data, Ascent	56
Fig. 9.5	Aerobee 4.58 UI Band 2 Data, Descent	57
Fig. 9.6	Aerobee 4.58 UI Band 2 Data with Calibrations	59
Fig. 9.7	Aerobee 4.58 UI Band 3 Data with Calibrations	60
Fig. 9.8	Amplitude of NAA and 17.8-kc Noise, Ascent	62
Fig. 9.9	Amplitude of NAA and 17.8-kc Noise, Descent	63
Fig. 9.10	Amplitude of NSS, Ascent	64
Fig. 9.11	Amplitude of NSS, Descent	65
Fig. 9.12	Amplitude of LORAN C and 100-kc Noise, Ascent	66
Fig. 9.13	Amplitude of LORAN C and 100-kc Noise, Descent	67
Fig. 9.14	Amplitude of 26.7-kc Noise	68
Fig. 9.15	Amplitude of 48.9-kc Noise	69
Fig. 9.16	Amplitude of 56.9-kc Noise	70
Fig. 9.17	Amplitude of 61.8-kc Noise	71

ILLUSTRATIONS (Continued)

Fig. 9.18	Amplitude of WESR at 1330 kc, Ascent	73
Fig. 9.19	Amplitude of WESR at 1330 kc, Descent	74
Fig. 9.20	Amplitude of WHIH at 1400 kc, Ascent	75
Fig. 9.21	Amplitude of WHIH at 1400 kc, Descent	76
Fig. 9.22	Amplitude of WJDY at 1470 kc, Ascent	77
Fig. 9.23	Amplitude of WJDY at 1470 kc, Descent	78
Fig. 9.24	Amplitude of WTOP at 1500 kc, Ascent	79
Fig. 9.25	Amplitude of WTOP at 1500 kc, Descent	80
Fig. 9.26	Amplitude of WBOF at 1550 kc, Ascent	81
Fig. 9.27	Amplitude of WBOF at 1550 kc, Descent	82
Fig. 9.28	Electron Density Calculated from Plasma Cutoff Observations	84
Fig. 9.29	Aerobee 4.59 UI Bands 1, 2, and 3 Sweeping Receiver Data, Ascent	87
Fig. 9.30	Aerobee 4.59 UI Bands 1, 2, and 3 Sweeping Receiver Data, Descent	89
Fig. 9.31	Amplitude of NAA and 14.7-kc Noise, Ascent	94
Fig. 9.32	Amplitude of NAA and 14.7-kc Noise, Descent	95
Fig. 9.33	Amplitude of NSS, Ascent	96
Fig. 9.34	Amplitude of NSS, Descent	97
Fig. 9.35	Amplitude of NSS (64.2 kc), Ascent	98
Fig. 9.36	Amplitude of NSS (64.2 kc), Descent	99
Fig. 9.37	Amplitude of NSS (88.0 kc), Ascent	100
Fig. 9.38	Amplitude of NSS (88.0 kc), Descent	101
Fig. 9.39	Sporadic-E Layer: Bands 3 and 4, Impedance Probe, and Electron Density, Ascent	103
Fig. 9.40	Sporadic-E Layer: Bands 3 and 4, Impedance Probe, and Electron Density, Descent	105
Fig. 9.41	Amplitude of 1320 kc, Ascent	107
Fig. 9.42	Amplitude of 1320 kc, Descent	108
Fig. 9.43	Amplitude of WHIH at 1400 kc, Ascent	109
Fig. 9.44	Amplitude of WHIH at 1400 kc, Descent	110
Fig. 9.45	Amplitude of WOL at 1450 kc, Ascent	111
Fig. 9.46	Amplitude of WOL at 1450 kc, Descent	112

ILLUSTRATIONS (Continued)

Fig. 9.47	Amplitude of WTOP at 1500 kc, Ascent	113
Fig. 9.48	Amplitude of WTOP at 1500 kc, Descent	114
Fig. 9.49	Aeorbee 4.58 UI Broadband Receiver Spectral Data, 0 to 70 km, Ascent	118
Fig. 9.50	Aerobee 4.58 UI Broadband Receiver Spectral Data, 150 km to Apogee, Ascent	120
Fig. 9.51	Aerobee 4.58 UI Broadband Receiver Spectral Data, 200 to 110 km, Descent	122
Fig. 9.52	Aerobee 4.59 UI Broadband Receiver Spectral Data	124
Fig. 9.53	Aerobee 4.59 UI Broadband Receiver Amplitude Data	125
Fig. 9.54	Aerobee 4.58 UI and 4.59 UI Broadband Receiver Amplitude Data (Compressed Time Scale)	127
Fig. 9.55	Ray Path of Subprotonospheric Whistler	130
Fig. 9.56	Low-Frequency Impedance Probe Calibration Curve	133
Fig. 9.57	High-Frequency Impedance Probe Calibration Curve	134
Fig. 9.58	Low-Frequency Impedance Probe Conductance Data	135
Fig. 9.59	Low-Frequency Impedance Probe Capacitance Data	136
Fig. 9.60	High-Frequency Impedance Probe Capacitance Data	137
Fig. 9.61	Impedance Probe, Low-Frequency Impedance in the Sporadic-E Ionization Layer	138
Fig. 9.62	Impedance Probe, High-Frequency Impedance in the Sporadic-E Ionization Layer	139
Fig. 9.63	Rocket Spin Modulation of Impedance	140
Fig. 9.64	VLF Doppler Experiment (Simplified Block Diagram)	145
Fig. 9.65	Illustration of Geometry for Doppler Calculations	146
Fig. 9.66	Daytime Phase Delay at 22.3 kc	152
Fig. 9.67	Daytime Refractive Index at 22.3 kc	153
Fig. 9.68	Daytime Electron Density Profile	155
Fig. 9.69	Nighttime Phase Delay at 22.3 kc	157
Fig. 9.70	Nighttime Refractive Index at 22.3 kc	159
Fig. 9.71	Nighttime Electron Density Profile	160
Fig. 9.72	Daytime Amplitudes at 22.3 kc	163
Fig. 9.73	Daytime Power Density at 22.3 kc	166
Fig. 9.74	Daytime Wave-Normal Angles at 22.3 kc	168
Fig. 9.75	Nighttime Amplitudes at 22.3 kc	169

ILLUSTRATIONS (Concluded)

Fig. 9.76	Nighttime Power Density at 22.3 kc	172
Fig. 9.77	Nighttime Wave-Normal Angles at 22.3 kc	173
Fig. 9.78	Ratio of Magnetic to Electric Field Strength at 22.3 kc	174
Fig. 9.79	Probe Peak Conductance, Electron Density from Doppler Data, and Probe Bias Resulting in Peak Conductance . . .	183
Fig. 9.80	Calculated and Measured Probe Conductance vs. Bias for 200-km Altitude	184
Fig. 9.81	Payload Temperature Data	188
Fig. A.1	Ion Current Factor ψ as a Function of Cylinder Radius for Several Potentials	200

TABLES

Table 4.1	Experiments on Aerobee 4.58 UI and Aerobee 4.59 UI . . .	9
-----------	--	---

ACKNOWLEDGMENTS

The helpful cooperation of personnel at Goddard Space Flight Center, Sounding Rockets Branch, is gratefully acknowledged. The cooperation of the telemetry station, ionosonde, and launch personnel at NASA Wallops Island Station was invaluable.

Thanks go to the offices of Chief of Naval Operations for the special transmissions from NSS Naval transmitter.

The participation of the Stanford University Radio Science Laboratory in the reduction and analysis of the broadband data and recording ground data is gratefully acknowledged.

1. INTRODUCTION

The experiments described in this report have been designed and performed with the fundamental purpose of exploring the effects of the lower ionosphere on VLF waves. Since there had been few previous measurements at VLF in the ionosphere, the intent of this project was to perform a broad survey of the many types of observations that could be made on sounding rockets. At the same time, these flights provided a perfect opportunity to test the instrumentation designed by SRI for the Stanford-SRI VLF experiment on the EOGO satellites. As anticipated, these flights of EOGO-type instruments provided scientifically valuable data, as well as verifying that correct assumptions had been made in the design of the EOGO instruments. The records also proved valuable in developing data-reduction methods for the EOGO experiment. The first EOGO (OGO-1) experiment was successfully launched in September 1964 but no results will be reported here.

This report summarizes the combined results of the various instruments flown, presents analyses of some of the phenomena observed, and discusses the potential future use of the existing data and development of additional experiments of a similar nature.

Since various independent experiments were flown on the two rockets fired during this investigation, details of the instrumentation and results of each experiment are reported in separate sections. The wealth of data resulting from the successful flight of the many experiments flown has precluded a complete analysis, at this time, of all pertinent observations. It has therefore been our intent to present and discuss as large a volume of reduced data as practical, to allow the reader to draw his own conclusions on phenomena that have not yet been developed in detail.

2. OBJECTIVES

In support of the ultimate purpose discussed in Sec. 1, the following objectives were defined for this project:

Perform a survey of VLF noise observed in the ionosphere. This survey is intended to outline the general level of natural noise to be found in the D, E, and lower F regions over the entire range of frequencies from 200 cps to 100 kc, plus a 1250 to 1600-kc band, which includes the local electron gyrofrequency. Comparison with noise levels observed below the ionosphere, and with other ground measurements, allow a check on the anticipated values of reflection and absorption losses. Even more important is the opportunity to record phenomena that are not normally observed on the ground but should exist in the ionosphere, such as daytime whistlers. Also, for the purpose of designing future rocket and satellite experiments, knowing the amplitude and frequency ranges to be expected is invaluable.

Flight test the EOGO satellite VLF experiment. The Aerobee flights were not intended as an environmental test of EOGO instrumentation so much as a preview of results to be obtained from the EOGO experiment. If the rocket flights had shown any serious flaws in the EOGO design philosophy, the EOGO instruments would have been corrected before the EOGO was sent aloft. Although no such difficulties were found, the results of the Aerobee experiments were used extensively to develop data reduction methods, and to plan experiments to be performed with EOGO.

Investigate VLF propagation in the ionosphere, and through its lower boundary region. Theoretical treatment of these problems is complicated not only by extremely involved mathematics, but also by relatively poor knowledge of the D and E regions, which are highly variable and difficult to explore experimentally. Since these regions exert a strong influence on VLF propagation, however, their composition can be largely determined from the propagation data. In this project, several

experiments have been performed for propagation studies, which are proving very useful in attacking the composition problem as well. The more immediate goal, however, is to obtain direct evidence on the nature of absorption, refraction, reflection, and polarization change in the D and E regions, and to determine the nature and depth of penetration of downcoming whistler-mode signals.

Investigate the effect of the ionosphere on VLF antennas. Although substantial theoretical progress has been made in the last few years, the problem of the complex impedance of an electric dipole surrounded by an ion sheath in a gyrotropic medium is still far from solved. Therefore, the impedance experiments performed on this project have been directed toward a survey of the predominant effects, in order to get some hints at the best ways to proceed in breaking down the problem. Once the effects of the medium are understood well enough, it is expected that VLF impedance probes will prove their value in exploring regions of low ionization. At a less sophisticated level, the impedance data obtained will be of direct engineering value in designing antenna matching systems for future experiments.

Evaluate potential improvements in instrumentation. As more is learned about the physics being investigated, better or more precise methods of measurement will suggest themselves, or completely new approaches may be seen. These, together with engineering improvements that could be made on existing instrument designs, will be discussed as appropriate in the sections which follow.

3. GENERAL EXPERIMENT AND FLIGHT OPERATIONS

3.1 Aerobee 4.58 UI

The design of the instrumentation for Aerobee 4.58 UI began 1 July 1961 and continued at a normal level of effort until 31 December 1961; at which time work was essentially reduced to zero in order that personnel might be utilized to develop an experiment to be orbited on NASA's EOGO satellite. During this six-month period (1 July 1961 to 31 December 1961), the basic design of the Aerobee experiment was established and most critical breadboard testing was carried out. Procurement of long-lead-time items was also accomplished.

Work on the Aerobee 4.58 UI payload resumed at maximum level on 1 October 1962 and continued up to an expected launch date of 22 January 1963. During January the payload was completed and taken to Goddard Space Flight Center (GSFC) for environmental testing. Due to launcher repairs, the launch was postponed to 5 February 1963. On 29 January the firing date was postponed indefinitely because of previous Aerobee rocket failures. At this time the payload had already passed all tests and was in the Aerobee launch tower preparatory area ready to be integrated with the rocket motor. The payload was partially disassembled and stored in the preparatory area pending further Aerobee scheduling developments.

Definite causes of the failures of previous Aerobee rockets were not established in all cases; however, two rockets had payloads that were lightweight, long length, and utilized a fiberglass nosecone in place of the more usual aluminum nosecone. Since the Aerobee 4.58 UI payload was lightweight and utilized a fiberglass nosecone, it was decided that additional weight should be added, even though the anticipated altitude (≈ 300 km) would not be reached and a reduced altitude (≈ 225 km) would result. For maximum effectiveness the weight should be placed as near the forward tip as possible. Increasing the stiffness

of the fiberglass nosecone to perform more nearly like an aluminum nosecone was also desirable. The delayed schedule (2 April 1963) allowed time to design and construct a support structure inside the nosecone to support lead weight (30 lb) very near the tip of the rocket and to support the fiberglass nosecone from the inside. The new support structure, when buffered against the fiberglass nosecone with hard rubber bushings, proved to be as stiff as an aluminum nosecone.

The new support structure was fabricated at SRI and assembled with the payload at GSFC. The payload had been returned to GSFC from Wallops Island. The payload was then subjected again to vibration tests and to a bending test to test the new structure, and satisfactory results were obtained. Electrical integration tests were performed at GSFC, and the payload was then returned to Wallops Island for integration with the rocket and for a scheduled launch on 2 April 1963.

Due to range-scheduling difficulties, the firing date was delayed to 3 April 1963, on which day the firing took place at 1646:22.32Z (1146:22.32 EST or LMT).

Before launch, the ground receiver had been installed in the blockhouse for recording ground data for comparison with the rocket data and for real-time comparison of the phase of the NSS signal received on the ground with the phase of a reference oscillator flown in the rocket. Special key-down transmissions from NSS during the rocket flight had been arranged through the offices of Chief of Naval Operations. Ionosonde data were obtained by the Wallops Island ionosonde station. The VLF ground station at Greenbank, West Virginia was also operating.

A tense moment occurred when, instead of the rocket ignition occurring at X minus zero time when the "fire" switch is actuated, the ignition took place at X minus eight seconds when the "arm" switch was actuated. Fortunately, recorders had already been turned on and the rocket payload had been switched to internal batteries. What might have been a disaster had no effect on the experiment performance.

The rocket performance was excellent, resulting in an extremely stable flight to an altitude slightly higher than estimated.

With the exception of the electric dipole antenna, all experimental systems performed satisfactorily. Examination of the data indicated that the electric dipole antenna, consisting of two strips of copper attached to the fiberglass nosecone, was torn loose shortly before rocket burnout. Because of this failure, no impedance data on the electric dipole were obtained, and the phase and amplitude of the electric field of the NSS (22.3 kc) transmission were uncalibrated.

First inspection of the data took place prior to the Aerobee 4.59 UI flight in order to determine if changes in the experiment were desirable for Aerobee 4.59 UI.

3.2 Aerobee 4.59 UI

The instrumentation for Aerobee 4.59 UI was completed during the second quarter of 1963 in preparation for a launch schedule of 9 July 1963.

Since an excellent daytime sample of data was obtained by Aerobee 4.58 UI, Aerobee 4.59 UI was scheduled for nighttime. The sun-earth sensor used on Aerobee 4.58 UI was replaced by a moon sensor on Aerobee 4.59 UI. Only moderate temperature changes were experienced on Aerobee 4.58 UI; therefore, the temperature monitor was replaced by an additional experiment, a conductance probe. This conductance probe was added to provide data on electron temperature and plasma potential for correlation with data from the impedance probe and the NSS phase-tracking receiver. Two lateral accelerometers, provided and installed by NASA, were mounted on the rocket sustainer near the booster to observe lateral accelerations produced by the booster. An acceleration-actuated timer was provided by NASA to disconnect the accelerometer data from the telemetry channels after 15 seconds and connect the conductance probe data to these same channels. Ground command backup of the G-actuated timer was provided by the DRW-13 command receiver.

The two strips of copper which comprised the electric dipole antenna were more securely attached on Aerobee 4.59 UI with screws as well as adhesive to prevent a reoccurrence of the Aerobee 4.58 UI failure.

The loop antennas on Aerobee 4.59 UI were shielded (no shields were used on Aerobee 4.58 UI) to reduce their sensitivity to electric fields. To facilitate the shielding, the number of turns on each loop was reduced and the antenna matching transformers changed to accommodate the new antenna impedances.

Magnetic shields of high permeability material were used to enclose the VCO's in the telemetry system to reduce their radiated interference.

The Aerobee 4.59 UI payload, identical to Aerobee 4.58 UI except as described above, was taken to GSFC for environmental testing and telemetry checks. Satisfactory performance was obtained in all respects. The payload was then taken to Wallops Island for integration with the rocket, further telemetry checks, and firing.

As in the Aerobee 4.58 UI operation, a ground receiver was installed in the blockhouse. Special key-down transmissions from NSS were again arranged through the offices of Chief of Naval Operations. Ionosonde data at Wallops Island were obtained and the VLF ground station at Greenbank, West Virginia was operating.

The rocket was fired at night on 10 July 1963 at 0246:00.0 z (2246 EDT or 2146 LMT on 9 July). All the experiment and rocket systems functioned normally, resulting in a completely successful experiment.

4. INSTRUMENTATION

The experiments flown on Aerobee 4.58 UI and Aerobee 4.59 UI are given in Table 4.1.

Table 4.1
EXPERIMENTS ON AEROBEE 4.58 UI AND AEROBEE 4.59 UI

Experiments on Aerobee 4.58 UI	Experiments on Aerobee 4.59 UI
Band 1 Receiver (0.2-1.6 kc)	Band 1 Receiver (0.2-1.6 kc)
Band 2 Receiver (1.6-12.5 kc)	Band 2 Receiver (1.6-12.5 kc)
Band 3 Receiver (12.5-100 kc)	Band 3 Receiver (12.5-100 kc)
Band 4 Receiver (1.25-1.6 Mc)	Band 4 Receiver (1.25-1.6 Mc)
Broadband Receiver (0.2-12.5 kc)	Broadband Receiver (0.2-12.5 kc)
NSS Receiver (22.3 kc)	NSS Receiver (22.3 kc)
Impedance Probe (1.54 and 120 kc)	Impedance Probe (1.54 and 120 kc)
Magnetometer (spin coil)	Magnetometer (spin coil)
Chamber Pressure	Chamber Pressure
Sun-Earth Aspect	Moon Aspect
Temperature and Voltage	Conductance Probe
Linear Accelerometer	Lateral Accelerometer
	Lateral Accelerometer

A major portion of the instrumentation was duplicated on Aerobee 4.58 UI and Aerobee 4.59 UI; the common portions will be described first, then the differences.

Refer to the block diagrams in Figs. 4.1 and 4.2 for the following discussion.

The output of the vertical low-frequency loop is applied to the low-frequency preamplifier and to the magnetometer. The magnetometer amplifies the signal produced by the rocket spin, equalizes the frequency response for constant output regardless of rocket spin rate, and applies

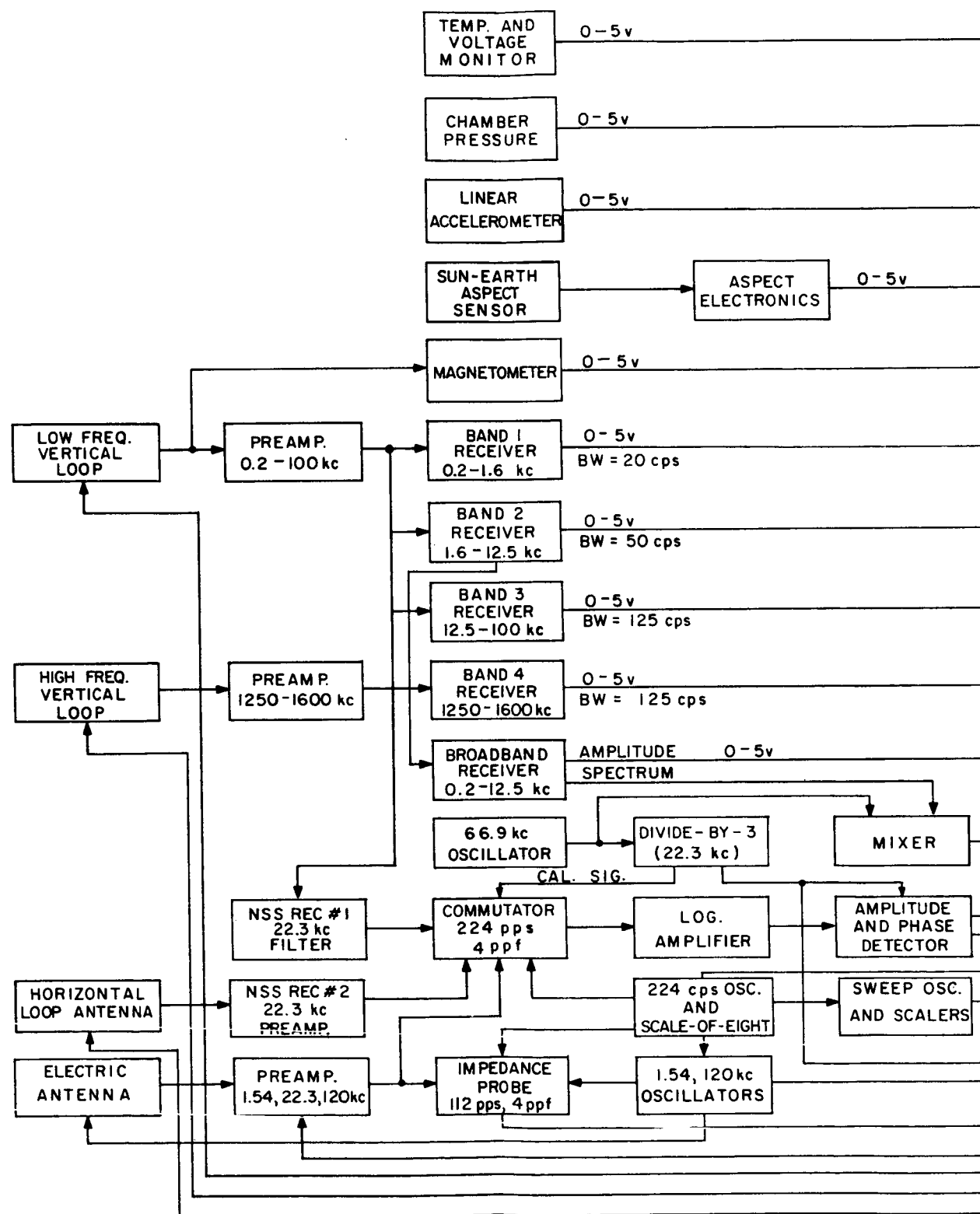
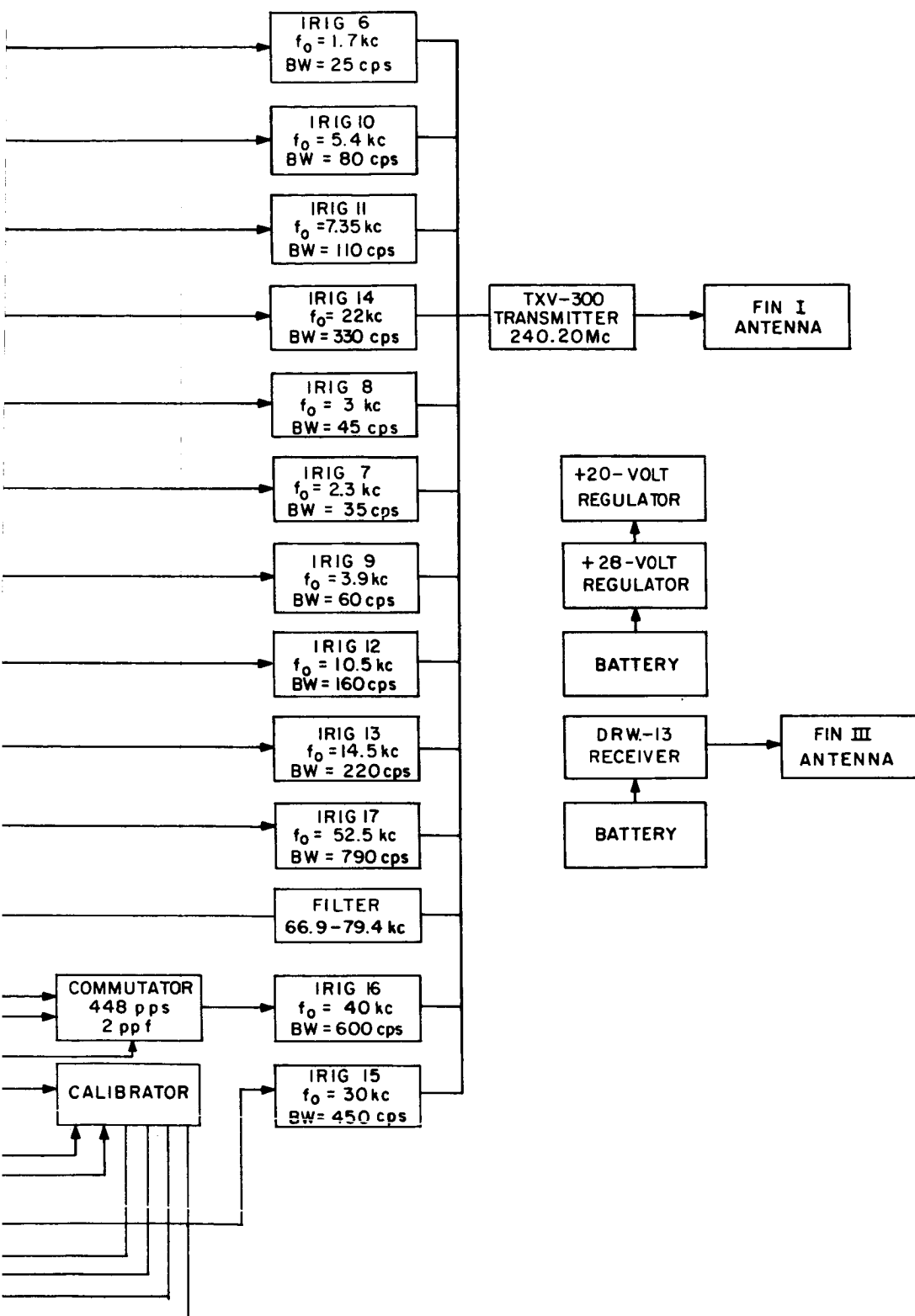


FIG. 4.1 AEROBEE 4.58 UI INSTRUMENT



D-3749-115

ENTATION (Block Diagram)

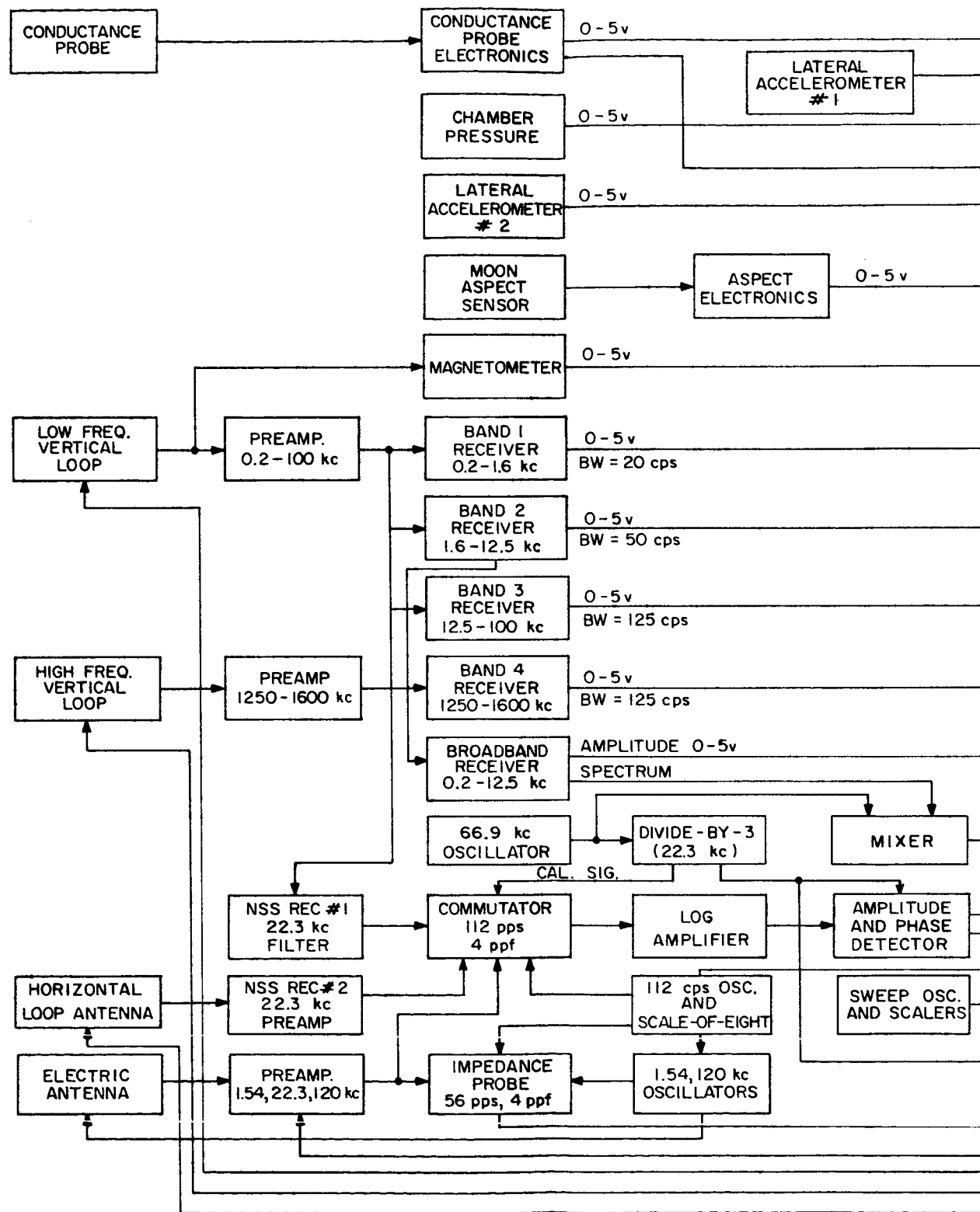
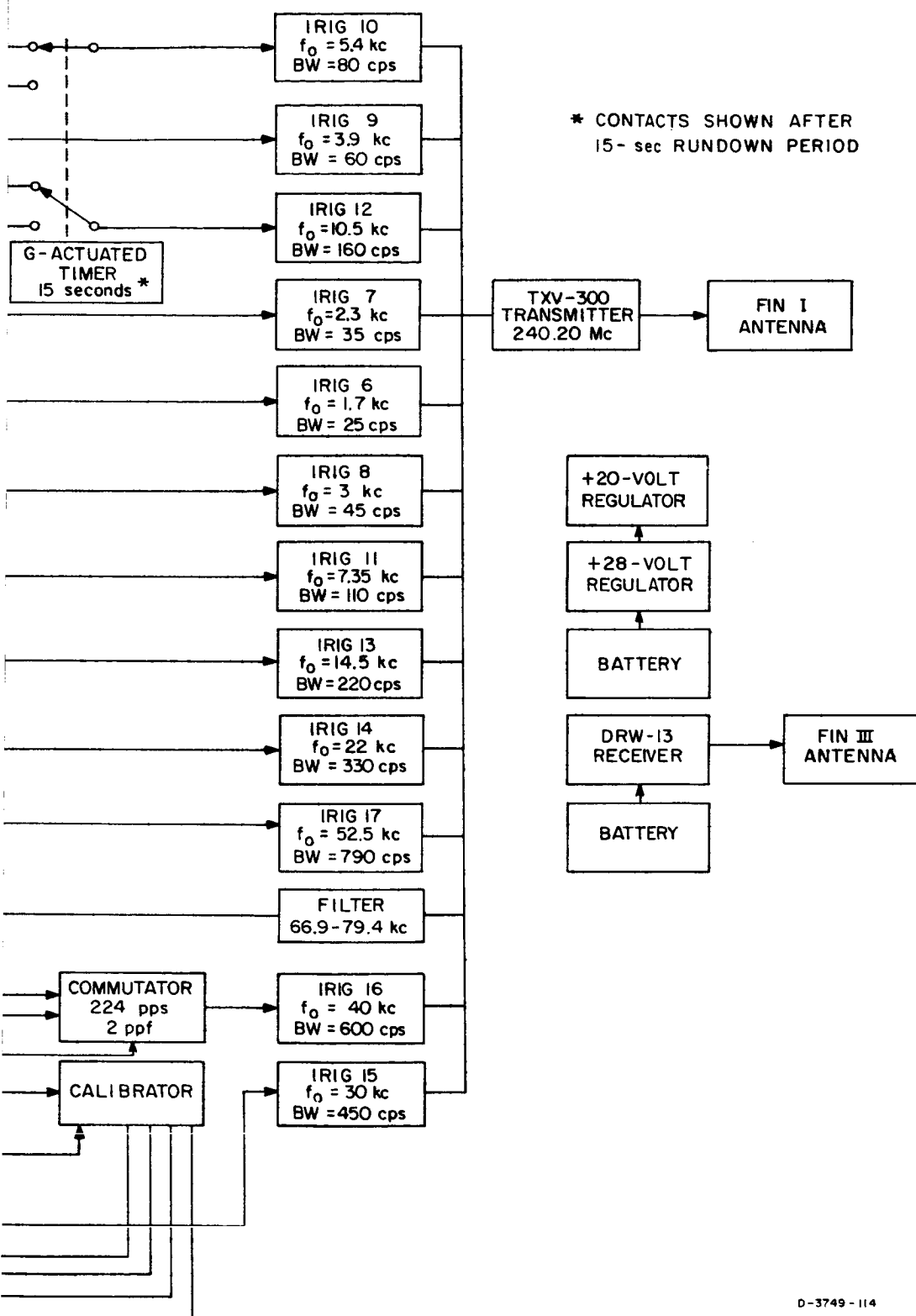


FIG. 4.2 AEROBEE 4.59 UI INSTRUMENT



D-3749-114

ENTATION (Block Diagram)

this output to a standard IRIG voltage-controlled oscillator (VCO). The output of the low-frequency preamplifier is used for the Band 1, 2, and 3 receivers and the NSS receiver. The outputs of the Band 1, 2, and 3 receivers are applied to IRIG VCO's. Following an RF filter in Band 2, a signal is obtained to apply to the broadband receiver input. Two outputs are obtained from the broadband receiver: (1) the amplitude (envelope) of the signal in the total band; and (2) a spectrum of the signals in the band, derived by clipping the signals. The amplitude data are applied directly to an IRIG VCO; however, the broadband spectrum is translated to a frequency range 67.1 to 79.4 kc by using a 66.9-kc local oscillator and then applied directly to the telemetry baseband. The 66.9-kc signal, used also as a phase reference for the NSS receiver, is also applied to the telemetry baseband.

The NSS receiver is actually three receivers operating on signals from the low-frequency vertical loop, the horizontal loop, and the electric antenna. The output from each of these receivers is commutated into a common logarithmic amplifier, amplitude detector, and phase detector. Alternate samples of amplitude and phase from each receiver in succession are applied to an IRIG VCO by means of another commutator.

The impedance probe measures the complex impedance of the electric antenna at 1.54 and 120 kc. Two oscillators operating at 1.54 and 120 kc supply signals, which are current injected into the antenna and used as a reference for measuring the phase of the resulting voltage. Common amplitude and phase detectors are used for both signals alternately and the detected amplitude and phase are applied alternately to a single IRIG VCO by a commutator.

An oscillator (224 cps on Aerobee 4.58 UI and 112 cps on Aerobee 4.59 UI) is used to provide signals for the commutators used in the NSS receiver and impedance probe. This same signal is used on Aerobee 4.58 UI to operate the scalars which step the sweep oscillator used as a local oscillator for Bands 1, 2, and 3. A separate oscillator at 515 cps is used on Aerobee 4.59 UI. The sweep oscillator is also used to sweep the sweeping oscillator for Band 4 by using first a frequency-to-voltage converter (discriminator) and then applying this voltage to a VCO operating

at a frequency appropriate for Band 4. The Band 4 receiver thereby sweeps (steps) over its frequency range in synchronism with Bands 1, 2, and 3.

A calibrator generates signals in each of the receiver frequency bands; these signals are applied periodically during the flight. The calibrator also operates a relay in the electric antenna preamplifier to connect a known impedance in place of the antenna. In addition, signals (22.3 kc) are applied to the common portions of the NSS receivers whenever the calibrator operates.

Rocket sustainer chamber pressure signal is obtained by a pressure sensor mounted in the combustion chamber and applied directly to an IRIG VCO.

On Aerobee 4.58 UI, a sun-earth aspect sensor provides signals in turn to electronics for amplification and to an IRIG VCO. The data are in the form of received intensity of the sun's radiation, which is related to the angle between the rocket axis and the sun direction, and to times when the earth sensor is observing either the earth or space, which indicates angular displacement of the rocket about its axis.

On Aerobee 4.59 UI, a moon sensor provides signals in turn to electronics for amplification and to an IRIG VCO. The moon sensor consists of a sensing device mounted behind a mask that is perforated with unambiguously coded slots to give a direct indication of the angle between the sensor direction and the moon direction. The conic half-angle between the moon direction and the rocket axis is then known.

On Aerobee 4.58 UI, the temperature is measured at two locations on the fiberglass nosecone and one place in the instrumentation section. A voltage measurement is made to determine the status of the 20-volt regulator. This data is commutated onto a single IRIG VCO.

On Aerobee 4.58 UI, a linear accelerometer measures longitudinal acceleration. The output is applied directly to an IRIG VCO.

On Aerobee 4.59 UI, a pair of orthogonal accelerometers measure lateral acceleration near the combustion chamber of the sustainer. These

data are applied to two IRIG VCO's during the first 15 sec of flight and then are disconnected by a 15-sec G-actuated timer. The two IRIG channels are then available for data from the conductance probe. The conductance probe measures the conductance of a small antenna (probe) at 112 cps. The voltage (dc) is varied on the probe to obtain variation of conductance with biasing potential. The conductance and bias data are then applied to two VCO's as indicated above.

The data from all VCO's as well as the broadband data are applied to an FM transmitter operating at 240.20 Mc and transmitting 0.5 w via the Fin I antenna.

A battery consisting of 21 1-amp-hour, rechargeable, silver-zinc cells supplies power to all instrumentation except the DRW-13 cutoff receiver. The 28-v regulator supplies power to the telemetry transmitter and VCO's and to a 20-v subregulator. The 20-v subregulator supplies all power to the experiment instrumentation.

The DRW-13 receiver has its own battery and utilizes the Fin III antenna. On Aerobee 4.58 UI, the DRW-13 was used strictly for cutoff purposes; on Aerobee 4.59 UI, the DRW-13 was also used for command back-up of the G-actuated timer and for resetting the calibration sequence.

5. MECHANICAL DESCRIPTION OF PAYLOAD

In the following discussion, reference is made to Fig. 5.1.

Although it was desirable to have receiving antennas of large size and to isolate the various antennas from one another, the experiment instrumentation was designed to fit substantially inside the profile of a standard Aerobee nosecone and 15-inch payload extension. This design criterion was established to eliminate the complexity and possible unreliability of protruding or deployed apparatus, which would have been necessary in order to increase the size and isolation of the various antennas. A dielectric nosecone was employed to prevent the antennas from being electrically shielded by the nosecone. An alternative would have been to eject an aluminum nosecone at high altitude; however, this would have prevented satisfactory operation in the launch tower (for final operation tests) and at low altitudes where background data were desirable.

The loop antennas were placed on a phenolic structure inside the nosecone. The two orthogonal loops with vertical planes were designed to have the maximum possible area and had a shape very nearly that of the vertical cross-section of the nosecone. A third horizontal loop was wound around the vertical loops in a circle very nearly equal in area to the horizontal cross-section of the nosecone at its base. An electric antenna consisting of two 1-inch-wide strips of thin brass was attached to the outside of the nosecone. Phenolic discs, which acted as cross supports for the vertical loop antenna structure were also used to support the preamplifiers associated with the various antennas.

All of the remaining electronics, including power supply, batteries, command receiver, and telemetry system, were located in the 15-inch extension. This compartment was electrically closed to prevent coupling of electromagnetic interference into the antennas. Two openings were made in the extension: one for mounting an aspect sensor and one for an inspection port. The entire payload was pressurized during flight.

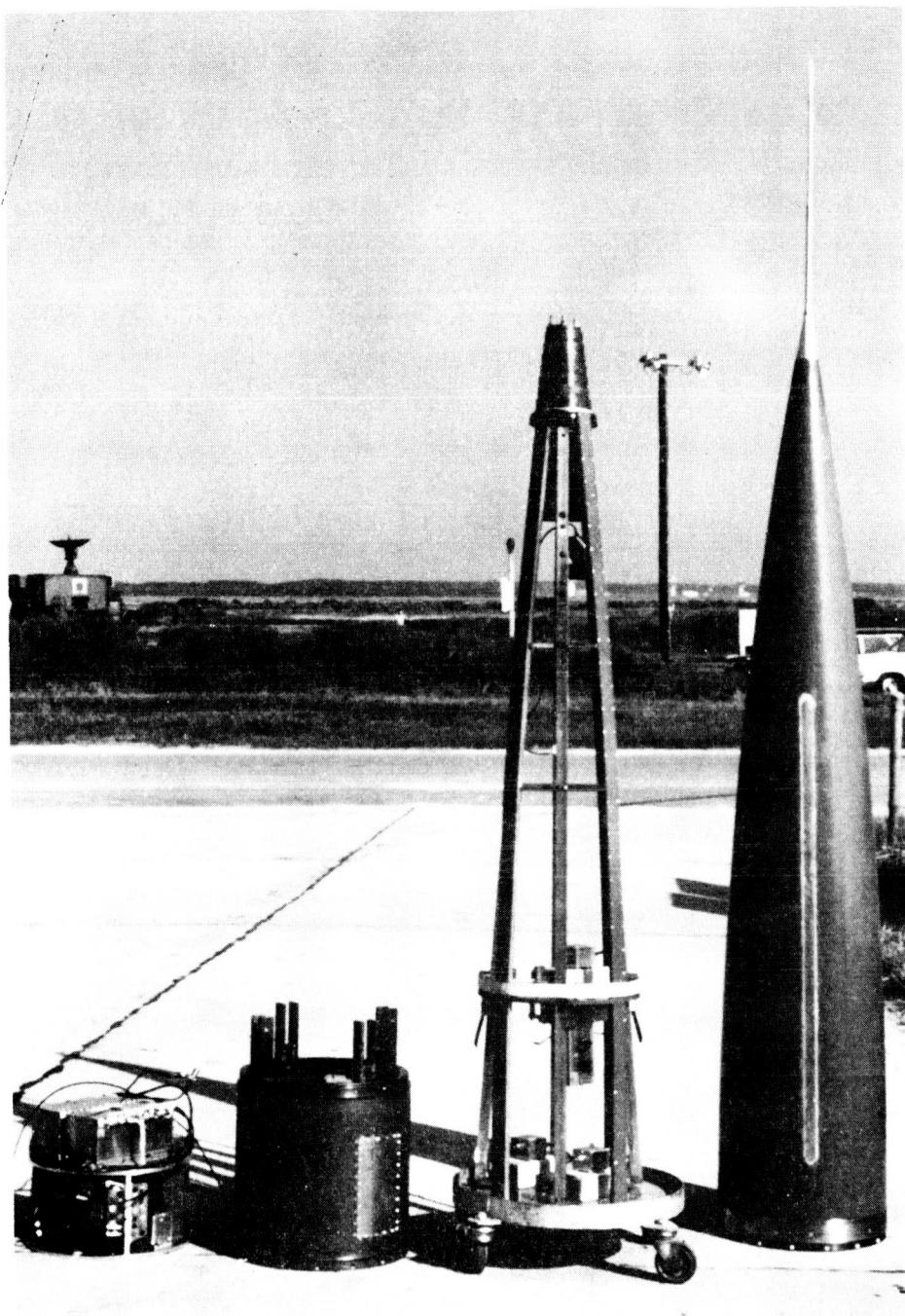


FIG. 5.1 AEROBEE 4.59 UI PAYLOAD

On Aerobee 4.59 UI, a protrusion from the nosecone was made. This was a probe consisting of a pointed aluminum $3/8$ -inch rod about 24 inches long with an insulated concentric aluminum sleeve $1/2$ inch in diameter enclosing the bottom half of the rod. This probe was mounted in a modified stainless steel nosecone tip. The size, shape, and rigidity of the probe were designed to have least aerodynamic effects.

Telemetry and command receiver antennas were standard Aerobee fin antennas and were connected to the payload with cables routed through the sustainer regulator compartment and then through the sustainer shrouds.

At the time that the payload for Aerobee 4.58 UI was ready for launch, two Aerobee rockets with similar payload weight distribution and employing dielectric nosecones sustained catastrophic mechanical failures during the early stages of their flight (see Sec. 3). Investigation of the failures indicated that it was reasonable to assume that the payload configuration contributed substantially to the failures. It was therefore recommended that payload configuration of Aerobee 4.58 UI and Aerobee 4.59 UI be modified. As a result, two significant changes in payload configuration were made:

- (1) A support structure consisting of four 1-inch aluminum bars in the form of two orthogonal A-frames was placed inside the nosecone and buffered against the nosecone to provide support for the nosecone to make the dielectric nosecone essentially as rigid as an aluminum one; and
- (2) This same support structure was used to support thirty pounds of lead weight very near to the nosecone tip, which substantially changed the location of the center of gravity of the payload.

6. GROUND SUPPORT EQUIPMENT

6.1 Checkout Sets

To operate the payload during prelaunch tests, two checkout sets were designed and constructed, one power control unit and one signal monitor unit. These were built into portable cases which could be easily hand carried to desired testing facilities.

The power control unit was designed to operate directly into an internal connector on the payload or through the umbilical cable, which was brought into the blockhouse at Wallops Island. This unit had the following capabilities:

- (1) Supply and monitor external power, with or without the payload batteries connected;
- (2) Charge the payload batteries, with or without the payload operating;
- (3) Operate and monitor the payload latching relay, which switched between internal and external power;
- (4) Monitor the 20-volt regulator and the instrumentation temperature;
- (5) Supply power to a payload heater (on Aerobee 4.58 UI, deleted on Aerobee 4.59 UI).

The signal monitor unit was used to monitor the telemetry data by observing the composite modulation being applied to the transmitter, by observing the output of the transmitter, or by observing the output of a telemetry receiver receiving the transmitted data. In each case the appropriate IRIG VCO signal was filtered from the remaining data, discriminated, and appropriately scaled to represent the data being applied to the VCO's in the payload. For monitoring the transmitter, a 50-ohm load was applied and the output power was monitored. An external oscillator input was provided to calibrate the discriminator and output amplifier.

The signal monitor unit could also be connected to an internal monitoring connector, which brought out points for monitoring various critical

data before the data were applied to the telemetry system. These monitoring points were wired to test points on the signal monitor unit.

6.2 Ground Receiver

In order to compare the NSS and broadband signals received in the rocket with these same signals received on the ground, a ground receiver was designed and constructed for operation at Wallops Island during launch.

A short whip and broadband (0.2-100 kc) preamplifier were located near the blockhouse; the preamplifier output was connected to the receiver in the blockhouse with a coaxial cable. Several outputs were available from the receiver for recording on chart and magnetic tape. The ground broadband data were recorded on tape for direct comparison with the broadband data from the rocket. The broadband data from the rocket (in the form of translated data, as described in the section on rocket broadband receiver) were recorded on magnetic tape by recording the telemetry receiver base-band signal. To obtain rocket broadband data with a minimum of interference from the VCO channels and a minimum of tape recorder noise contamination and to obtain the signals in the original frequency spectrum, the ground receiver was designed to retranslate the broadband data from the 70.1-79.4 kc range back to the 0.2-12.5 kc range. These data were then recorded on a tape recorder channel. The retranslation was performed by using the oscillator signal (66.9 kc) transmitted from the rocket; thereby preserving the phase of the broadband data (except for telemetry propagation delay). The phase of the 66.9-kc oscillator signal from the rocket was compared with the phase of the NSS signal received on the ground and the output of the phase comparator was recorded on strip chart. In this way, except for telemetry propagation delay, the relative phase of the NSS signal received in the rocket with respect to that received on the ground could be determined.

7. DATA RECORDING AND DATA REDUCTION

7.1 General

All data from the rocket flights were recorded by the telemetry stations at Wallops Island. Both the blockhouse and the main-base telemetry stations participated in receiving and recording the data transmitted from the rocket via the single FM/FM transmitter aboard. Excellent telemetry signals were obtained for the entire flight on both Aerobee 4.58 UI and Aerobee 4.59 UI, providing high-quality recordings in each case. The data were recorded on magnetic tape and on oscillograph chart paper. The magnetic tape recordings included the output from a ground receiver at the blockhouse on Aerobee 4.58 UI and from ground receivers at both the blockhouse and the main base on Aerobee 4.59 UI. The phase comparison between the reference oscillator in the rocket payload and the NSS signal received on the ground at the blockhouse was also recorded on the chart record. The broadband spectral data from the rocket as well as from the ground receiver were recorded only on magnetic tape because of its large bandwidth. The oscillograph recordings also included lift-off signal, timing signals, and telemetry receiver AGC signal. Samples of the oscillograph recordings are shown in Figs. 7.1 and 7.2. Due to the relatively short duration of each flight (≈ 7 min), the majority of the data were hand-scaled directly from these oscillograph recordings. The broadband spectral data and the spectral data obtained by the sweeping receivers required processing as described in Sec. 7.4 and 7.5.

7.2 Radar and Photography

Rocket flight trajectory data on both flights were obtained by skin-track radar. The data were in the form of plot-board curves as well as tabulated data. Slant range, azimuth, and elevation angle were obtained. Ground range, ground track, and altitude were hand-calculated from these data.

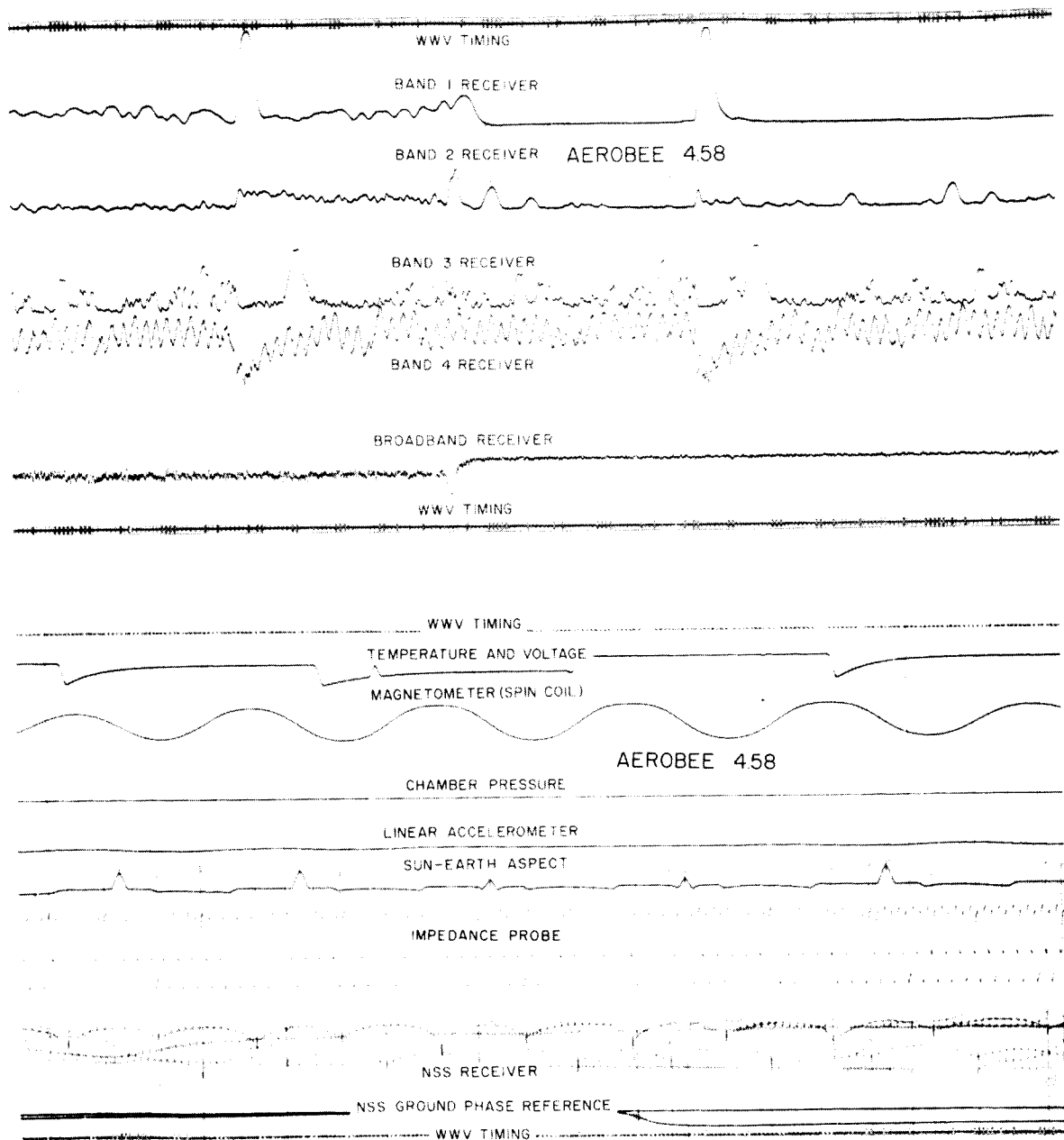


FIG. 7.1 AEROBEE 4.58 UI OSCILLOGRAPH CHART RECORDINGS

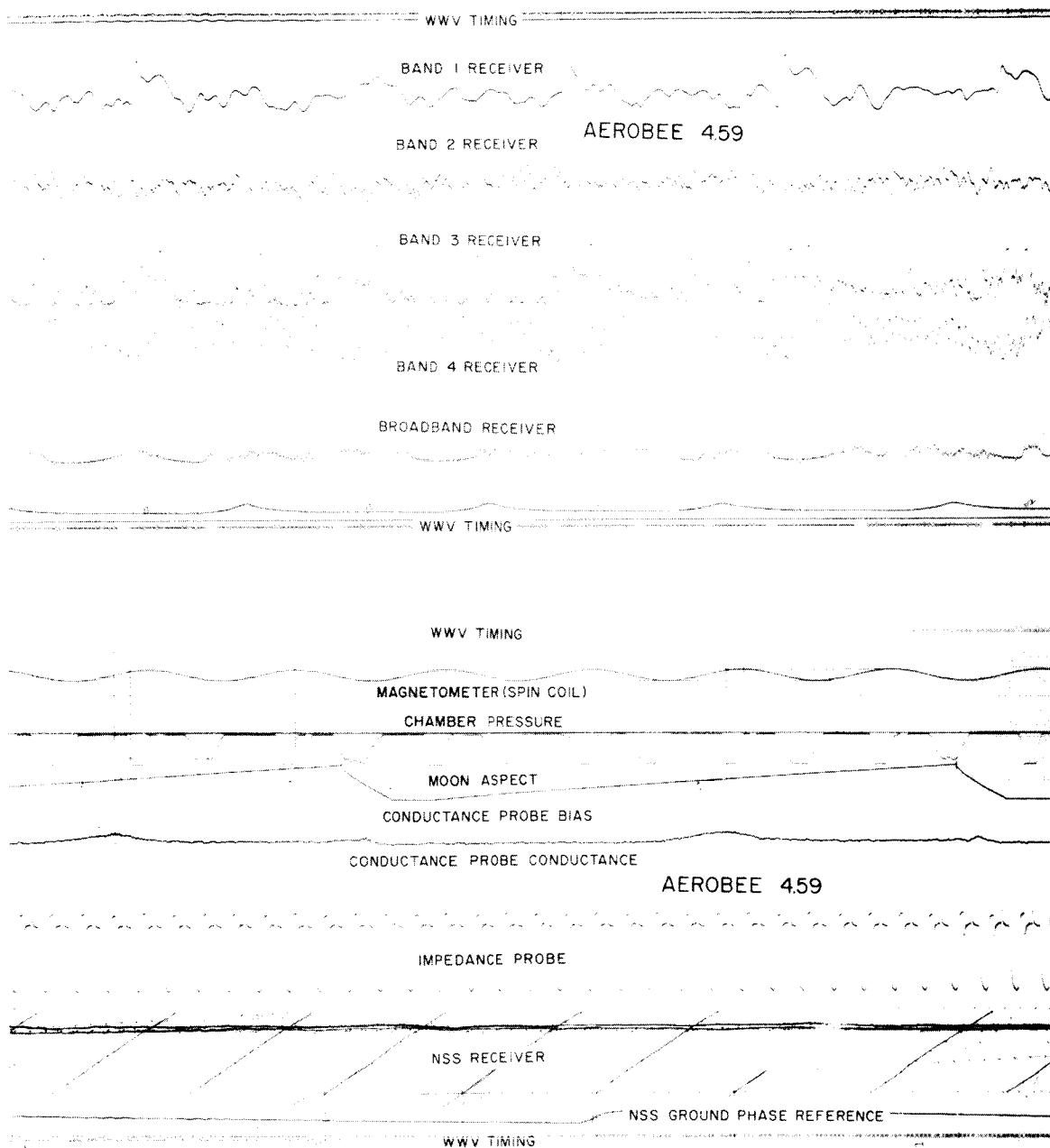


FIG. 7.2 AEROBEE 4.59 UI OSCILLOGRAPH CHART RECORDINGS

The initial portions of the rocket flights were photographed with high-speed movie cameras by Wallops Island personnel. These photographs gave an indication of initial rocket performance.

7.3 Ionosonde

Ionosonde data were taken by the ionosonde station at Wallops Island. Ionosonde records were taken at 15-minute intervals for two hours before and after the flight and at 30-second intervals during the flight. These ionosonde recordings, in the form of photographs, were scaled to give critical frequency versus altitude, thus providing an electron density profile.

7.4 Broadband Spectrum Analysis

The broadband spectrum from the broadband receivers in the rocket and on the ground were recorded on magnetic tape, and a spectrum analysis was performed with a spectrum analyzer (Rayspan) at Stanford University. Several samples of spectrum produced by the Rayspan are shown in Sec. 8. The Rayspan consists of a set of narrow-band filters equally spaced in frequency (comb filter), a cathode ray tube intensity-modulated display of the output of each filter, and a camera for recording the display. The Rayspan spectrum analysis covered the frequency range of 0 to 20 kc.

7.5 Panoramic Data Display, Sweeping Receivers

Because of the large amount of data obtained from the sweeping receivers a method was sought which would allow viewing of the data in a short time. All four of the sweeping receivers' outputs, which appeared as consecutive sweeps on one chart recording, were photographed on motion picture film. On Aerobee 4.58 UI, each receiver sweep was photographed on two consecutive frames of film to reduce flicker when the film was projected at low speeds. On Aerobee 4.59 UI each receiver sweep was photographed on two consecutive frames; however, each frame contained two sweeps and the photograph of an individual sweep would first appear in the right half of the frame and then on the left half of the frame. The sweep appearing on the left half of the frame had a frequency- and amplitude-scale overlay. The sweep on the right appeared uncluttered.

By operating the projector at 16 frames per second, the receiver data could be displayed in one eighth the time in which it was received by the rocket. By varying the projector speed, interesting features of the data could be examined for longer times. In this way the data could be very conveniently displayed in a form of panoramic spectrum display that could be observed at variable rates.

A similar technique is to be used to scan the sweeping receiver data gathered by the EOGO satellite. Each bit of digital data obtained from EOGO will be displayed on a CRT by a specialized computer in a form to reconstruct the spectral display. This CRT may be viewed directly or photographed by a step-frame motion picture camera. This film may be viewed as described above and the time contraction of the display will be even more pronounced. It is expected that an entire year's data may be displayed in approximately one day of continuous film viewing. The EOGO display will also contain other data helpful for data analysis such as time, satellite orbit data, geophysical data, etc.

8. FLIGHT TRAJECTORY AND DISCUSSION

8.1 Trajectory

The altitude and ground track for each flight were calculated from the data obtained from the tracking radar data (slant range azimuth, and elevation angle). The calculated trajectories are shown in Figs. 8.1 and 8.2. Note that the altitude is not corrected for curvature of the earth; instead the altitude shown is with respect to a plane tangent to the earth at the launcher site. The correction for true altitude is minor, less than 1 km at 100-km range.

Figure 8.3 shows an azimuth projection about the launcher giving directions of trajectories and other useful directions.

8.2 Aspect

8.2.1 General

The aspect of the rocket spin axis was determined from data obtained from the spin-coil magnetometer and sun-earth sensor on Aerobee 4.58 UI and the spin-coil magnetometer and moon sensor on Aerobee 4.59 UI. The results are given in Sec. 8.2.4.

8.2.2 Sun-Earth Sensor, Aerobee 4.58 UI

The sun-earth sensor flown on Aerobee 4.58 UI was supplied by NASA. This sensor was an analog device that gave an output proportional to the intensity of the solar radiation. With respect to the output given when the radiation is normal to the sensor, the output decreases as the cosine of the angle between the radiation and the normal to the sensor. It is difficult to obtain a calibration source that is representative of sunlight at the rocket altitudes; however, in principle at least, a calibration point can be obtained during the powered portion of the flight by assuming the spin axis to be aligned with the trajectory direction. The sensor is best suited to solar directions near the normal to the sensor. Unfortunately, on Aerobee 4.58 UI the angle between the solar direction and the normal to the sensor was approximately 75 degrees.

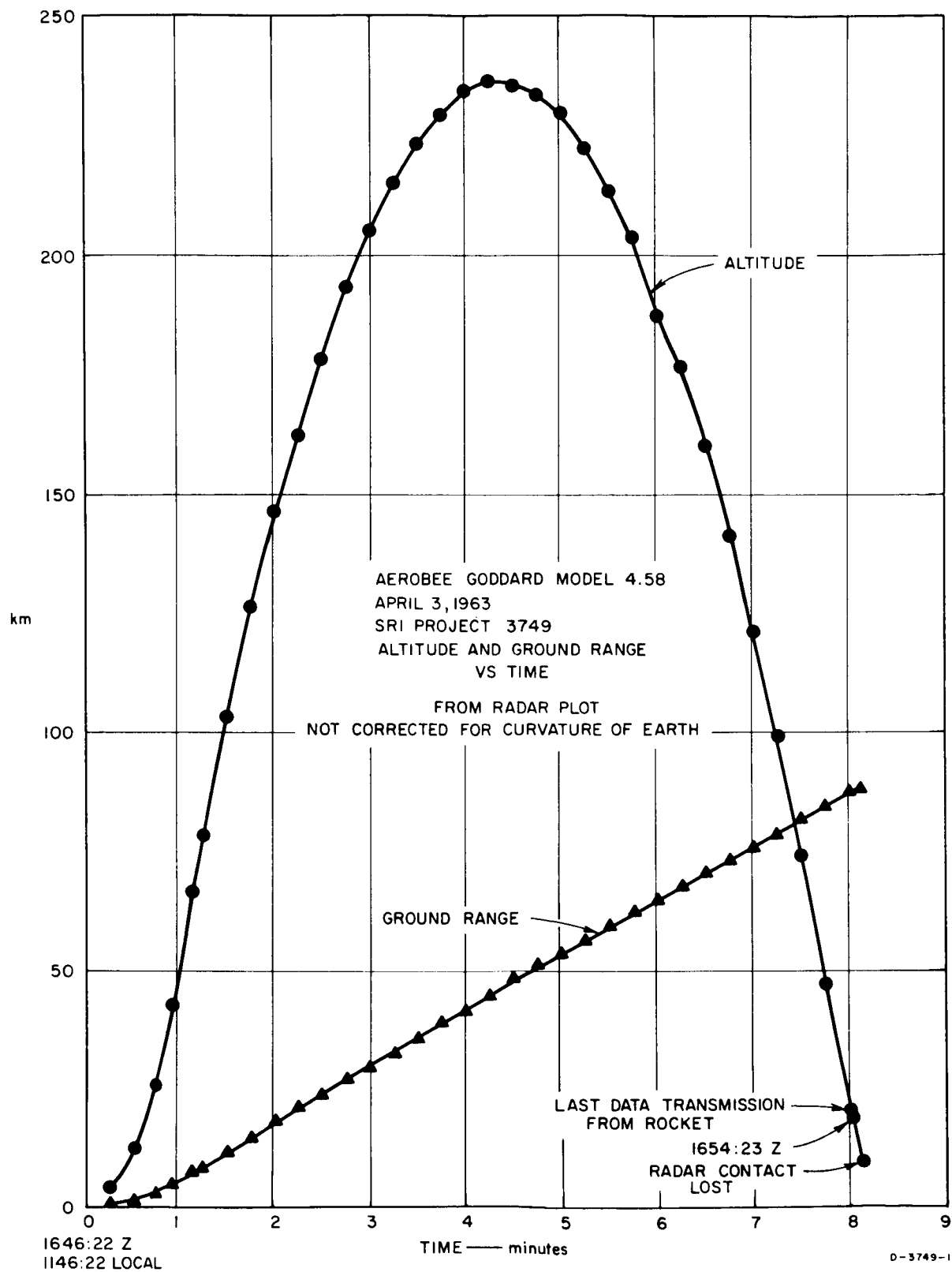


FIG. 8.1 AEROBEE 4.58 UI TRAJECTORY

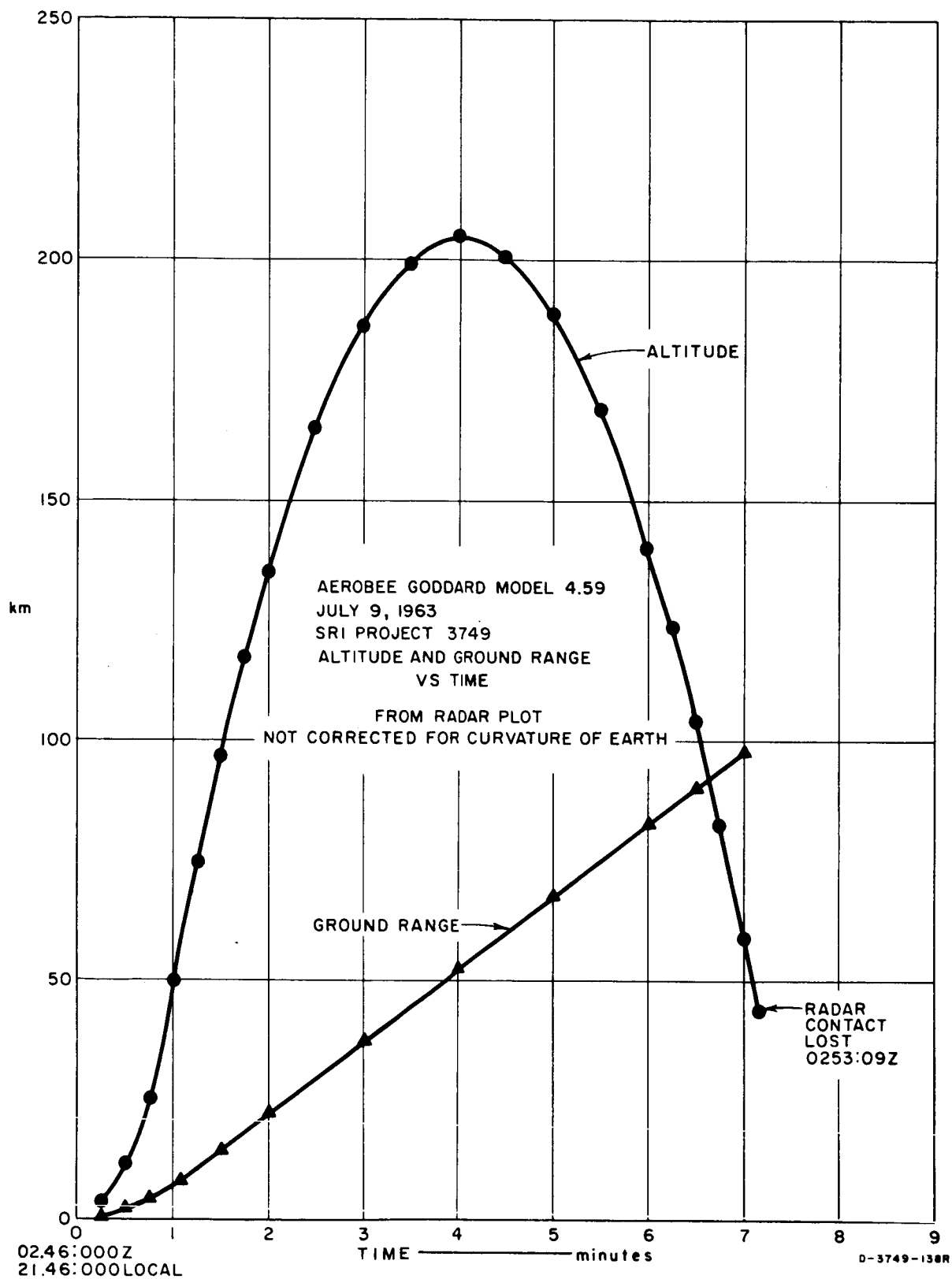


FIG. 8.2 AEROBEE 4.59 UI TRAJECTORY

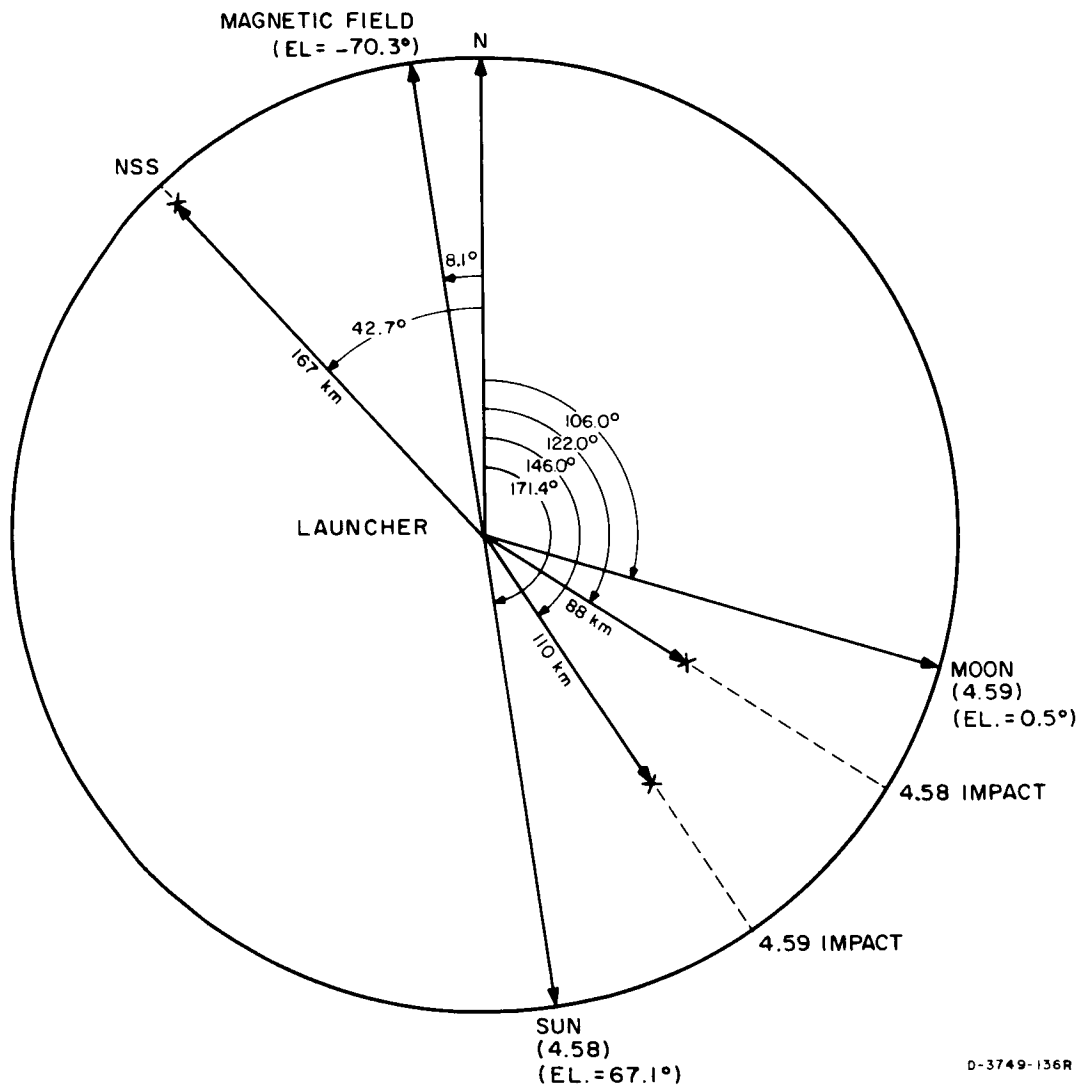


FIG. 8.3 FLIGHT GEOMETRY

This gave very low-level output signals, which were not considered accurate. The sun sensor did, however, give the times when the sensor was pointing (in azimuth) at the sun, thereby giving data concerning the spin angular displacement. This data was used to resolve the ambiguity in the magnetometer data.

The earth sensor on the unit is used to resolve ambiguities in the sun sensor; however, due to the near-vertical flight trajectory, the earth was not in the field of view until very near the end of the flight and the sensor proved not to be particularly useful.

8.2.3 Moon Sensor Aerobee 4.59 UI

During the night shot (Aerobee 4.59 UI), attitude information was provided by a spin-coil magnetometer (see Sec. 8.2.4) and a moon sensor. Since the photomultiplier sensor available from NASA was too big to fit in the electronics section of the payload without a complete redesign, and putting it in the plastic nosecone was undesirable for both structural and electrical interference reasons, a small all-transistor sensor was developed and flown.

In principle, the sensor used was a simple shadow-mask mounted in front of a phototransistor. As the rocket spun on its axis, the moon-light pattern penetrating the mask scanned across the phototransistor, generating a distinct sequence of pulses for each 2 degrees of elevation angle. The pulse sequences used formed a six-bit Gray code, preceded and followed by "on" bits. The entire eight-bit sequence occupied 90 degrees of spin angular displacement, or 0.1 second at the nominal spin rate of 2.5 rps. The system response was adequate (100 cps) for spin rates of at least 6 rps, well above the maximum expected.

The construction of the instrument was kept simple by using a wide-angle phototransistor without lens, placed 2.54 cm behind the mask. The mask itself was a photographic negative cemented to the back of a 6 cm X 10 cm Pyrex window 1 cm thick, which was mounted nearly flush with the rocket skin in a doubler contoured to the skin inside radius. A boxlike aluminum cover supported the phototransistor and enclosed it over the mask. The remaining circuitry was mounted on the back of the

cover and protected by a dust cover. Connection to +20 v power (at about 3 ma) and a telemetry VCO completed the system.

In operation, direct moonlight could fall on the sensor within a sector 90 degrees wide in azimuth, and from -30 to +60 in degrees elevation, where +90 degrees is the direction of the nose. Since no commercial photosensors were found that combined the necessary speed, sensitivity, and wide angle, they were constructed by cutting the tops off of type 2N929 silicon transistors selected for low leakage ($< 10^{-11}$ amp) and high beta. The exposed base region was less than 0.4 mm in diameter, giving theoretical resolution better than 1 degree. In practice, the transition from one 2 degree band of elevation to the next could be determined to less than 0.5 degree, the apparent diameter of the moon.

The electronic circuitry consisted of a simple seven-stage transistor amplifier, including field-effect input stage, designed to respond to frequencies from about 0.5 to 200 cps and to clip the output to a constant level (0 to +5 v) without disturbing bias levels. This arrangement, which incorporated nonlinear feedback, resulted in dynamic range sufficient to allow the same device to be used as a moon sensor or sun sensor, although it has not yet been used in the latter capacity.

Data reduction consisted of simply reading the binary pattern from the strip chart (see Fig. 7.2) each revolution to determine the moon's elevation with respect to the rocket axis. The phase delay between the moon sensor and the magnetometer was also scaled, to give the relative azimuth of the moon and magnetic field projected on a plane normal to the rocket axis. These data were combined with the magnetometer amplitude data to determine rocket attitude, as discussed in Sec. 8.2.4.

Performance of the moon sensor was excellent during the first half of the flight, which was adequate to define attitude for the entire flight until the violent re-entry maneuvers. Near apogee, the noise level rose slowly, over a period of tens of seconds, while the moon pulses slowly dropped until they were no longer visible. Although the cause of this failure is not definitely known, the most plausible explanation seems to be loss of detector sensitivity due to temperature rise.

The inside skin temperature of the instrument section would not normally be expected to rise more than 20 or 30°C. In this case, however, the window cutout may have produced severe local heating, which was transferred, with several minutes' delay, to the sensor. This problem could easily be eliminated in the future by thermal isolation of the sensor.

Several other effects were observed in the moon sensor records, but had no effect on their use for attitude determination. The first was a period of high noise bursts for about the last second before burnout, followed by two seconds at the band edge corresponding to no illumination. Within the next few seconds, while the sensor was recovering to its normal operation, a 60-msec light burst appeared at the time of command cutoff. At this time, squib-actuated valves closed the propellant lines. This behavior is consistent with the appearance of incandescent gases in the sensor's view (greater than 60 degrees off axis) at command cutoff and during the final second of burning, a time when combustion was no longer smooth, as shown by fluctuations appearing in the longitudinal acceleration. It is also possible, but seems less likely, that the vibration induced noise in the electronics. The combustion gas explanation is further supported by the electromagnetic noise spectra (Sec. 9.2.2), the simultaneous anomalies in the impedance probe data (Sec. 9.3.2), and the conductance probe data (Sec. 9.5.3) at both burnout and command cutoff, in the absence of transients on any of the other data channels except the moon sensor.

The second unexpected observation was the appearance of a diffuse light source, too large to show distinct chopping by the mask, above about 123 km altitude. It was centered at an apparent azimuth of about -24 degrees, and increased in intensity with altitude. The source was presumably scattered sunlight, since the sun was at an azimuth of -32.7 degrees and an elevation of -21.3 degrees. This put the sun 11.2 degrees below the horizon at 100-km altitude, and only 7.0 degrees below the horizon at apogee (205 km). The azimuth discrepancy is due to the nonuniform aperture of the mask.

Additional bursts, which could be scattered sunlight, appeared earlier, during the second that the rocket was penetrating the sporadic-E

layer at 108-km altitude. However, these are accompanied by other bursts in different apparent directions, some of them stronger than those in the sun's direction. To make matters still more puzzling, most of these bursts show well-defined durations, which correspond to the time it took the aperture to scan a small source. For the time being, they are simply being recorded as anomalies.

8.2.4 Magnetometer

By using a loop antenna and relying on the rocket roll or spin to rotate this loop antenna in the earth's magnetic field, the magnitude of the component of the earth's magnetic field in the direction perpendicular to the rocket axis can be measured. To the extent that the total field is known, the conic half-angle between the earth field direction and the rocket axis can be determined. By observing the zero crossings of the antenna output, the time during a spin revolution when the plane of the antenna and the plane that includes the magnetic field vector and the rocket axis are coincident can be determined. One additional independent aspect parameter--such as the angle to sun, earth, or moon-- is necessary to give unambiguous aspect.

The magnetometer consisted of the antenna and a low-frequency amplifier. The antenna was equalized so that constant output amplitude was maintained for input frequency or rocket spin rate over the range 0.25 to 30 cps. The gain of the amplifier was adjusted to give full telemetry channel output for the maximum signals that would be encountered if the rocket axis were perpendicular to the magnetic field vector. For small angles, the expected error in determining the rocket axis with respect to the magnetic field vector was in the order of 1 or 2 degrees.

The same loop antenna was used for the magnetometer and the low-frequency receivers. Precautions were necessary to prevent thermal noise from the magnetometer electronics from degrading the sensitivity of the other receivers. This was relatively easy, because of the wide frequency separation.

The outputs of the magnetometer for Aerobee 4.58 UI and Aerobee 4.59 UI are shown in Fig. 8.4.

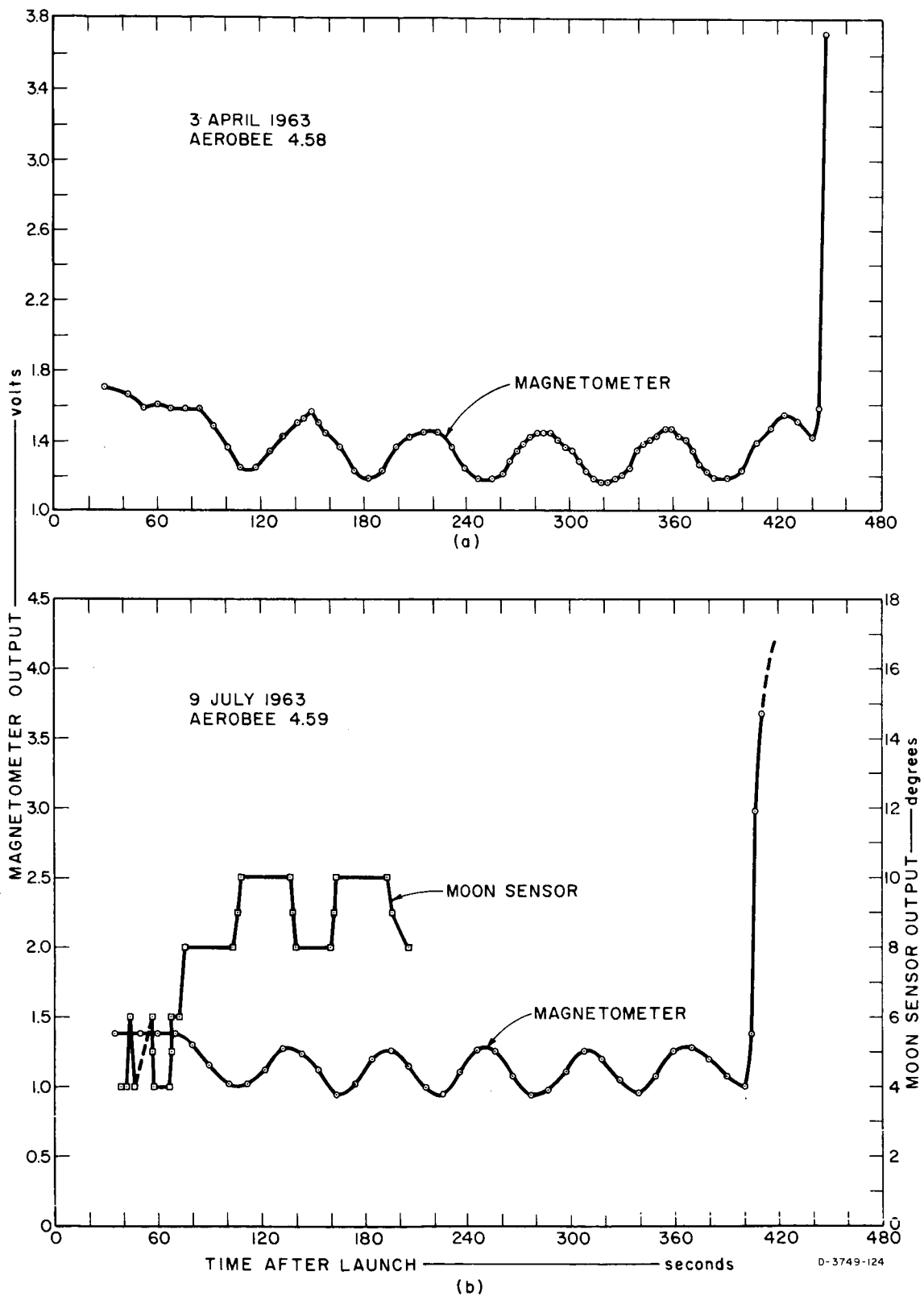


FIG. 8.4 MAGNETOMETER AND MOON SENSOR OUTPUT

By using the magnetometer and sun or moon aspect data, the attitude of the rocket can be calculated. The calculated results in the form of azimuth and elevation are shown in Fig. 8.5. Note that between the times 50 and 85 sec on Aerobee 4.58 UI and 35 and 70 sec on Aerobee 4.59 UI the rocket attitude was constant; after these times, the rocket attitude began to cone (precess). The coning angle was approximately 3.5 degrees on both flights. Since it is unlikely that any external force was exerted on the rocket at altitudes corresponding to these times, the probable cause of coning is due to a redistribution of the liquid propellants remaining in the rocket tanks. During powered flight, the propellants are kept aft in the tanks by rocket acceleration; after this acceleration ceases (burnout), the remaining propellants may redistribute themselves in a more stable position and result in the rocket axis no longer being aligned with the angular momentum vector (simple coning). The burnout distribution of the propellants may be conditionally stable and the time of redistribution will then be arbitrary, thus explaining the different times at which Aerobee 4.58 UI and Aerobee 4.59 UI began to cone.

In addition to attitude, the rocket spin rate and the instantaneous angular displacement of the rocket about the spin axis can be determined from the magnetometer as well as from the moon and sun sensors. The angular displacement data is not presented here but was used to determine the orientation of the loop and electric antennas. The spin rate varied during the flight preceding burnout but remained constant thereafter. The constant rates were 2.455 and 2.900 rps for Aerobee 4.58 UI and 4.59 UI respectively. The relationship between spin rate and velocity for Aerobee 4.59 UI is shown in Fig. 8.6. During booster burn (less than 3 sec) the spin increased rapidly; however, as soon as the booster was expended, the spin rate immediately decreased to a value determined by the total rocket velocity and the rocket effective fin angles. Except for a short time between 19 and 25 sec, the spin rate variation followed very closely the velocity variation indicating a

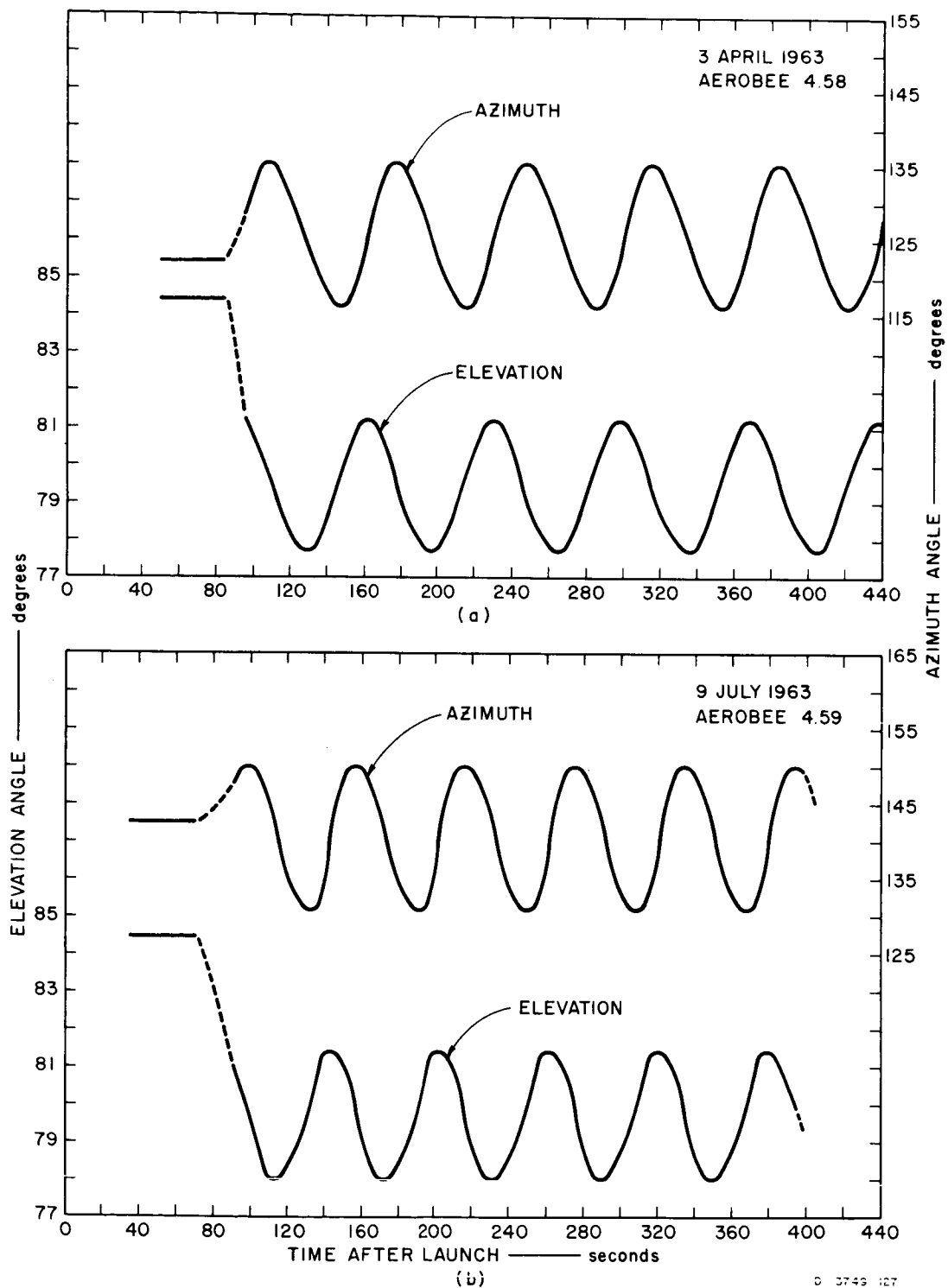


FIG. 8.5 ATTITUDE OF ROCKET SPIN AXIS

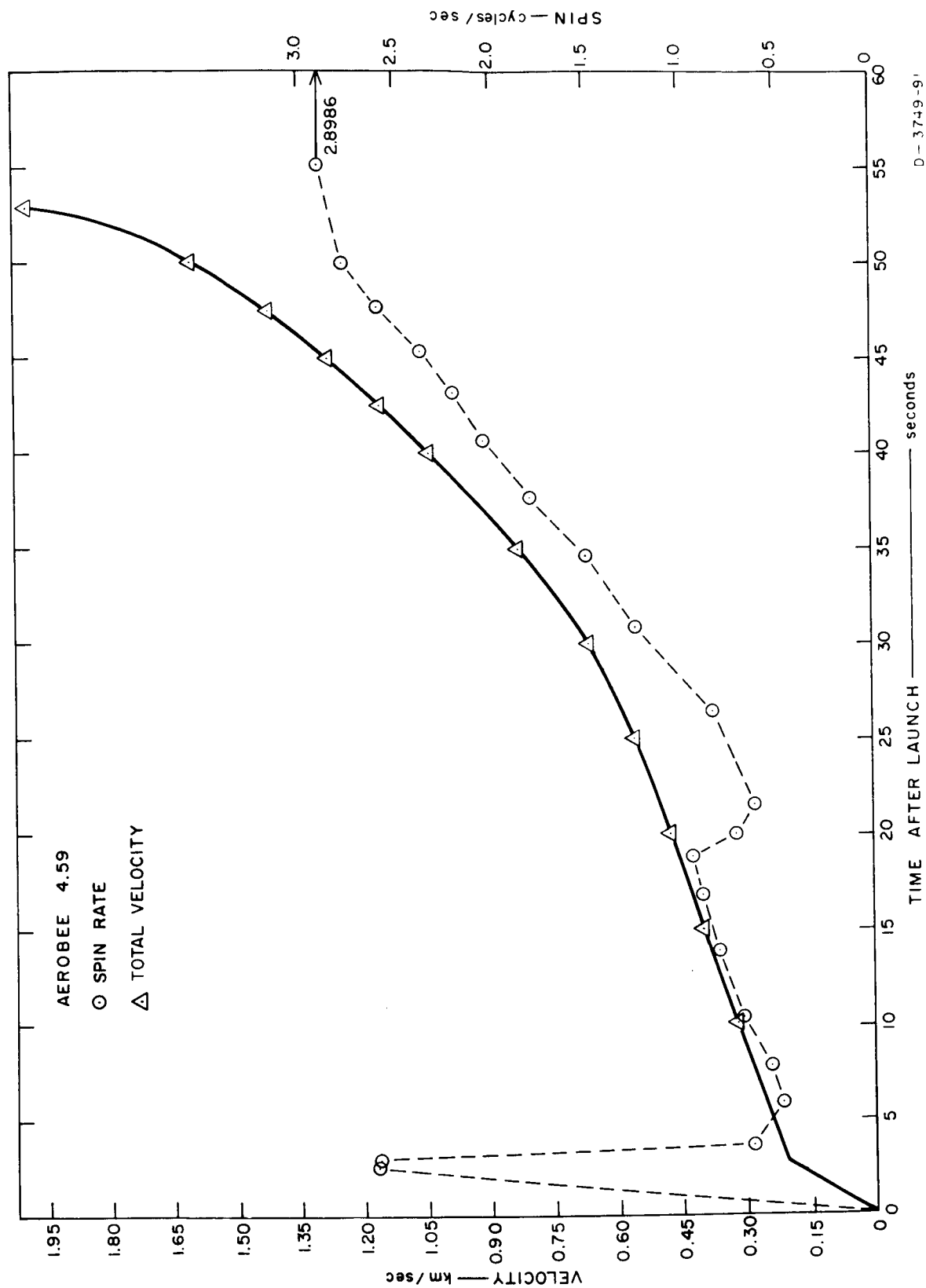


FIG. 8.6 ROCKET SPIN RATE AND TOTAL VELOCITY

tight coupling of the fins to the atmosphere. As the atmospheric density decreases with altitude, the fin coupling decreases and spin no longer follows the total velocity. At 50 sec (35 km altitude) the spin becomes very nearly constant, independent of the increasing velocity.

9. DATA ANALYSIS AND DISCUSSION

9.1 Narrow-Band Sweeping Receivers

9.1.1 Instrumentation

The four sweeping receivers flown on Aerobee 4.58 UI and Aerobee 4.59 UI were: Band 1, 0.20 to 1.6 kc; Band 2, 1.6 to 12.5 kc; Band 3, 12.5 to 100 kc; and Band 4, 1250 to 1600 kc.

The electrical design and individual circuit boards for Bands 1, 2, and 3 corresponded to the three narrow-band sweeping receivers that were flown on the EOGO satellite. Mechanical mounting of the circuitry was modified for the rocket payloads.

Refer to the simplified block diagram in Fig. 9.1 for the following discussion.

Bands 1, 2, and 3 share a low-frequency vertical loop antenna and low-noise preamplifier. On Aerobee 4.58 UI, a 42-turn unshielded loop was used; on Aerobee 4.59 UI, a 12-turn shielded loop was used. The area on both was 0.48m^2 and the inductance was 5.0 and 0.41 mh, respectively. A matching network between the antenna and the preamplifier allows a magnetometer output to be obtained as well as calibration signals to be injected. The matching network is broadband, as is the preamplifier. The impedance presented to the preamplifier input gave optimum signal-to-noise performance at 100 kc on Aerobee 4.58 UI and at 10 kc on Aerobee 4.59 UI. The preamplifier noise temperature was approximately 50°K . Over the frequency range 0.2-100 kc, the sensitivity varied approximately from 45 to 100 db below 1 gamma* rms on Aerobee 4.58 UI and from 60 to 90 db below 1 gamma rms on Aerobee 4.59 UI. The output impedance of the preamplifier is low to provide isolation between the receiver bands that obtain their inputs from a distribution transformer at the preamplifier output.

* 1 gamma = 10^{-5} gauss.

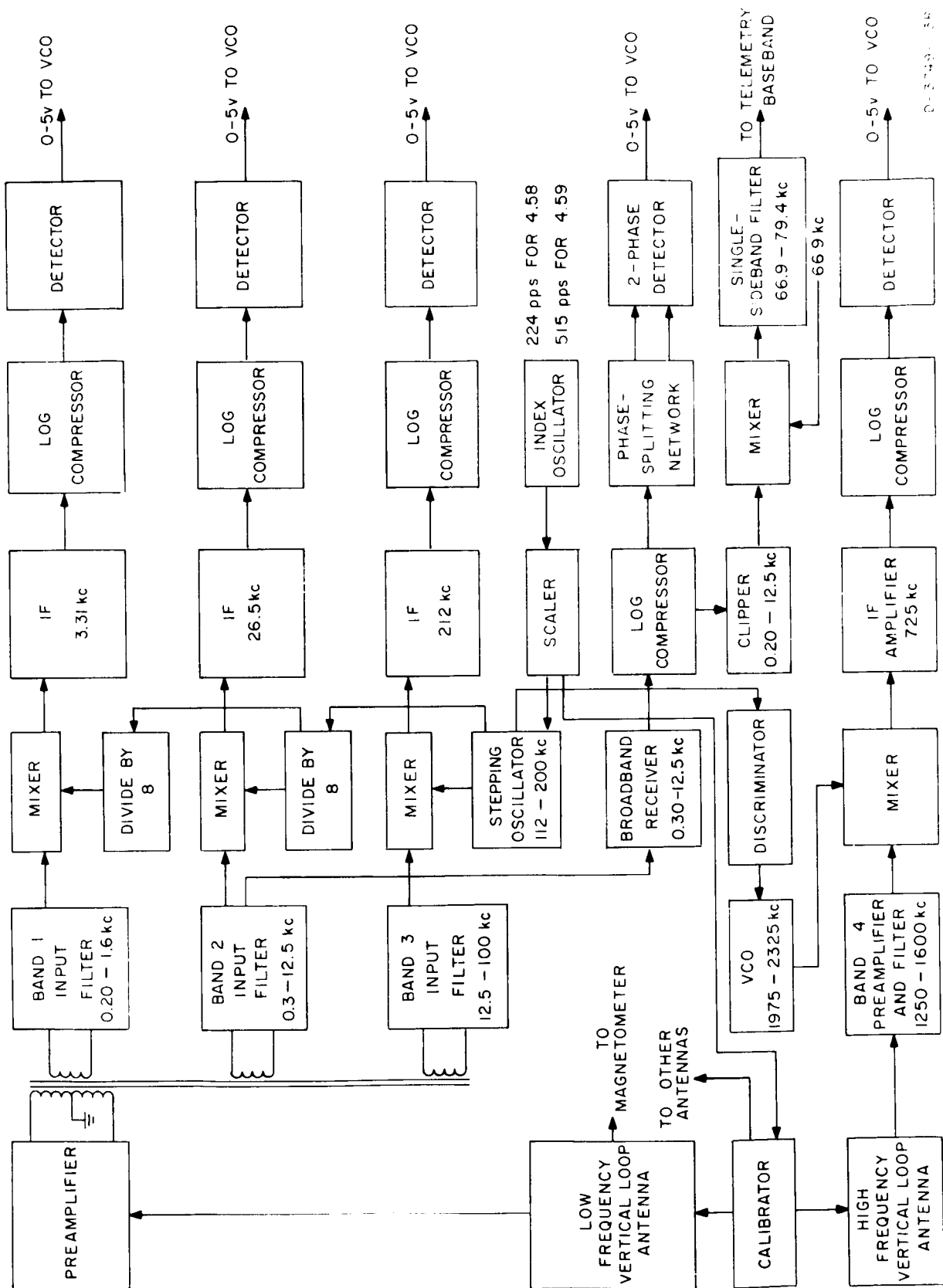


FIG. 9.1 NARROW-BAND SWEEPING AND BROADBAND RECEIVERS (Simplified Block Diagram)

The local oscillator for each of the bands is derived from a single sweep- or step-frequency oscillator operating at a frequency suitable for Band 3. For Band 3, the oscillator steps over the frequency range 112 to 200 kc; dividing by eight, the frequency range becomes 14 to 25 kc for Band 2; and dividing by eight again, the frequency range becomes 1.75 to 3.13 kc for Band 1. The Band 3 oscillator repeatedly steps from 200 to 112 kc in 256 discrete steps by varying the charging current in the timing capacitors of an astable multivibrator. The current is controlled by an eight-stage ($2^8 = 256$) binary scaler, which is stepped by index pulses from an index oscillator. The index oscillator frequency determines the sweep oscillator stepping rate and consequently the receiver sweep rate. On Aerobee 4.58 UI, the index oscillator frequency was 224 cps resulting in a sweep rate of 0.875 sweeps per second; on Aerobee 4.59 UI, the index oscillator frequency was 515 cps, resulting in a sweep rate of 2.01 sweeps per second.

The oscillator for the Band 4 receiver is also derived from the Band 3 oscillator, so that the Band 4 receiver sweeps in synchronism with Bands 1, 2, and 3.

9.1.1.1 Circuit Description of Band 1 Receiver

Refer to Fig. 9.1 for the following discussion:

The Band 1 receiver has an input low-pass filter with passband to 1.6 kc and stopband above 3.2 kc. The pass-band ripple is less than 0.5 db and the stop-band attenuation exceeds 90 db. The filter zeros exist at the IF frequency and in the image band to give additional protection against IF and image band signals.

The mixer is a saturating switching transistor operated in inverted (interchange of collector and emitter operation) configuration to reduce local oscillator feedthrough. The local oscillator signal at the output of the mixer is approximately 50 db less than the IF signal at maximum IF signal level.

The IF amplifier consists of several LC filter sections (two single-pole and two double-pole stages) with amplifiers between

stages. The IF frequency is 3.31 kc; the 3-db bandwidth is 40 cps; and the 60-db bandwidth is 450 cps. The IF amplifier is followed by a logarithmic compressor that compresses an 80-db dynamic range of input signal into approximately 20-db output range. A typical response curve is shown in Fig. 9.2. The log-compressed signal is average detected, low-pass filtered, and applied to the telemetry VCO in the form of a 0- to 5-v signal for an 80-db range in input signal. The output low-pass filter is a single-section RC filter with a time of constant 6 msec on Aerobee 4.58 UI and 5 msec on Aerobee 4.59 UI.

9.1.1.2 Circuit Description of Band 2 Receiver

Refer to Fig. 9.1 for the following discussion:

The Band 2 receiver has an input low-pass filter with passband to 12.5 kc and stopband above 25 kc. The pass-band ripple is less than 0.5 db and the stop-band attenuation exceeds 90 db. The filter zeros exist at the IF frequency and in the image band to give additional protection against IF and image band signals.

The mixer is a saturating switching transistor operated in inverted (interchange of collector and emitter operation) configuration to reduce local oscillator feedthrough. The local oscillator signal at the output of the mixer is approximately 50 db less than the IF signal at maximum IF signal level.

The IF amplifier consists of two two-pole LC filter sections with amplifiers between stages. The IF frequency is 26.5 kc; the 3-db bandwidth is 160 cps; and the 60-db bandwidth is 1300 cps. The IF amplifier is followed by a logarithmic compressor that compresses an 80-db dynamic range of input signal into approximately 20-db output range. A typical response curve is shown in Fig. 9.2. The log-compressed signal is average detected, low-pass filtered, and applied to the telemetry VCO in the form of a 0- to 5-volt signal for an 80-db range in input signal. The output low-pass filter is a single-section RC filter with time a constant of 2.3 msec on Aerobee 4.58 UI and 1.5 msec on Aerobee 4.59 UI.

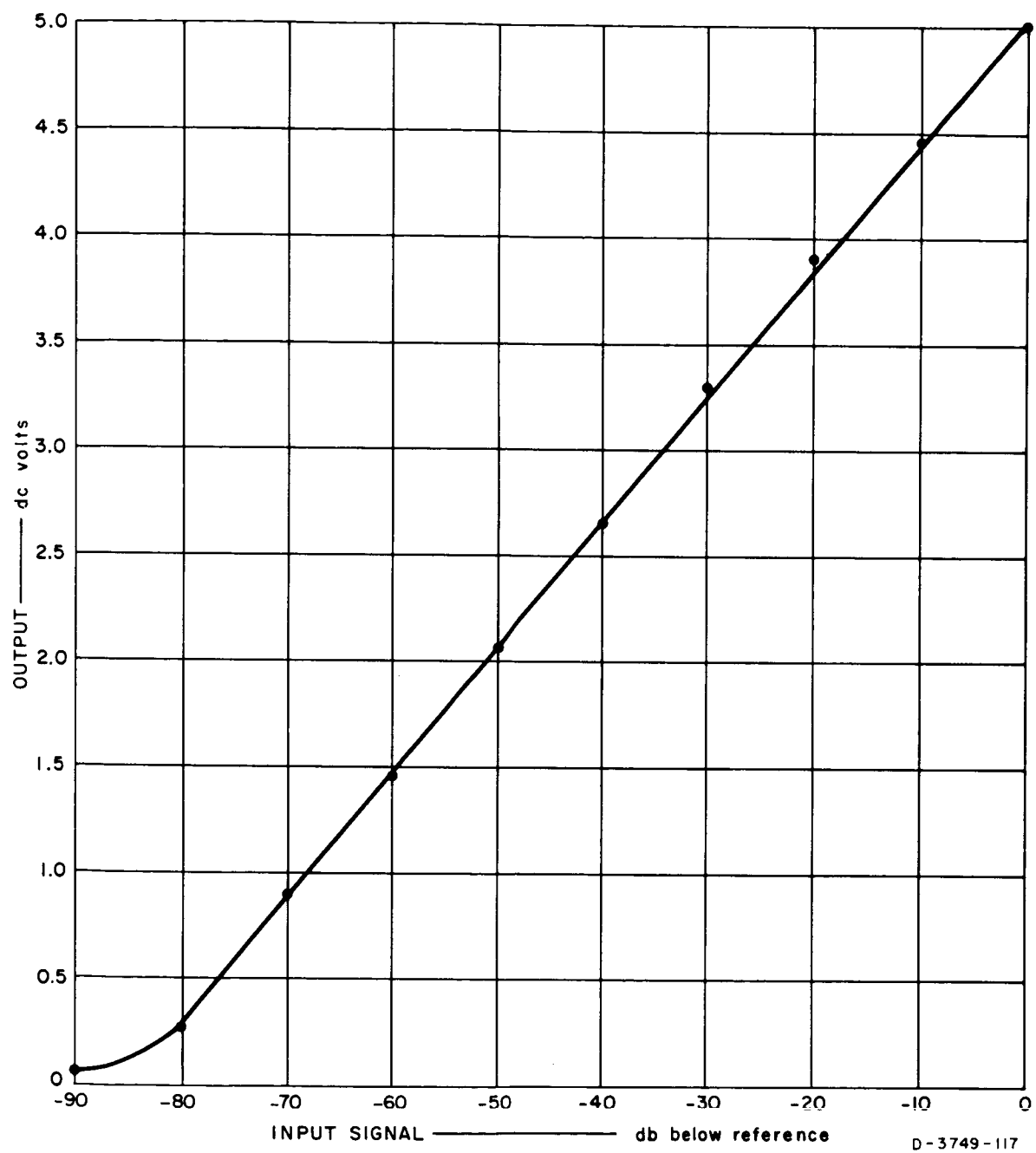


FIG. 9.2 TYPICAL LOGARITHMIC COMPRESSOR RESPONSE

9.1.1.3 Circuit Description of Band 3 Receiver

Refer to Fig. 9.1 for the following discussion:

The Band 3 receiver has an input low-pass filter with passband to 100 kc and stopband above 200 kc. The pass-band ripple is less than 0.5 db and the stop-band attenuation is approximately 90 db. The filter zeros exist at the IF frequency and in the image band to give additional protection against IF and image band signals.

The mixer is a saturating transistor operated in inverted (interchange of collector and emitter operation) configuration to reduce local oscillator feedthrough. The local oscillator signal at the output of the mixer is approximately 40 db less than the IF signal at maximum IF signal level. The IF amplifier consists of two two-pole LC filter sections with amplifiers between stages. The IF frequency is 212 kc; the 3-db bandwidth is 600 cps; and the 60-db bandwidth is 4500 cps. The IF amplifier is followed by a logarithmic compressor that compresses a 80-db dynamic range of input signal into approximately 20-db output range. A typical response curve is shown in Fig. 9.2. The log-compressed signal is average detected, low-pass filtered, and applied to the telemetry VCO in the form of a 0- to 5-volt signal for an 80-db range in input signal. The output low-pass filter is a single-section RC filter with time a constant of 1.0 msec on Aerobee 4.58 UI and 0.75 msec on Aerobee 4.59 UI.

9.1.1.4 Circuit Description of Band 4 Receiver

Refer to Fig. 9.1 for the following discussion:

The Band 4 receiver consisted of an independent vertical loop antenna, preamplifier, local oscillator, mixer, IF amplifier, logarithmic compressor, and average detector.

On Aerobee 4.58 UI, a four-turn unshielded loop of 96/36 litz wire was wound in the approximate shape of the nosecone. The area was 0.48 m^2 and the inductance was 52 μh . This inductance was made an element in the RF preselection filter. On Aerobee 4.59 UI, a single-turn shielded loop of RG-58/U coaxial cable was used and wound in the

same shape and had the same area as on Aerobee 4.58 UI. The outer conductor of the coaxial cable was used as the shield. This conductor was broken at the top to prevent coupling a shorted turn to the antenna. The shield was grounded at the bottom to the center tap of the input transformer, thus providing a balanced shield to minimize sensitivity to electric fields. The antenna and balanced-to-unbalanced input transformer were made an integral part of the input filter. A calibration signal was injected at the input filter on both Aerobee 4.58 UI and Aerobee 4.59 UI.

The preamplifier consisted of the input filter mentioned above; a low-noise, broadband amplifier; and another filter. The preamplifier noise temperature was approximately 60°K . The minimum detectable signal field strength was approximately 110 db below 1 gamma rms. The filters at the input and output of the preamplifier were identical except for impedance level; the input impedance level was chosen for optimum preamplifier signal-to-noise ratio; and the output impedance was chosen to match the mixer. The filters were band-pass (1250 to 1600 kc) with 3-db ripple in the pass band and 45 db attenuation in the stop band. The filter zeros were placed at the IF frequency and in the image band to provide additional suppression of IF and image band signals.

The mixer consisted of a single transistor used as a series gate in the RF signal path and turned on and off at the local oscillator frequency. The RF signal was applied to the transistor emitter and the local oscillator signal to the base. The output was taken from the collector of the transistor, which was tuned to the IF frequency to filter out undesirable local oscillator and mixer frequencies and provided voltage gain.

The local oscillator frequency was controlled by a frequency-to-voltage-to-frequency process. To synchronize the Band 4 sweep with the other sweeping receivers, the Band 4 local oscillator was derived from the Band 3 local oscillator by first using a frequency-to-voltage converter (discriminator) to generate a sweeping voltage and then applying this voltage to a voltage-controlled oscillator, the Band 4 local oscillator. The Band 4 oscillator was an emitter-coupled astable

multivibrator which covered the frequency range 1975 to 2325 kc. The linearity of the sweep was approximately 0.1 percent and the frequency stability over expected operating conditions was approximately 1 percent. This signal was applied to the base of the Band 4 mixer.

The IF amplifier consisted of two amplifiers each followed by a two-pole LC filter. The IF frequency was 725 kc; the 3-db bandwidth was 2.0 kc and the 50-db bandwidth was 10 kc.

The output of the IF amplifier was applied to a logarithmic compressor, which compressed an 80-db input signal range into approximately a 20-db output range (see Fig. 9.2). The log compressor was followed by an average detector and low-pass filter. The output of the low-pass filter (0 to 5 v) was applied to the telemetry VCO. The output filter was a single-section RC filter with time a constant of 0.8 msec on Aerobee 4.58 UI and 0.6 msec on Aerobee 4.59 UI.

9.1.1.5 In-Flight Calibrator

Every 16th sweep of the sweeping receiver, a spectrum of signals was injected into the high- and low-frequency vertical loop antennas to provide in-flight calibration of the four sweeping receivers. This calibrator also injected 22.3-kc signals into the NSS receiver and connected a known impedance in place of the electric dipole antenna for impedance probe calibration. The calibration of the sweeping receivers continued for one full sweep (256 steps); however, the NSS receiver and impedance probe calibrations continued for only four steps. On Aerobee 4.58 UI, signals derived from the impedance probe reference oscillators (1.54 and 120 kc) were used for receiver calibration. On Aerobee 4.59 UI, to obtain a more uniform spectrum in each band, a separate spectrum was generated for each band. Oscillators on frequencies 0.2, 1.6, 12.5, and 105 kc were used to generate spectra for Bands 1, 2, 3, and 4, respectively. In both flights, the calibrator spectrum included signals in the broadband receiver frequency range, thus calibrating that receiver also.

9.1.2 Data and Discussion

9.1.2.1 General

During the flights, the outputs from the four sweeping receivers were recorded on magnetic tape along with other telemetry data; however, the data used exclusively for data analysis were recorded in real time on oscillograph chart paper by the telemetry receiving stations at Wallops Island. For convenience, the outputs of the four sweeping receivers occupied exclusively one chart record. Samples of this data, modified to show frequency and amplitude calibrations, are included with the discussions of the data from each receiver in the following sections. To preserve all the data exhibited at the output of the receivers, fast recorder chart speeds were required, resulting in several hundred feet of recording on each rocket flight. To analyze the data on these chart recordings, a movie (described in Sec. 7.5), which displayed the data in the form of time-varying spectrograms, proved invaluable.

In the following discussions, significant features of the data are pointed out but not necessarily explained. Due to the great detail contained in the spectra, some significant features of the data undoubtedly remain to be discovered by a deeper penetration; also to maintain brevity some data are not presented.

9.1.2.2 Band 1 Receiver, Aerobee 4.58 UI

The output of Band 1 contained considerable noise during the powered portion of the rocket flight. Two explanations are likely:

- (1) Signals generated in the electronics by mechanical stresses (microphonics), and
- (2) Signals generated by the lateral motion of the loop antenna in the earth's magnetic field.

The latter explanation is supported by the fact that the noise was amplitude modulated at twice the spin rate of the rocket. Between rocket burn-out at approximately 54 sec (41 km) and command cutoff at 66 sec (64 km) signals appeared in Band 1. At command cutoff the signals disappeared. This phenomena was also evident in Band 2 and a possible mechanism for generation of these signals is discussed in Sec. 9.1.2.3.

After command cutoff (64 km) there were no signals above the threshold in Band 1. The samples of data taken by this receiver, shown in Fig. 9.3, essentially depict the receiver threshold. The apparent large signal at the low-frequency end of the sweep is a synchronizing pulse.

9.1.2.3 Band 2 Receiver, Aerobee 4.58 UI

The output of the Band 2 receiver during the ascending and descending portions of Aerobee 4.58 UI above 85 km shows a hiss band (so called because of its broadband nature). Selected portions of the output are shown in Figs. 9.4 and 9.5. The frequency range of the receiver is 1.5 to 12.5 kc and one sweep or frame takes approximately 1.14 sec.

Figures 9.4 and 9.5 were made after observing a film of the data from which it was determined that signals received at a particular altitude showed similar amplitude and frequency structure. Several frames were overlayed around selected altitudes to obtain an integrated effect and to emphasize the characteristics of the noise at that altitude.

Below 64 km, the signals were very noisy and for the most part associated with the burning of the rocket. It is interesting to note that between the time of burn-out (54 sec, 41 km) and command cutoff (66 sec, 64 km) signals in Bands 1 and 2 appeared, which increased in amplitude and decreased in frequency. These signals ceased abruptly when the command cutoff was received by the rocket; therefore, they are undoubtedly caused by some rocket disturbance. Additionally, these signals were not amplitude modulated by the rocket spin, which indicates an isotropic signal source. A plausible source of these signals is the ionized exhaust plume, which is caused by gases escaping from the hot rocket exhaust. The mechanism for signal generation in the ionized exhaust is not known. At 64 km, almost all external signals have dropped below the receiver threshold and the only signals in Band 2 are interference signals from the rocket telemetry system and signals from Omega stations at 10.2 kc. The telemetry signals located at approximately

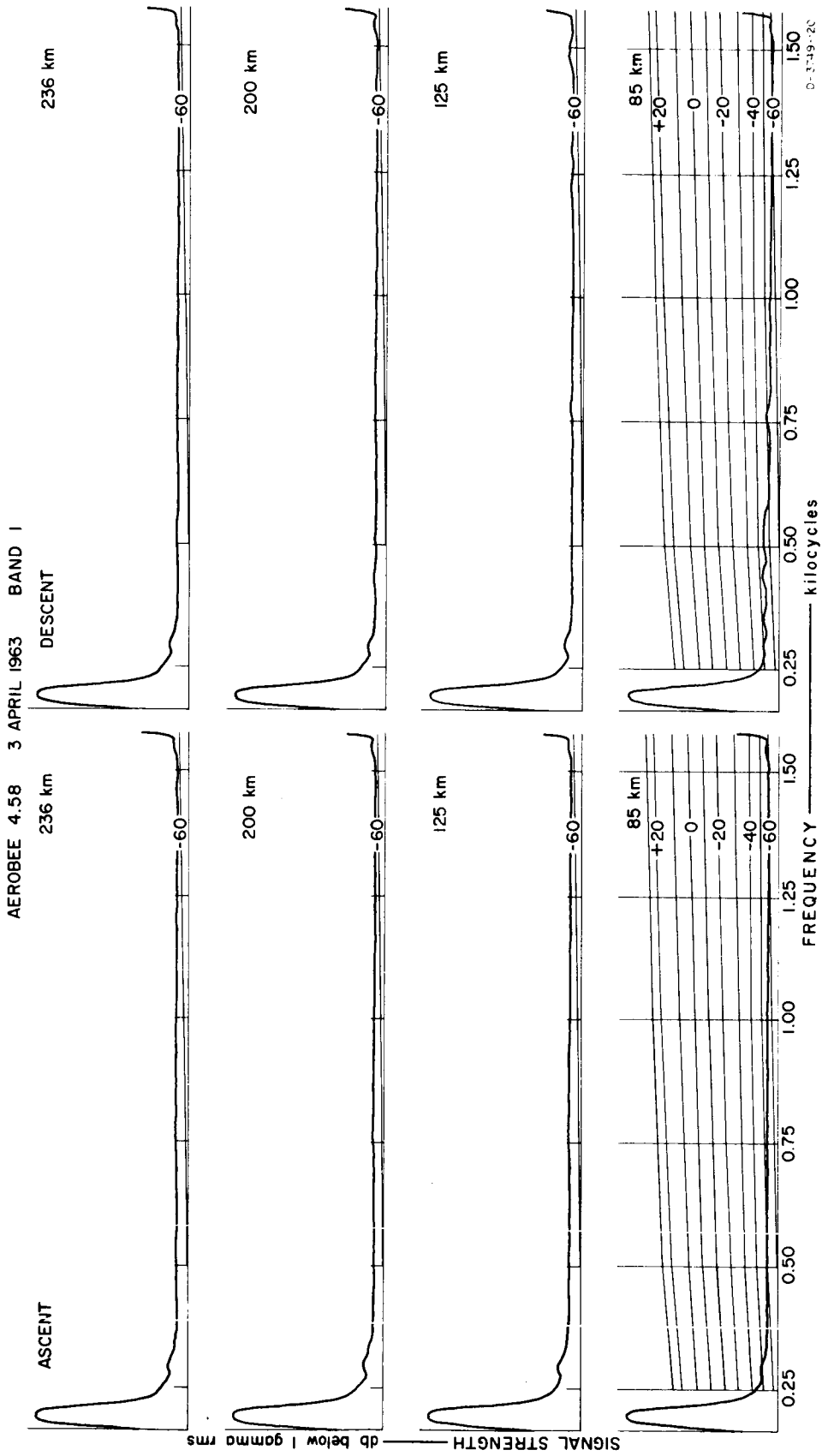


FIG. 9.3 AEROBEE 4.58 UI BAND 1 DATA WITH CALIBRATIONS

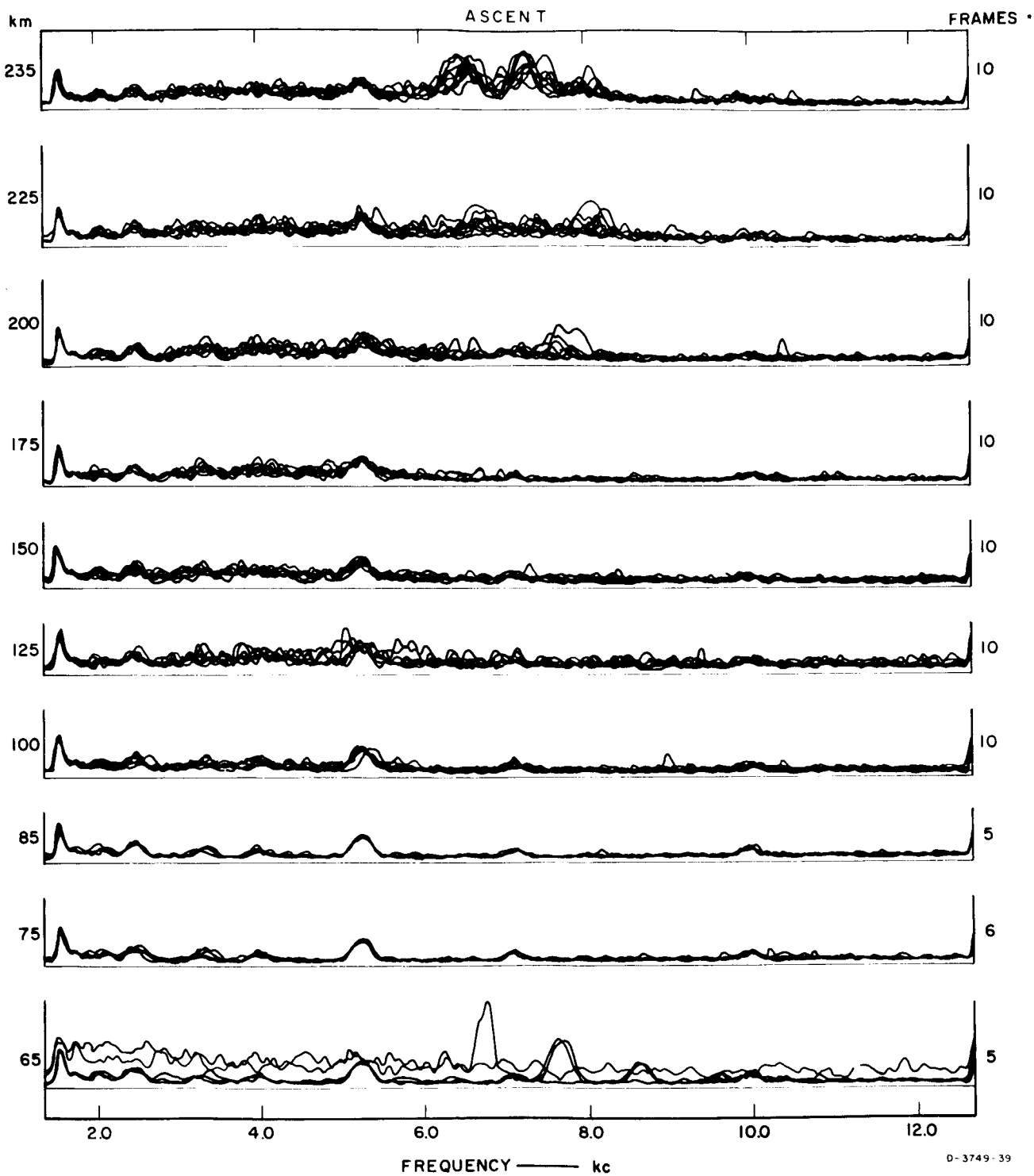


FIG. 9.4 AEROBEE 4.58 UI BAND 2 DATA, ASCENT

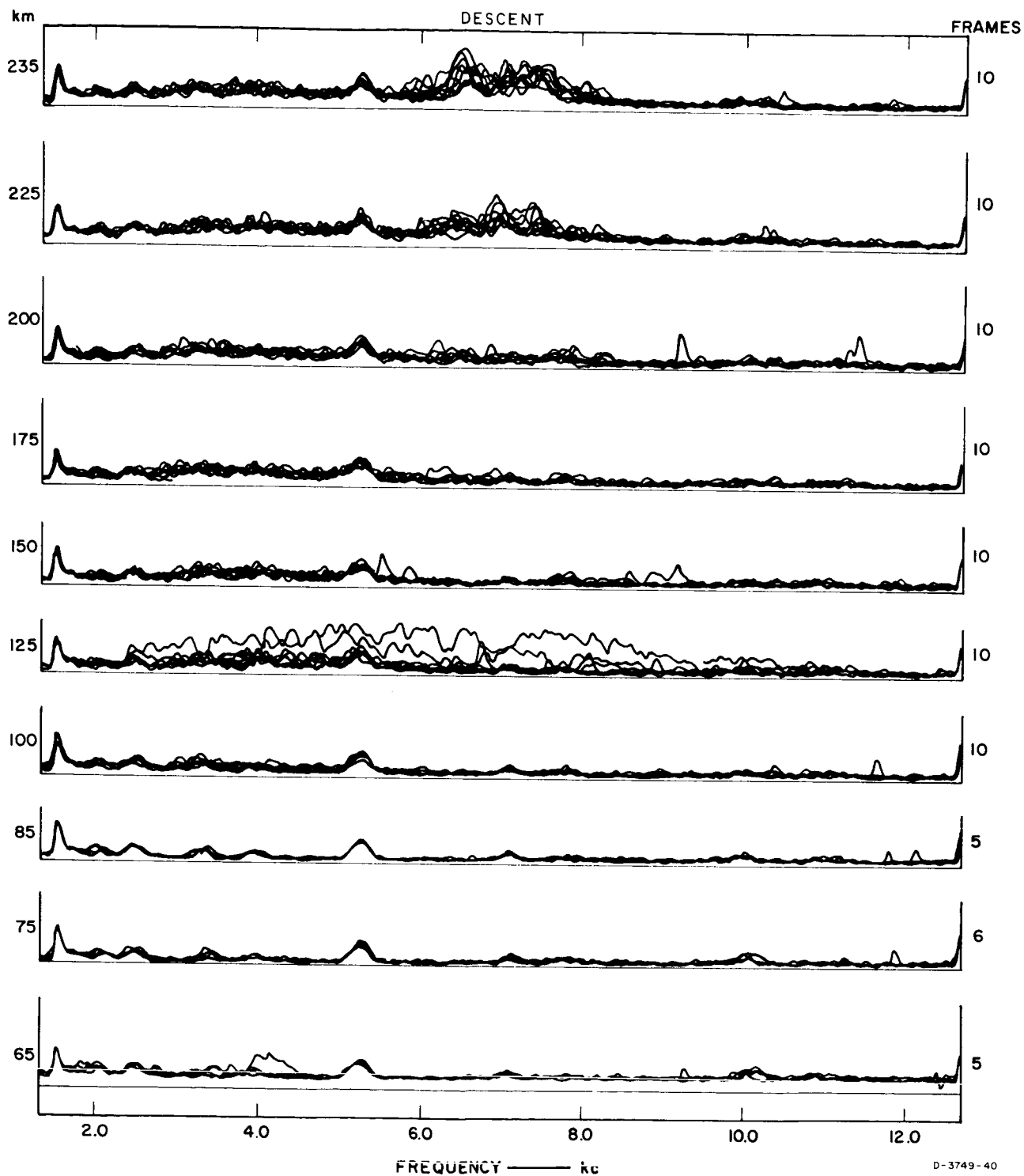


FIG. 9.5 AEROBEE 4.58 UI BAND 2 DATA, DESCENT

1.7, 2.3, 3.0, 3.9, 5.4, and 7.35 kc remain at a constant level throughout the flight. The peak at 1.5 kc is caused by local oscillator punch through and marks the start of each frame. Ten frames immediately above and below 100 km were overlaid, and at that altitude in Figs. 9.4 and 9.5 a slight rise in the background noise throughout the band can be seen. The receiver threshold is 70 db below 1 gamma rms at 1.5 kc to about 80 db below 1 gamma rms at 12.5 kc (see Fig. 9.6).

At 125 km the noise has increased in amplitude and still covers the complete band. On the descending portion of the flight one frame contains a dispersed whistler. (From Fig. 9.68 it is seen that there is a knee in the electron density profile at 125 km.) At 150 km, the higher-frequency noise shows a decrease in amplitude, while at 175 km signals above 7.5 kc have practically disappeared below the receiver threshold. Above 200 km, the signals increase in amplitude but remain cut off above 9.0 kc. Above 225 km, a strong band of noise between 6 kc and 8 kc predominates. The peak amplitude measured at 235 km and 7.2 kc is 50 db below 1 gamma rms.

To summarize, the hiss starts above 85 km and is about 75 db below 1 gamma rms in amplitude and contains frequencies up to 5 kc. It increases in amplitude and frequency with altitude up to about 175 km, where signals above 7.5 kc decrease. Above 175 km there appears a strong hiss band from 6 to 8 kc with a few distinct peaks around 6.7, 7.2, and 8.1 kc.

Omega stations (10.2 kc) are observed throughout most of the flight with amplitudes of approximately 76 db below 1 gamma rms at 85 km ascending, 82 db below 1 gamma rms at 175 km ascending, and 82 db below 1 rms at 100 km descending.

9.1.2.4 Band 3 Receiver, Aerobee 4.58 UI

The output of the Band 3 receiver on Flight 4.58 UI, as seen in Fig. 9.7, contained many signals and interferences sources. Figure 9.7 was drawn by tracing eight different sweeps from the strip chart recordings taken during the rocket flight. Each sweep, from 10 to 102 kc, took 1.14 sec to complete. The receiver threshold varied

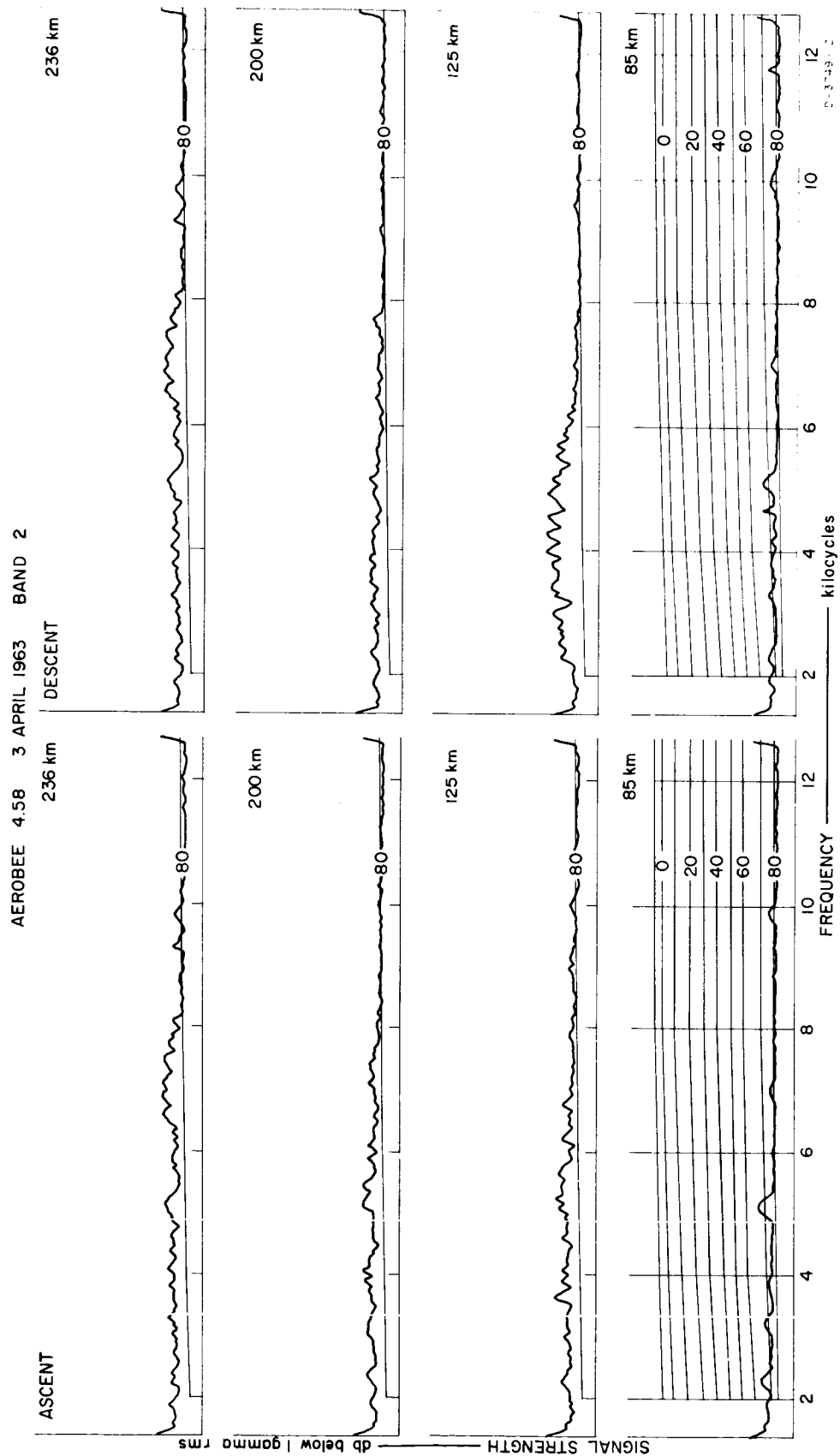


FIG. 9.6 AEROBEE 4.58 UI BAND 2 DATA WITH CALIBRATIONS

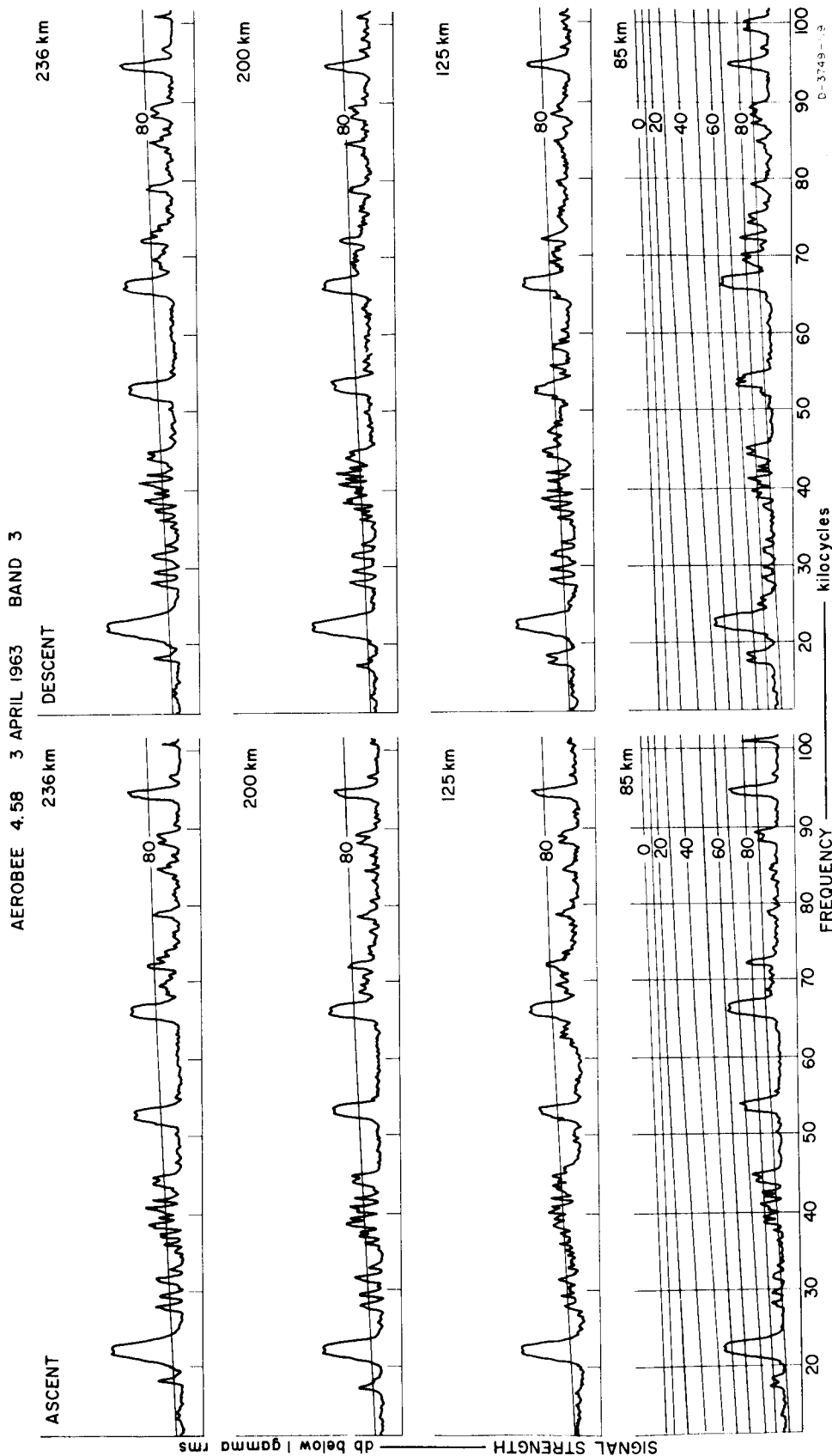


FIG. 9.7 AEROBEE 4.58 UI BAND 3 DATA WITH CALIBRATIONS

from about 86 db below 1 gamma rms at 10 kc to greater than 100 db below 1 gamma rms at 100 kc. The interference sources were the telemetry sub-carrier oscillators located at 14.5, 22.0, 30.0, 40.0, 52.5, and 66.9 kc. There are receiver spurious responses located at 95 and 102 kc.

In this band the broadcast stations received were NAA at 17.8 kc, NSS at 22.3 kc, and Loran C around 100 kc. Signal strengths versus altitude for these stations are shown in Figs. 9.8, 9.9, 9.10, 9.11, 9.12, and 9.13.

The signal strength versus altitude plots for NAA at 17.8 kc shown in Figs. 9.8 and 9.9 also contain a spot noise measurement. Every sweep, a data sample was taken at 17.8 kc; and since the station was sending traffic during the flight, the samples represent received signals, noise, or some level between. From the data there is seen a sharp drop in level at about 85 km of both the signal and noise. The signal returns above 100 km and is seen to increase in field strength until the peak of the flight.

The amplitude versus altitude plots for NSS at 22.3 kc are shown in Figs. 9.10 and 9.11. These measurements were taken with the sweeping receiver and can be compared with data in Fig. 9.72 which were taken with the phase-tracking receiver. By prior arrangement, NSS was transmitting continuously throughout the flight.

By measuring the amplitude or level at fixed frequencies where no interference or known signals appear, a profile of the noise versus altitude may be obtained as in Figs. 9.14, 9.15, 9.16, and 9.17. It can be seen that there is a sharp decrease in the noise at 86 km and a slight increase around 125 km. From 9.68, the curve of electron density versus altitude, there appears to be a knee in the electron density curve at this altitude.

Figures 9.12 and 9.13 show Loran C signal strengths versus altitude until they decreased below the receiver noise level around 75 km. Above 75 km the figures show the ambient noise level (near receiver threshold) as a function of altitude. In the vicinity of 125 km, there appears a rise in the noise level similar to the lower frequencies.

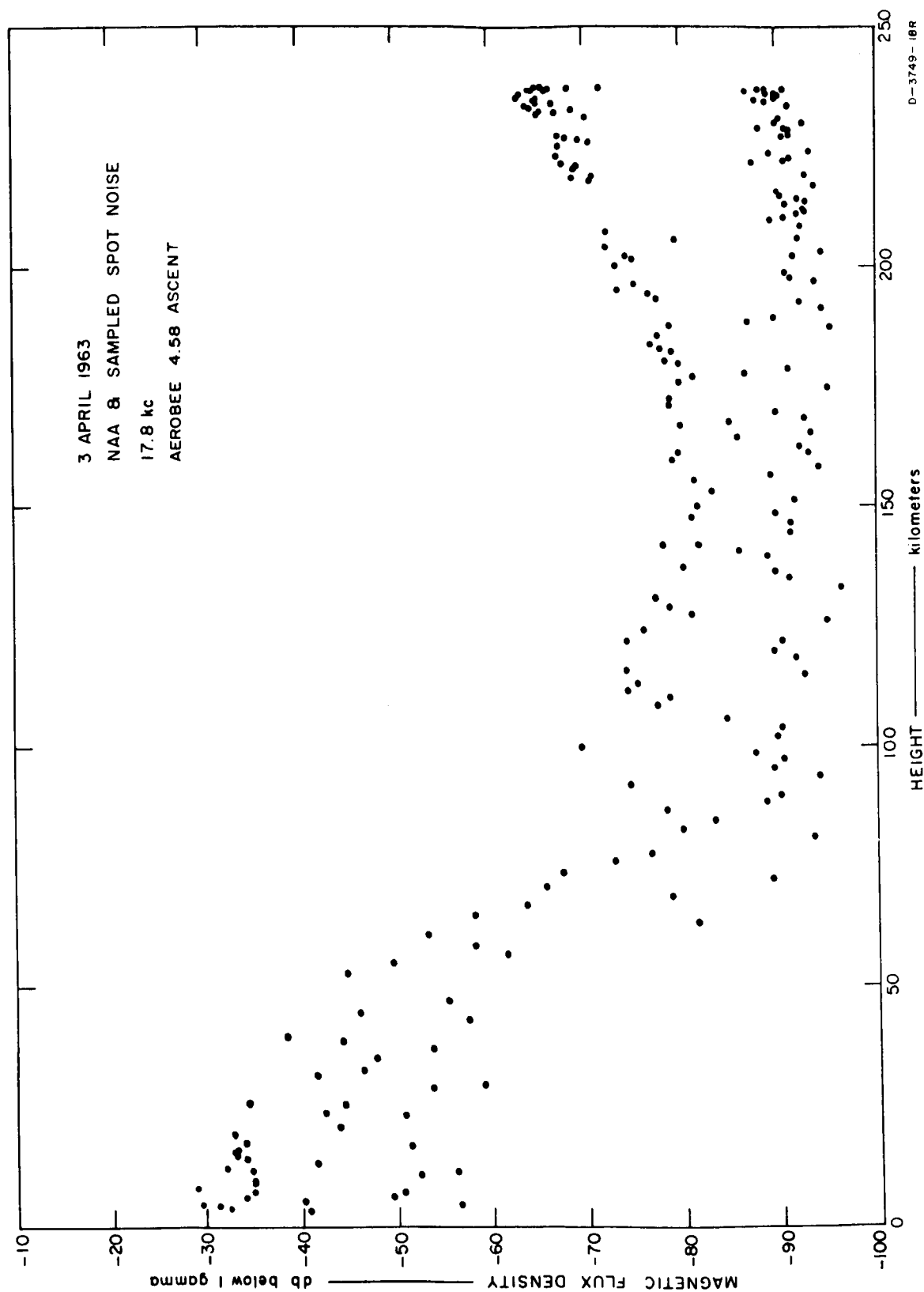


FIG. 9.8 AMPLITUDE OF NAA AND 17.8-kc NOISE, ASCENT

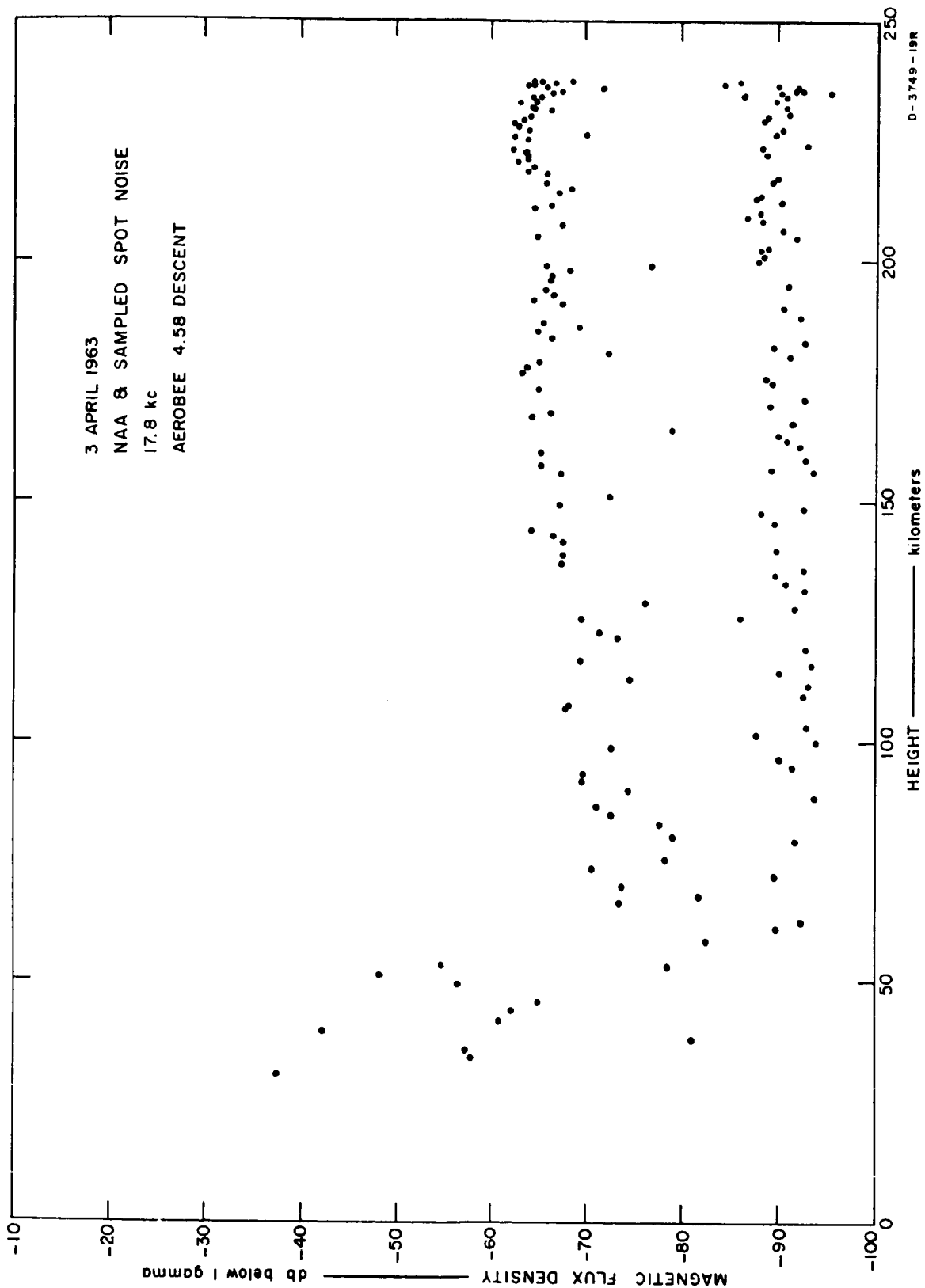


FIG. 9.9 AMPLITUDE OF NAA AND 17.8-kc NOISE, DESCENT

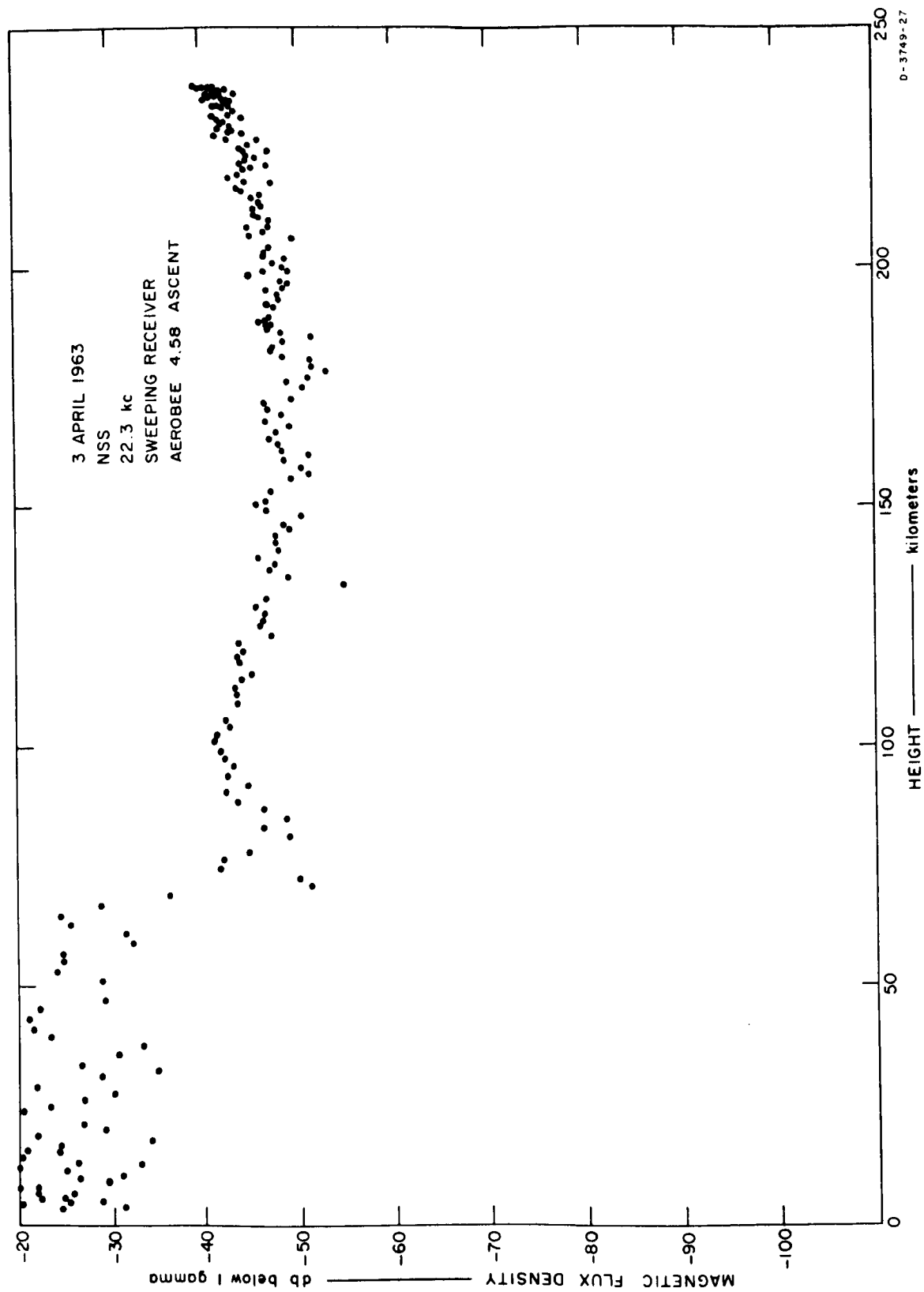


FIG. 9.10 AMPLITUDE OF NSS, ASCENT

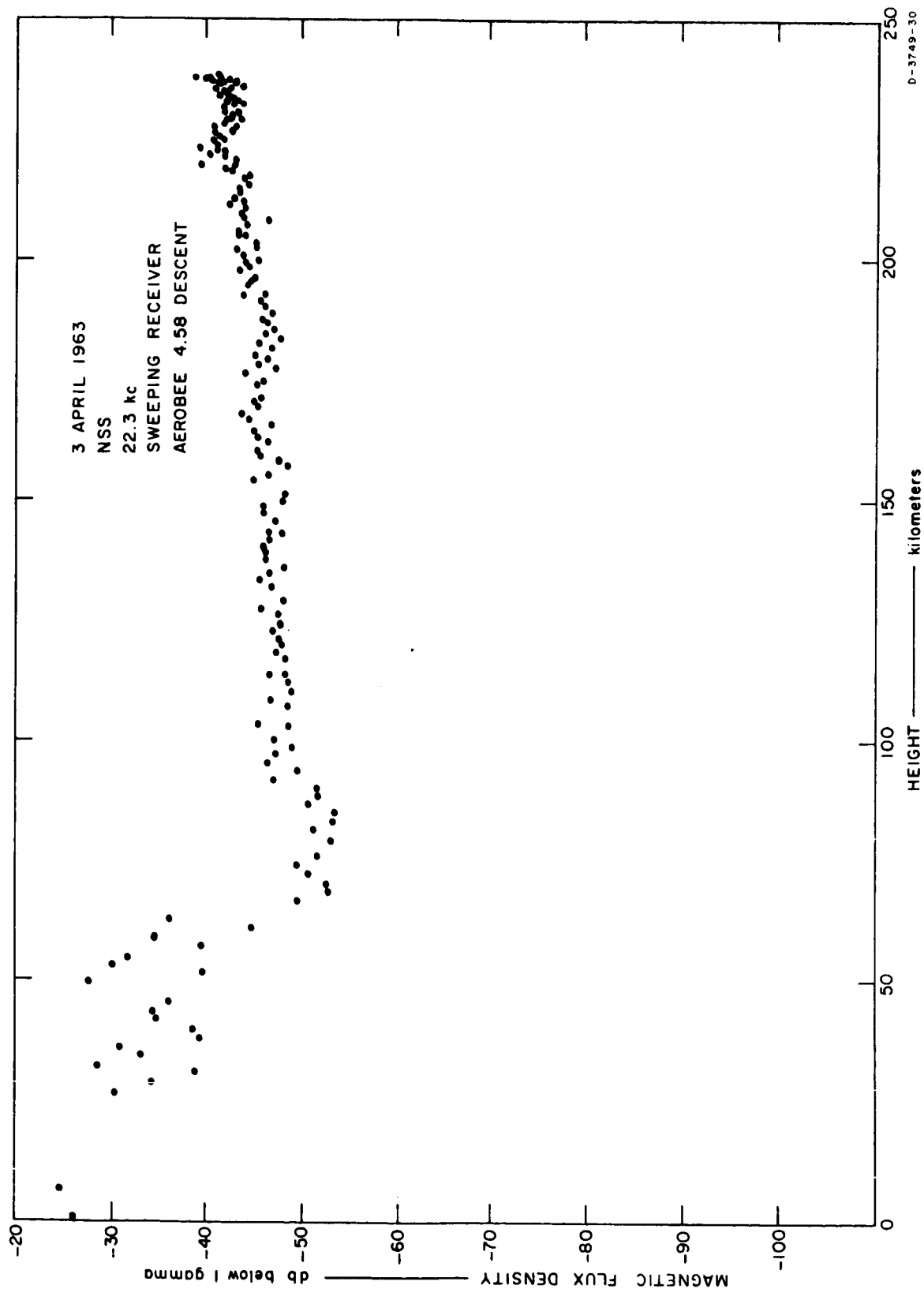


FIG. 9.11 AMPLITUDE OF NSS, DESCENT

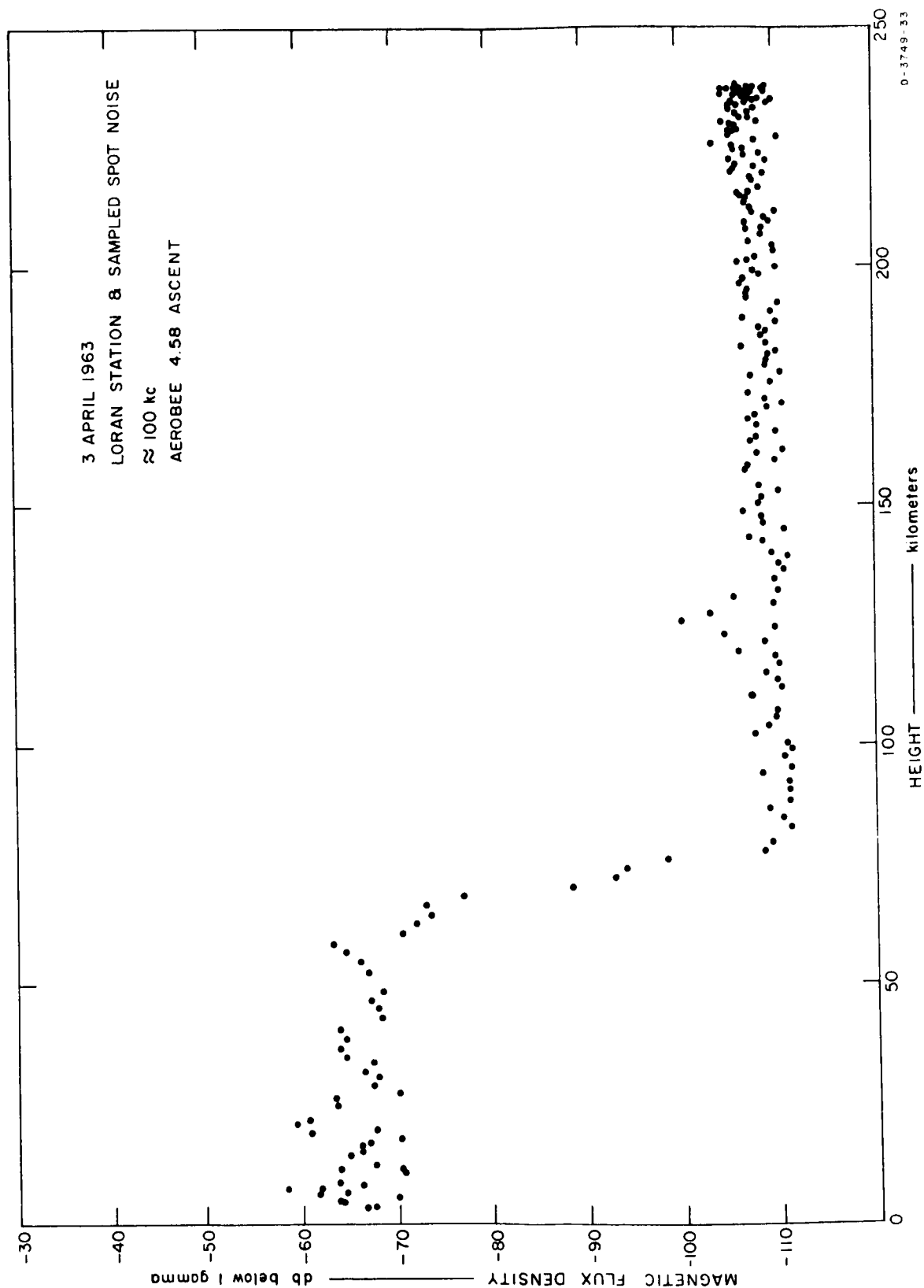


FIG. 9.12 AMPLITUDE OF LORAN C AND 100-kc NOISE, ASCENT

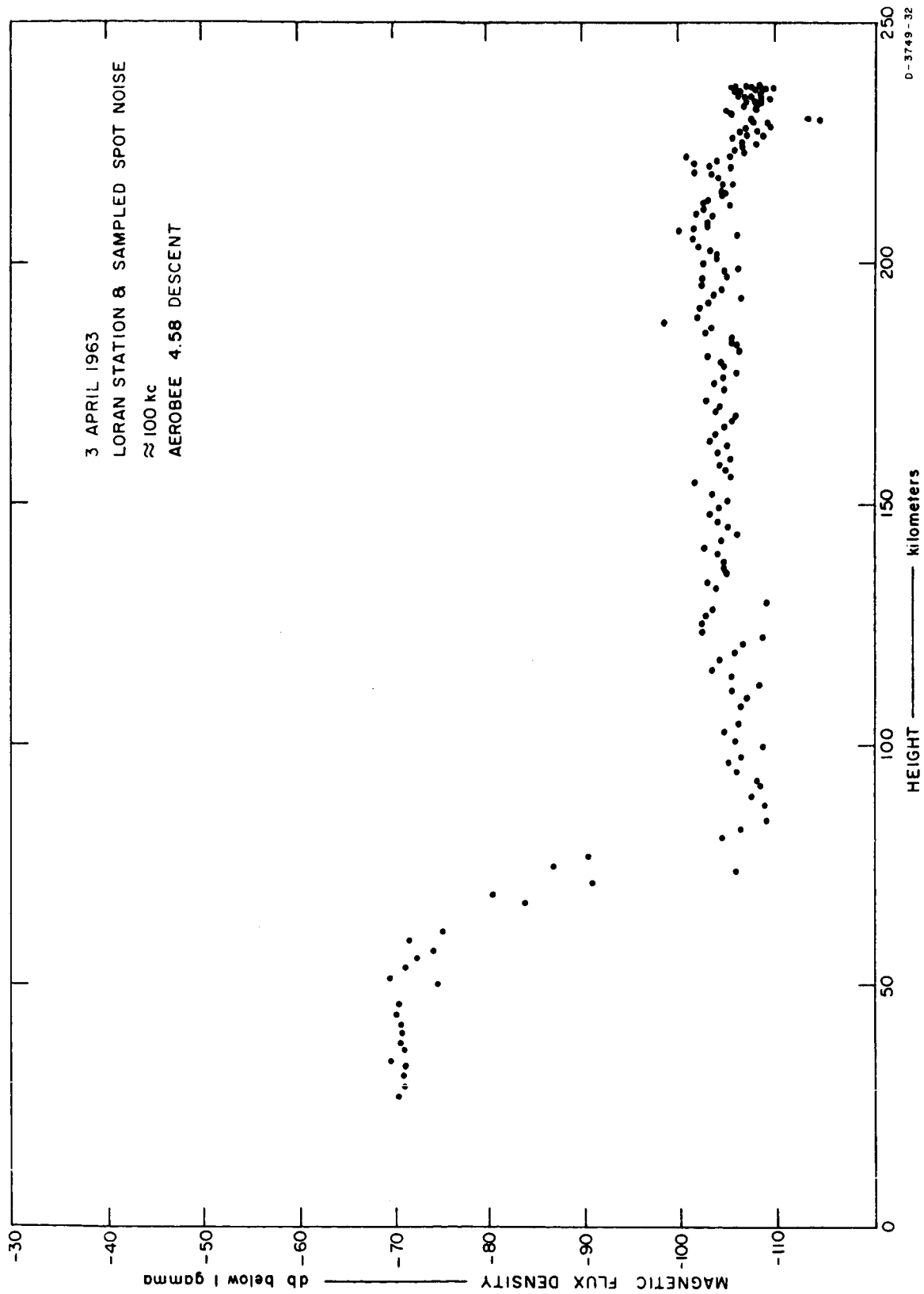
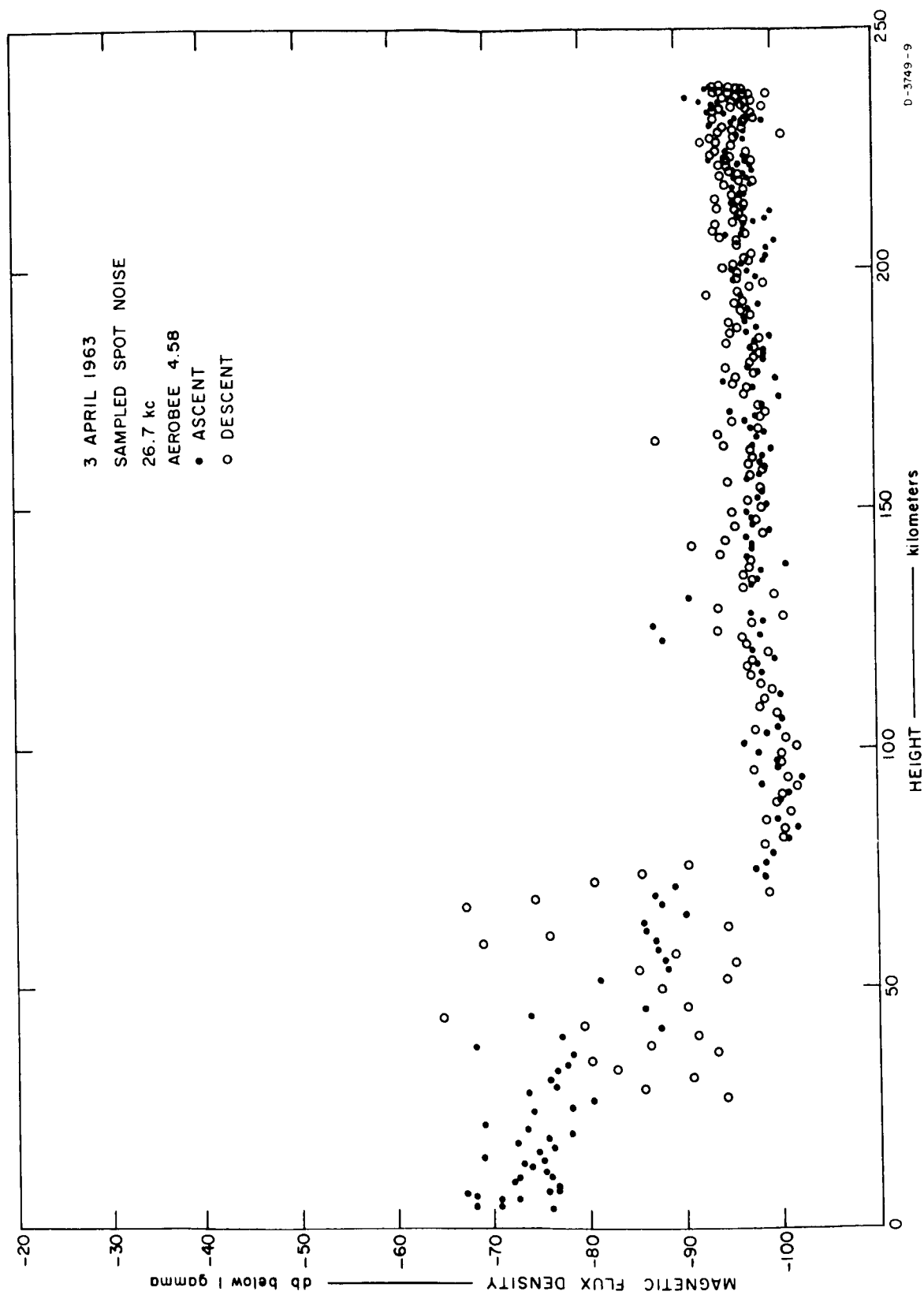


FIG. 9.13 AMPLITUDE OF LORAN C AND 100-kc NOISE, DESCENT



D-3749-9

FIG. 9.14 AMPLITUDE OF 26.7-kc NOISE

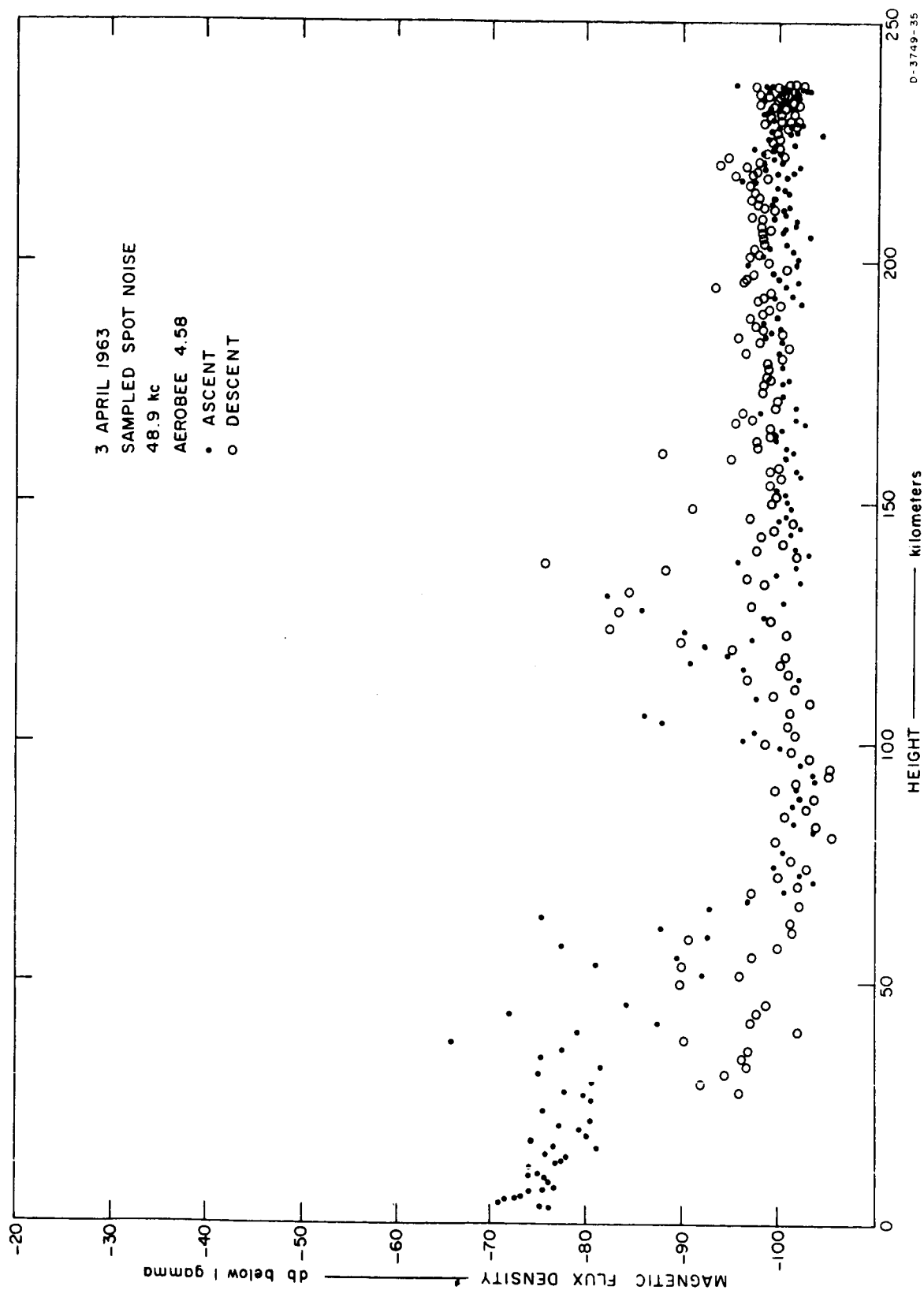


FIG. 9.15 AMPLITUDE OF 48.9-kc NOISE

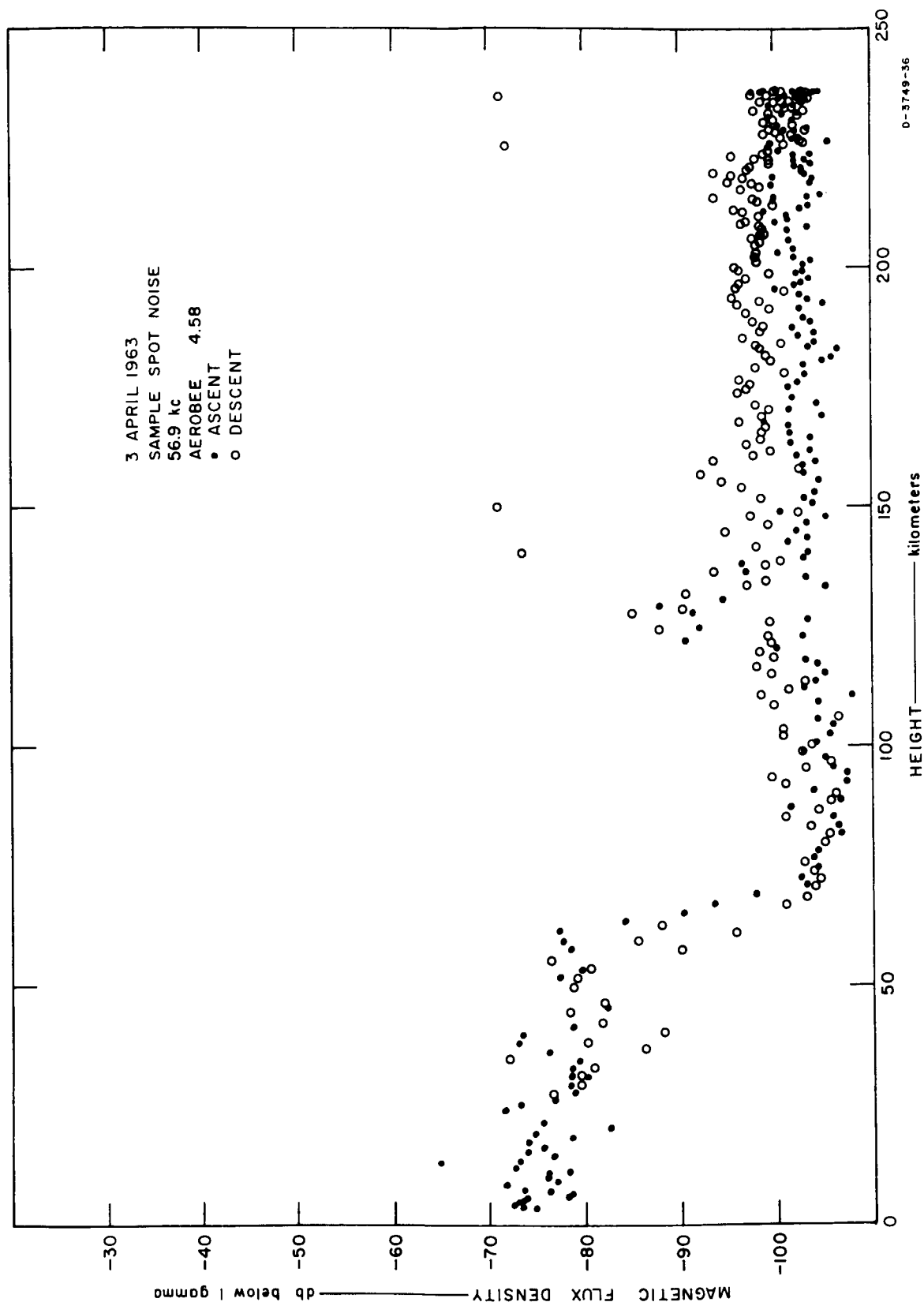


FIG. 9.16 AMPLITUDE OF 56.9-kc NOISE

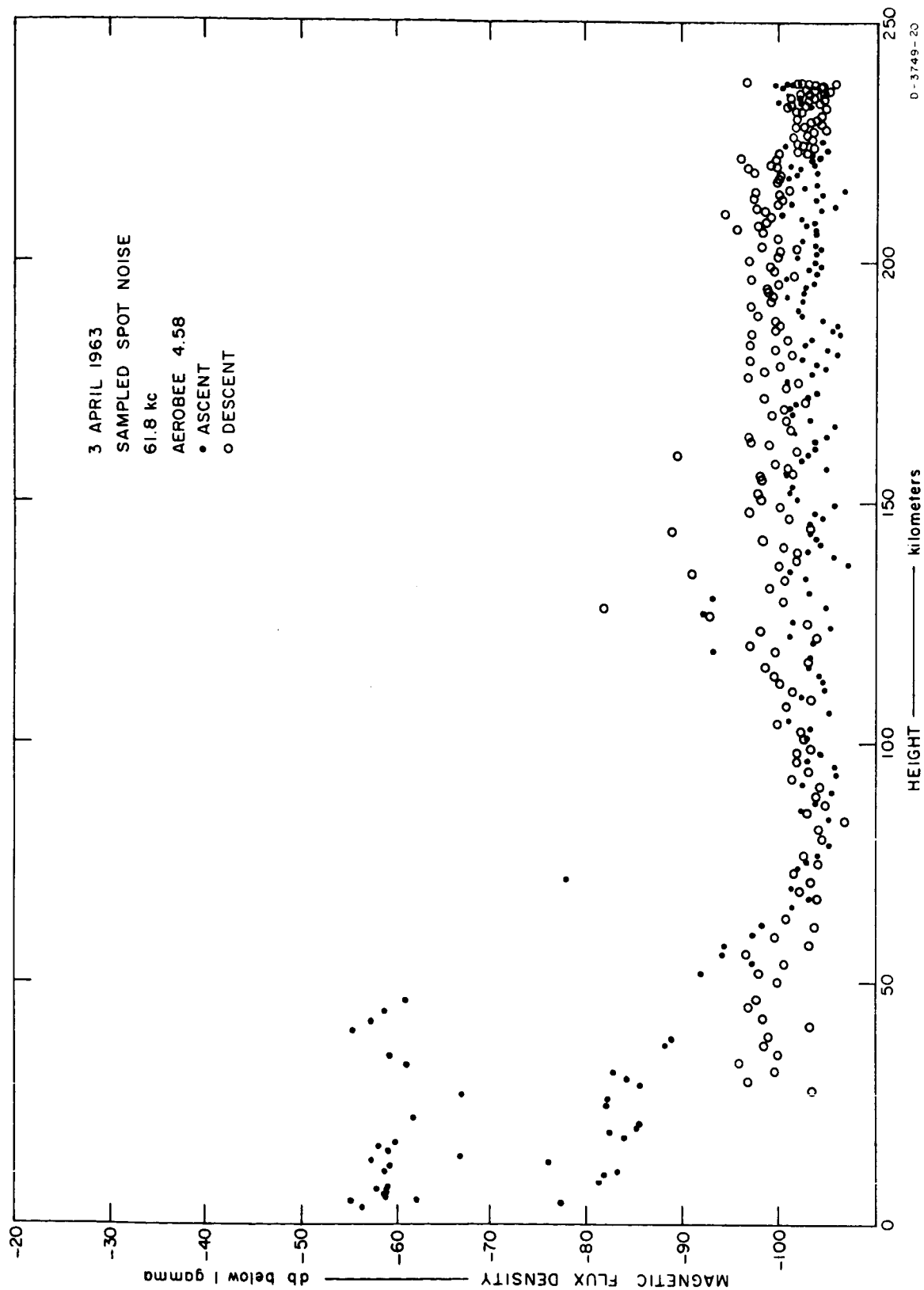


FIG. 9.17 AMPLITUDE OF 61.8-kc NOISE

9.1.2.5 Band 4 Receiver, Aerobee 4.58 UI

The output of the Band 4 receiver clearly shows one broadcast station every 10 kc across its band (1250 to 1600 kc) during the portions of the flight below the ionosphere (see Fig. 9.39 in Sec. 9.1.2.9). An expected sharp change in attenuation due to the electron gyrofrequency resonance at one or more stations in this band as the rocket penetrated the ionosphere was not apparent. The probable reason this effect was not seen is that the high collision frequency dominated the attenuation and reduced the effect. In addition, it would not be seen easily due to the low data-sampling rate (once per second at a particular frequency), the high rocket velocity, and the large gradient in electron density.

In general, each signal started to decrease in amplitude above 65 km. The absorption rate ranged from 0.75 to 2.05 db/km for 10 different signals in the band. The total attenuation was approximately 20 db while the rocket moved through the 65 to 85 km region. Around 85 km there appeared slight increases in strength before the signals were reflected at about 90 km. Plots of some of the amplitude versus altitude data are shown in Figs. 9.18 through 9.27.

Above 95 km there was an increase in the noise picked up by this receiver. The noise appeared to be impulsive in nature covering the frequency band with amplitude impulses at the higher frequencies. There are several possible explanations for this phenomenon; one is that the noise is local electric field signals generated within the rocket. On this flight, the antenna was an unbalanced loop and fairly sensitive to electric fields. As the rocket went into regions of higher electron density the conducting plasma increased the coupling between the antenna and electronics sections of the rocket.

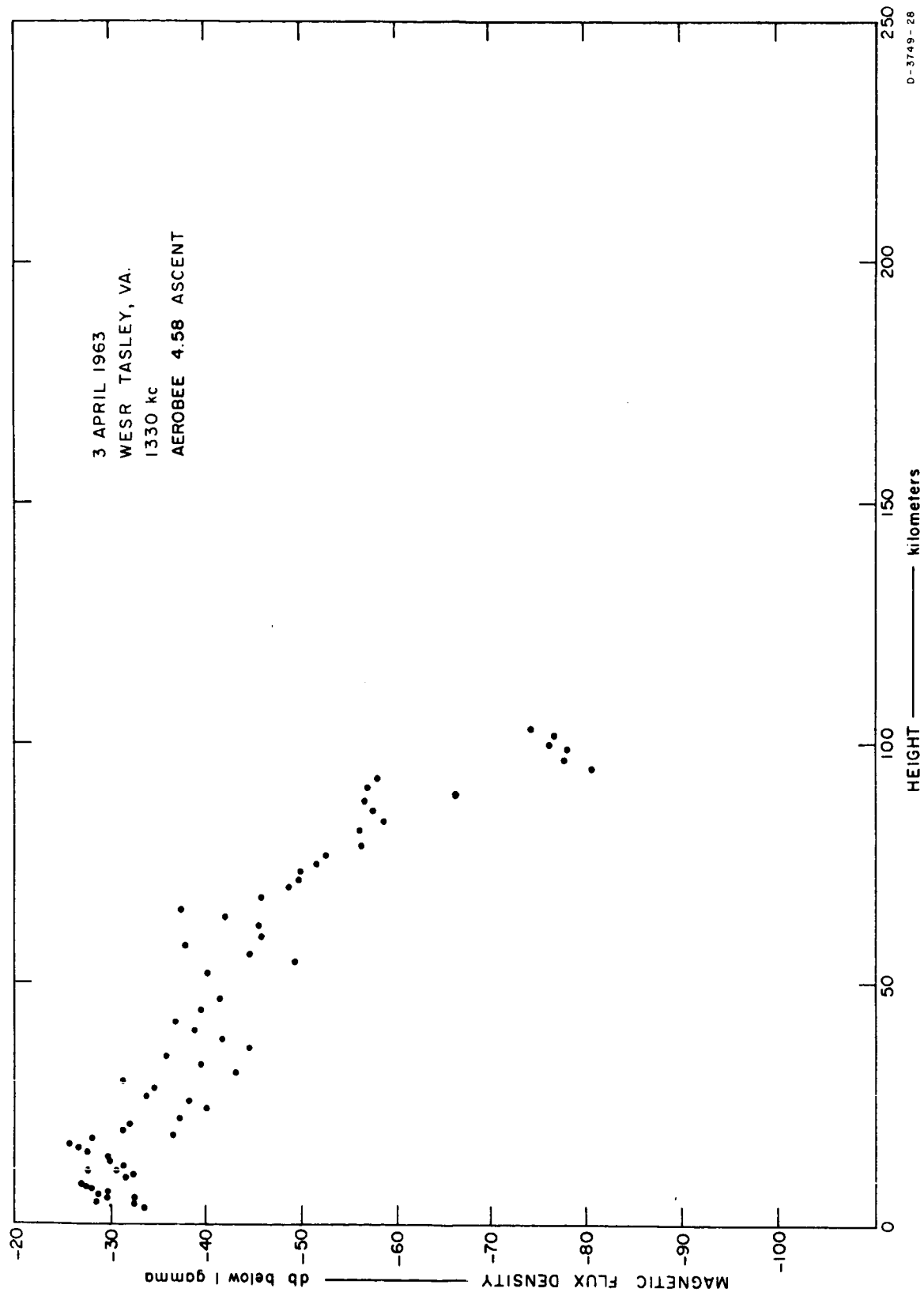
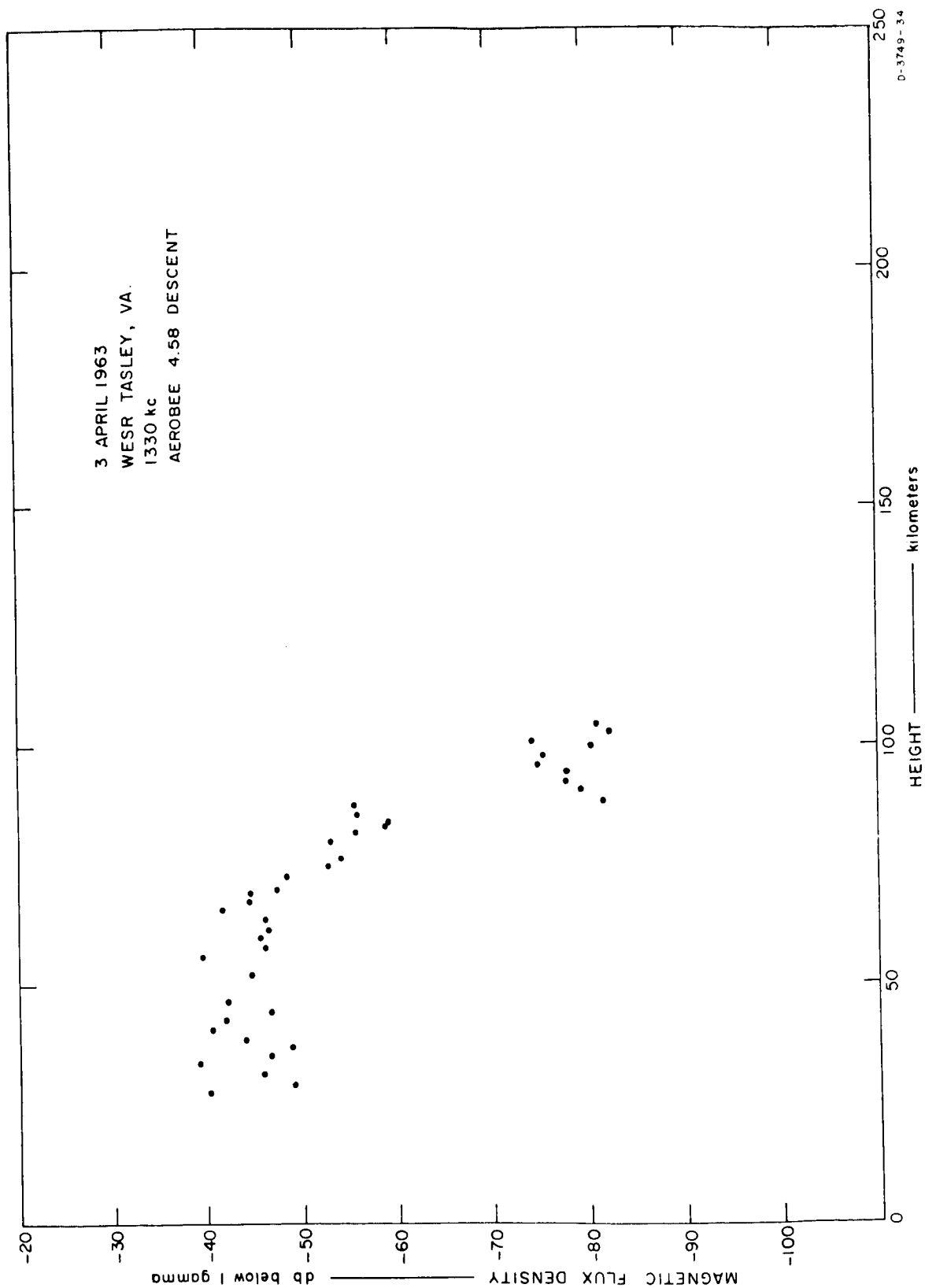


FIG. 9.18 AMPLITUDE OF WESR AT 1330 kc, ASCENT



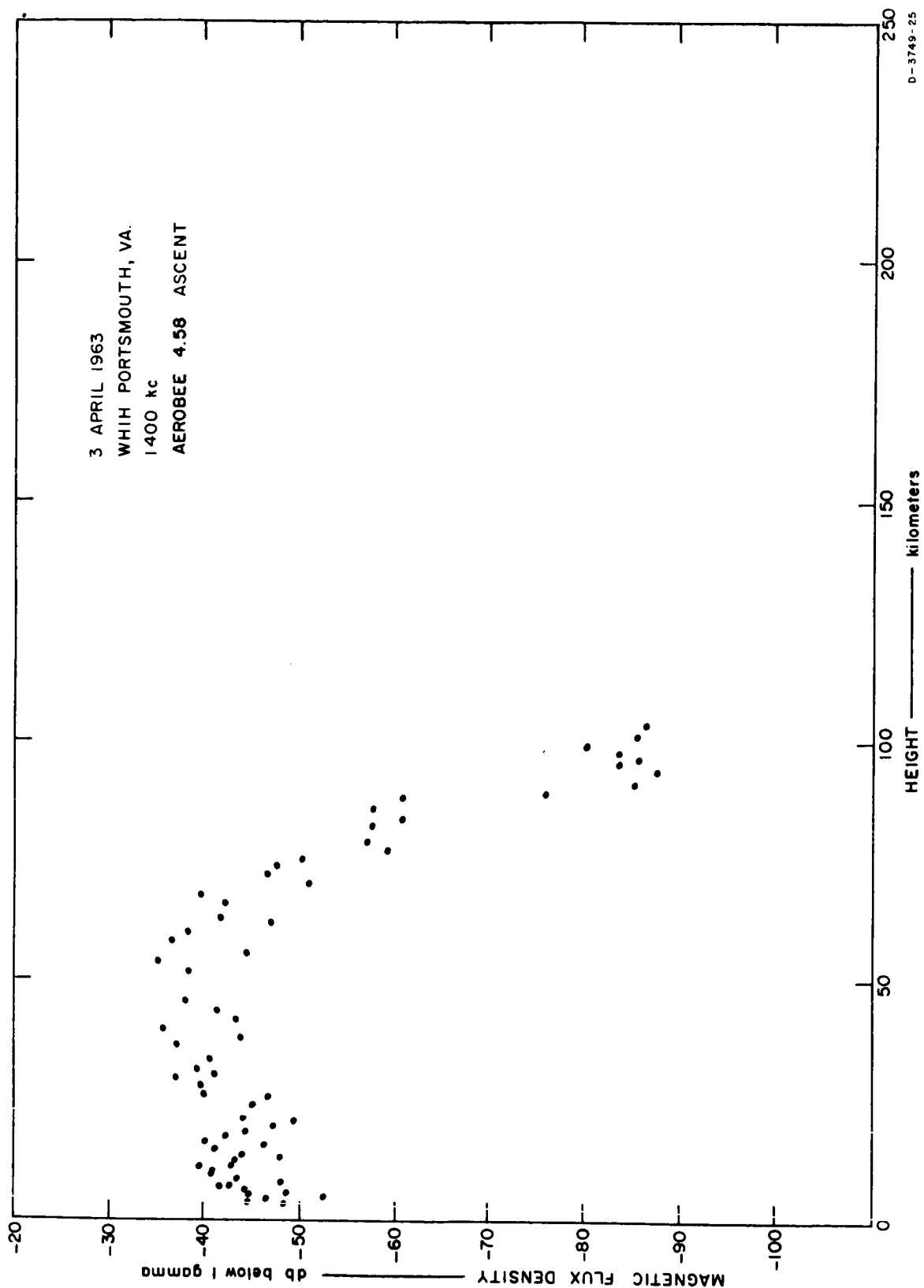


FIG. 9.20 AMPLITUDE OF WHIH AT 1400 kc, ASCENT

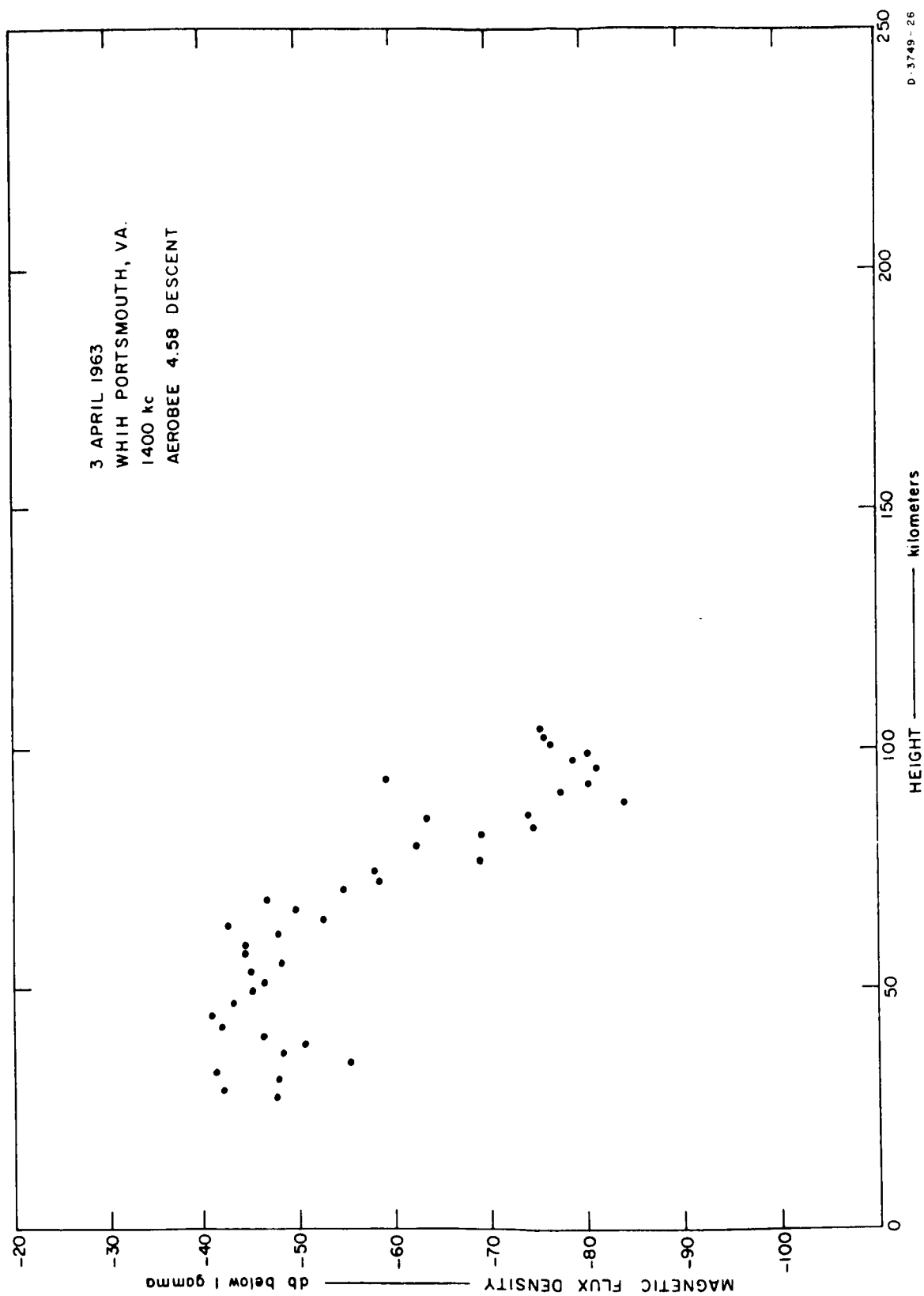


FIG. 9.21 AMPLITUDE OF WHIH AT 1400 kc, DESCENT

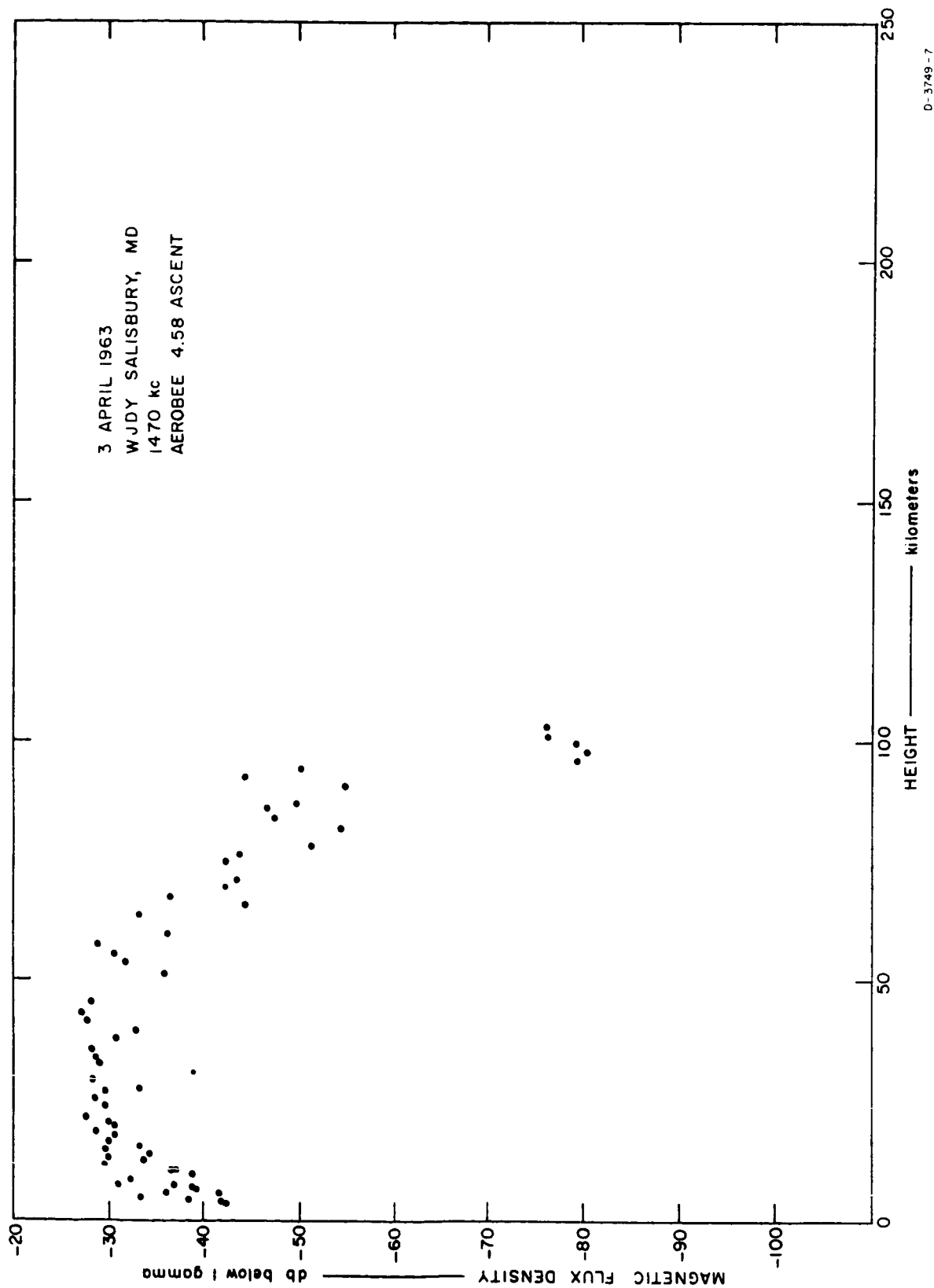


FIG. 9.22 AMPLITUDE OF WJDY AT 1470 kc, ASCENT

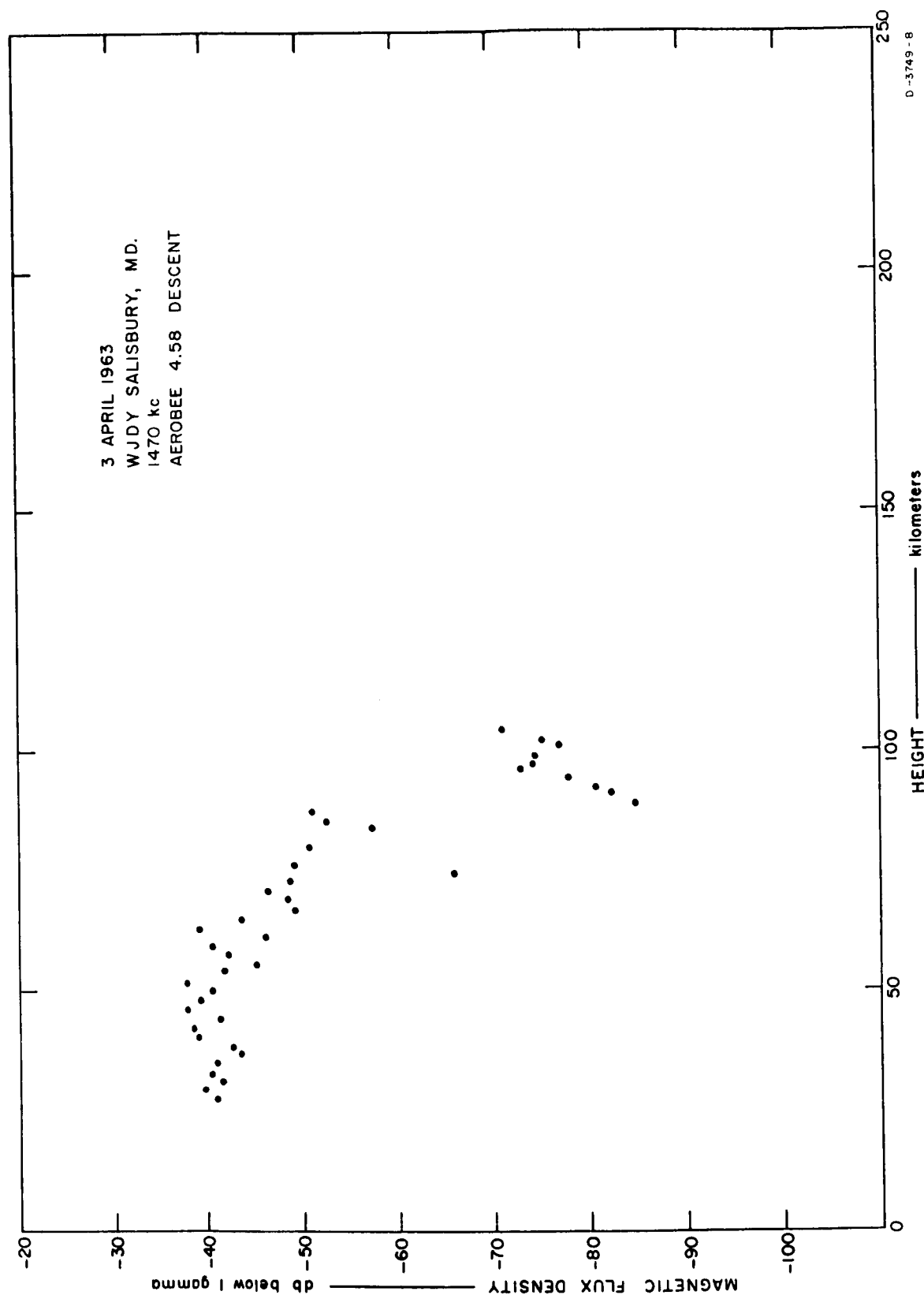


FIG. 9.23 AMPLITUDE OF WJDY AT 1470 kc, DESCENT

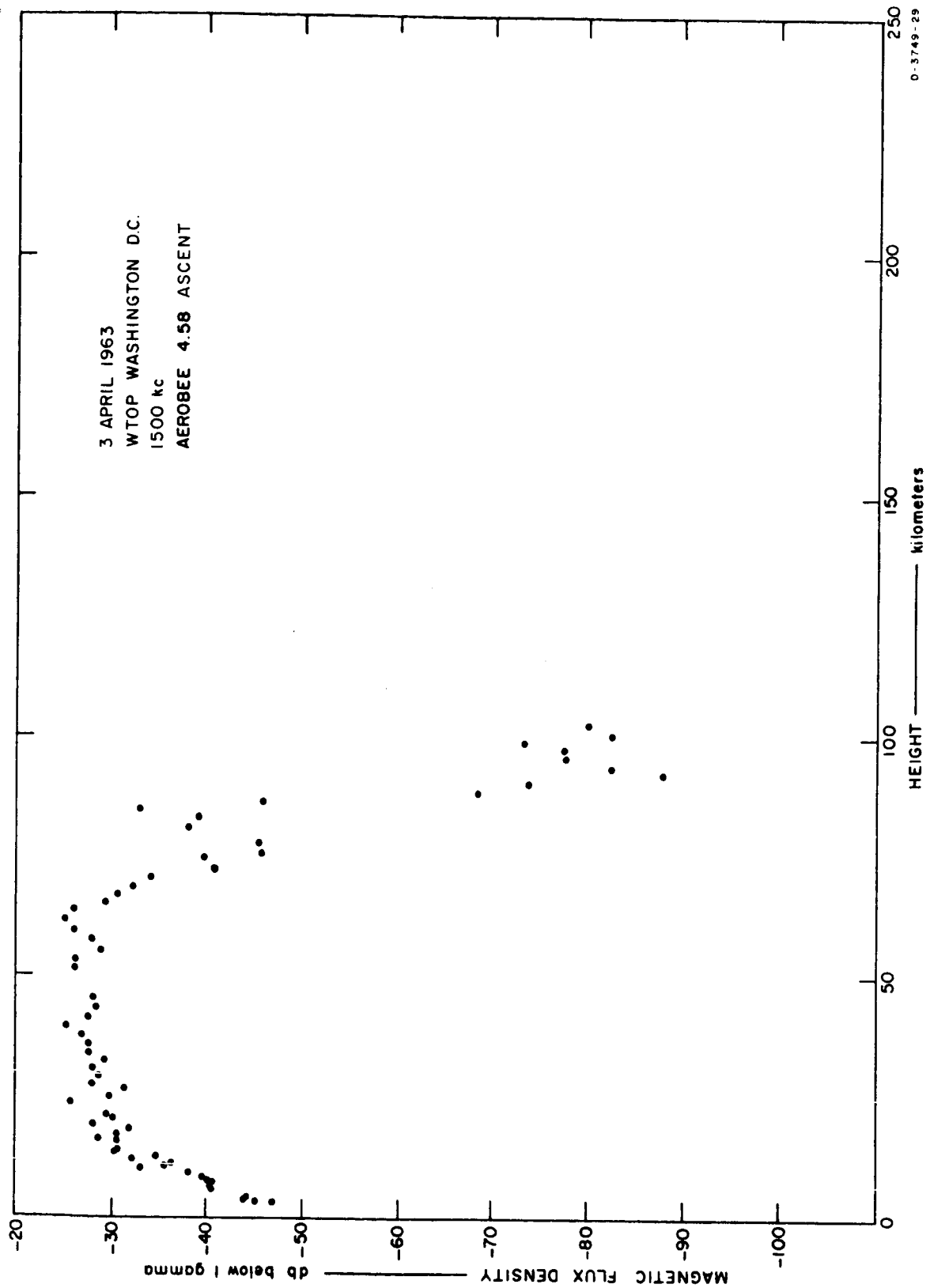


FIG. 9.24 AMPLITUDE OF WTOP AT 1500 kc, ASCENT

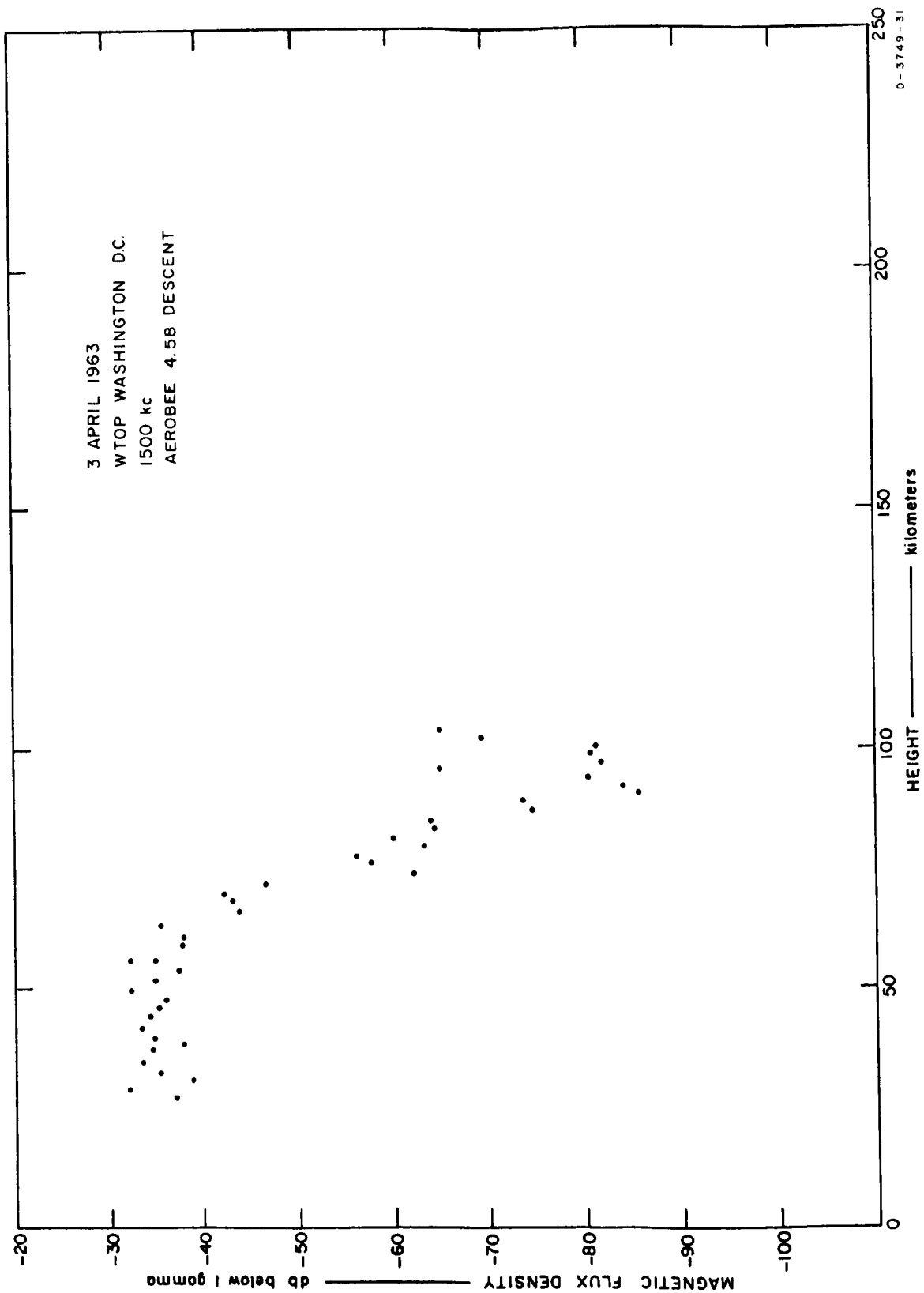


FIG. 9.25 AMPLITUDE OF WTOW AT 1500 kc, DESCENT

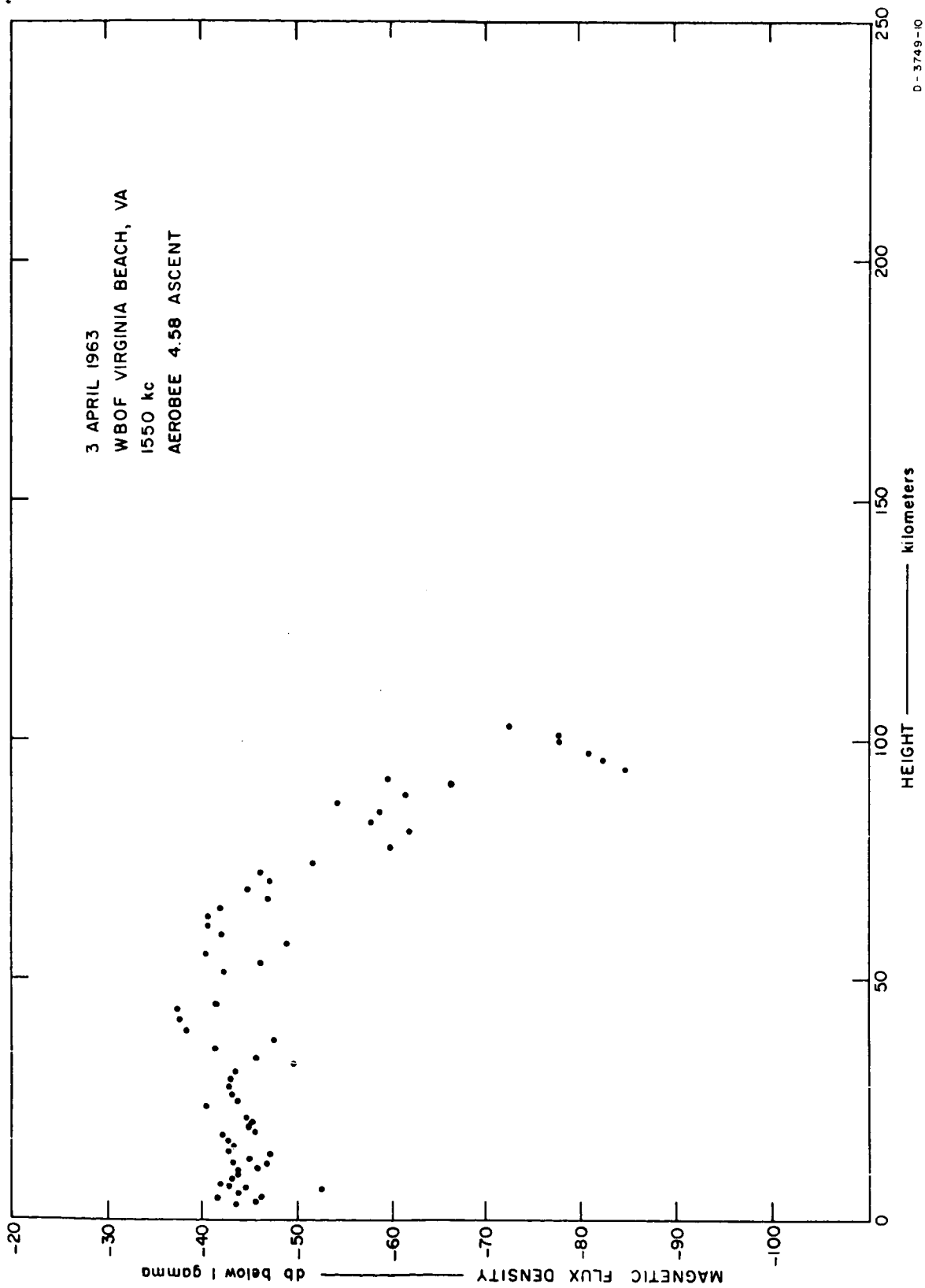


FIG. 9.26 AMPLITUDE OF WBOF AT 1550 kc, ASCENT

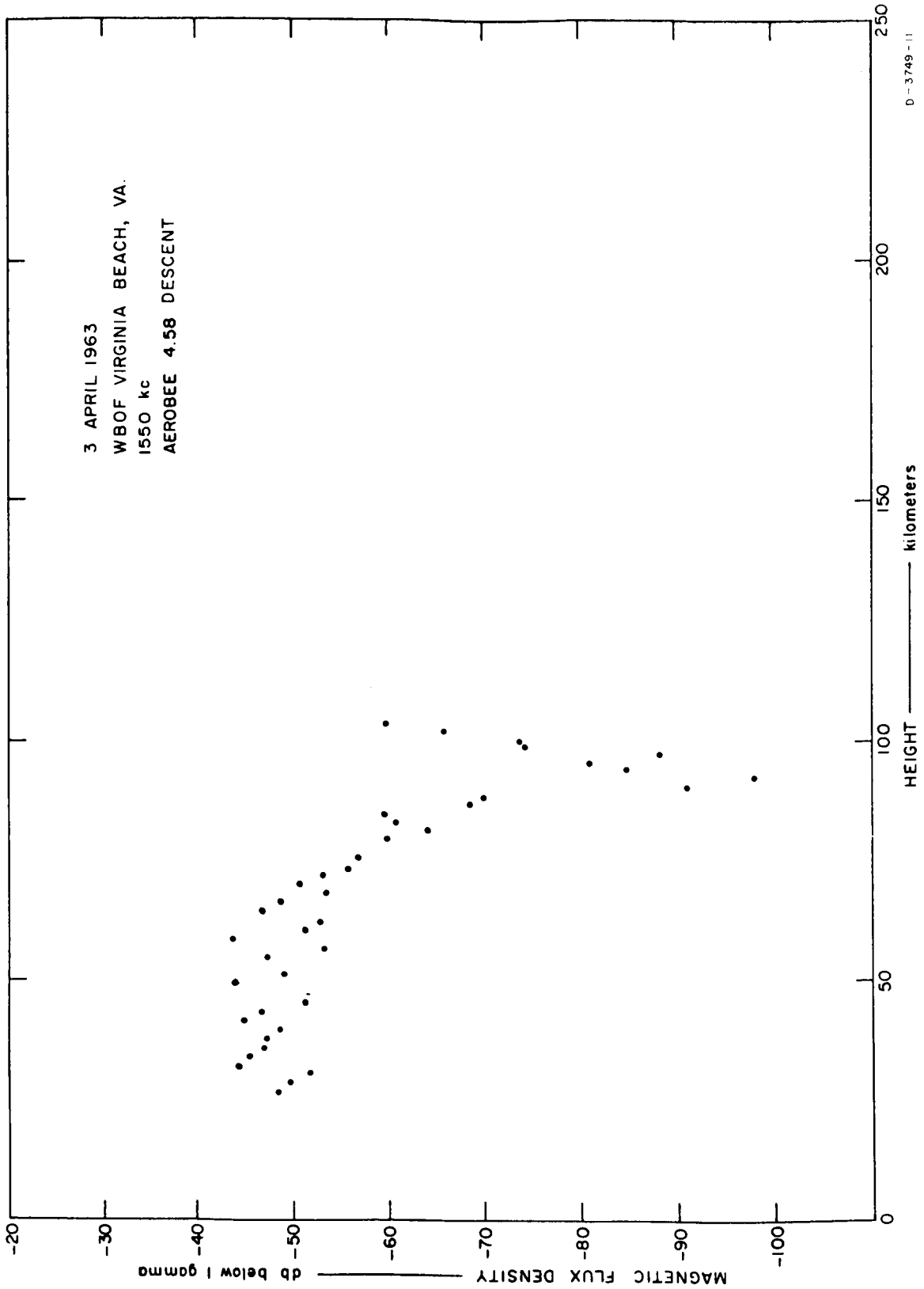


FIG. 9.27 AMPLITUDE OF WBOF AT 1550 kc, DESCENT

An upper bound on the electron density around 86 km was obtained from the points where various signals were reflected. By assuming straight-line paths from the transmitter to points where the signal was cut off, the maximum electron density for plasma cutoff (where wave frequency equals plasma frequency, $X = 1$) may be calculated by the formula:

$$N = \frac{f^2 (\cos \theta_i)^2}{81} \text{ electrons/cm}^3$$

where

f = wave frequency

θ_i = angle of incidence.

Because the sampling rate was low and the rocket spinning, the exact altitude at which the signal was totally reflected cannot be determined. The range of altitudes from where the signal was definitely present to where it completely disappeared is small except in a couple of cases. From Fig. 9.28 it can be seen that the majority of the signals were reflected from around 88 km. An explanation why the electron densities computed from plasma cutoff in Fig. 9.28 do not agree with the densities calculated via phase delay of NSS is that the radio waves were bent downward by either the plasma below 85 km, the sharp change in electron density near 86 km, or both.

One case is shown in Fig. 9.28 at 1470 kc, where the electron density calculated at $X = 1$ is less than the density calculated by phase changes in NSS. It is probable that the reflection seen at this point occurs when $X = Y + 1 \approx 2$ (Y is the ratio of electron gyrofrequency to wave frequency).

Because of the low sampling rate and high speed of the rocket in the region where the important effects took place, many questions remain unanswered. With a higher sampling rate it would be possible to obtain good attenuation characteristics of signals in the lower ionosphere. Very accurate phase delay measurements could be made on signals in this band from 65 to 85 km in the daytime, because reflections

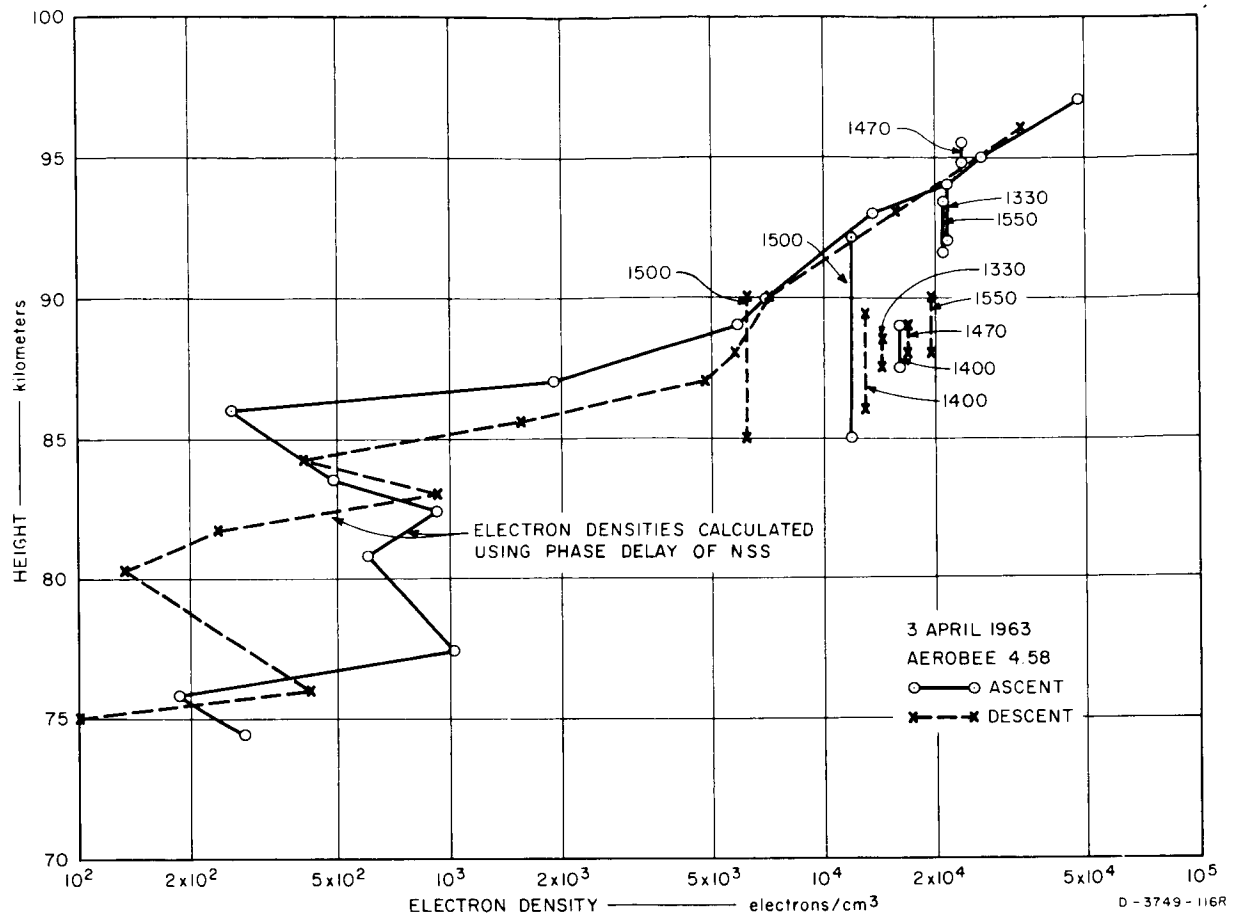


FIG. 9.28 ELECTRON DENSITY CALCULATED FROM PLASMA CUTOFF OBSERVATIONS

should not be a problem. With another loop antenna, all magnetic components of the wave could be measured and the direction of the wave front calculated to help resolve the question as to the effect of the earth's magnetic field on signals with frequencies near the electron gyrofrequency.

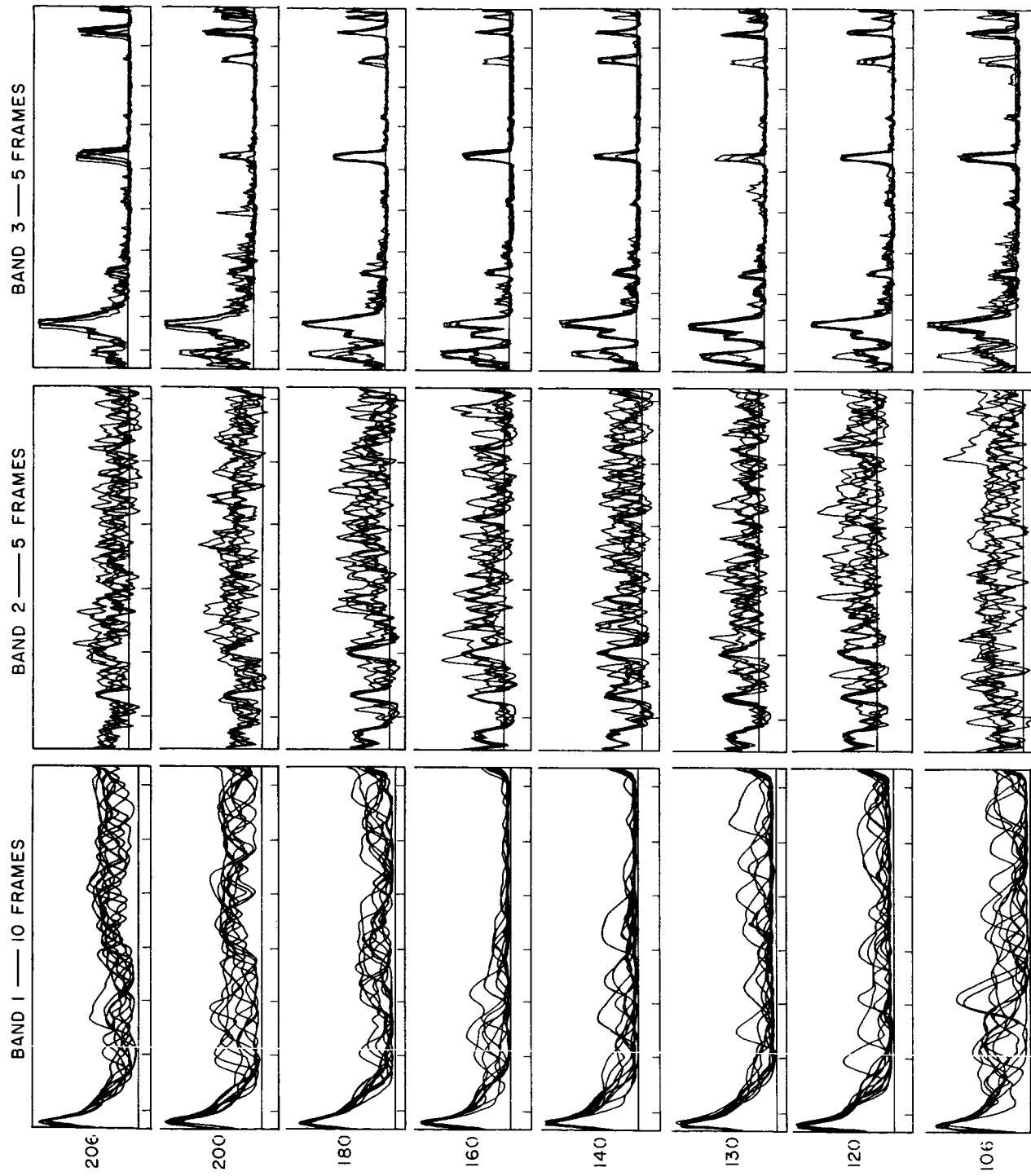
Another reason for a higher data rate is that, as the rocket went through the cutoff region, some signals reappeared for a sample or two after first being apparently cut off at a lower altitude. Although not conclusive, this suggests that the electron density at the lower edge of the daytime ionosphere is either rapidly varying in time or is heterogeneous, with horizontal gradients.

The noise seen around the gyrofrequency above the wave cutoff region, if not caused by the rocket instrumentation, could be gyrofrequency noise caused by interaction between electrons, ions, and the earth's magnetic field excited by solar radiation, the rocket, or ground sources. By reducing the instrumentation interference and properly shielding the loop antenna and preamplifiers, this noise if it exists should be easily detectable.

9.1.2.6 Aerobee 4.59 UI Sweeping Receivers

Portions of the outputs of the Band 1, 2, and 3 receivers during Aerobee 4.59 UI are shown in Figs. 9.29 and 9.30. The amplitude and frequency scales are shown at the bottom of each figure. In each set of sweeps there are marks on a horizontal line, which indicate frequencies. Also in each set is a reference line which in Band 1 represents the receiver threshold; in Band 2, 90 db below 1 gamma rms at 2 kc; and in Band 3, 80 db below 1 gamma rms. The amplitude scales are all in db below 1 gamma rms. The number to the left of each set of frames is the altitude in kilometers of the middle of the set (for example, the set in Band 2 at 60 km contains five sweeps, one of which was taken as the rocket moved through 60 km, two of the other sweeps were above and two were below the 60-km altitude). The sweep rate was 2.01 sweeps per second, and these receivers shared a common vertical loop antenna and preamplifier.

In looking at the receiver data displayed in Figs. 9.29 and 9.30, it is important to recognize first the interference sources and spurious responses. The major sources of interference are the telemetry subcarrier oscillators. An attempt was made to minimize these sources by rotating the receiving antenna for minimum coupling to the telemetry oscillators and by shielding the oscillators with high permeability material. The telemetry interference sources appear at constant levels as a function of time at approximately these frequencies: 1.7, 2.3, 3.0, 3.9, 5.4, 7.35, 10.5, 14.5, 22.0, 30.0, 40.0, and 66.9 kcs.



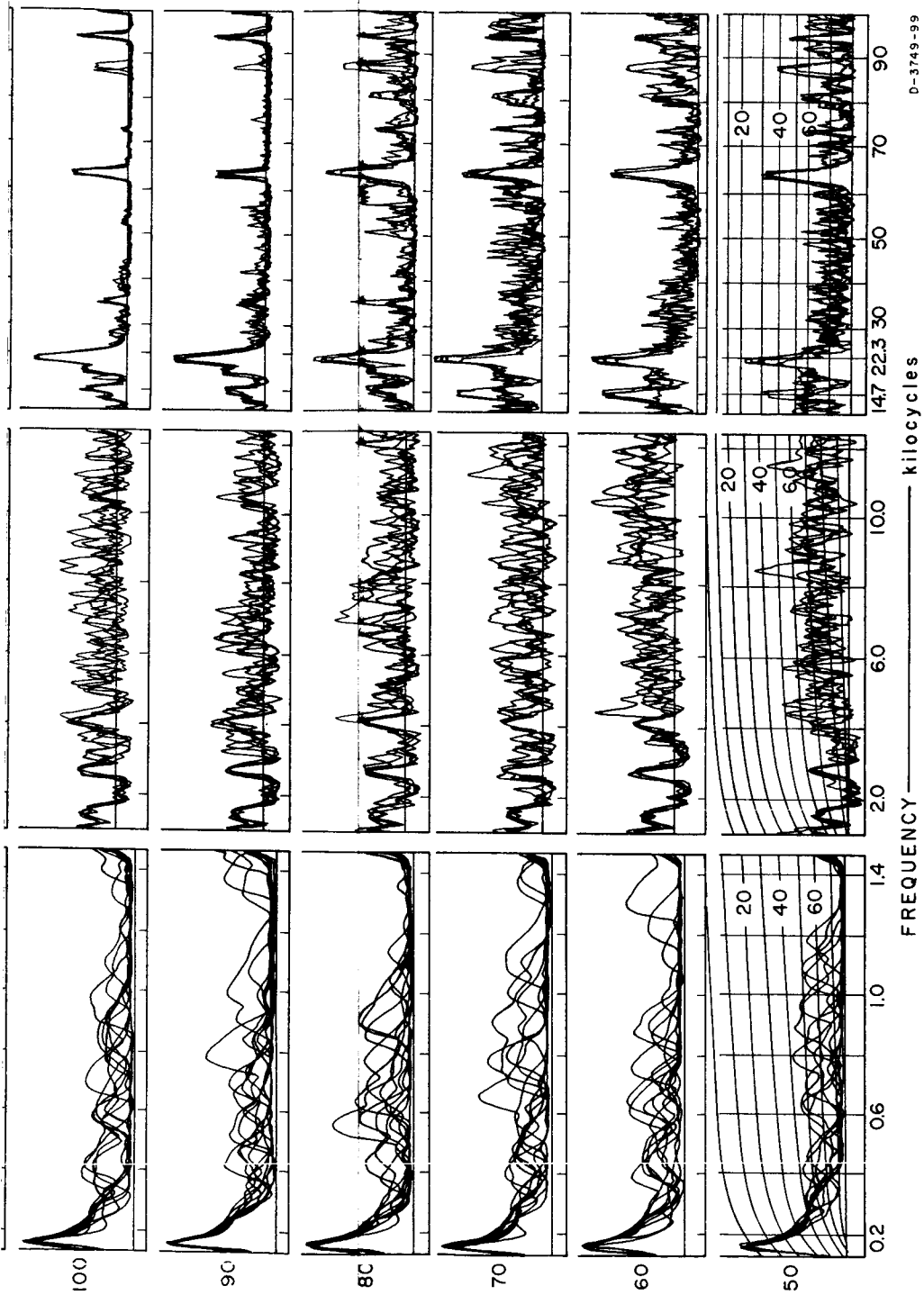
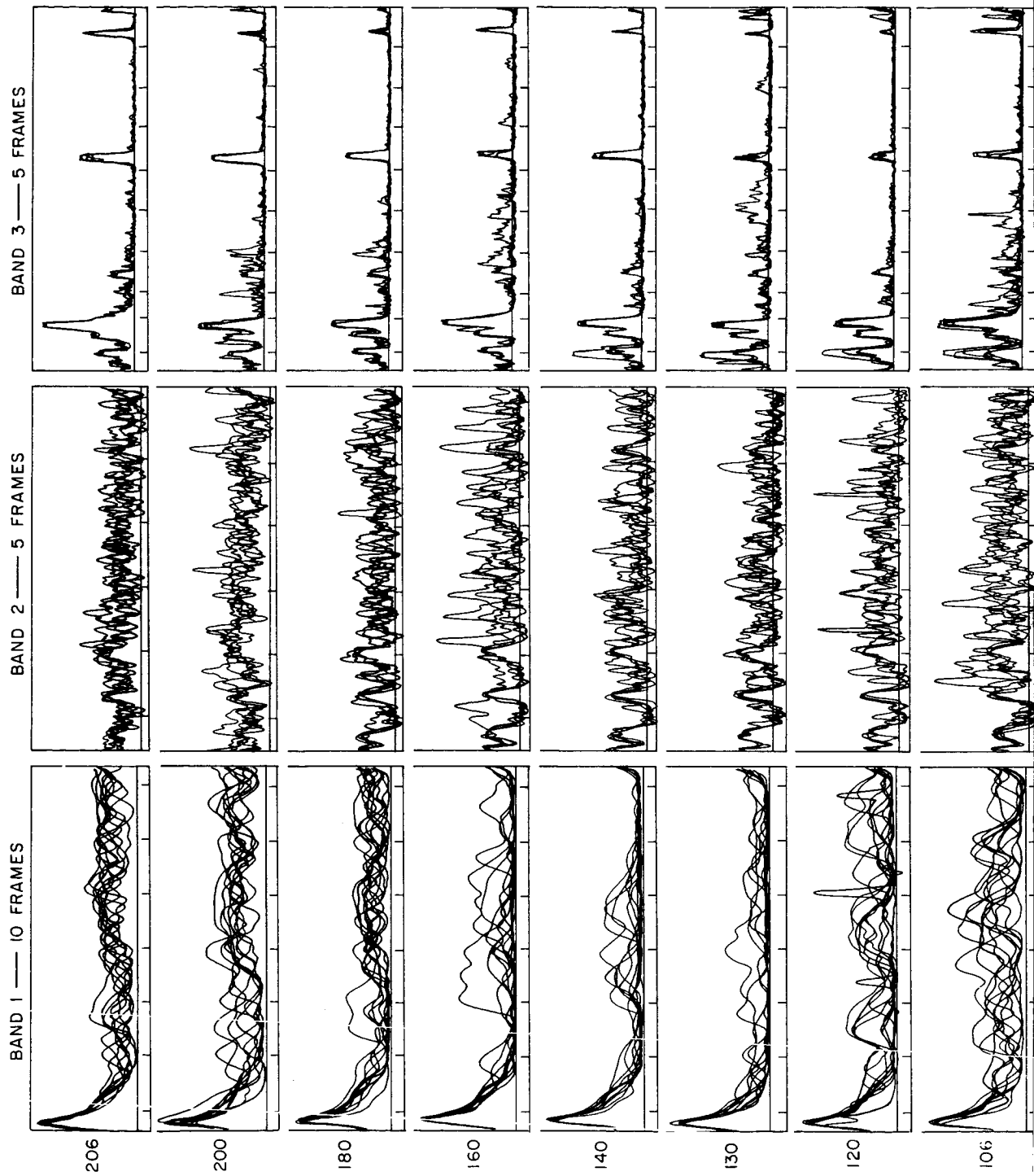


FIG. 9.29 AEROBEE 4.59 UI BANDS 1, 2, AND 3 SWEEPING RECEIVER DATA, ASCENT



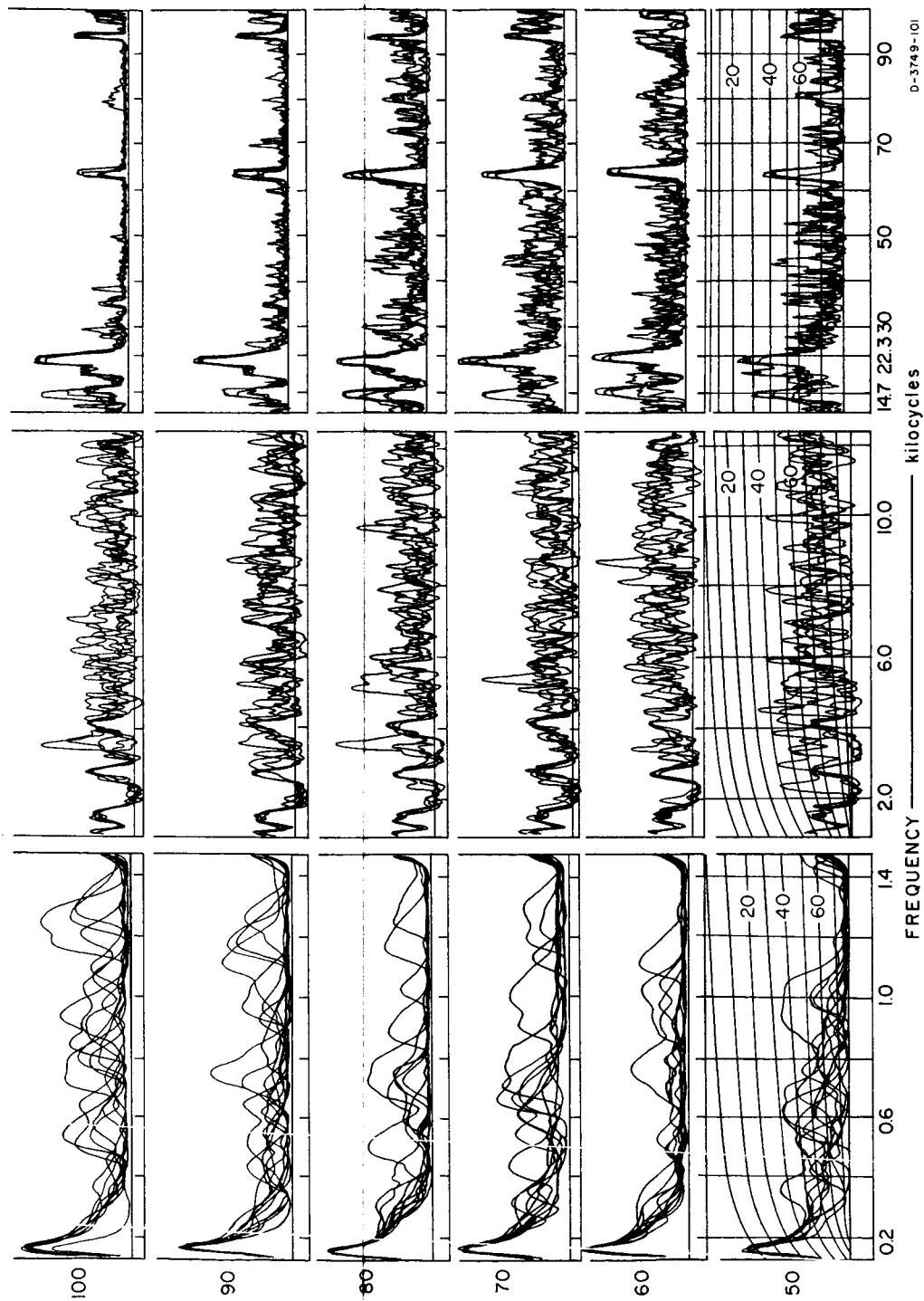


FIG. 9.30 AEROBEE 4.59 UI BANDS 1, 2, AND 3 SWEEPING RECEIVER DATA, DESCENT

There are several spurious responses caused when the second harmonic of the local oscillator minus the signal frequency is equal to the IF frequency. For example, NSS at 22.3 kc creates a response when the local oscillator is at 117.1 kc ($117.1 \times 2 - 22.3 = 212$). This appears as an output at the time when a $(212-117) = 95$ kc signal should appear. There are also spurious responses from other strong sources such as the one at 98.6 kc from NAA at 14.7 kc. The spurious responses are down approximately 35 db from the original source and are a result of a nonlinearity in the mixer.

The start of each sweep is signaled by a full-scale sync pulse in Band 1. There is a slight rise at the end of the Band 1 sweep, which is caused by the 1.7 kc telemetry oscillator. The start and end of Band 2 and the end of Band 3 also have outputs caused by the local oscillator feeding through the IF amplifier.

The data shown in Figs. 9.29 and 9.30 do not contain calibration signals.

Disregarding the coherent signals (interference, spurious responses, and broadcast stations) the remaining information on Figs. 9.29 and 9.30 is a picture of the frequency and amplitude distribution of magnetic noise at various altitudes for the conditions that existed at the time of Flight 4.59 UI. The most notable characteristics of the flight were a sporadic E layer at approximately 108 km and considerable sferic activity.

9.1.2.7 Band 1 Receiver, Aerobee 4.59 UI

In Figs. 9.29 and 9.30 ten sweeps of the output of the Band 1 receiver were overlaid and traced around selected altitudes to give an integrated picture that is characteristic of that region. At an altitude of 50 km, which is below the ionosphere and above the powered portion of the flight, it is seen that the noise covers the band from the lowest frequency (0.2 kc) to about 1.3 kc. The peak amplitudes of the signals around 50 km on the ascending portion of the flight are about 40 to 50 db below 1 gamma rms. It is presumed that these signals were caused by distant sferics and that the null starting at 3 kc (in

Band 2) is caused by the earth-ionosphere waveguide cutoff effect (Johler, 1962). The notch is a predominant feature of this band throughout the flight except during the sporadic E layer at 106 km and when the rocket is above 180 km. This phenomenon is discussed in Sec. 9.1.2.8. The maximum signals in this band on the ascent occur around 80 and 106 km and measure 25 db below 1 gamma rms. The strong signal at 80 km is caused by a strong spheric, which also can be seen in the other bands at similar positions in the sweep.

Around the sporadic E layer and above 180 km the amplitudes of signals appear to be larger than at other regions. As the refractive index increases it is expected that the magnetic field strengths would also increase. The Band 1 receiver shows strong signals over the flight of the rocket and indicates that there are probably strong signals below the 200-cps receiver range.

9.1.2.8 Band 2 Receiver, Aerobee 4.59 UI

In both ascending and descending portions of Aerobee 4.59 UI the most prominent feature of the output of the Band 2 receiver is a notch that occurs about 3 kc. The notch is somewhat obscured by telemetry interference from the 1.7, 2.3, 3.0, and 3.9 kc VCO's. It is presumed that the notch is caused by the earth-ionosphere waveguide cutoff effect (Johler, 1962). It is interesting to note that the notch does not appear when the rocket is in the sporadic E layer during ascent or above approximately 180 km, and the general level of signal strength rises in these regions. The increase in noise level in these regions can be explained as an increase in magnetic field strength due to increased refractive index; however, the disappearance of the notch is not understood. The disappearance of the notch and the increase in signal levels is not significantly apparent during descent through the sporadic E layer possibly because the effective thickness of the layer is too small, or because the layer may be disappearing to the east (dark side). Possibly the notch is obscured by signals generated locally due to the disturbance of the layer by the rocket, or due to electron-ion gyro-frequency interaction phenomena. Enhancement of signals due to reflections from these boundaries (standing waves) is possible.

The minimum signals in the band occur when the rocket is in the regions around 130 km; this agrees with the electron density (see Fig. 9.71) and refractive index minimums.

From the data that are available it would appear that the amplitude versus frequency profiles of sferics received in a particular region are a function of the region and not constant with altitude.

9.1.2.9 Band 3 Receiver, Aerobee 4.59 UI

Figures 9.31 through 9.38 show signal strength versus altitude of NAA at 14.7 kc, and NSS at 22.3, 64.2, and 88.0 kc, both ascending and descending. These stations except NSS at 22.3 kcs were keying on and off during the greater part of the descending portion of the flight. The majority of these signals show a decrease in amplitude starting at the 70- to 80-km level with a minimum point around 90 km, but they definitely increase again at higher altitudes and become circularly polarized at the peak of the trajectory. An indication of the noise level as a function of altitude can be obtained by looking at the amplitude when the signal is keyed off. There are some Loran C signals around 100 kc during the ascending part of the flight up to just above 80 km, which reappear at about 90 km on the descending portion. There are some unidentified broadcast signals at approximately 70, 72, and 80 kc, which are below receiver threshold above 80 km.

The noise in Band 3 is quite strong up to 80 km and shows a definite decrease at 90 and 100 km. The ground station signals also show a definite amplitude decrease between 80 and 90 km. There is a slight increase around 106 km when the missile is in the sporadic E cloud; then the amplitude decreases until a minimum is reached at 160 km. At heights above 160 km there is a slight increase in signal strength. It is interesting to compare the noise in the output of Band 3 with the electron density measurements as shown in Fig. 9.71. Since the loop antenna is sensitive to magnetic fields it is to be expected that the amplitudes would show an increase when the refractive index increases.

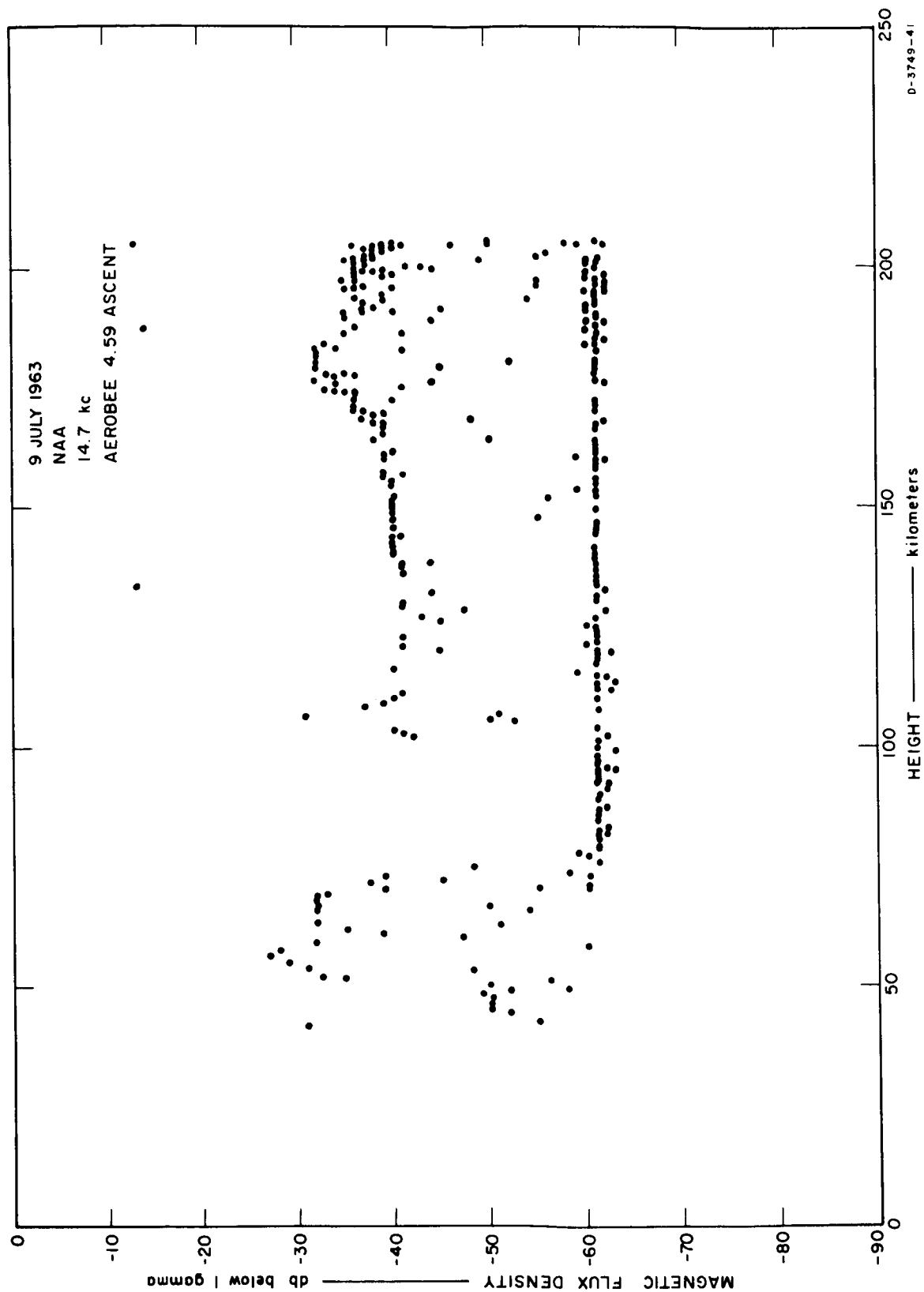


FIG. 9.31 AMPLITUDE OF NAA AND 14.7-kc NOISE, ASCENT

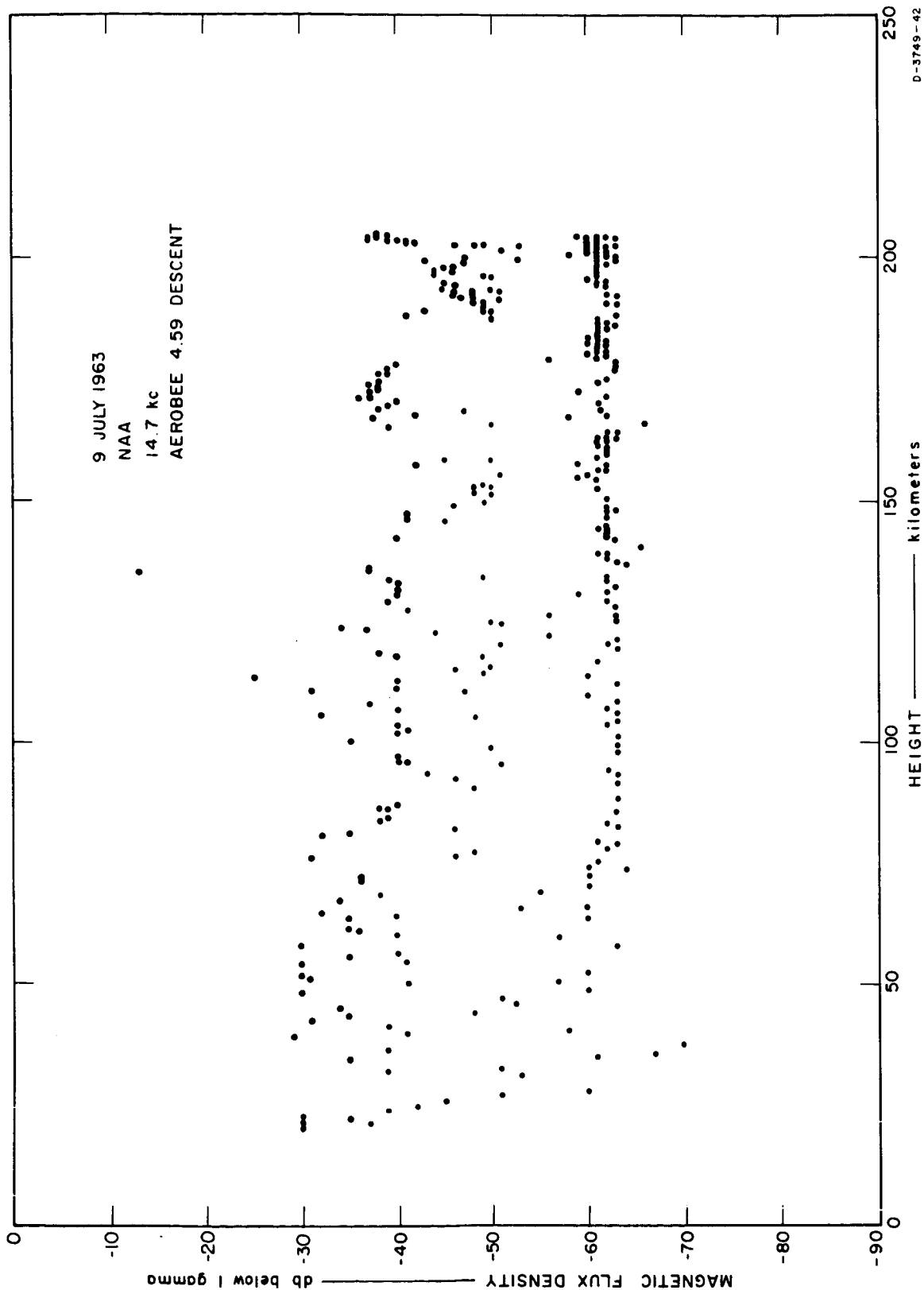


FIG. 9.32 AMPLITUDE OF NAA AND 14.7-kc NOISE, DESCENT

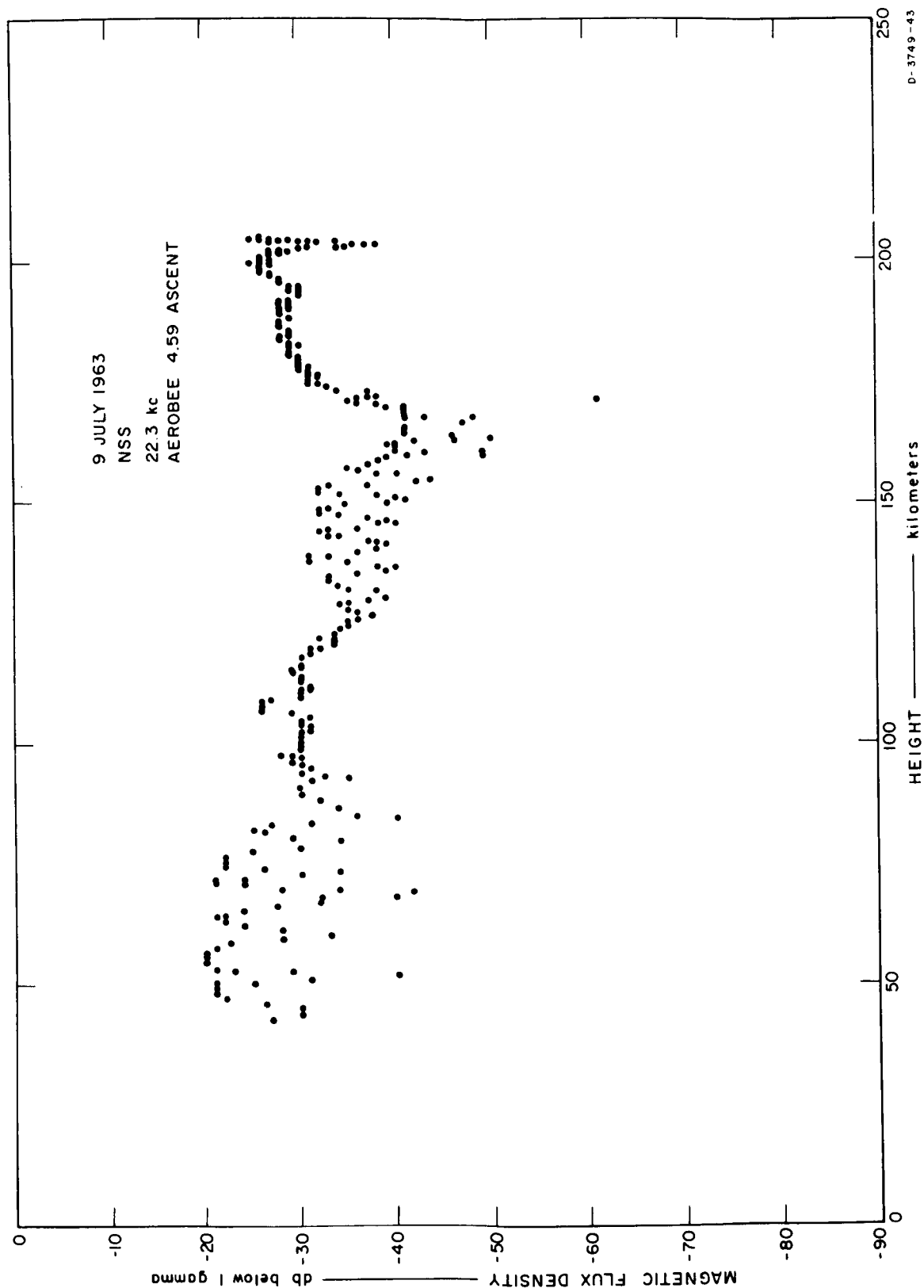


FIG. 9.33 AMPLITUDE OF NSS, ASCENT

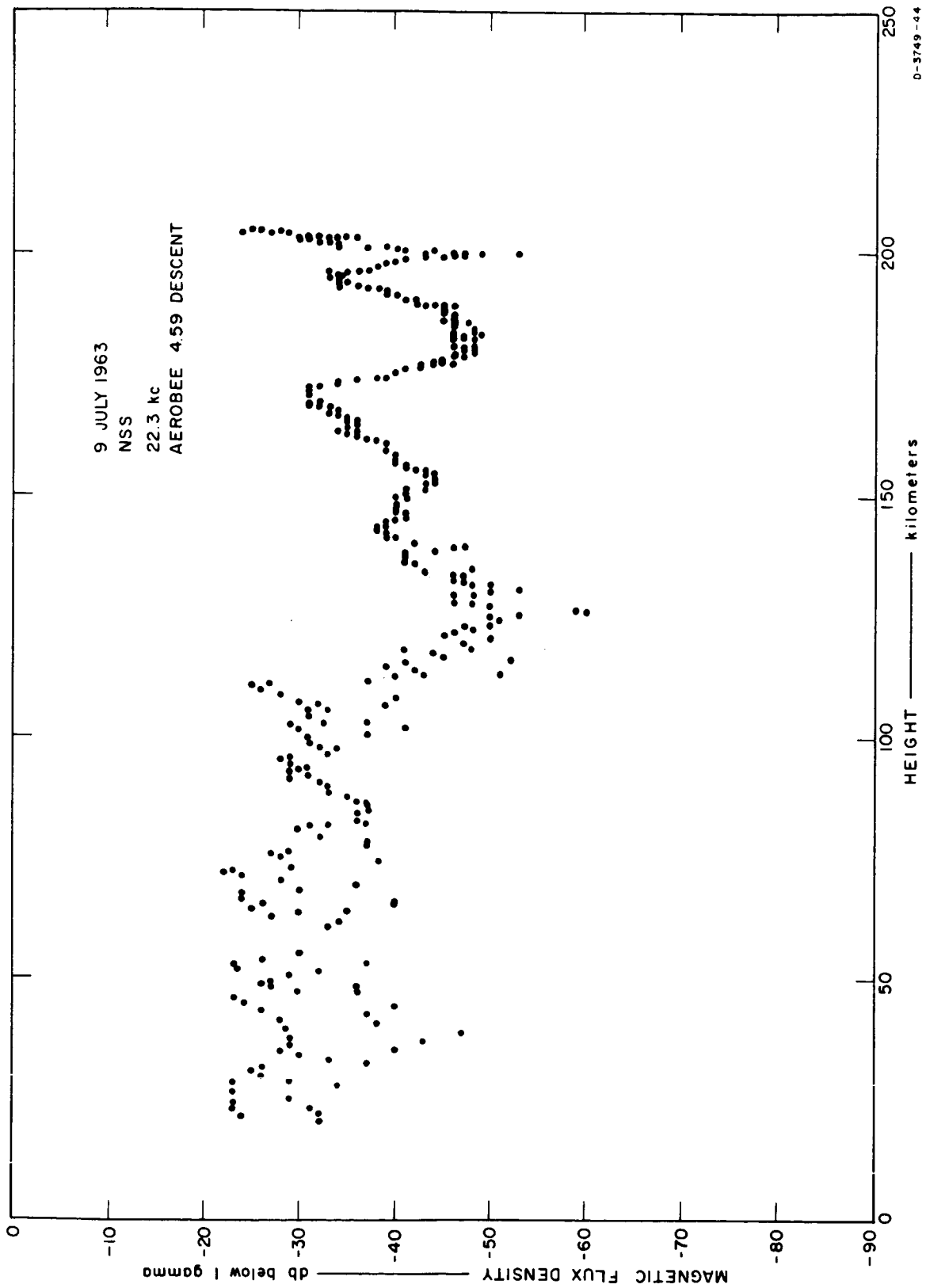


FIG. 9.34 AMPLITUDE OF NSS, DESCENT

D-3749-44

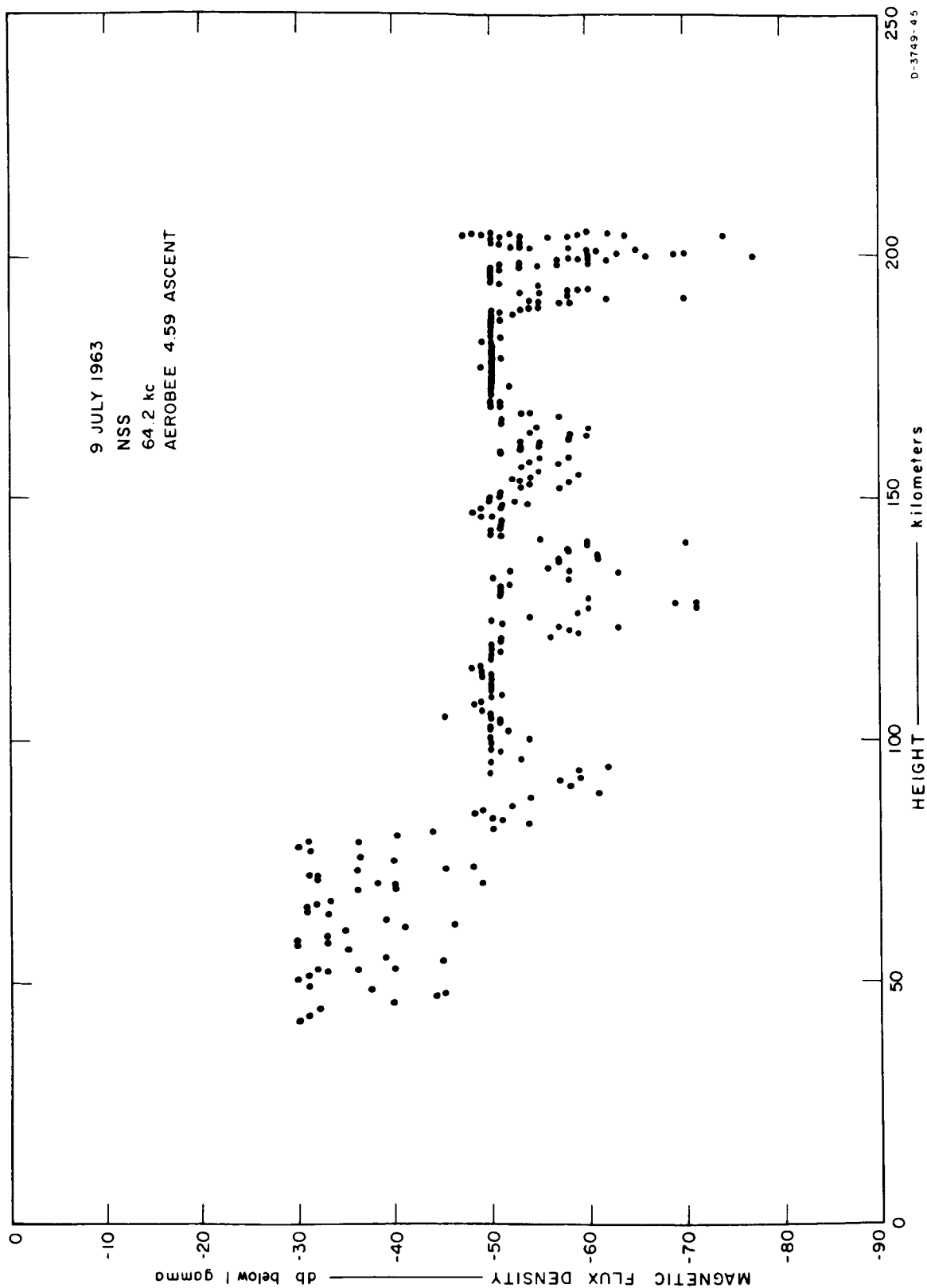


FIG. 9.35 AMPLITUDE OF NSS (64.2 kc), ASCENT

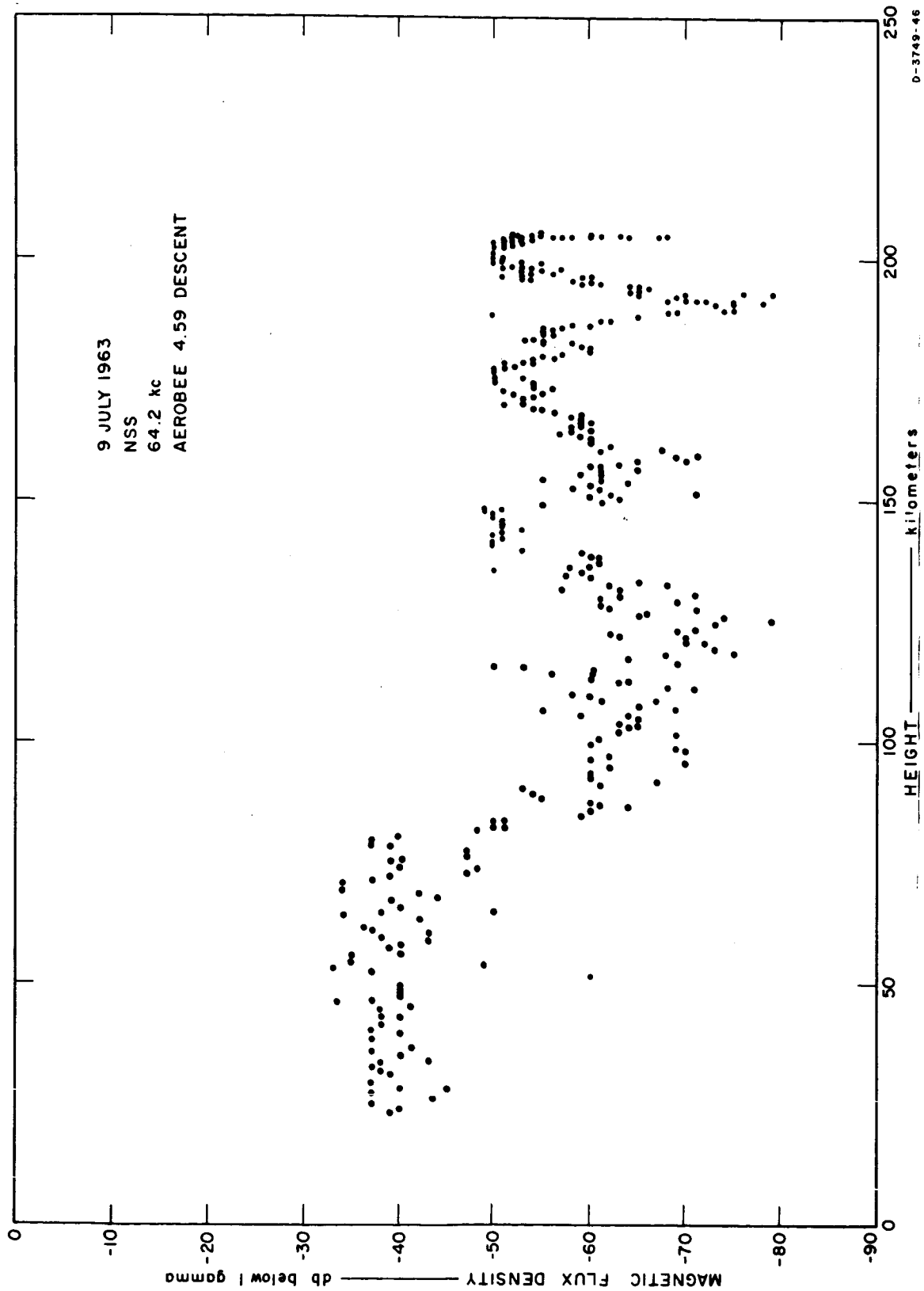


FIG. 9.36 AMPLITUDE OF NSS (64.2 kc), DESCENT

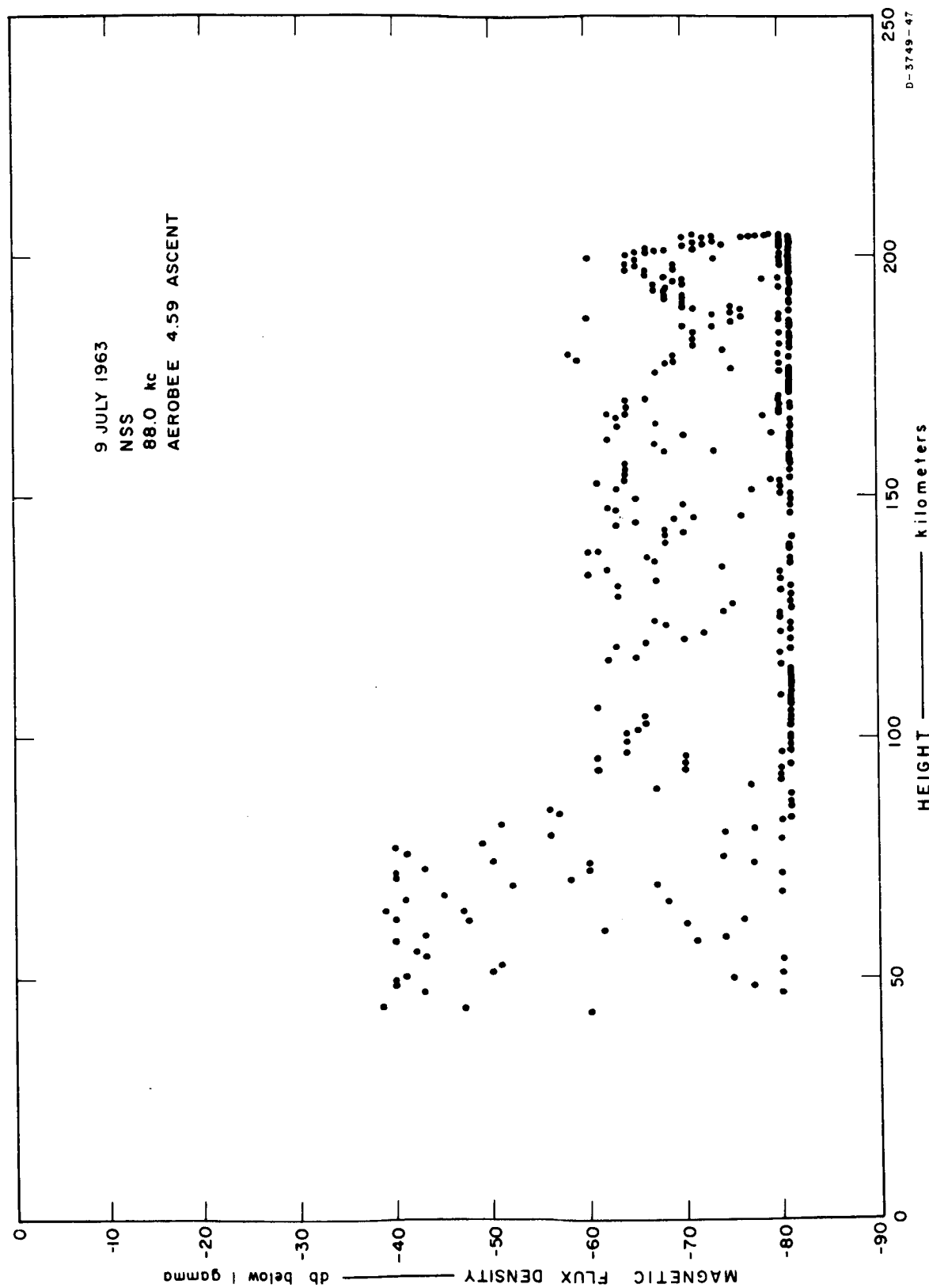


FIG. 9.37 AMPLITUDE OF NSS (88.0 kc), ASCENT

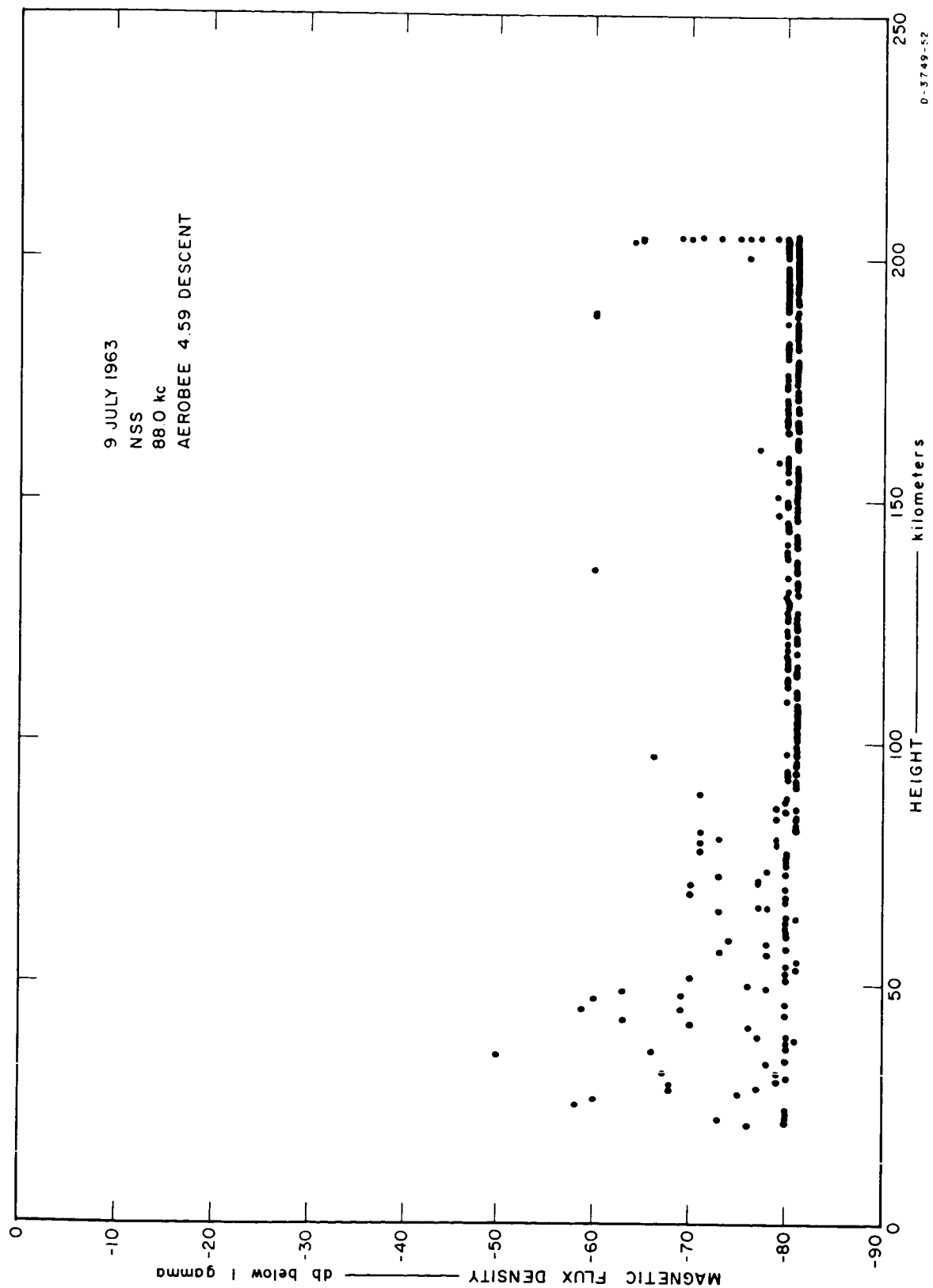


FIG. 9.38 AMPLITUDE OF NSS (88.0 kc), DESCENT

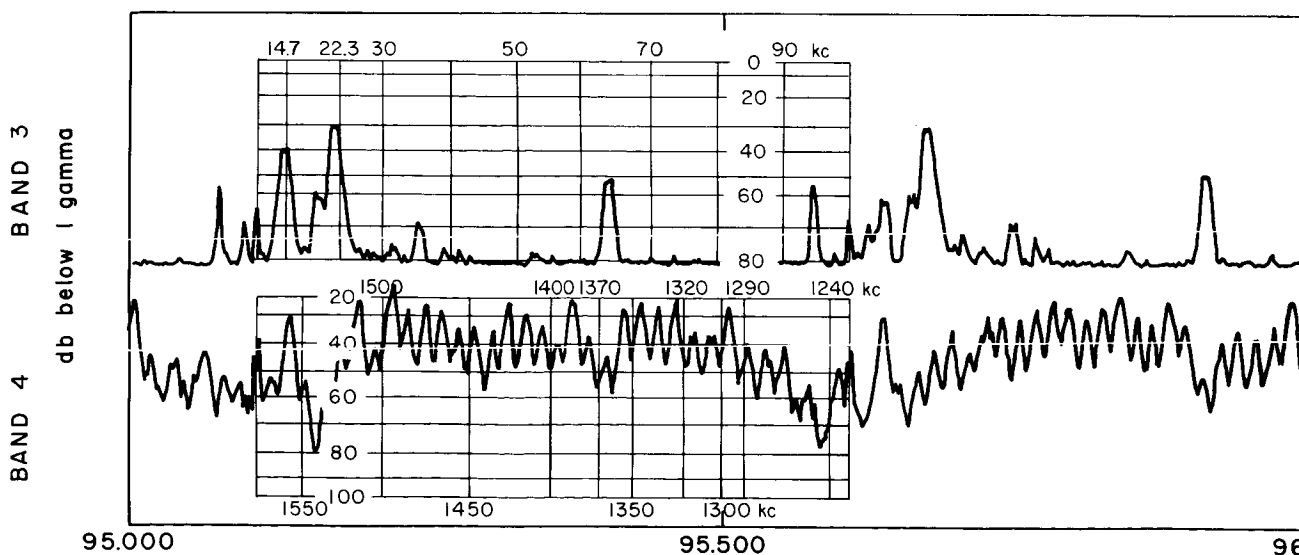
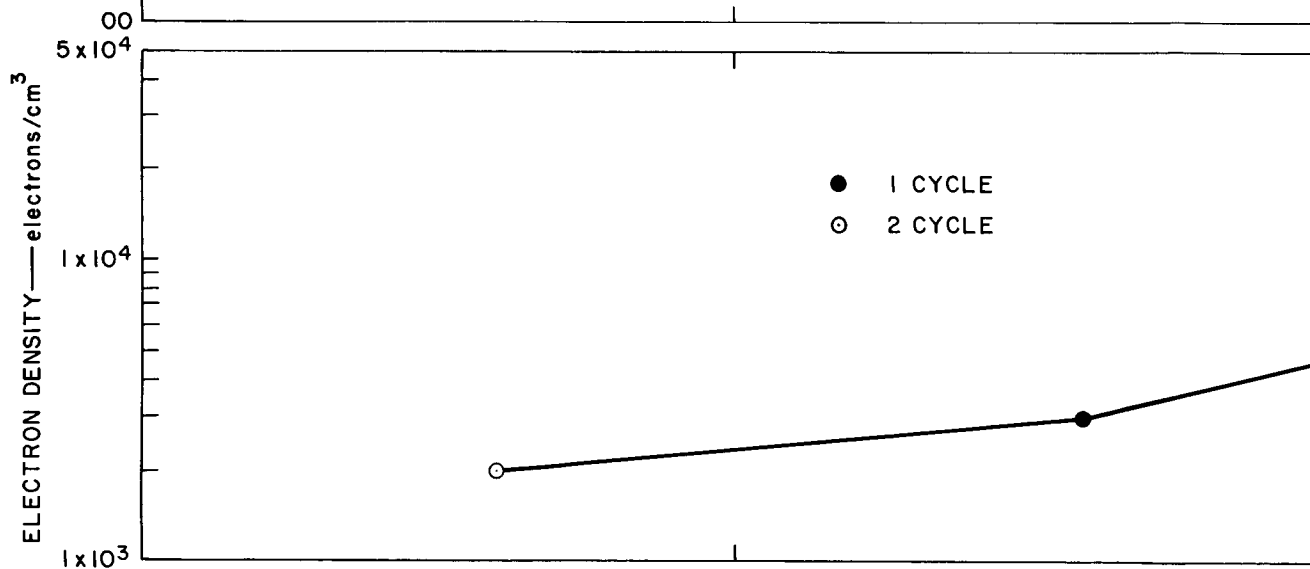
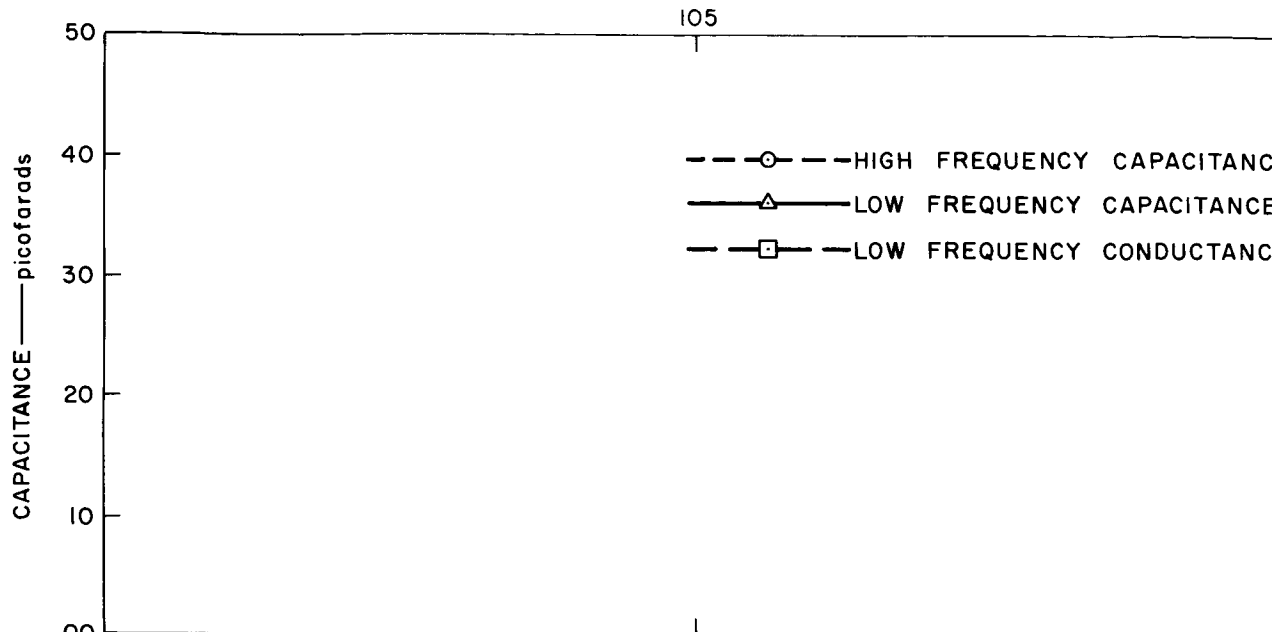
9.1.2.10 Band 4 Receiver, Aerobee 4.59 UI

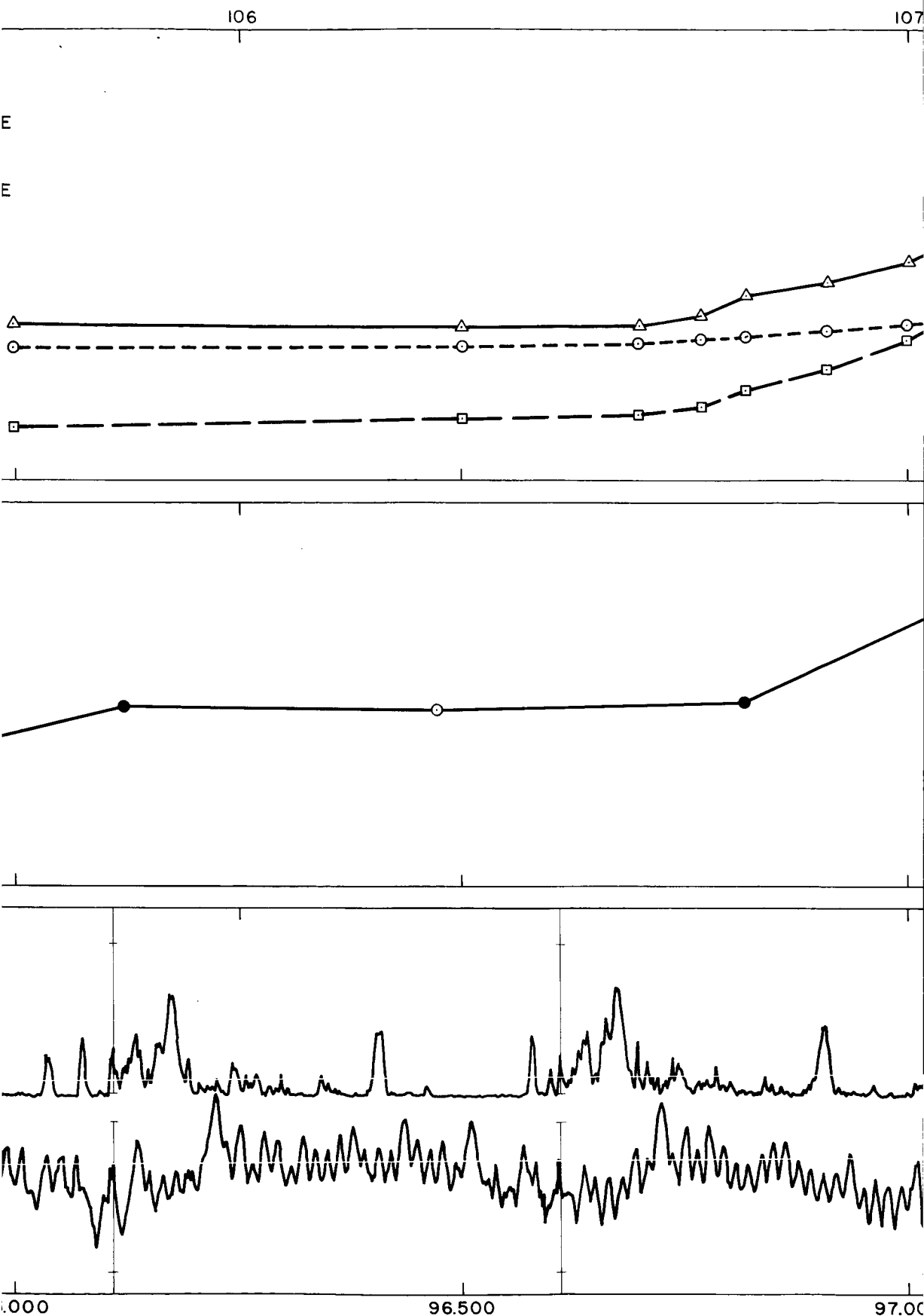
There appears one broadcast station every 10 kc across the band of the receiver (see Figs. 9.39 and 9.40). Four stations were selected and point-by-point plots of signal strength versus altitude were made over the complete flight (see Figs. 9.41 through 9.48). Only in one place did the signals decrease below the receiver threshold-- during the descending pass through the sporadic E layer (see Fig. 9.40).

Most of the signals showed slight decreases starting above 80 km. There was then a sharp decrease at the sporadic E layer and the signals stabilized to a lower level immediately above the layer. As the rocket approached the peak of its flight, the spin modulation of the signals decrease indicating that the waves were becoming circularly polarized. There was also a decrease in amplitude at the extreme altitude.

The remarkable feature about this band of signals was the strength of the signals above the E layer. Since the coverage of the layer is not known, it is presumed that the signals came through regions of low electron density, were reflected from the F layer, and returned to the top side of the E. The fact that signals appeared inside the sporadic E layer on the ascending portion of the flight where the electron density was greater than that required for plasma cutoff is also remarkable and yet to be analyzed in detail.

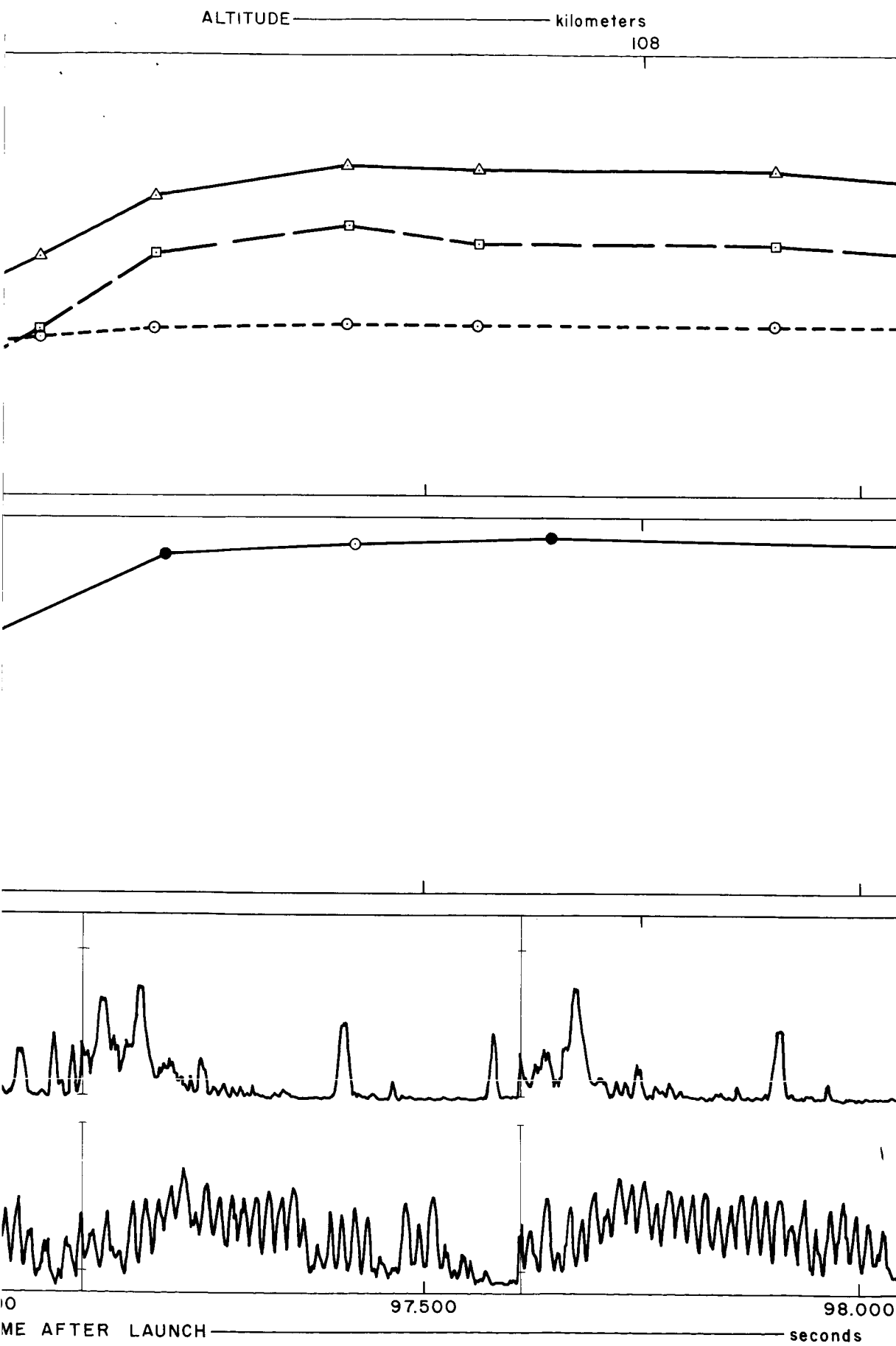
A large volume of data from this receiver has not been reduced or analyzed. It is expected that some useful information could be extracted from the data taken around the peak of the flight. Because of the complex geometry and reflections produced by the sporadic E cloud, the analysis of these data would require more effort than was available. As a result this interesting work was not undertaken.





2#

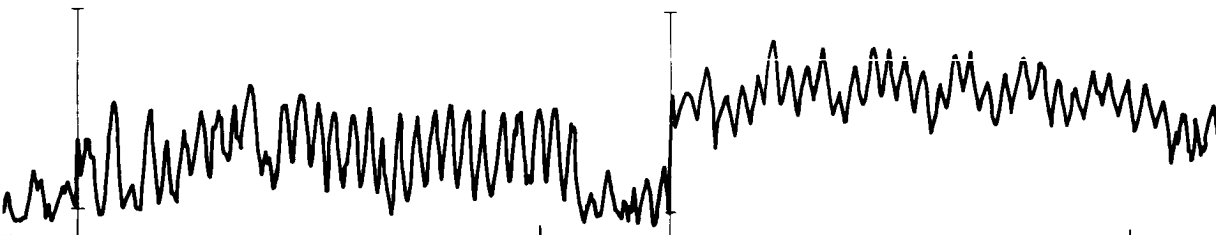
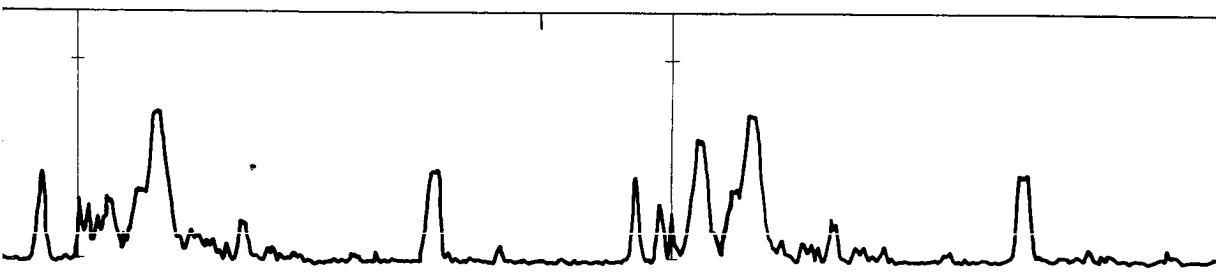
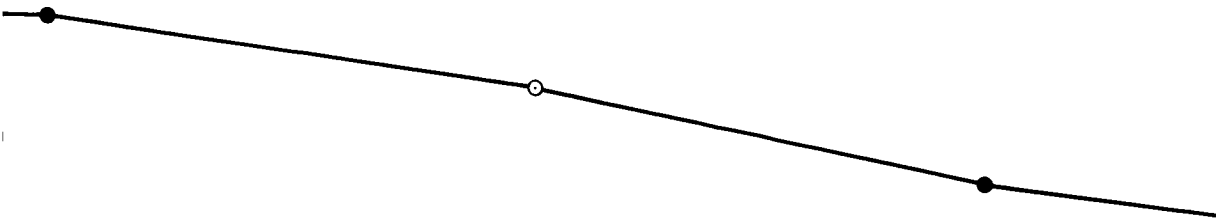
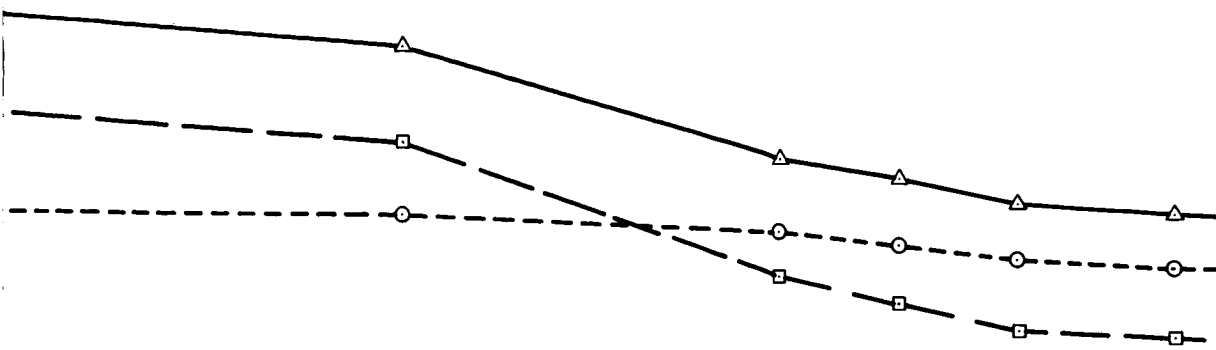
FIG. 9.39



SPORADIC-E LAYER: BANDS 3 AND 4, IMPEDANCE PROBE, AND ELECTRON DENSITY, AS

3#

109

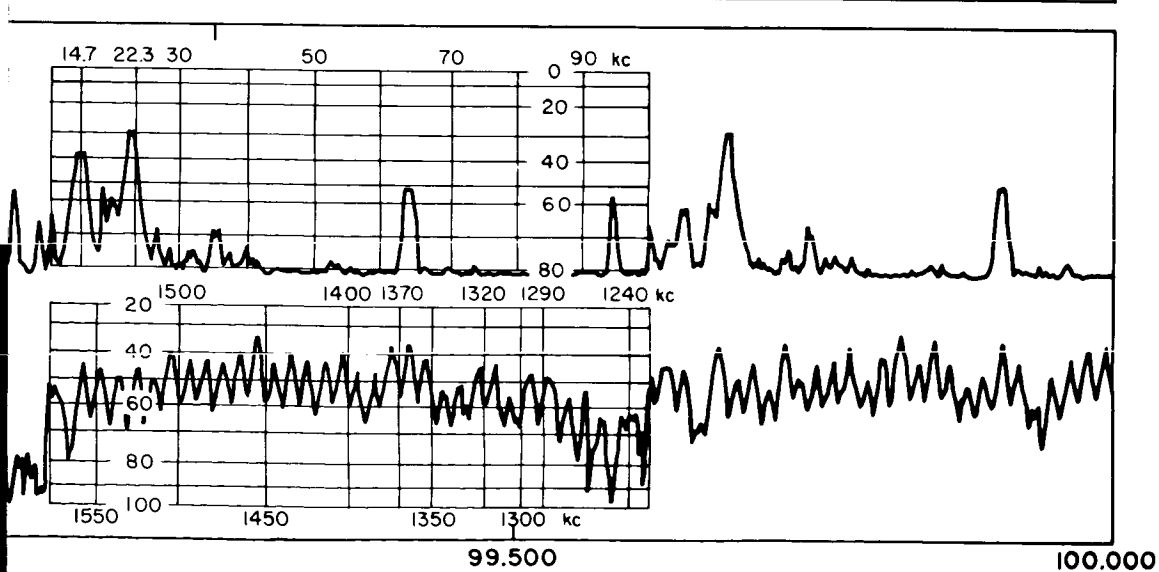
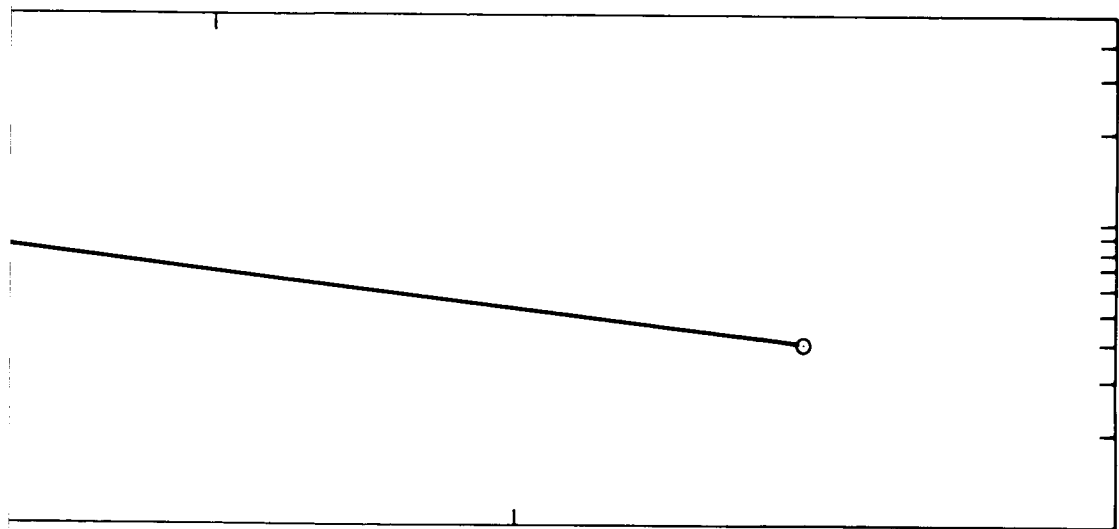
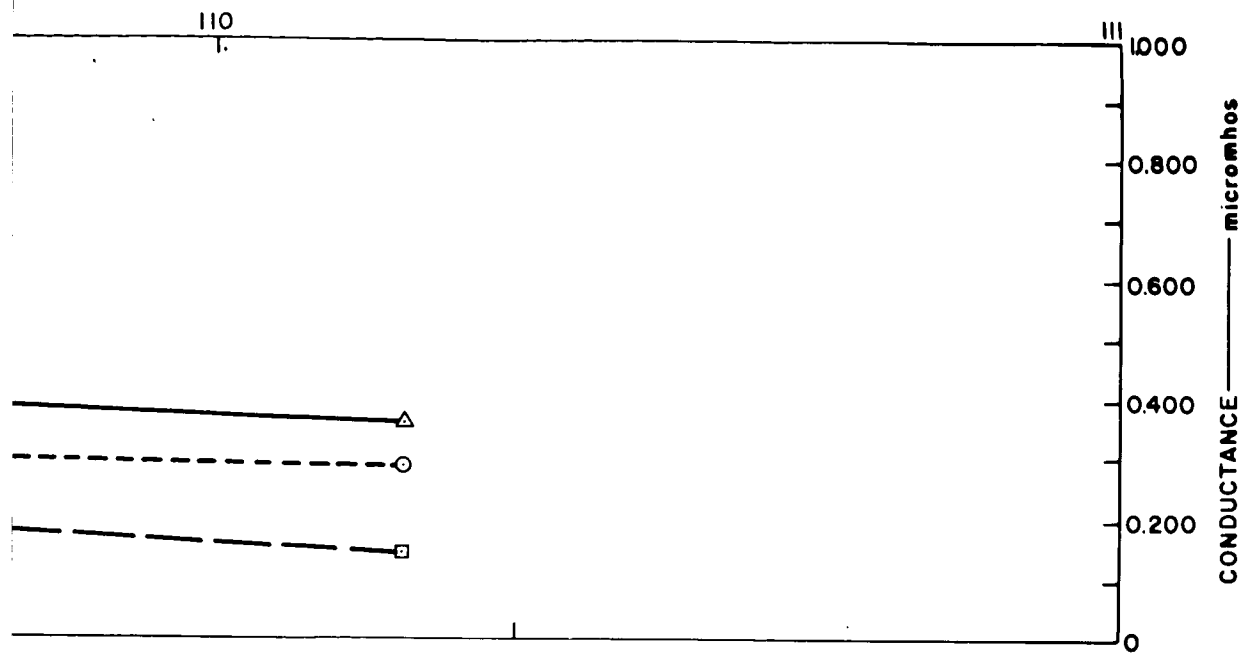


98.500

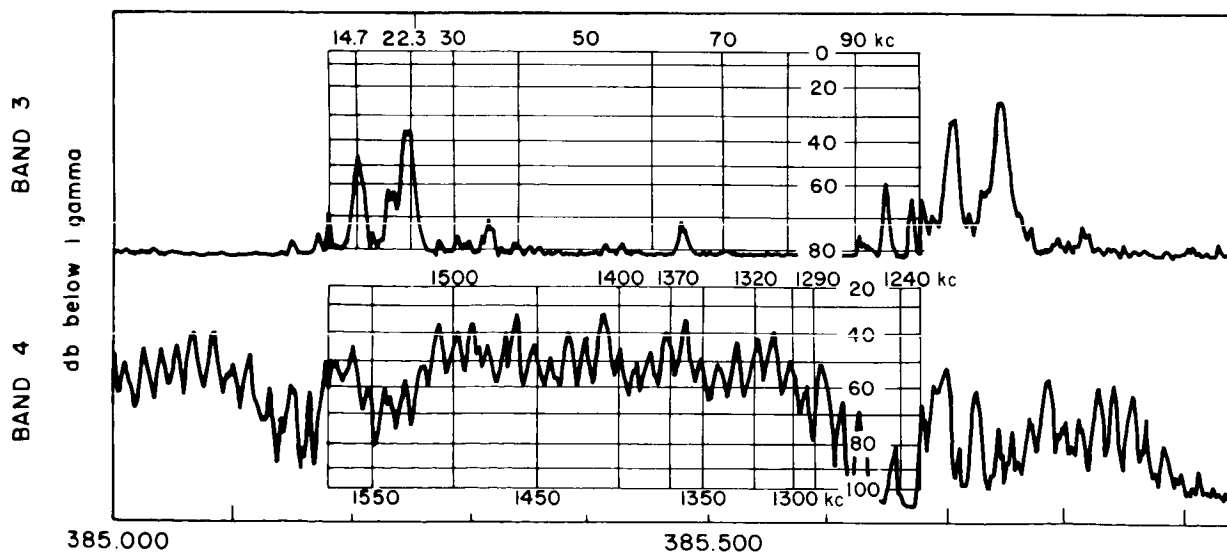
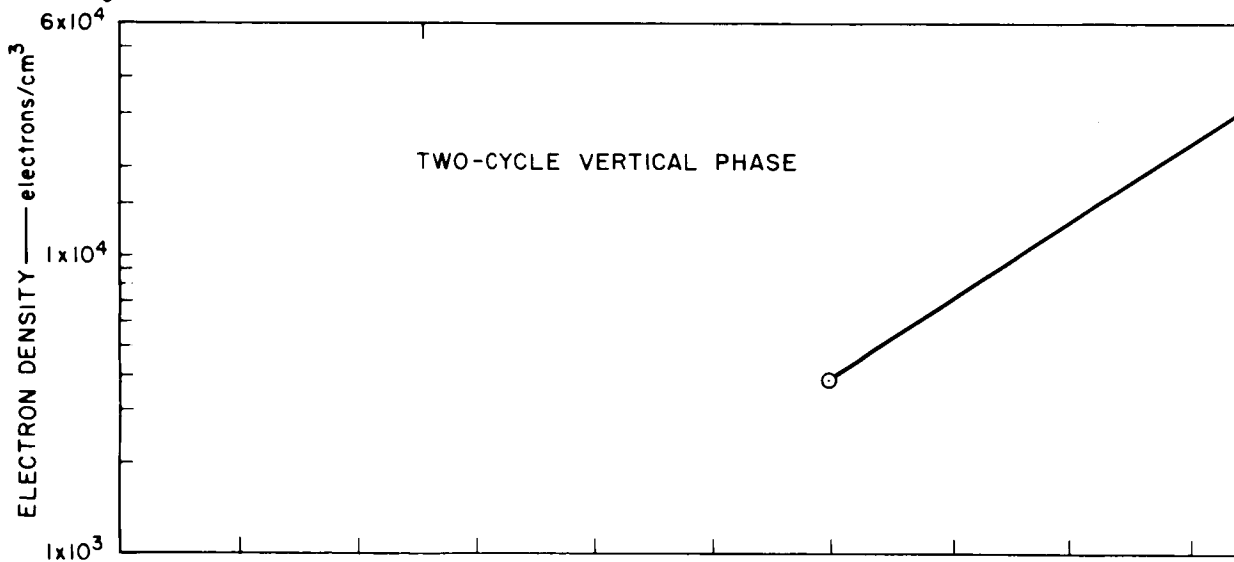
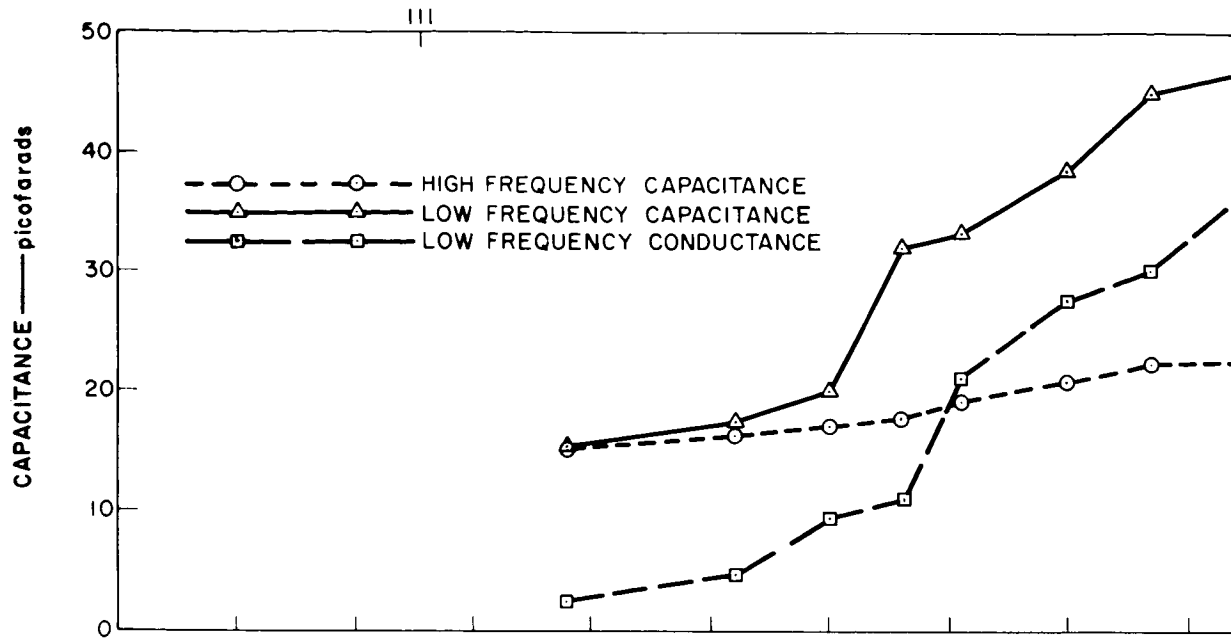
99.000

CENT

4 #



5#



1.11

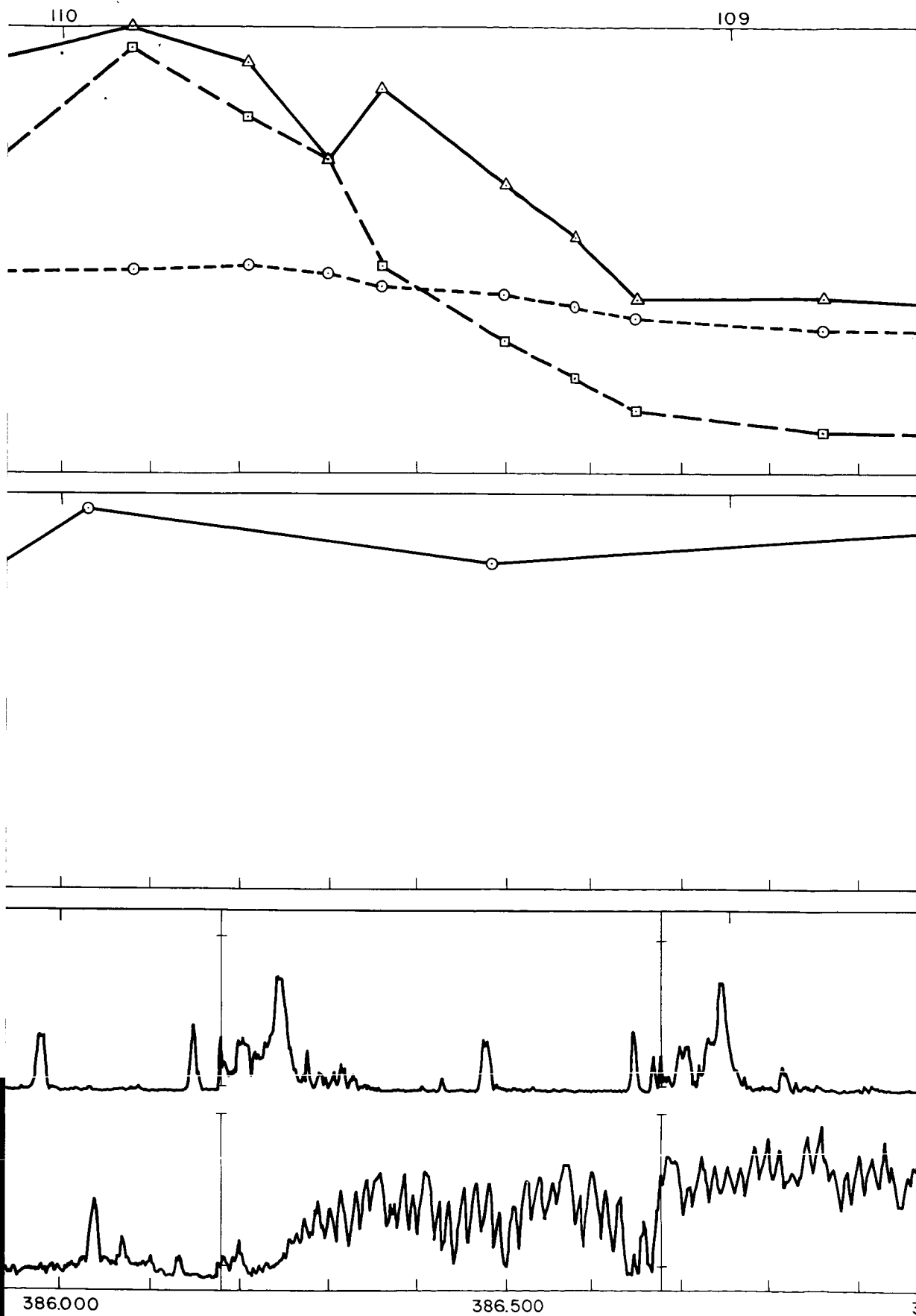


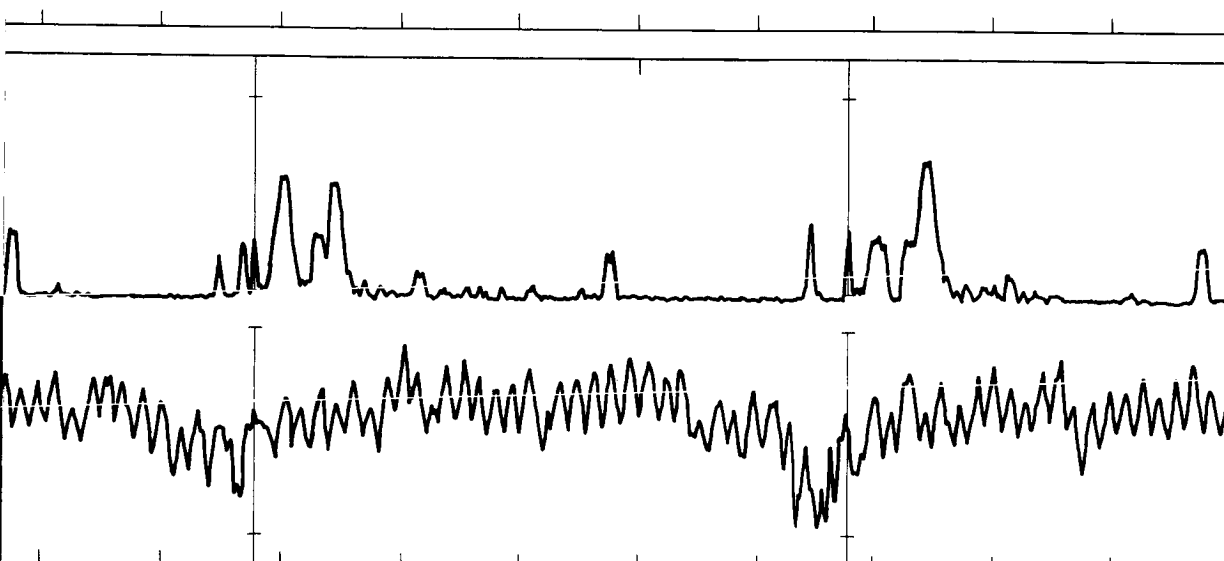
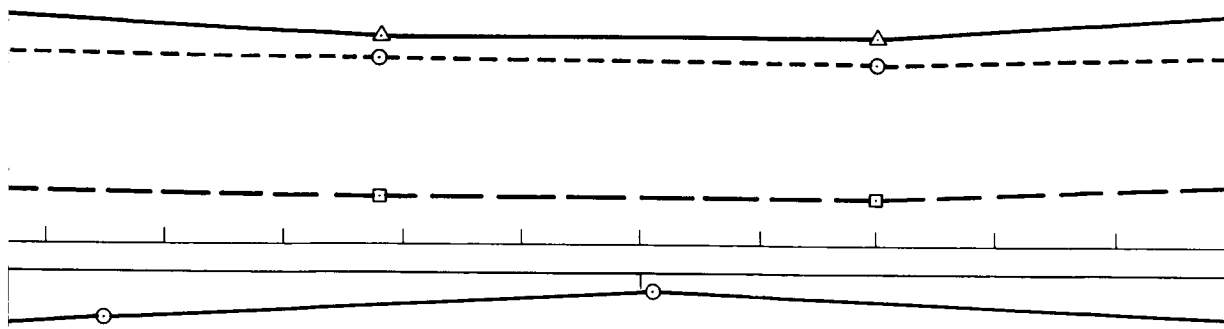
FIG. 9.40

27

ALTITUDE

kilometers

108



387.000

387.500

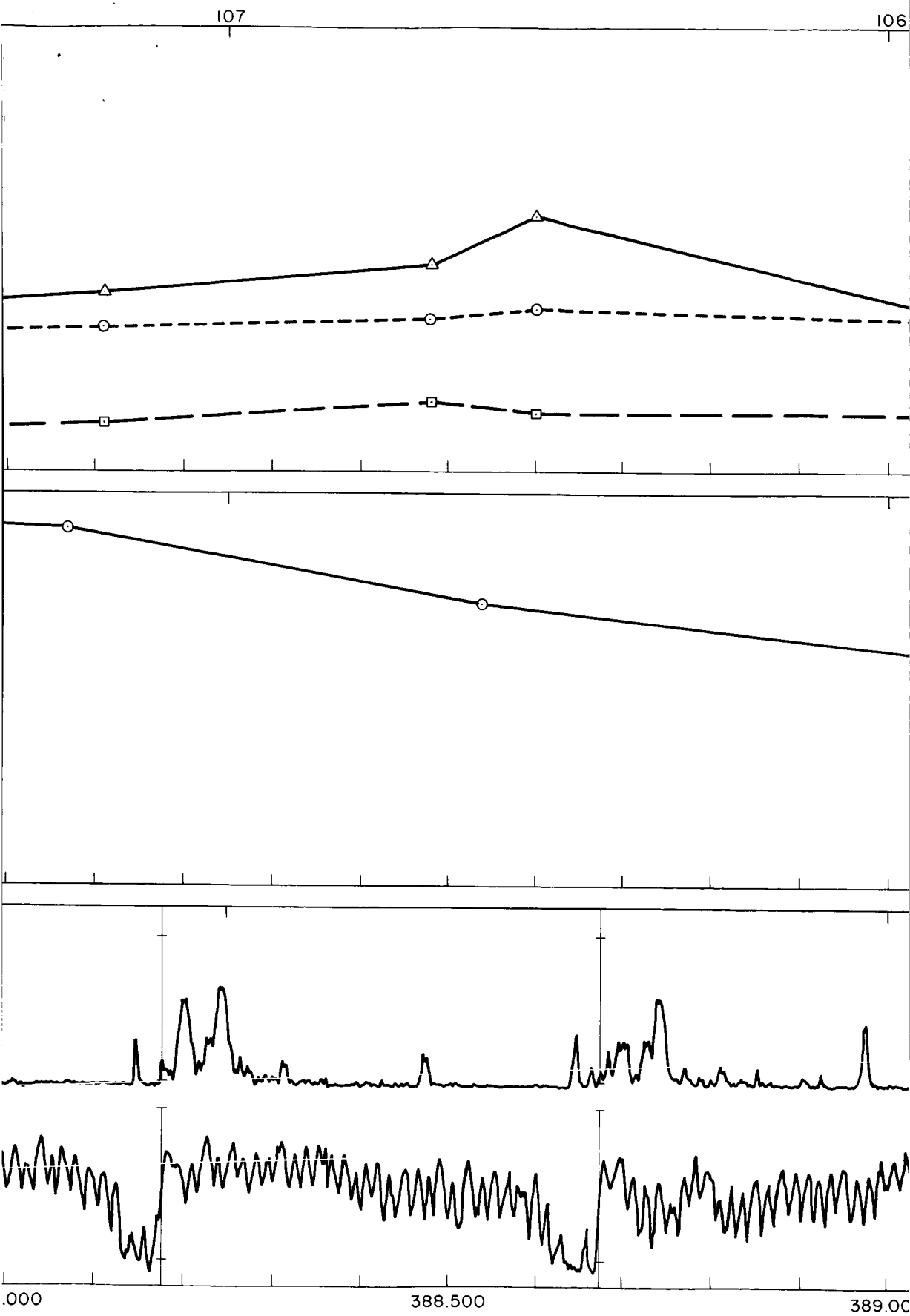
388.000

TIME AFTER LAUNCH

seconds

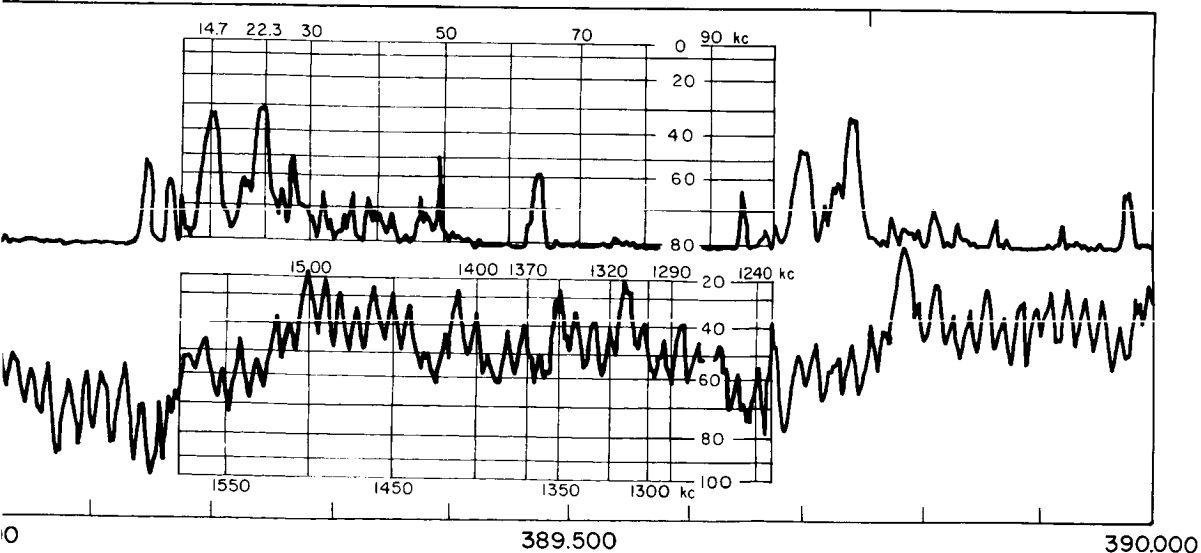
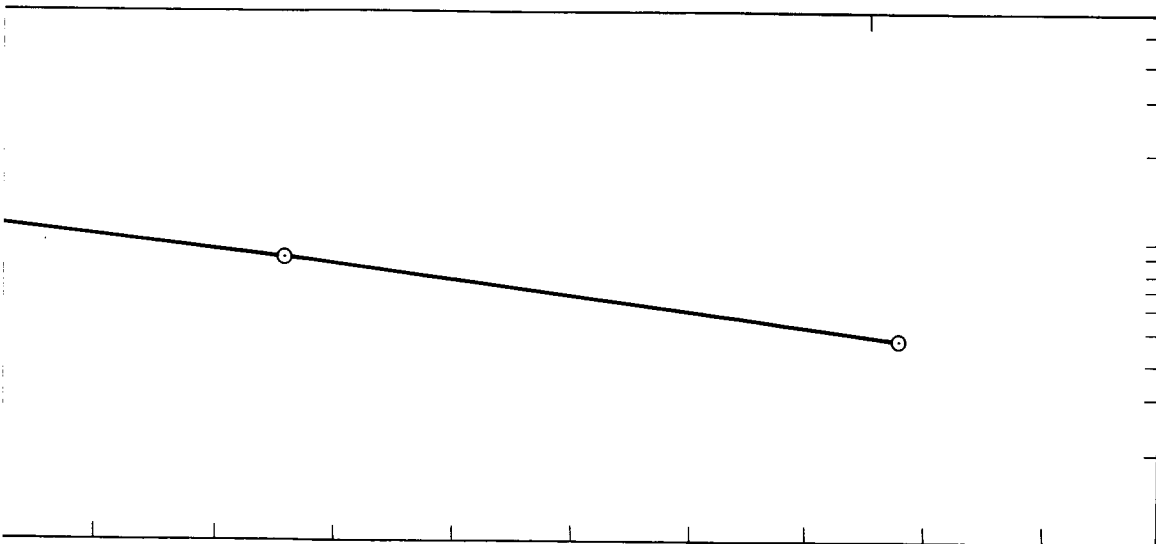
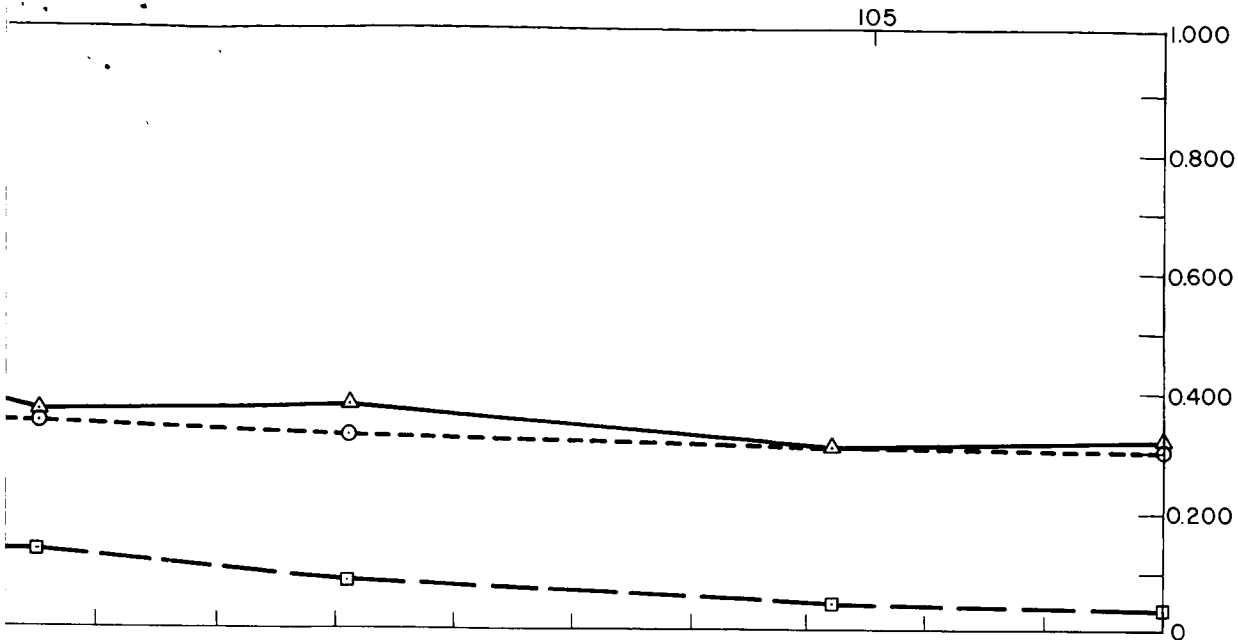
SPORADIC-E LAYER: BANDS 3 AND 4, IMPEDANCE PROBE, AND ELECTRON DENSITY, D

34



ESCENT

4 #



5th

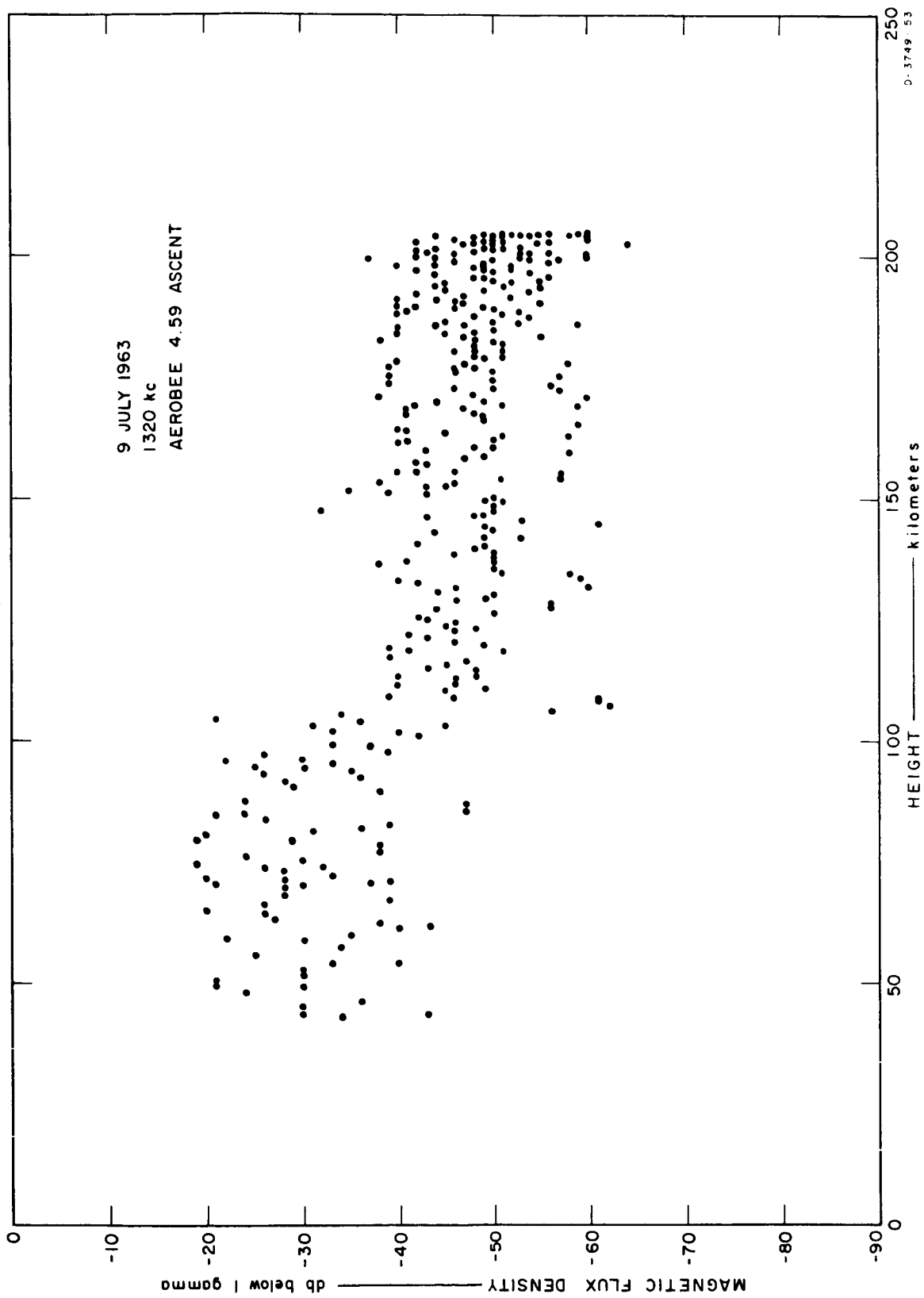


FIG. 9.41 AMPLITUDE OF 1320 kc, ASCENT

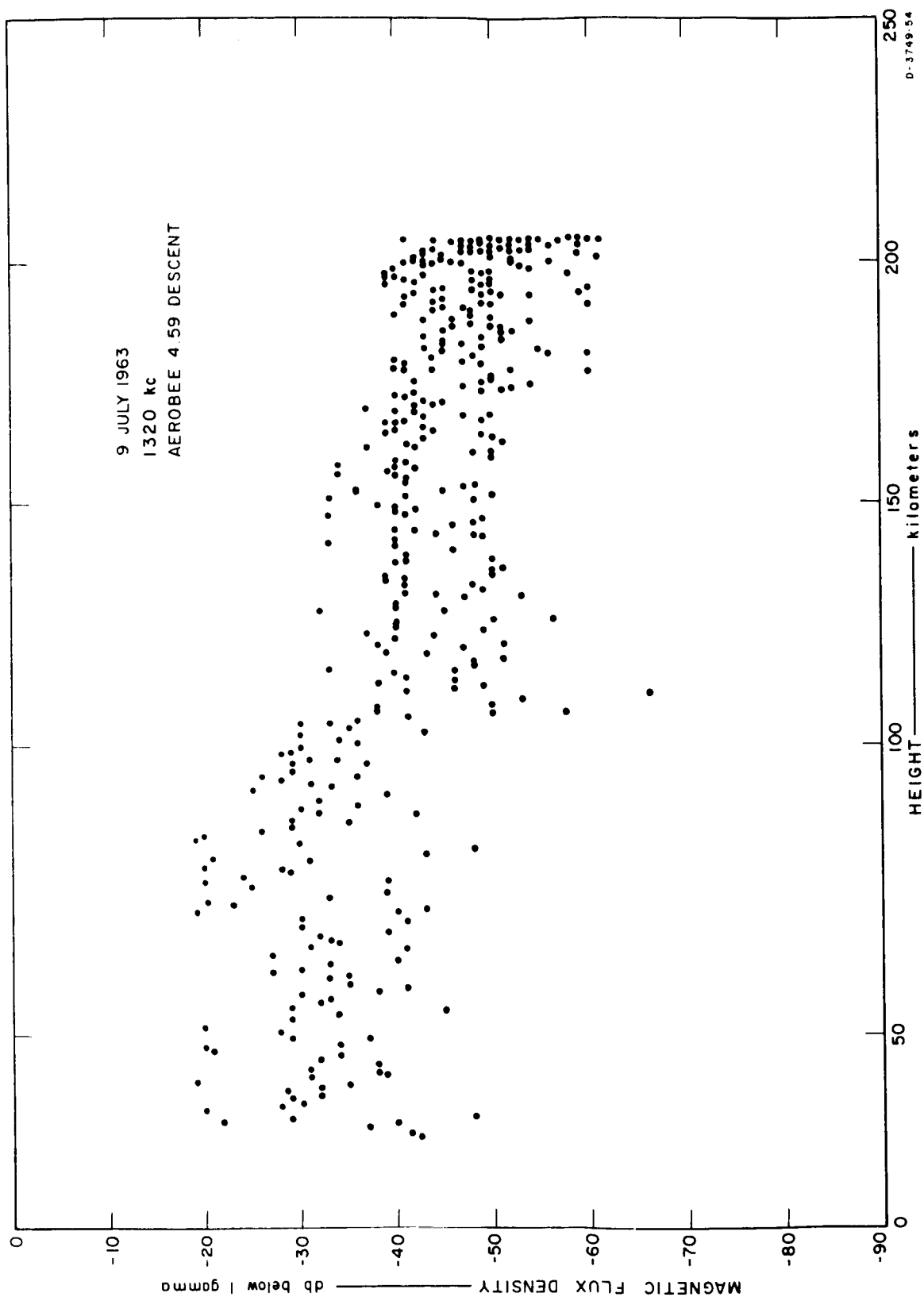


FIG. 9.42 AMPLITUDE OF 1320 kc, DESCENT

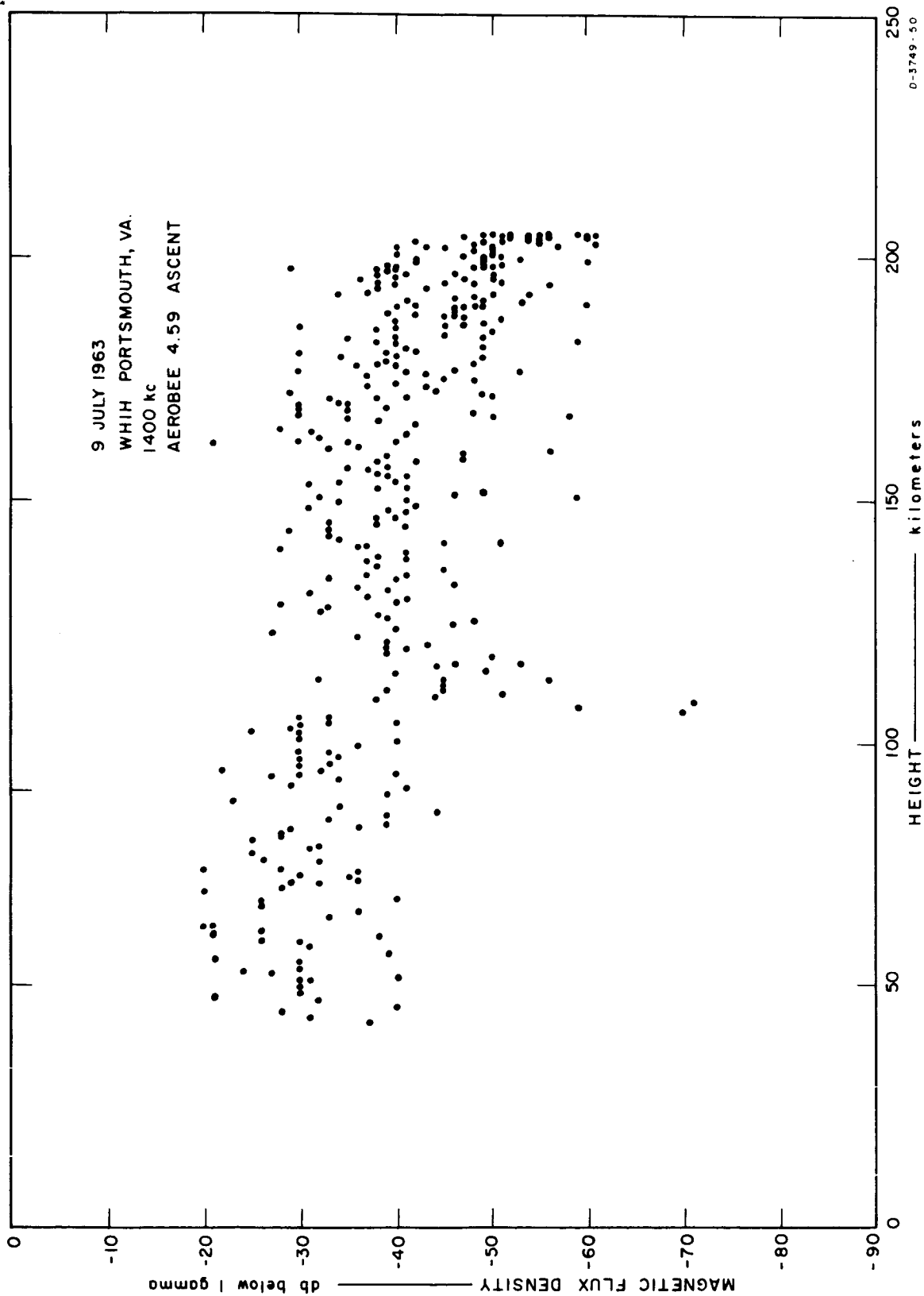


FIG. 9.43 AMPLITUDE OF WHIH AT 1400 kc, ASCENT

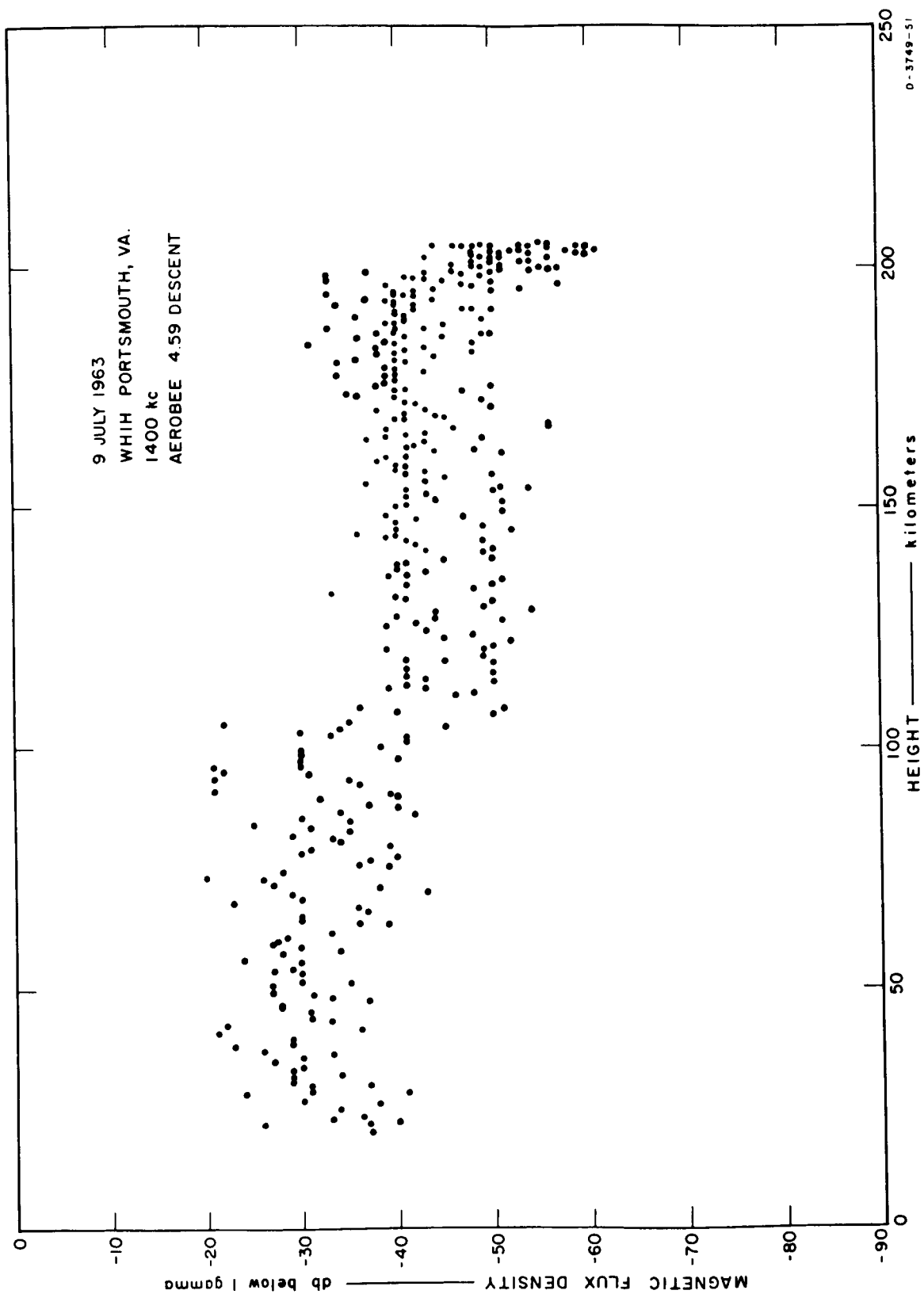


FIG. 9.44 AMPLITUDE OF WHIH AT 1400 kc, DESCENT

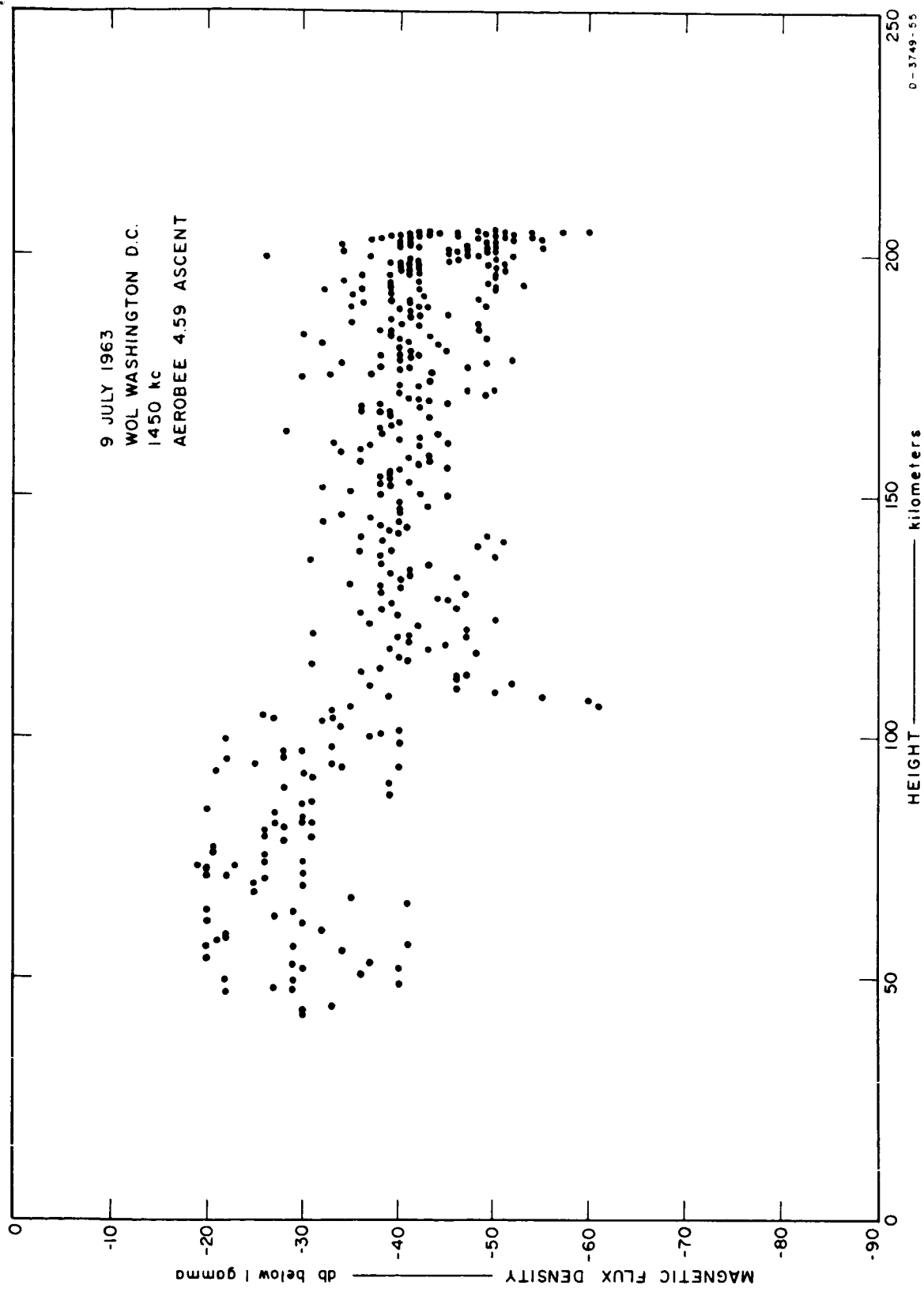


FIG. 9.45 AMPLITUDE OF WOL AT 1450 kc, ASCENT

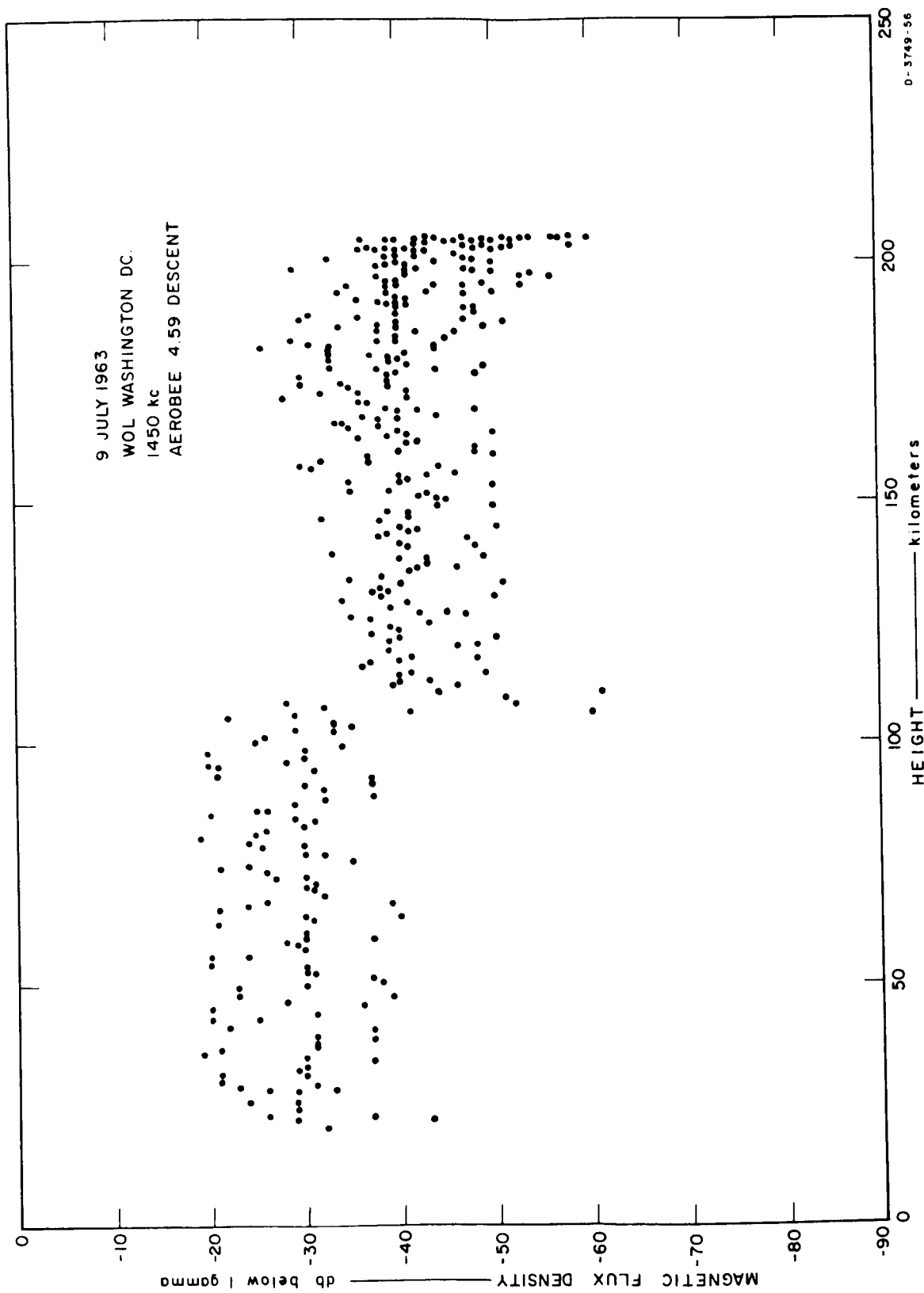


FIG. 9.46 AMPLITUDE OF WOL AT 1450 kc, DESCENT

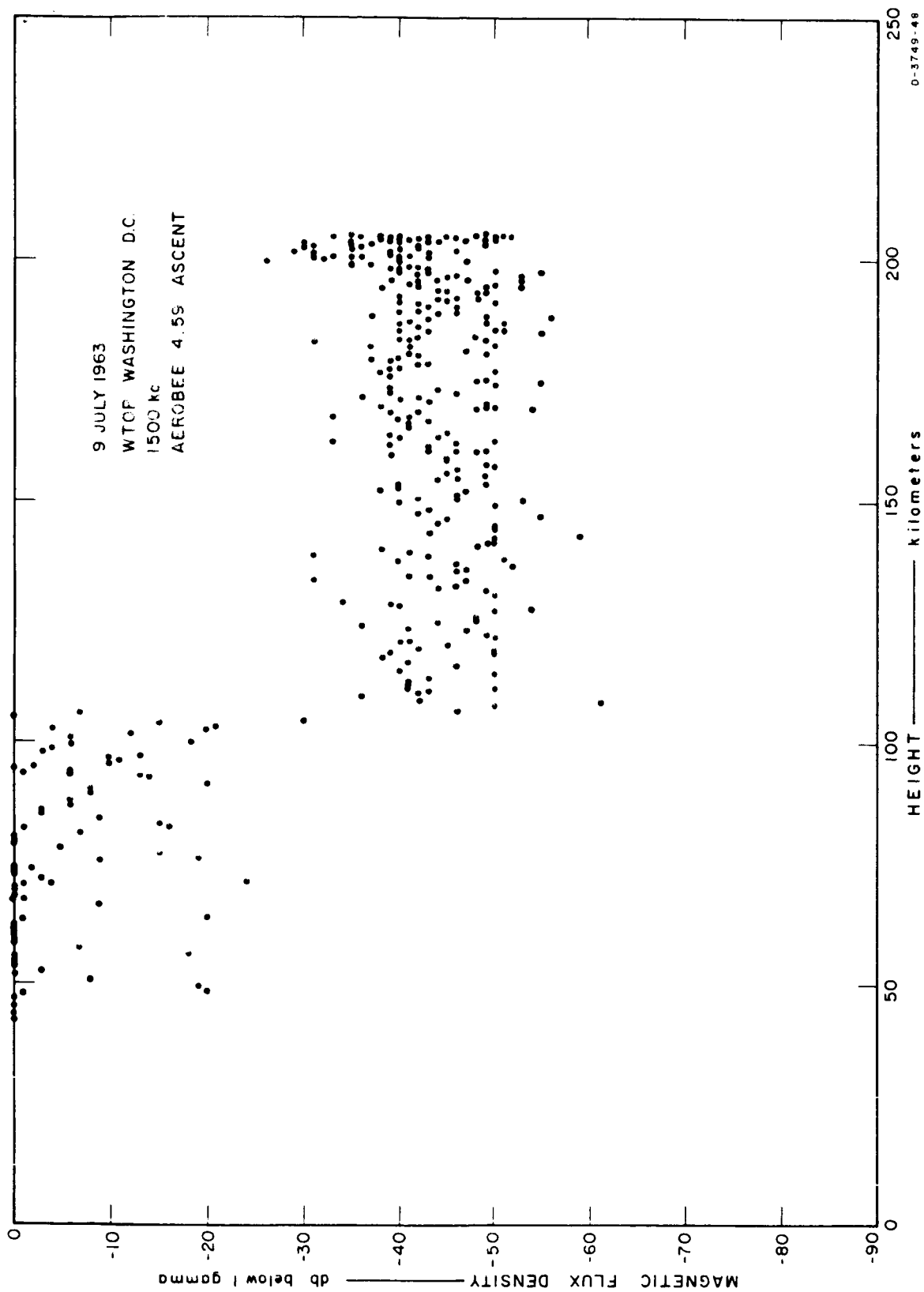


FIG. 9.47 AMPLITUDE OF WTOP AT 1500 kc, ASCENT

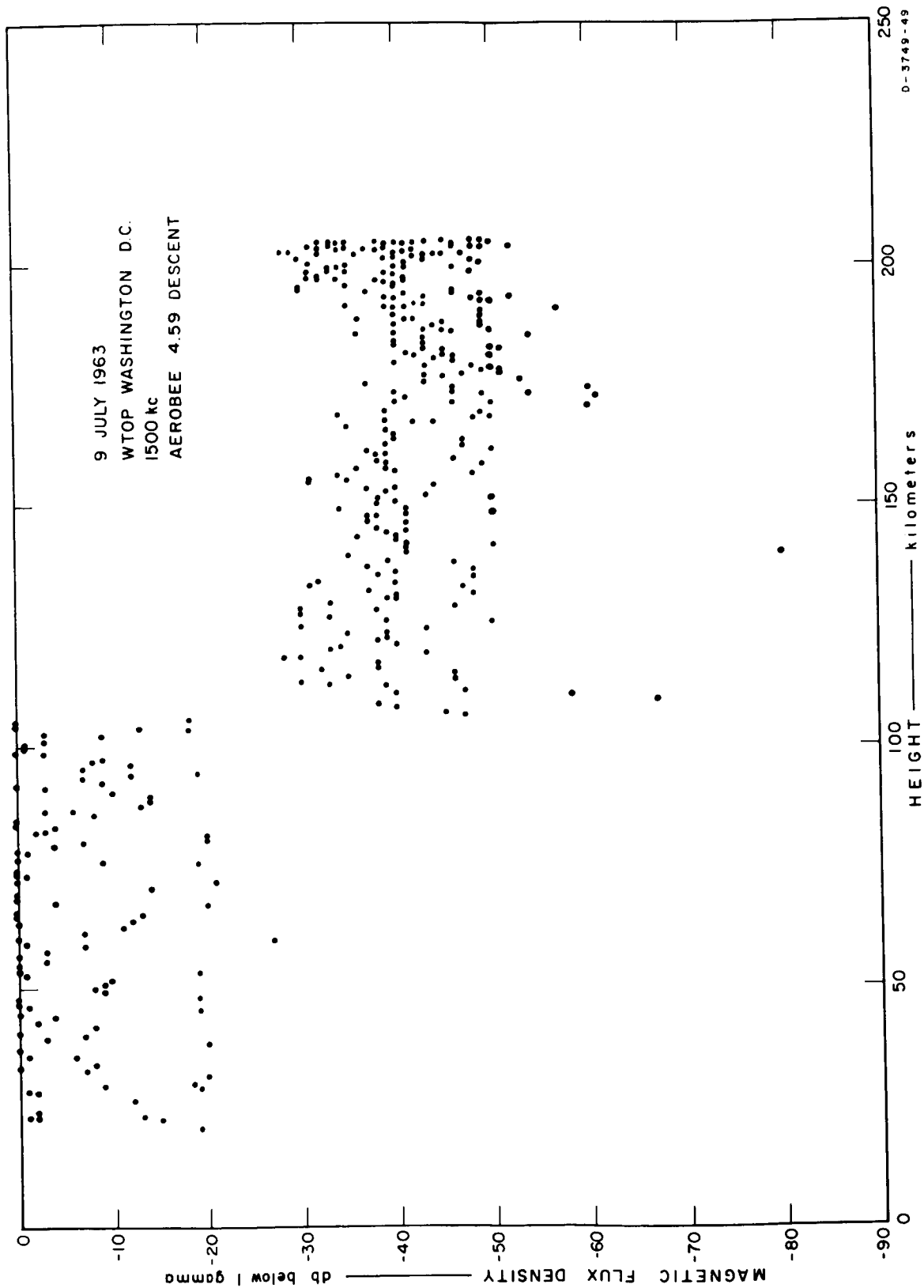


FIG. 9.48 AMPLITUDE OF WTOP AT 1500 kc, DESCENT

9.2 Broadband Receiver

9.2.1 Instrumentation

The broadband receivers flown aboard Aerobee 4.58 UI and Aerobee 4.59 UI are identical to the receiver presently orbiting on the OGO-I spacecraft (see Figure 9.1 for simplified block diagram). They derive their input signal from the output of the low-pass filter of the Band 2 sweeping receiver, and are therefore sensitive to signals up to 12.5 kc. The input signals in the frequency range 0.3 to 12.5 kc are logarithmically compressed and split into two channels. One channel retains the phase or spectral information and the other amplitude information.

In the spectral or phase channel the output of the log compressor is fed into a clipper, which retains the original frequencies and adds the odd harmonics. The clipper is followed by a filter to suppress the harmonics above 12.5 kc. The filtered output is then translated in frequency to the band from 67.2 to 79.4 kc and applied to the telemetry baseband. This translation is with respect to a crystal oscillator in the rocket operating at 66.9 kc. The crystal oscillator signal is also transmitted as a phase reference.

In the amplitude channel, a two-phase detector follows the logarithmic amplifier. A two-phase detector is used so that a 300-cps bandwidth can be maintained at the output for signals down to 300 cps. The output on the detector is used to frequency modulate a subcarrier oscillator (VCO) of the telemetry system. A 0.5-to-5 v output corresponds approximately to an 80-db dynamic range.

9.2.2 Data and Discussion

The spectral portion of the broadband data was processed and partially analyzed at Stanford University, while the amplitude portion of the data recorded directly on charts at the telemetry receiving station has received little attention to date except to interpret the spectral data. The discussion that follows, except for the Stanford University findings, is mainly qualitative.

9.2.2.1 Spectral Data

9.2.2.1.1 General

The spectral data contained on magnetic tapes were transcribed to obtain intensity-modulated film strips permitting visual examination. The transcription process using a Rayspan spectrum analyzer is described elsewhere (Helliwell et al, 1961). The preliminary Rayspan records covered a frequency range of 0 to 20 kc and provided a resolution of better than 0.1 sec. Features observed on these records were further investigated on additional Rayspan intensity records and on sonograms (Kay Electric Sonograph). Samples of the Rayspan film records are shown in Figs. 9.49 through 9.52 to facilitate discussion of receiver operation and to illustrate features of the data.

Figures 9.49 through 9.51 display data related to Aerobee 4.58 UI (daytime). Two pairs of records are shown in each of the figures; the upper record of each pair is for data telemetered from the rocket, while the lower record is data recorded on the ground at Greenbank, W. Va. Each of the records displays signals from 0 to 20 kc over an interval of approximately 20 sec. Time elapsed following lift off is indicated along the lower edge of each record pair and rocket height along the upper edge. Data for Aerobee 4.59 UI (nighttime) are illustrated in Fig. 9.52, which was prepared at Stanford University. Two pairs of records are arranged in a manner similar to those on the daytime displays. The nighttime records display signals from 0 to 10 kc over an interval of approximately 10 sec.

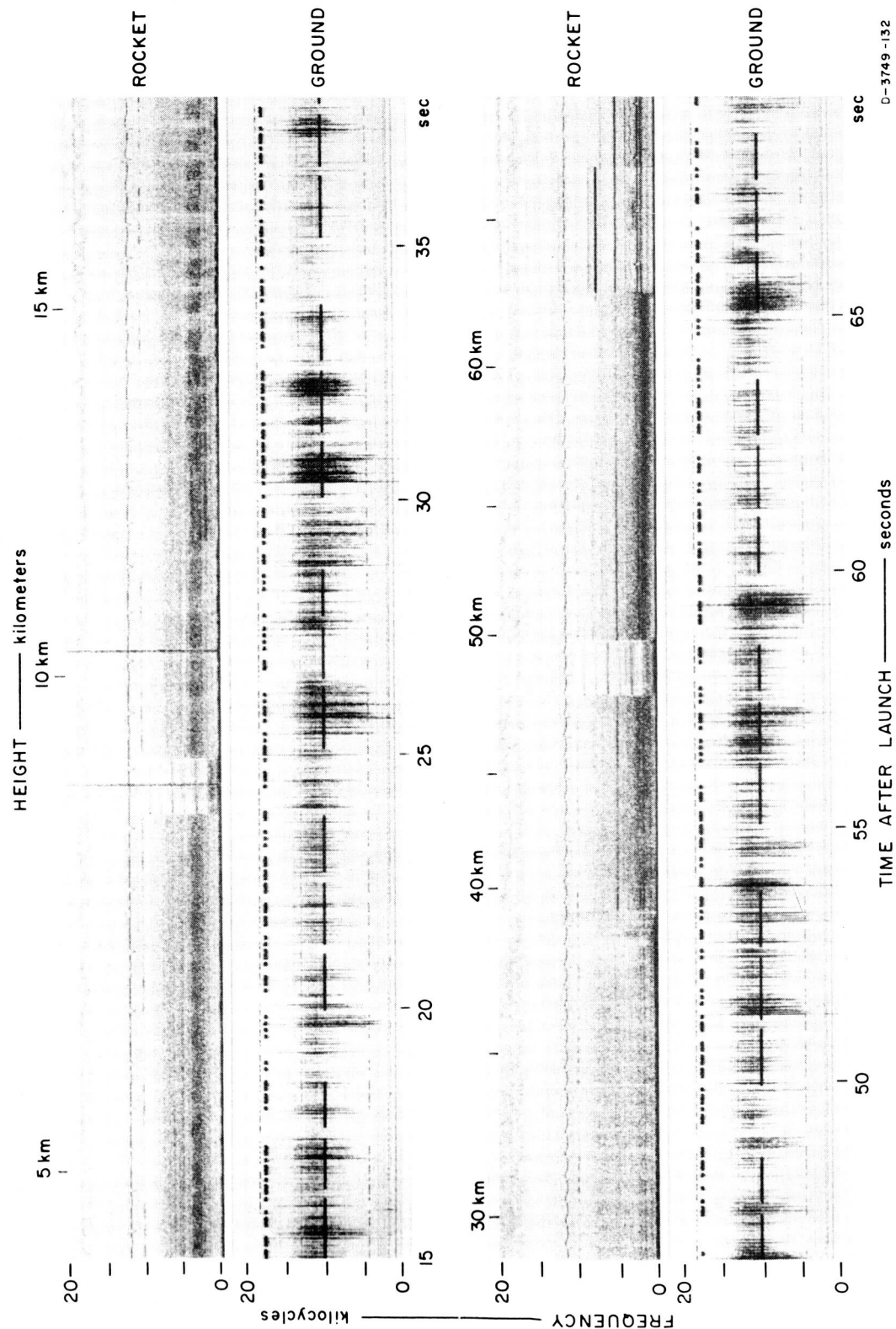
A number of horizontal lines representing signals of approximately constant-frequency are evident on the Rayspan spectral records. On the ground records for the daytime flight, nearly all the fixed-frequency signals originated from VLF transmitters (NPG, NAA, OMEGA). (The apparent NAA signal near 4 kc is due to overload in the recording system.) The fixed-frequency signals on both the daytime and nighttime rocket records are mainly due to interference from telemetry subcarrier oscillators. Subcarrier interference can be identified near 2, 2.5, 5.5 and 12 kc on the daytime records and near 1.5, 3, and 4.2 kc on the nighttime records. Omega 10.2-kc transmissions from both

Forestport and Balboa are present on the daytime rocket record for a short time after launch and again before breakup. On both the rocket and ground records for the nighttime flight the NAA transmissions have been translated from 14.7 kc down to a frequency of a few hundred cycles. The NAA signal has been translated as an aid in explaining the apparent variation in signal intensity on the data telemetered from the rocket. Each time the NAA transmitter is keyed on, the relative intensity of the background noise appears to decrease (see record 3 of Fig. 9.52). This feature is attributed to the action of the limiter in the spectral channel. The limited output is constant regardless of input amplitude or spectral distribution. A change in record intensity at a particular frequency does not necessarily represent an amplitude change at that frequency, but does represent a change in spectral distribution in the entire band. The largest signal, which in this case is NAA, predominates and the record intensity at other frequencies is effectively reduced.

A number of whistlers, including a new class, are evident on the telemetered records in Fig. 9.52. The initiating sferic of each is indicated by a small arrow on the abscissa of the record. The findings of the whistler study by workers at Stanford University are discussed later. Other features of the spectral data are described below.

9.2.2.1.2 Aerobee 4.58 UI

The powered portion of Aerobee 4.58 UI lasts 54 sec and appears responsible for generation of noise in two different frequency bands, as illustrated in the two pairs of records in Fig. 9.49. The lower band from 0 to about 300 cps is the predominant signal during the first 6 sec and last 16 sec of powered flight. This band appears to be amplitude modulated at twice the rocket spin rate. The second noise band from 2 to 4 kc is dominant from 8 to 33 sec after lift-off and is not spin modulated. As this latter band becomes less prominent from 33 to 46 sec, spin-modulated lower-frequency noise again becomes apparent. Within 1 or 2 sec following burn-out (and cessation of the lower noise band) noise from 2 to 4 kc again appears weakly, and increases in amplitude as it decreases in frequency to a final band from 1 to 2.5 kc at 66 sec. This noise band is completely absent following a 2-sec command



D-3749-132

FIG. 9.49 AEROBEE 4.58 UI BROADBAND RECEIVER SPECTRAL DATA, 0 TO 70 km, ASCENT

tone to cut off the rocket propellant inputs. Previously suppressed telemetry interference then becomes evident below 4 kc. The command tone was not sent until 12 sec after burn-out and it appears that the frequency and amplitude variable noise band is related to the escape of ionized gas from the hot exhaust. There is some evidence that a similar condition was beginning to build up on the nighttime flight following burn-out, but the cut-off command was much earlier, approximately 2 seconds after burn-out.

Another feature observed (Fig. 9.49) throughout the powered flight, and to an altitude of approximately 60 km, is the 10.2-kc transmissions from Forestport, N.Y. and Balboa, Canal Zone. These signals were amplitude modulated at twice the rocket spin rate. The 10.2-kc signals were observed again below 60 km on descent.

One of the most prominent features of the Aerobee 4.58 UI spectral data is a hiss-like band of noise between 2 and 5 kc (see Fig. 9.50) that begins near 100 km on ascent and ceases near 100 km on descent. The noise energy remains nearly constant, or changes only gradually, and is not spin modulated. (Apparent amplitude modulation near the top of the trajectory is due to an increase in spin-modulated noise in the 6.5 to 8 kc bands, to be discussed later.) The 2 to 5 kc noise band is not detectable on the ground at Greenbank and may be generated by the rocket itself passing through an ionized region.

As many as nine whistlers or associated phenomena were observed during the daytime flight. The first of these signals observed on ascent and the last observed on descent both occur when the rocket was at 125 km. None were observed in 1.5 minutes spent above 225 km. The discrete signals are of two general types. The first type (see upper record in Fig. 9.50) comprising four of the nine signals begins with a relatively strong burst of energy usually confined in the frequency range 7 to 9 kc. The intensity modulated Rayspan records, although of low time resolution for this purpose, suggest that the initial energy is dispersed as a function of frequency and resembles a short section of a normal whistler trace. The initial burst is followed by several usually well-defined whistler traces with energy in the range

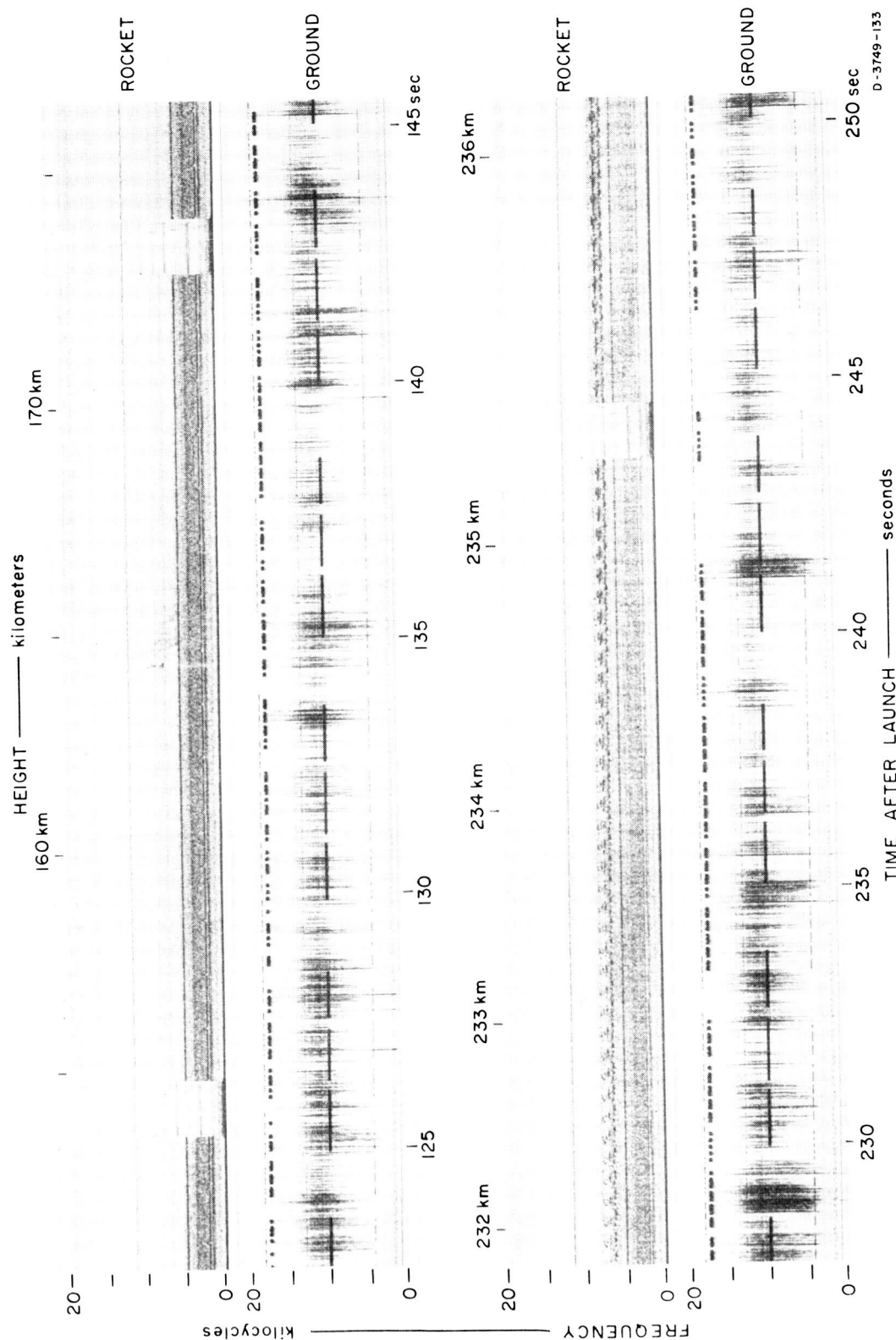


FIG. 9.50 AEROBEE 4.58 UI BROADBAND RECEIVER SPECTRAL DATA, 150 km TO APOGEE, ASCENT

3 to 10 kc. Four of the identifiable traces follow the initial burst by approximately 0.3, 0.5, 0.8, and 1.0 sec at a frequency of 8 kc. These times are increased by approximately 0.2 sec at 4 kc. None of the whistler-mode signals of the first type were observed at the Greenbank ground station.

The second type of discrete signal (see Fig. 9.51) does not have the well-defined traces of the first type. Their appearance ranges from several very thick or broad whistler traces to a broad noise band decreasing in frequency over a period as long as 5 sec. A second Type 2 signal often follows the first by about 5 sec. Energy of the second-type signal lies between 2 and 8 kc, with a greater proportion at the low-frequency end than is observed in the first-type signal. Some characteristic structure is evident in these long bands that suggests superposition of many whistler traces. Another significant feature of each of the second-type signals is that a discrete noise band is observed on the ground associated with the low-frequency end of the signal observed in the rocket. The ground noise observed at Greenbank (see Fig. 9.51) is confined between 3 and 6 kc and has a duration of 2 to 3 sec. Characteristic rising tones can be observed in the ground noise that are essentially absent in the rocket noise.

At an altitude of approximately 190 km (on ascent) a noise band near 8 kc of only a few hundred cycles width first makes its appearance. Relative amplitude of this band is modulated at the spin rate and not at twice the spin rate, as might be expected with a rotating loop antenna. The 8-kc band disappears at about 234 km, near the top of the path; but it has in the meantime been joined at 200 km by a band near 6.5 kc and at 210 km by a band near 7 kc. The 6.5- and 7-kc bands continue to an altitude of 200 km on descent and are accompanied near the top 10 km of the trajectory by several other bands between 6.5 and 8 kc. In addition to the apparent amplitude modulation at the spin rate, the bands also exhibit some degree of frequency modulation at the same rate. The narrowband spin-modulated noise is illustrated in the lower pair of records in Figure 9.50.

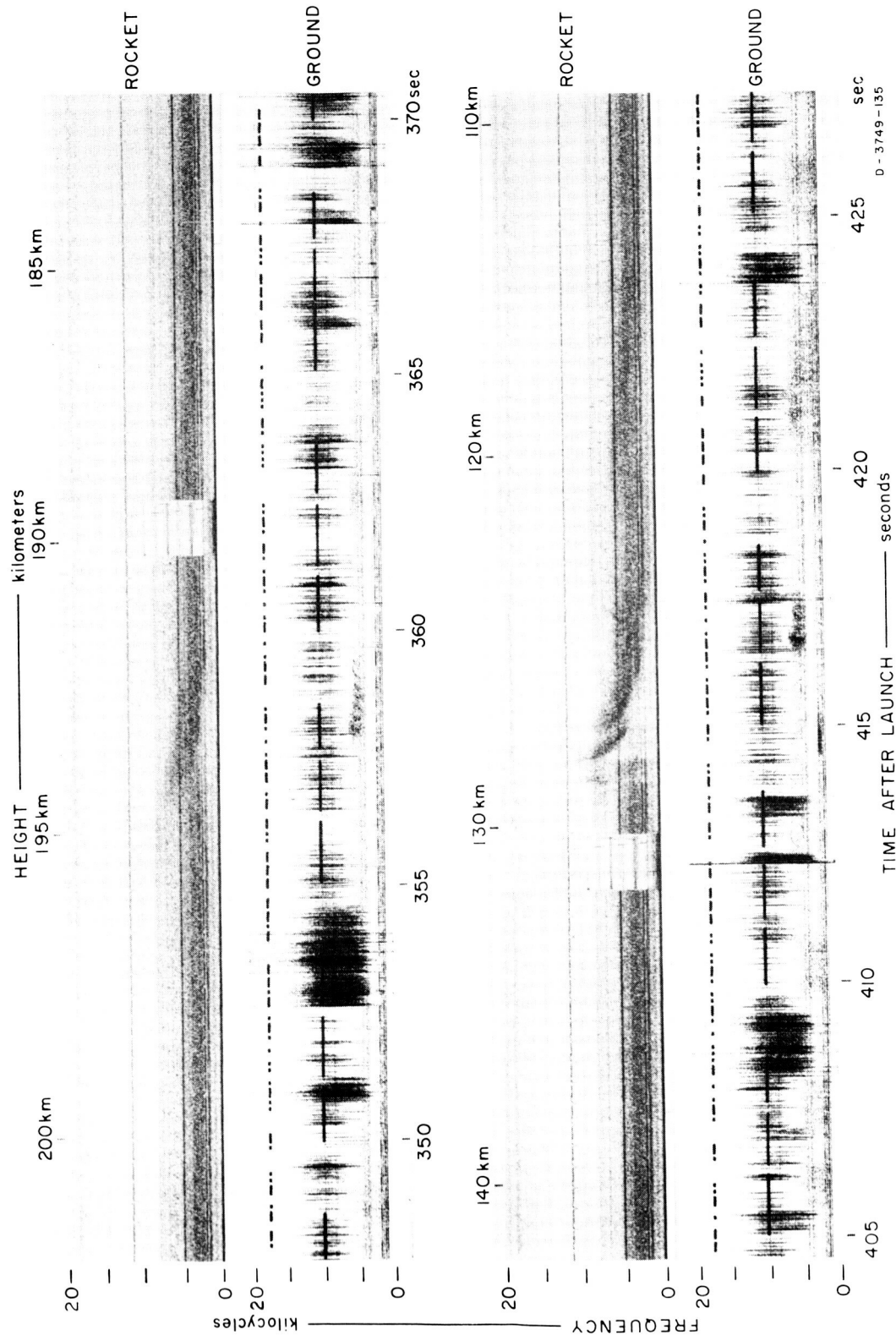


FIG. 9.51 AEROBEE 4.58 UI BROADBAND RECEIVER SPECTRAL DATA, 200 TO 110 km, DESCENT

9.2.2.1.3 Aerobee 4.59 UI

The powered portion of the nighttime flight lasts 52 sec and produces two noise bands similar to those on the daytime flight, with an almost identical sequence of interchange in relative amplitudes. Determination of the presence or absence of spin modulation on these bands is prevented by periodic predominance by NAA transmissions.

The most prominent feature of the Aerobee 4.59 UI spectral data is the presence of about 75 whistler signals, including a new class. These discrete signals were analyzed at Stanford University and their results are summarized later in this section.

Intermittent hiss-like noise in the frequency range 5 to 9 kc is observed between 85 and 110 km on both ascent and descent. The interesting feature of this noise is that it is composed of several bands that appear to change in frequency as a function of time and rocket altitude. The quasi-period bands appear to rise in frequency during rocket ascent and decrease in frequency during descent. The sweep period is about 4 to 5 sec at the lower altitudes and decreases to about 2 sec at the higher altitudes. These sweeping bands can be identified to some extent on record 3 of Fig. 9.52.

Identification of additional features of the nighttime data, other than sferics, is all but prevented by the presence of NAA signal and its dominance of the spectral distribution.

9.2.2.2 Amplitude Data

9.2.2.2.1 General

Amplitude VCO data, in addition to being recorded on magnetic tape with other telemetry subcarrier signals, were recorded directly on chart paper at the time of the flights. These chart records provide data with a resolution of 3 to 4 msec. Examples traced from the Aerobee 4.59 UI record are shown in Fig. 9.53 to illustrate the nature of the amplitude data. The tracings each show approximately 1 sec of data at the indicated altitudes. The amplitude scale in db below 1 gamma rms is appropriate for signals at a frequency of 5 kc. Signals

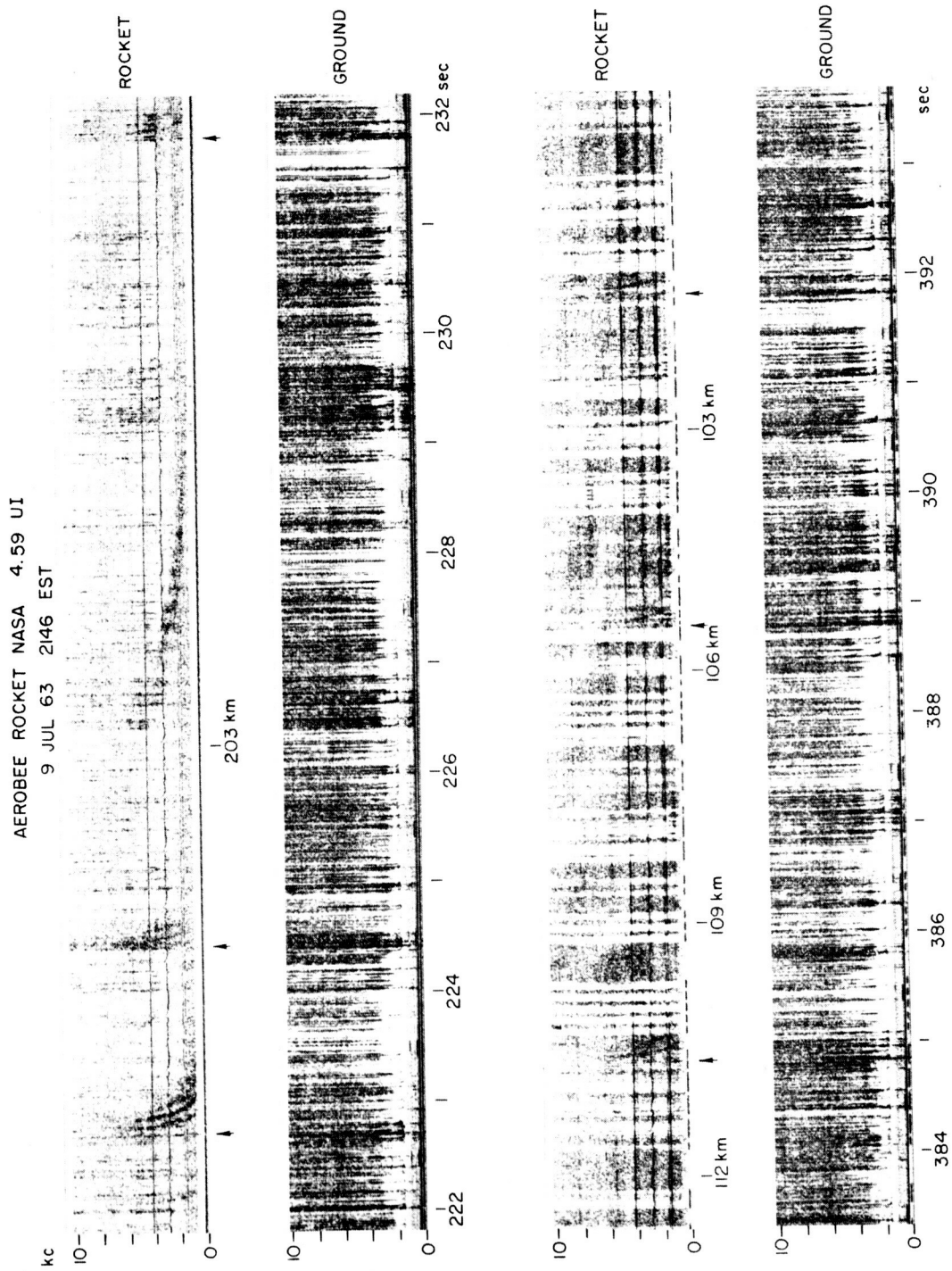


FIG. 9.52 AEROBEE 4.59 UI BROADBAND RECEIVER SPECTRAL DATA

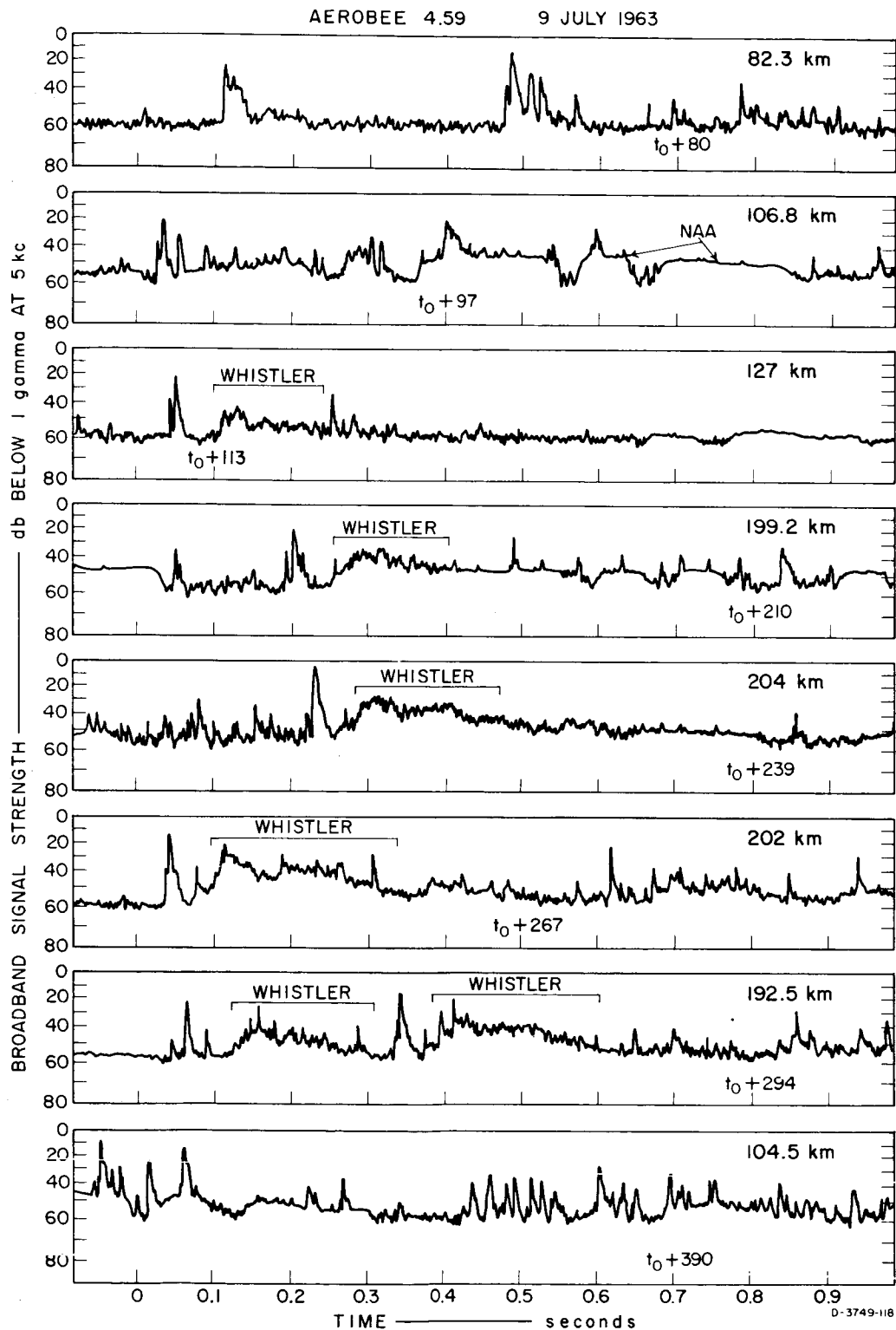


FIG. 9.53 AEROBEE 4.59 UI BROADBAND RECEIVER AMPLITUDE DATA

at other frequencies can be calibrated with the knowledge that the broadband response increases almost linearly with frequency.

The first, second, and eighth traces of Fig. 9.53 illustrate broadband noise in which impulsive sferics are superimposed on the background. The third through seventh traces also have impulsive sferics superimposed on the background, but in addition, include deflections due to whistler-mode energy. The sferic associated with each whistler is quite apparent. Periodic predominance by keyed NAA transmissions is evident on many of the traces.

Amplitude information for the entire duration of both the daytime and nighttime flights is shown in Fig. 9.54. The time scale on these records is highly compressed from that in Fig. 9.53, and provides visual integration. The amplitude scale shown in db below 1 gamma rms is appropriate for an equivalent single-frequency signal at 5 kc. Time elapsed following launch is shown along the lower edge of each record and reads from right to left. Rocket height is indicated along the upper edge of each of the records. The periodic (every 16.9 sec on Aerobee 4.58 UI and every 44.3 sec on Aerobee 4.59 UI) large-amplitude signal evident on the records is a calibration signal injected at the antenna terminals. The on-off nature of the NAA transmissions results in a very wide trace on the nighttime record. The upper edge of the trace corresponds to NAA amplitude and the lower edge to background noise level.

9.2.2.2.2 Aerobee 4.58 UI

The following discussion is related to the upper record in Fig. 9.54. The first 54 sec of amplitude data on Aerobee 4.58 UI are controlled by the two noise bands apparently generated during the powered portion of the flight (as discussed previously with regard to the spectral data). The rocket-generated noise reaches a level of about 45 db below 1 gamma rms (equivalent single-frequency level), which is some 15 db above the background. The average noise level drops abruptly following burn-out, but returns to its earlier level within 14 sec due to the presence of a sweeping noise band, also discussed earlier. The

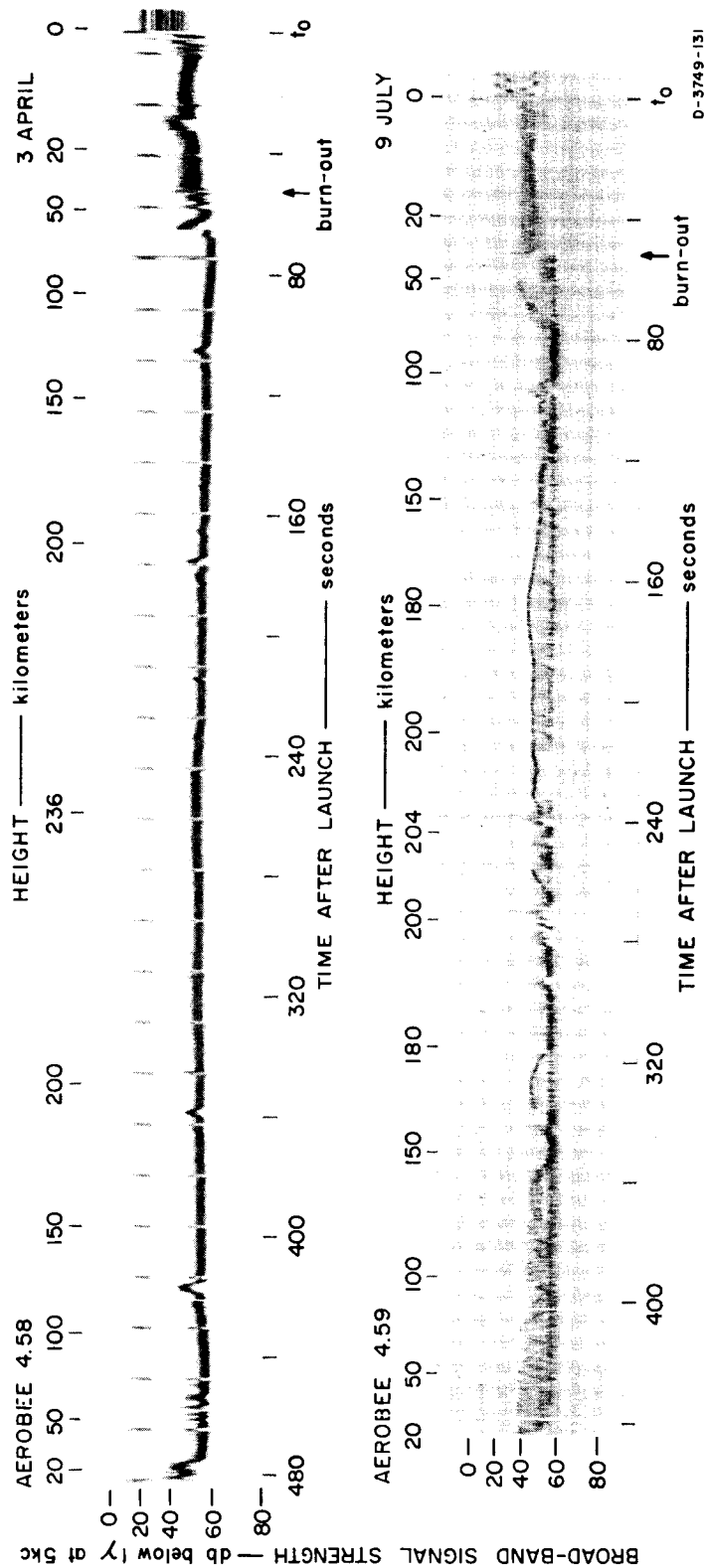


FIG. 9.54 AEROBEE 4.58 UI AND 4.59 UI BROADBAND RECEIVER AMPLITUDE DATA (Compressed Time Scale)

sweeping band ceases abruptly and the average signal level drops to its lowest value, about 60 db below 1 gamma rms, which appears to be set by telemetry interference within the rocket.

As the rocket ascends, the average noise level increases smoothly about 10 db to a peak of 50 db below 1 gamma rms at the top of the trajectory, then decreases smoothly again during descent. The hiss band above 100 km and the spin-modulated 6.5-to-8-kc bands near the top of the path both contribute to the increase in average noise with height.

A number of individual signals produce recognizable amplitude deflections. Included in this category are all but one or two whistler-mode signals. Some of these sources raise the signal level as high as 45 db below 1 gamma rms. The spin-modulated noise bands between 6.5 and 8 kc also produce characteristic amplitude deflections.

9.2.2.2.3 Aerobee 4.59 UI

The following discussion is related to the lower record in Fig. 9.54. As was the case on the daytime flight, the nighttime amplitude data are controlled until burn-out by rocket-generated noise, which reached a level in the neighborhood of 40 db below 1 gamma. Following burn-out, the most prominent feature of the data is the contribution of the keyed NAA transmissions on 14.7 kc. The VCO record provides a complete history of the amplitude of this fixed-frequency signal throughout the flight. The NAA amplitude decreases as height increases above 60 km to a minimum near 100 km, increases between 100 and 180 km, and then decreases again up to peak altitude. Signals of natural origin are evident between pulses of the keyed transmissions. The average background noise increases gradually from a low of about 60 db below 1 gamma rms following burn-out to a level of about 57 db below 1 gamma rms near peak altitude. This total change is less than on the daytime flight. The background level then decreases during descent until break-up. The minimum average noise level on Aerobee 4.59 UI appears to be determined more by natural noise than by telemetry interference within the rocket.

Many impulsive sferic signals produce recognizable deflections on Aerobee 4.59 UI amplitude records. Fluctuation of the night signal level is much greater than the day level because of the greater abundance of these sources. Nearly all of the whistlers on the night flight also produce recognizable deflections. These latter sources produce signal levels as high as 40 to 30 db below 1 gamma (equivalent single-frequency signal). The traces in Fig. 9.53 show both sferics and whistlers.

9.2.2.3 Results Obtained by Stanford University

The analysis of Aerobee broadband data at Stanford University was oriented mainly toward the spectral data, and was concerned primarily with discrete events associated with whistler-mode propagation. Because of the low rate of whistler-mode activity, the data for the 3 April daytime flight were given only minor consideration. In contrast, the 9 July nighttime records revealed many examples of a new whistler-mode phenomenon, a low-dispersion type of whistler [Carpenter et al. (1964)]. Most previously reported whistlers support a propagation model in which whistler-mode energy penetrates the ionosphere and propagates in the right-hand-circular mode along approximately field aligned paths to the opposite hemisphere. Travel times from one hemisphere to the other are typically of the order of 1 sec. Aboard Aerobee 4.59 UI, however, whistlers with travel times of the order of 0.1 sec were found.

The first example of a low-dispersion whistler was reported by Barrington and Belrose (1963) from their observation of Alouette records. However, not until the Aerobee tests was the widespread and frequent occurrence of this phenomenon appreciated, nor were its characteristics determined. Investigation of their respective records led both groups of workers to suggest that upgoing whistler energy is reflected at an altitude of roughly 1000 km, and that it may suffer multiple reflections back and forth between this altitude and the lower ionosphere or ground, as illustrated in Fig. 9.55. Since the ray paths are confined below the protonosphere, the region where hydrogen ions begin to predominate, Carpenter et al. [1964] and Smith [1964] labeled these whistlers subprotonospheric or "SP" whistlers.

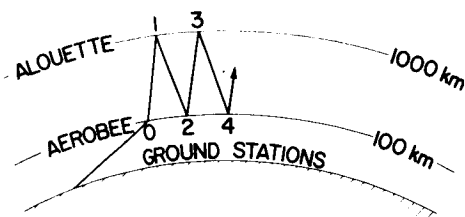


FIG. 9.55 RAY PATH OF
SUBPROTONOSPHERIC
WHISTLER

The first whistler event observed during the Aerobee 4.59 UI ascent did not occur until an altitude of 108 km, the approximate position of the sporadic-E layer. The rate of whistler occurrence remained nearly constant at 15 per minute during ascent to the peak altitude of 204 km, with a single burst of relatively high activity in the vicinity of 200 km. Three events are identified on the top record in Fig. 9.52 for a 10-sec period when the rocket was near the top of its trajectory: a strong SP whistler near 223 sec, an SP whistler plus conventional long whistler from the same spheric shortly after 224 sec, and a very faint SP whistler near 232 sec.

The last whistler event during descent was observed at 102 km, just below the double-peaked sporadic-E layer. Three SP whistler events are identified on the third record of Fig. 9.52 for a period when the rocket was descending near 110-100 km. Of the 75 whistlers observed aboard the Aerobee, all but one or two exhibited at least one SP component. It is significant to note that during the entire Aerobee 4.59 UI flight, not a single detectable whistler was observed at the Greenbank ground station (see, for example, records 2 and 4 of Fig. 9.52). This lack of whistler activity on the ground is confirmed by the rocket data itself at subionospheric heights.

Carpenter et al. (1964) have summarized the results of their detailed measurements on 11 of the best defined Aerobee 4.59 UI whistlers. Subscripts on the dispersion constant refer to the number of hops of whistler-mode travel (e.g., D_2 for the second hop dispersion).

- (1) Within the experimental error of about ± 5 percent, the dispersion $D = tf^{1/2}$ of the SP components is constant as a function of frequency. This is the expected dispersion law for propagation in the right-handed circularly polarized whistler-mode when wave frequency is well below the electron plasma frequency and gyrofrequency and when the wave normal is within a relatively

large range of angles with the geomagnetic field. Most of the dispersion measurements were made in the frequency range between about 1.5 and 4 kc. Below 1.5 kc, there is some indication of an increase in dispersion with decreasing frequency, but this point is not yet well established.

- (2) For 11 cases, the value of D_2 ranged from 4.4 $\text{sec}^{1/2}$ to 5.4 $\text{sec}^{1/2}$. (The value of D_2 for an event was determined by averaging the results of measurements at several frequencies.) The scatter of ± 10 percent around $D_2 = 4.9 \text{ sec}^{1/2}$ is probably attributable to experimental uncertainty in identifying the leading edge of a trace or impulse.
- (3) There is no apparent systematic variation in D_2 throughout the flight. The electron-density profile obtained at the time of the shot shows that electron density increased quite rapidly only above 175 km. The systematic dispersion variations that might be present under these conditions are approximately of the order of some of the experimental uncertainties involved.
- (4) The travel time at a given frequency between the second and fourth hops is approximately the same as that between the zero and second hops. The ratio of D_4 to D_2 , averaged for each event, remained within ± 10 percent of 2.0 throughout the flight. This uncertainty is approximately the same as that associated with experimental error.
- (5) The upper cutoff frequency of the second-hop, or first-dispersed SP component, is about 6.5 kc. Most values are in the range 6-8 kc. The upper cutoff frequency appeared to be somewhat higher near peak altitude. The cutoff of the fourth-hop SP component is about 5.5 kc, and the range throughout the flight is roughly 5-6 kc.
- (6) The lower cutoff frequencies of both the second-hop and fourth-hop SP components lie between about 700 and 750 cps throughout the flight.

Smith (1964) has proposed a theoretical model for the propagation of SP whistlers that seems capable of satisfying the observed

experimental data. It is suggested that since reflection near 1000 km due to discontinuity in refractive index is unlikely, energy follows a refracted path that is capable of returning toward earth when horizontal gradients of refractive index are present in the ionosphere. Whistler-mode propagation transverse to the magnetic field, normally not feasible, is possible at these altitudes due to the presence of ions. Following reflection of the down-coming energy from the bottom of the ionosphere or ground, the SP whistler may become trapped for several hops between these two reflection levels.

9.3 Impedance Probe

9.3.1 Instrumentation

The impedance probe was designed to measure the complex impedance of an electric dipole, which consisted of two copper strips 1 inch wide and 42 inches long mounted vertically 180 degrees apart on the nosecone. The measurements were made at two frequencies--1.54 and 120 kc.

A low, known level of oscillator signal current was injected into the antenna terminals and the phase and amplitude of the resulting voltage were measured. The oscillator voltage level on the antenna terminals was approximately 10 mv for free space antenna impedance. The relationship between the measured voltage and the antenna impedance was determined by performing a detailed calibration by connecting various known complex impedances to the probe input terminals before launch. The calibration circuit consisted of a parallel resistance and capacitance. A one-point calibration was performed periodically during the flight by substituting a known impedance for the antenna. The calibration curves for the low-frequency impedance measurement are shown in Fig. 9.56. The curves are shown only for values of impedance which are in the vicinity of the impedances measured in flight. At the high frequency the measured antenna impedance appeared to be purely capacitive with no measurable change in phase angle; therefore, the calibration curves degenerate to a single curve as shown in Fig. 9.57. A conservative estimate of the measurement accuracy is represented by an error of ± 0.05 cm on the amplitude and phase scales. The resolution was considerably better.

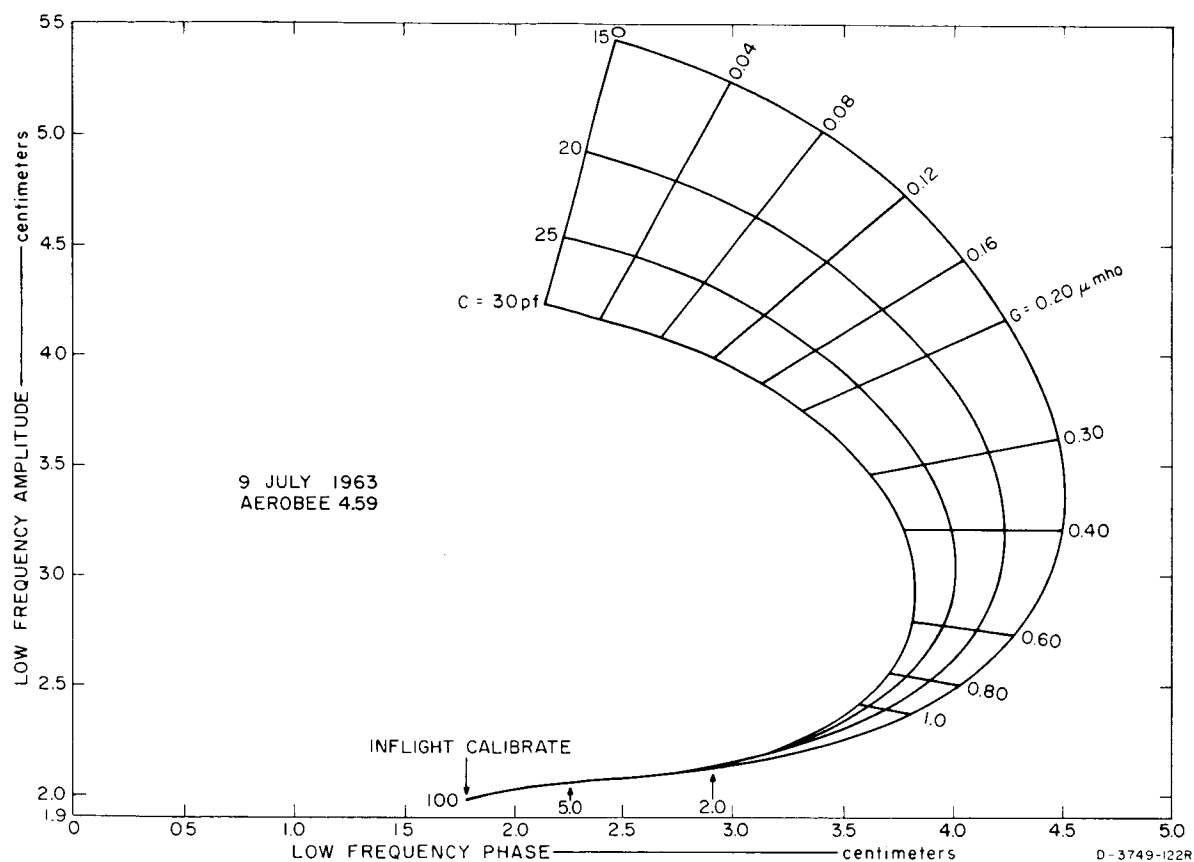


FIG. 9.56 LOW-FREQUENCY IMPEDANCE PROBE CALIBRATION CURVE

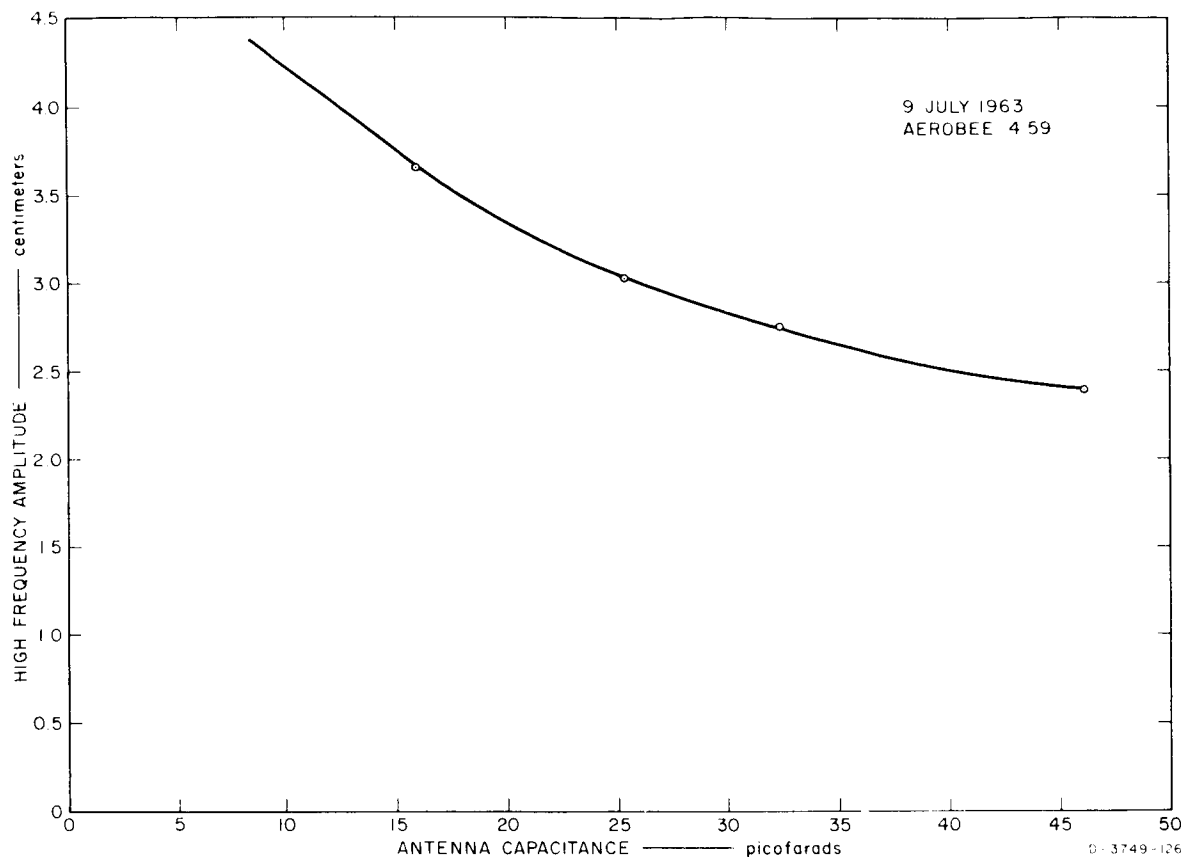
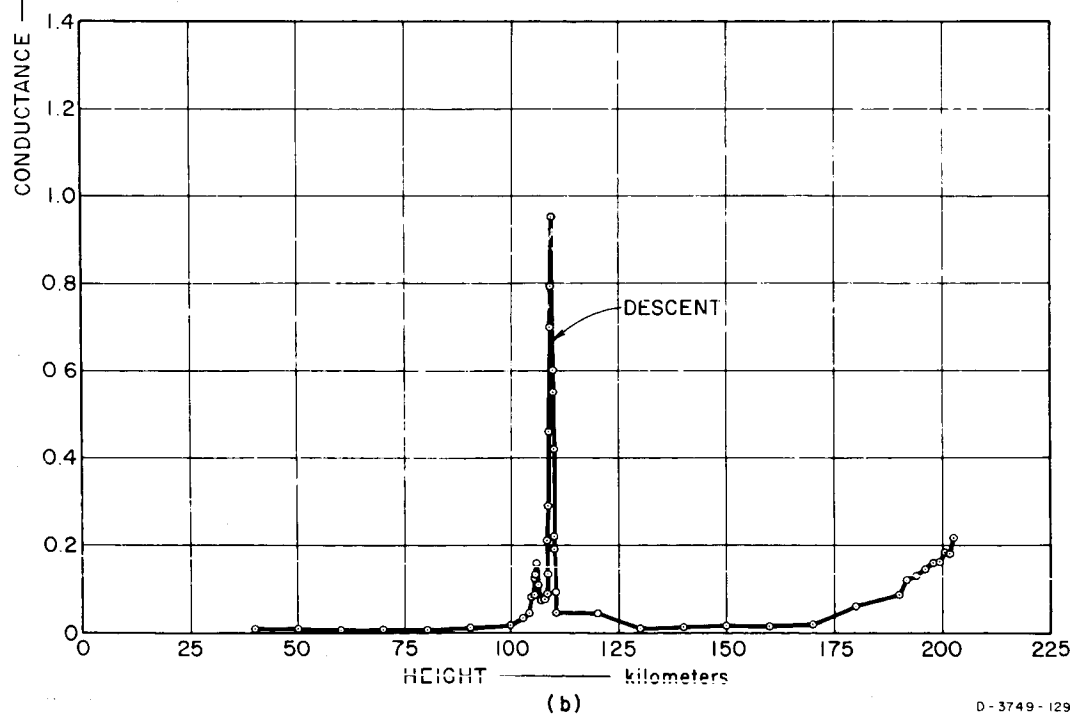
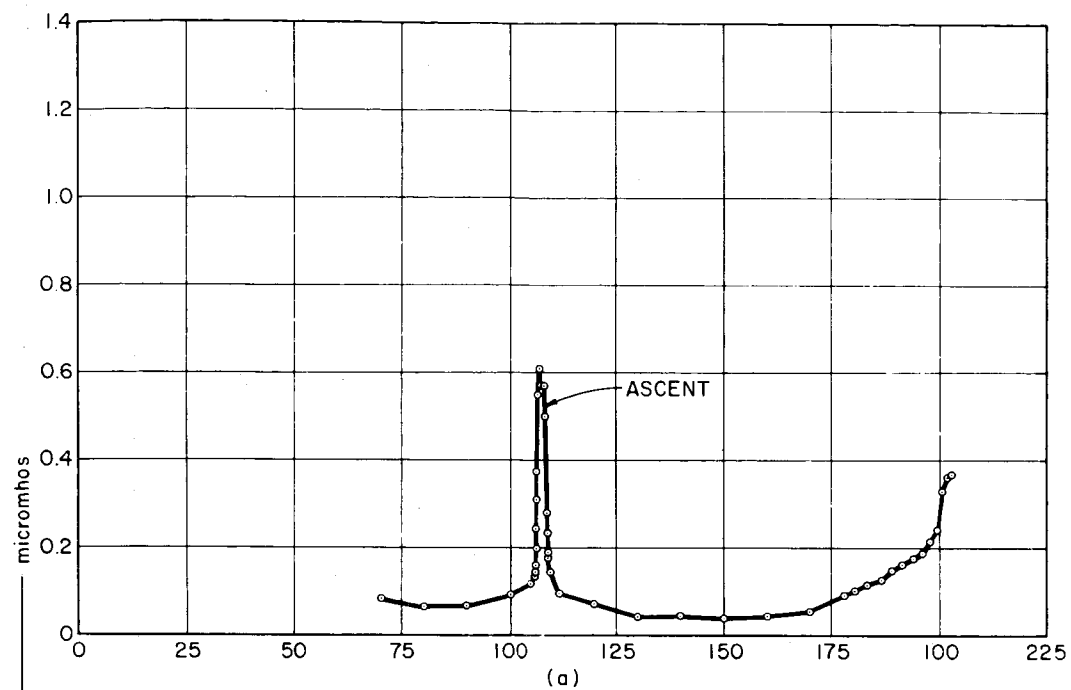


FIG. 9.57 HIGH-FREQUENCY IMPEDANCE PROBE CALIBRATION CURVE

The two oscillator signals were injected simultaneously into the antenna, and narrow-band filters at each frequency were used to separate the two signals. After separation, measurements were made in turn of 1540 cps amplitude and phase and 120 kc amplitude and phase and then recorded on a single data channel. Each measurement required approximately 17.5 msec, resulting in a sampling rate for each measurement of approximately 14.3 samples per second. A zero level was applied at the beginning of each 1540-cps amplitude data point for identification.

9.3.2 Data and Discussion

Data obtained on the impedance probe on Aerobee 4.59 UI are shown in Figs. 9.58 through 9.63. The impedance data are presented in the form of a parallel equivalent circuit of capacitance and conductance. No impedance data were obtained on Aerobee 4.58 UI. These data are strictly terminal impedances and conclusions regarding the characteristics of the ion sheath



D-3749-129

FIG. 9.58 LOW-FREQUENCY IMPEDANCE PROBE CONDUCTANCE DATA

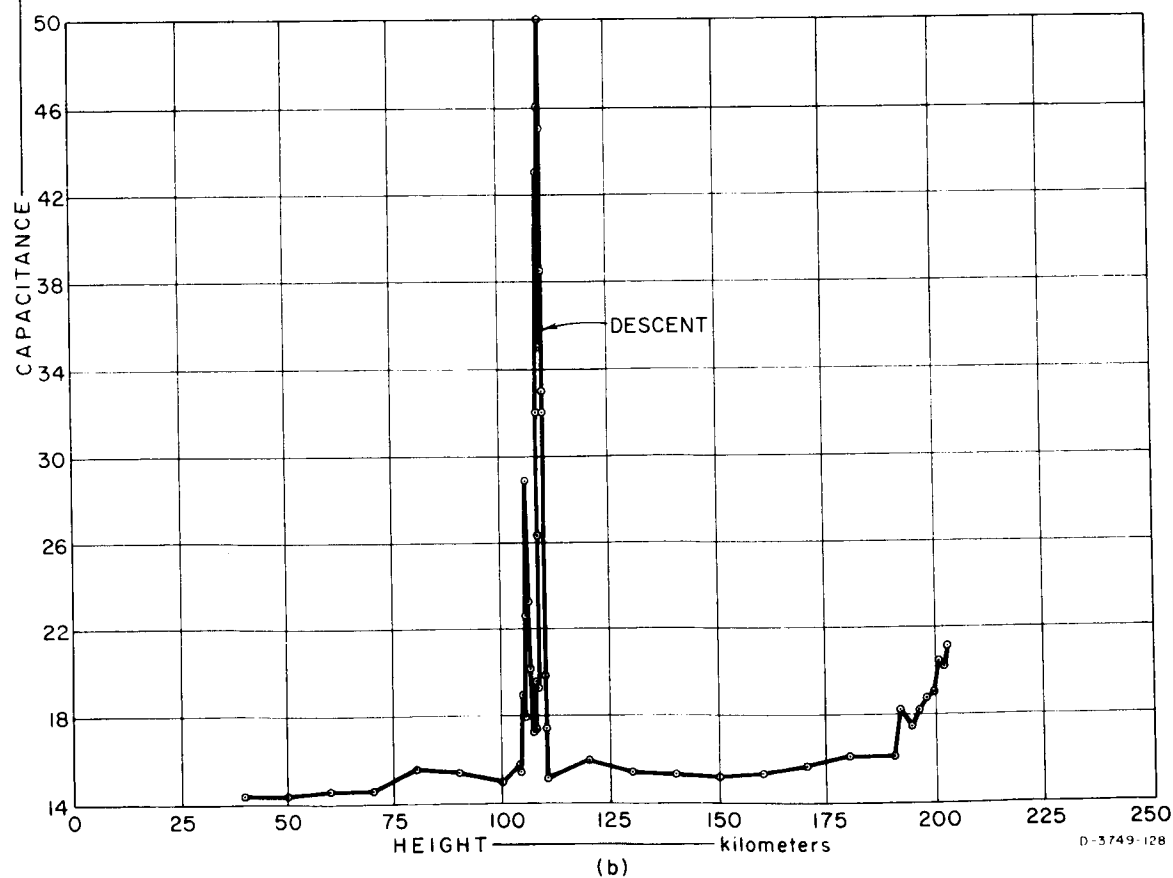
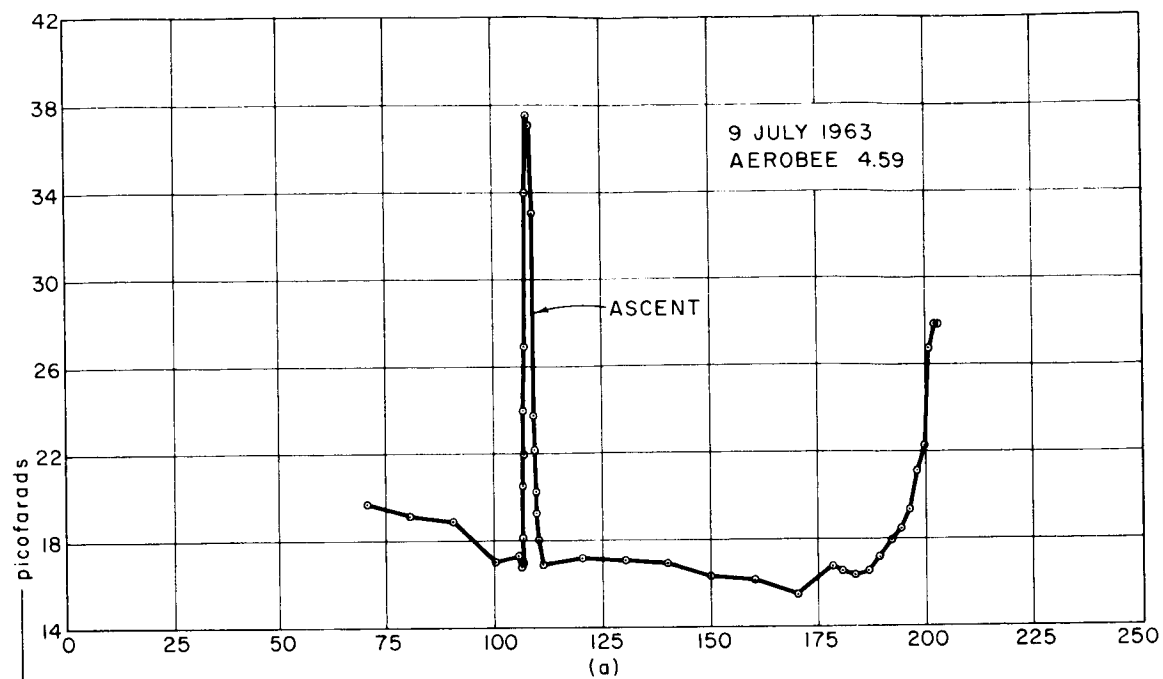


FIG. 9.59 LOW-FREQUENCY IMPEDANCE PROBE CAPACITANCE DATA

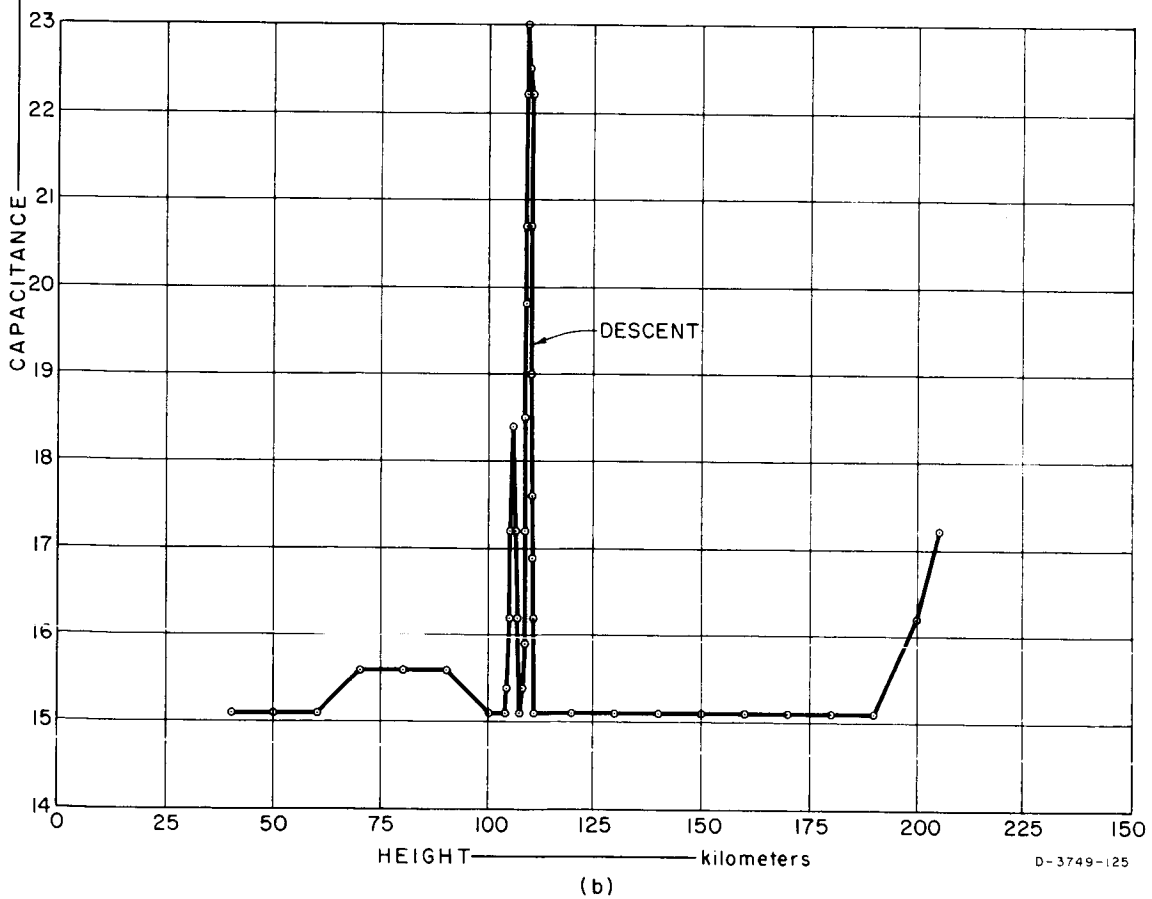
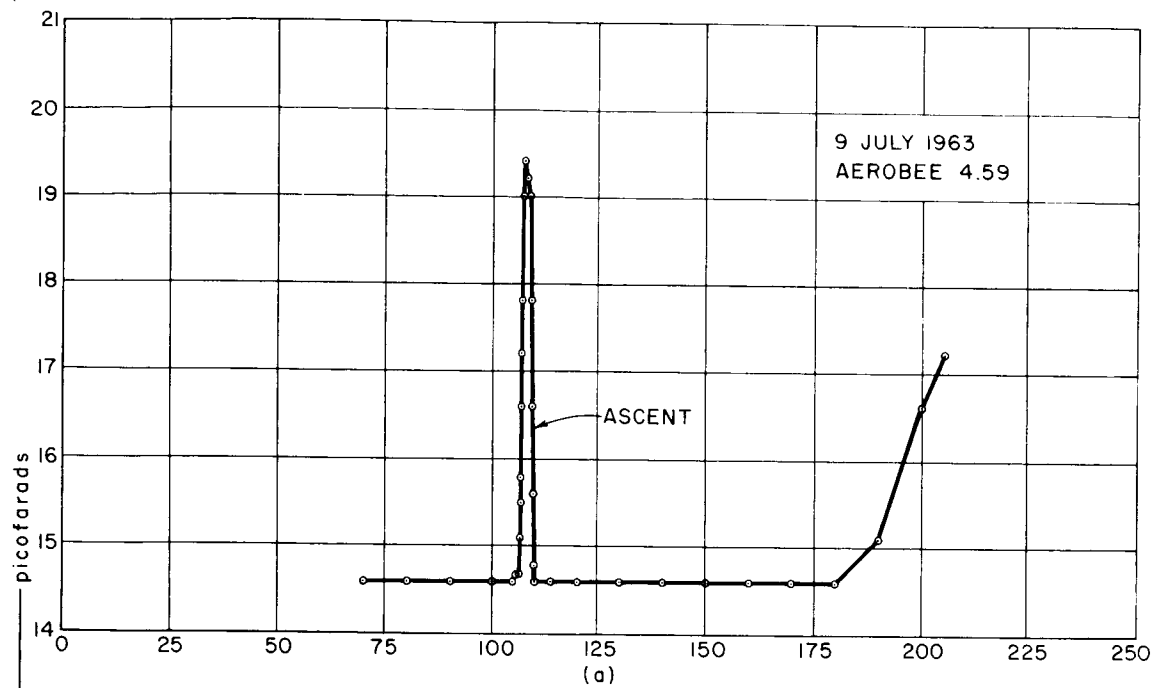


FIG. 9.60 HIGH - FREQUENCY IMPEDANCE PROBE CAPACITANCE DATA

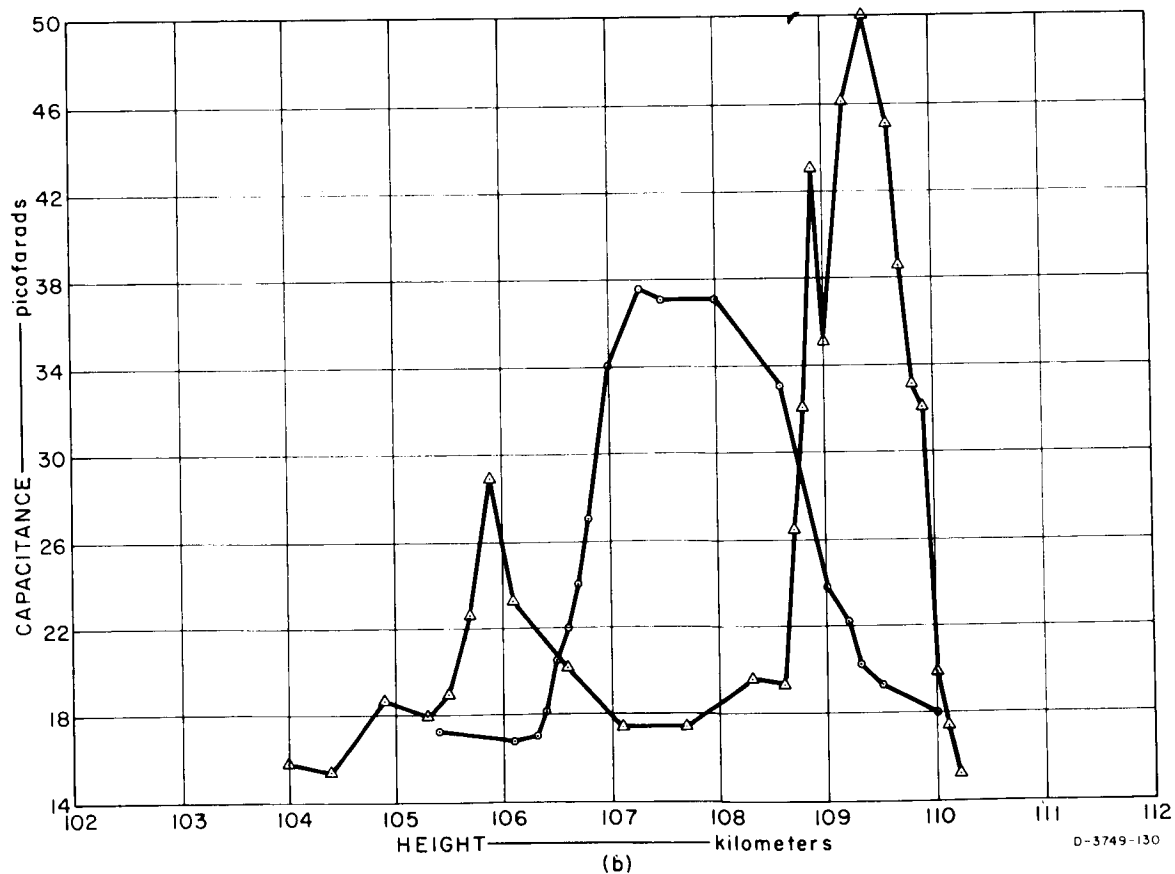
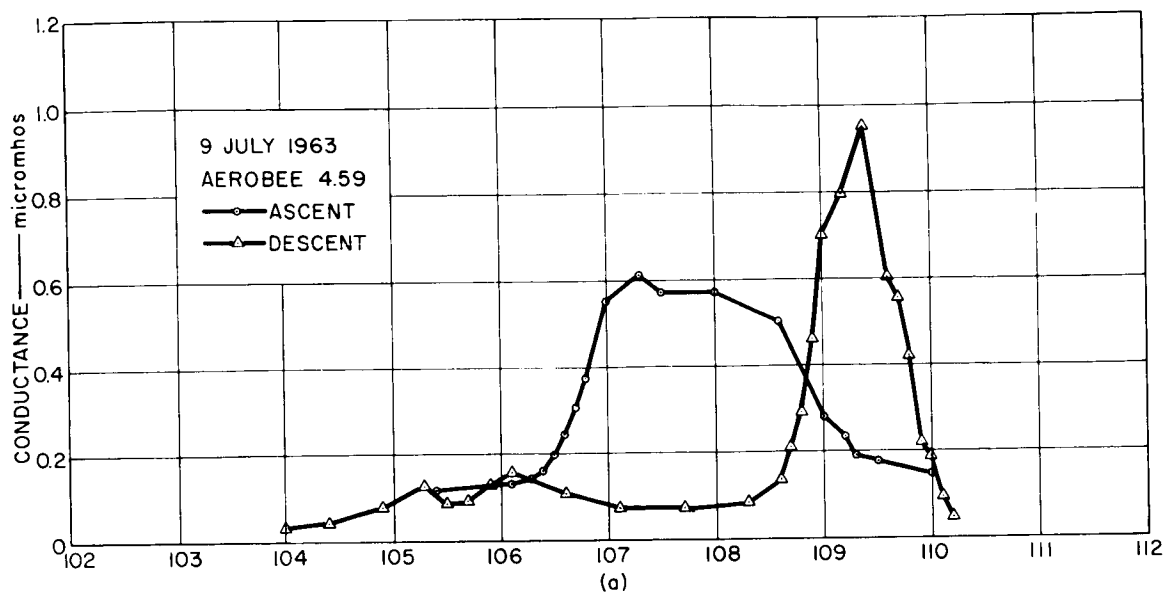


FIG. 9.61 IMPEDANCE PROBE, LOW-FREQUENCY IMPEDANCE
IN THE SPORADIC-E IONIZATION LAYER

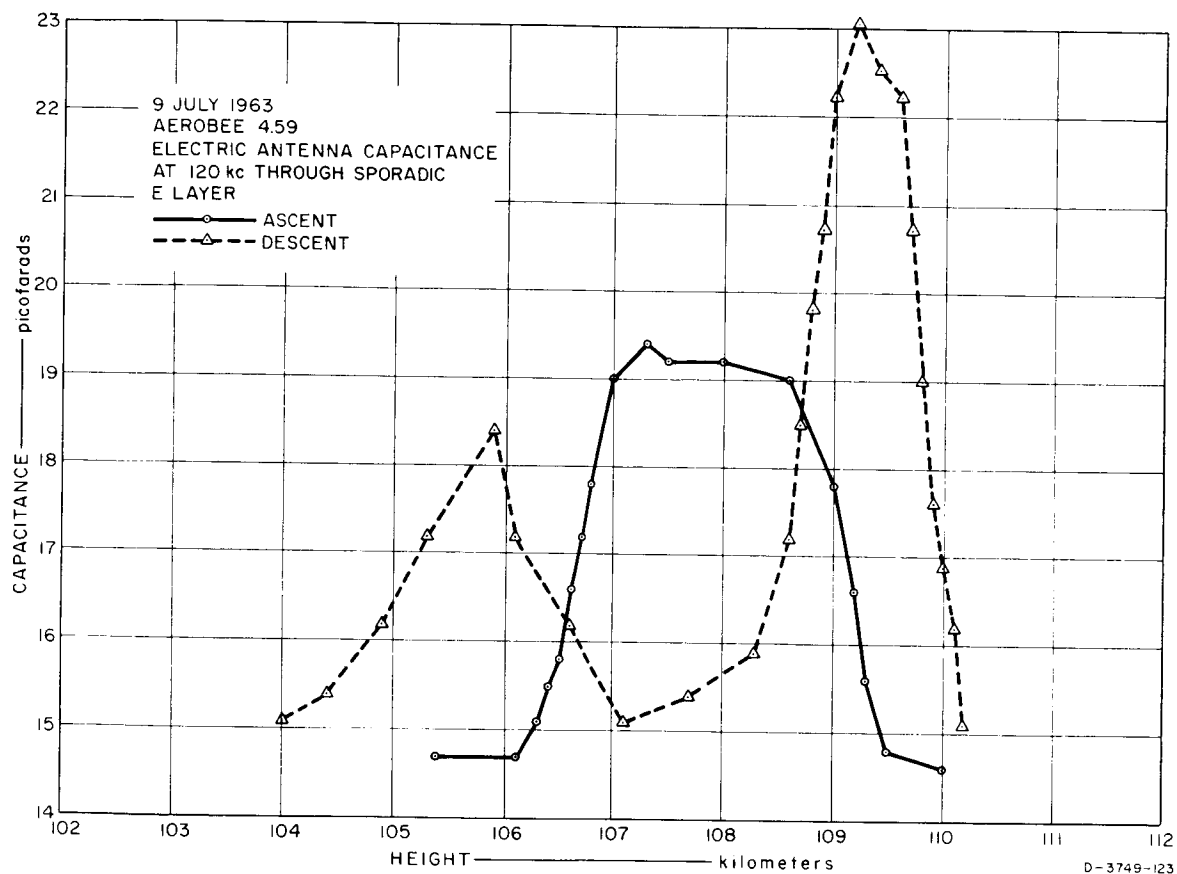


FIG. 9.62 IMPEDANCE PROBE, HIGH-FREQUENCY IMPEDANCE
IN THE SPORADIC-E IONIZATION LAYER

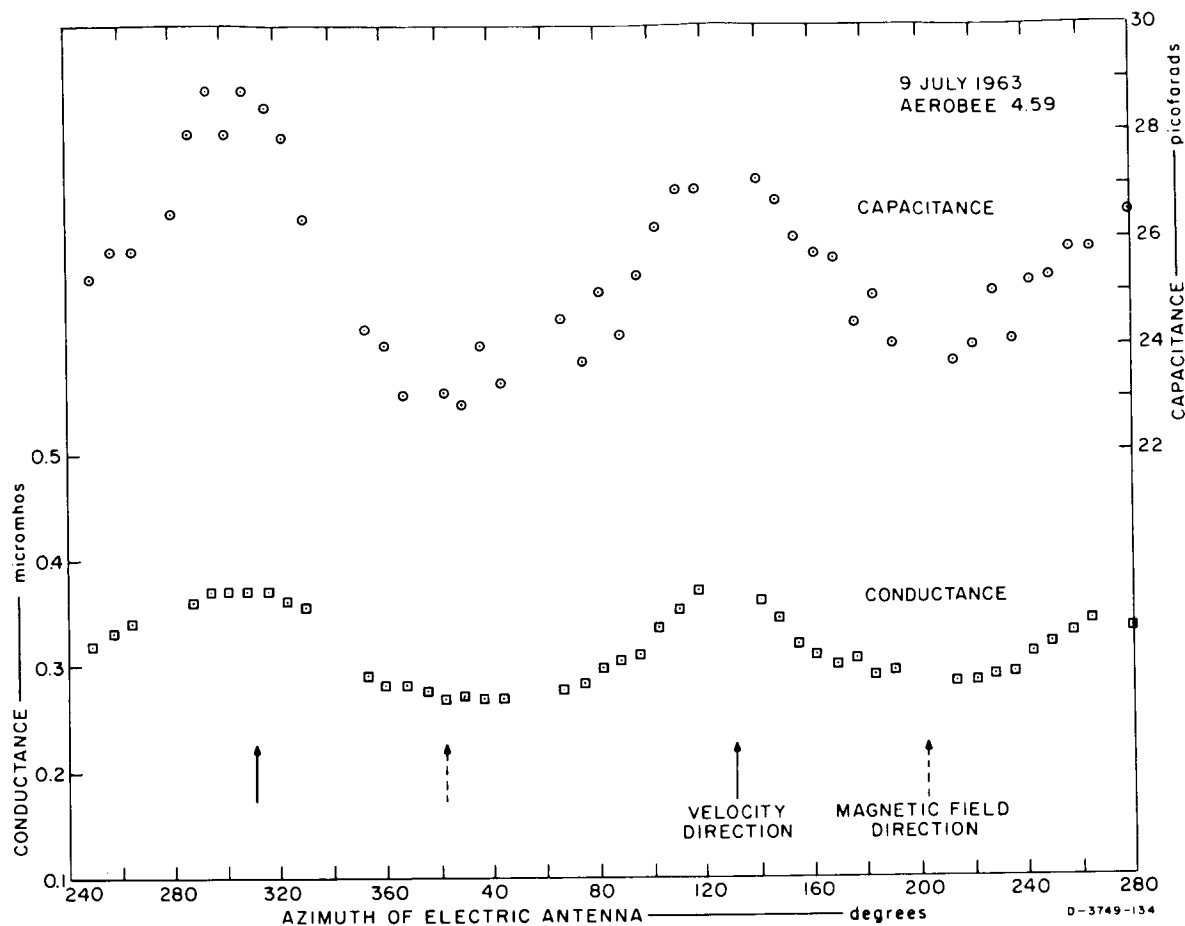


FIG. 9.63 ROCKET SPIN MODULATION OF IMPEDANCE

and of the surrounding plasma must be obtained by solving the multiple boundary problem, which consists of the rocket, the antenna, the ion sheath, and the undisturbed plasma. The geometry of the antenna does not lend itself to easy analytical solution; however, an approximate model, assuming that the antenna consisted of two parallel rods on a cylindrical rocket, that the ion sheath had sharp (step function) boundaries, and that the plasma was highly conducting, was solved to determine the change in antenna capacitance as a function of ion sheath thickness. This sheath thickness can then be compared with the thickness calculated from the electron density and electron temperature obtained by the phase receiver and conductance probe measurements. This comparison was made at about 200-km altitude with reasonable agreement; however, due to the simplified antenna model assumed, nothing can be said about the real (lossy) part of the antenna impedance.

Several characteristics of the data in Figs. 9.58 through 9.60 should be noted. There are significant changes in both capacitance and conductance in two regions; in a sporadic-E ionized layer at 110 km, and at altitudes above approximately 160 km. The conductance measurement was more sensitive to low electron densities; significant changes in conductance occur at electron densities of $\approx 1000/\text{cm}^3$ (compare with Fig. 9.71, electron density profile). Above 160 km, the antenna capacitance and conductance increased essentially monotonically to a maximum at the peak of the flight, indicating that the electron density is a smoothly varying function of altitude in this region; however, in the sporadic-E region, the rate of change with altitude was very fast. The level of ionization in the sporadic-E layer at 110 km exceeded that at 200 km. The detailed structure of the sporadic-E layer is shown in Figs. 9.61 and 9.62; note that the layer(s) may be as thin as 1 km. Note also that during ascent there is a single layer but that during descent there are two distinct layers. This is probably a spatial variation rather than a temporal one (the ascent penetration of the layer was approximately 73 km away from the descent penetration); however, this cannot be verified from the data.

Note that the low-frequency capacitance (Fig. 9.59) changed appreciably more than did the high-frequency capacitance (Fig. 9.60). This may be due to the smooth transition from ion sheath to undisturbed plasma rather than a step transition; at low frequencies the ion sheath appears thinner or, saying it another way, the plasma appears to be a conductor closer to the rocket surface. This frequency dependence of the impedance could be used to determine the sheath profile; however, this was not done in this case because of the complex antenna geometry.

It is not likely that the high conductance reading (Fig. 9.58) at low altitudes is an ionospheric effect. A probable explanation is that the nosecone was contaminated with absorbed salt vapor from the nearby ocean (or other contaminants); this evaporated gradually, explaining the slowly decreasing conductance which eventually went to zero on the down leg of the flight.

Variation of antenna impedance with rocket roll is shown in Fig. 9.63. Since the rocket was very nearly vertical (79 degrees at the time the data for Fig. 9.63 were obtained), the electric antenna dipole moment was very nearly horizontal. The rocket velocity and earth magnetic field horizontal component directions are shown with arrows. Since the maxima of capacitance and conductance occur very nearly in the velocity direction and the minima occur very nearly in the magnetic field direction, it is not possible to determine to what extent the cause is due to either the velocity or the magnetic field. The velocity may distort the ion sheath since the rocket horizontal velocity is significant compared to the ion thermal velocities, and the presence of the magnetic field of course makes the plasma anisotropic. A more detailed analysis of the data might separate the velocity and magnetic variation of impedance; however, this requires additional data scaling, which was not undertaken at this time.

Future impedance measurements should be made with an antenna having geometry that lends itself more easily to theoretical analysis (simple dipole), and the impedance function of bias on the antenna should be investigated.

9.4 NSS Receivers

9.4.1 Instrumentation

Several field components of the 22.3-kc transmissions from U.S. Navy Station NSS at Annapolis, Md., were measured during both flights for two reasons.

First, the details of VLF propagation through the D and E regions are being investigated as one of the primary objectives of this project. The availability of a high-powered transmitter near the firing range afforded an opportunity to observe the fine structure of fields in the absorbing, reflecting, and refracting regions of the lower ionosphere without danger of contamination by background noise. This effort was particularly successful as a result of the continuous transmissions provided by the Navy for both flights.

Second, the characteristics of the plasma--particularly electron density--can be determined from the propagation effects. This information is needed for a complete analysis of other experiments on the same rockets, as well as for its own value.

In order to determine the direction of wave propagation within the magnetoionic medium, where only a circularly-polarized wave can propagate, it is sufficient to measure the orientation of the plane containing the wave's magnetic field. This could be done with a single loop antenna on a spinning vehicle, measuring the wave amplitude normal to the spin axis as a function of spin angle. This would presuppose stability of the wave normal for one-half revolution, or as much as one-half second in this case. Since the rocket would travel about 2 km in a second at D- or E-region altitudes, where the wavelength would be a few km, it did not seem advisable to presume this stability. A second loop antenna to measure the wave's magnetic field in the direction of the rocket axis (approximately vertical) provided a means to observe rapid changes in the wave-normal angle, as well as to measure the component of magnetic field that would never have been sampled otherwise. To complete the determination of wave structure in the plasma, some knowledge of the electric fields was required. Since the rocket axis was to be close to the earth's magnetic field direction, the axial electric field component must be small. The remaining transverse components were sampled by the rotating transverse (essentially horizontal) dipole formed by the "plate" antenna strips used also by the impedance probe (see Sec. 5). Due to the difficulties of calculating the effects of the ion sheath and the capacitance to the internal structure, the electric field data were calibrated after the flight by matching the magnetic field amplitudes, using the refractive index calculated from the Doppler measurements.

Since one of the objectives of this experiment was the measurement of electron density by Doppler shift, it was necessary to determine the received frequency accurately with respect to the transmitted frequency. This was accomplished by comparing the phase of the signal on each antenna with a crystal-oscillator reference carried on the

rocket, and simultaneously recording the phase difference between this reference and the NSS signal received on the ground.

The dynamic range of amplitude measurement was also a critical question, since the attenuation due to absorption and reflection could only be estimated roughly from previous theoretical and experimental work. In view of the wide range of possible field strength, it was decided that the precision of measurement was less important than assurance that the level would not fall below the threshold of detection. The use of log compression, similar to that of the sweeping receivers (Sec. 9.1.1), allowed a 90-db range of field strength to be measured within about 1 db without range switching. The calculated maximum fields were 10 to 20 db below receiver saturation levels, leaving a useful range of 70 to 80 db, which proved to be adequate for continuous reception on all antennas throughout both daytime and nighttime flights.

For resolution of the expected wave components in the reflection region and below, amplitude changes that are faster than the spin rate would have to be observable, to follow phase reversals. Rather than load the telemetry system with separate subcarriers for each field measurement, an electronically-switched sampled-data receiver was used, which also avoided the problem of different time delay and frequency response in a set of IRIG channels. The receiving systems flown, shown in block form in Figs. 4.1 and 4.2, employed a 22.3-kc crystal filter in the preamplifier of each of the three antennas sampled. These filters, with a 3-db bandwidth of 20 cps, provided all the selectivity needed. Their outputs, and a calibration voltage, were sampled sequentially by the switching matrix for about 9 msec each on Aerobee 4.58 UI (28 frames per second) and 18 msec each (14 frames per second) on Aerobee 4.59 UI. The switching matrix output was log-compressed, then both amplitude and phase were measured. The phase reference was the (divided by three) 66.9-kc crystal oscillator, which was telemetered as the carrier for the vestigial-sideband "broadband" VLF spectrum (Sec. 9.2.1). In the rocket, as on the ground, the 66.9 kc was divided to 22.3 kc by a simple R-C locked oscillator, and used to "set" a flip-flop used as a linear phase detector. The flip-flop was "reset" by the signal, and the filtered

collector current of one transistor was the output. The duty cycle, and therefore output voltage, was then proportional to the signal-to-reference phase difference up to one cycle, repeating each cycle. The phase and amplitude detectors were then commutated to the telemetry channel, so the telemetered signal consisted of eight-segment frames containing a phase sample and an amplitude sample from each of the three antennas and the reference. Figures 7.1 and 7.2 show samples of telemetry records taken during both flights. The lines connecting samples of each field component have been added to facilitate data reduction.

9.4.2 Doppler Measurements

9.4.2.1 Procedure

The telemetered phase of the 22.3-kc wave received at the rocket, the telemetered phase reference, the 22.3-kc wave received at the ground telemetry station, and the known rocket trajectory were used to calculate electron density profiles. A simplified form of the method used is illustrated in Fig. 9.64, which represents a VLF trans-

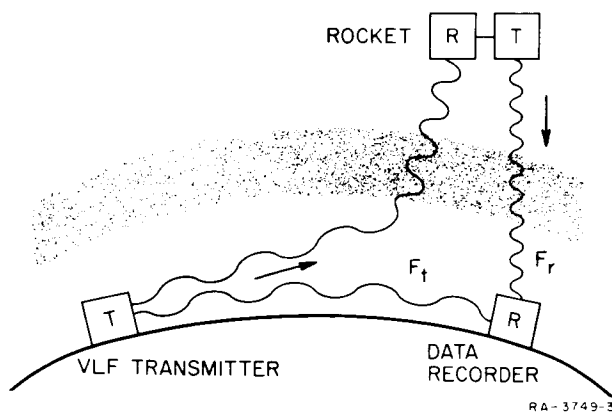


FIG. 9.64 VLF DOPPLER EXPERIMENT
(Simplified Block Diagram)

mitter on the ground radiating waves at a frequency F_t , which are refracted into the ionosphere with a phase velocity much lower than in free space. They are received in the moving rocket with a large Doppler shift due to the reduced wavelength in the plasma, which is a function of electron density. This Doppler-shifted VLF frequency F_r then modulates a transmitter, operating at a frequency far above the maximum

plasma frequency, which telemeters F_r to the ground. At the telemetry receiving station, a TRF receiver is tuned to F_t , and provides the frequency originally transmitted. The frequency difference between F_t and F_r measured on the ground is the rate of change of the total phase path

length, including telemetry Doppler shift. If the trajectory is known, the VLF phase velocity in the direction of motion of the rocket can be calculated. If the wave-normal direction is known, the local index of refraction μ , and consequently the local electron density N , can be determined.

If horizontal gradients in electron density are assumed to be negligible, and the refractive index in the ionosphere is high, the approximate wave-normal direction is easily calculable from the geometry, and does not have to be measured in flight. Referring to Fig. 9.65, β is the angle between the incident wave direction and the vertical. At a point in the ionosphere where the index of refraction is μ , the wave-normal angle with the vertical, β_2 , is given by Snell's law

$$\mu \sin \beta_2 = \sin \beta \quad . \quad (9.4.1)$$

Since the refracted wave will remain in the vertical plane containing the incident direction, the Doppler-shifted frequency observed at the rocket will be

$$F_r = F_t \left[1 - \frac{\mu V \cos \psi}{c} \right] + F_s \quad , \quad (9.4.2)$$

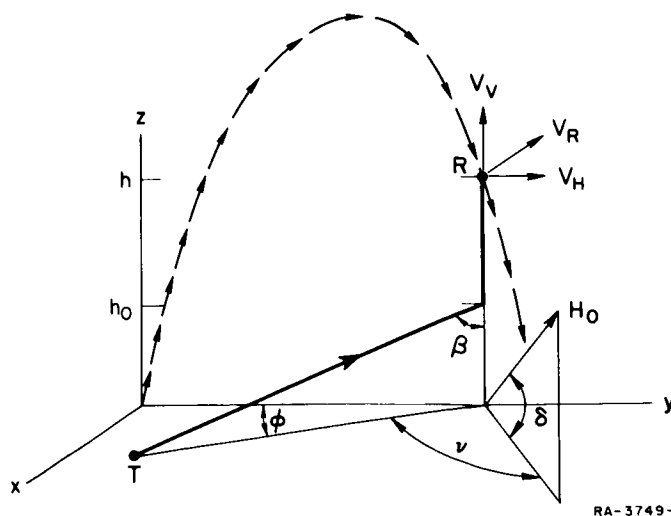


FIG. 9.65 ILLUSTRATION OF GEOMETRY FOR DOPPLER CALCULATIONS

where

V = rocket velocity

ψ = angle between V and wave normal

c = free-space velocity of light

F_s = rocket spin rate.

The spin rate enters due to the observation of a circularly polarized wave by a rotating antenna. F_s is positive if the rocket rotation is opposite to the polarization rotation of the propagating wave, as in this case, and is zero when applied to an antenna sensitive to a wave component in the direction of the rocket axis, such as the "horizontal" loop in this experiment. These polarization effects are clearly demonstrated in the data from these experiments.

Since

$$\begin{aligned} V \cos \psi &= V_v \cos \beta_2 + V_h \sin \beta_2 \cos \varphi \\ &= V_v \left(1 - \frac{\sin^2 \beta}{\mu^2} \right)^{1/2} + V_h \frac{\sin \beta}{v} \cos \varphi, \end{aligned} \quad (9.4.3)$$

where

V_v = vertical velocity component

V_h = horizontal velocity component

φ = angle between horizontal projection of wave normal and V_h ,

Eq. (9.4.2) can be written as

$$F_r = F_t \left[1 - \frac{V_v}{c} \left(\mu^2 - \sin^2 \beta \right)^{1/2} - \frac{V_h}{c} \sin \beta \cos \varphi \right] + F_s. \quad (9.4.4)$$

In this experiment, the received frequency F_r was not telemetered directly, but its phase was measured with respect to a reference frequency F_a , nominally equal to F_t , carried on the rocket. The phase difference, whose slope is the frequency difference $F_r - F_a$, and the reference

frequency $3F_a$ were telemetered. On the ground they were received Doppler-shifted by a factor $(1 - V_r/c)$ due to the rocket's radial velocity V_r from the telemetry station at the launcher. The received reference frequency was divided by three to $F_a (1 - V_r/c)$, and compared with the VLF ground wave at F_t . The resultant "ground reference" frequency F_g was recorded on the telemetry chart, where

$$F_g = F_t - F_a \left(1 - \frac{V_r}{c} \right) \quad (9.4.5)$$

and the data channels on the same chart contained the value of F_b for each antenna on the rocket, where

$$F_b = (F_r - F_a) \left(1 - \frac{V_r}{c} \right) . \quad (9.4.6)$$

In the data-reduction process, the difference frequency F_d was calculated, where

$$\begin{aligned} F_d &= F_b - F_g = F_r \left(1 - \frac{V_r}{c} \right) - F_t \\ &= \left\{ F_s - \frac{F_t}{c} \left[V_v \left(\mu^2 - \sin^2 \beta \right)^{1/2} + V_h \sin \beta \cos \varphi \right] \right\} \left(1 - \frac{V_r}{c} \right) - F_t \frac{V_r}{c} . \end{aligned} \quad (9.4.7)$$

Since $V_r/c < 10^{-5}$ in this case, $(1 - V_r/c)$, which modifies only the small difference frequency in brackets, can be considered 1 without affecting the resultant accuracy. Then

$$F_d \approx F_s - \frac{F_t}{c} \left[V_v \left(\mu^2 - \sin^2 \beta \right)^{1/2} + V_h \sin \beta \cos \varphi + V_r \right] . \quad (9.4.8)$$

Letting $c/F_t = \lambda$, the free-space VLF wavelength (13.4 km in this case), and solving for μ^2 ,

$$\mu^2 = \sin^2 \beta + \left[\frac{\lambda(F_d - F_s) + V_h \sin \beta \cos \varphi + V_r}{V_v} \right]^2 . \quad (9.4.9)$$

The angle θ between the wave-normal and the earth's magnetic field at this point in the ionosphere can now be calculated (see Fig. 9.6.5) from

$$\begin{aligned}\cos \theta &= \sin \beta_2 \cos \delta \cos \nu + \cos \beta_2 \sin \delta \\ &= \frac{1}{\mu} \left[\sin \beta \cos \delta \cos \nu + (\mu^2 - \sin^2 \beta) \sin \delta \right], \quad (9.4.10)\end{aligned}$$

where

δ = magnetic field dip angle from horizontal

ν = angle between horizontal projections of magnetic field and wave direction.

With μ and θ known, the electron density N can now be calculated from the "quasi-longitudinal" approximation to the Appleton-Hartree refractive index equation,

$$\mu^2 = 1 - \frac{X}{1 - Y \cos \theta}, \quad (9.4.11)$$

where

$$X = \frac{4\pi N q^2}{\epsilon m \omega^2}$$

$$Y = \omega_h / \omega$$

q = charge of an electron

ϵ = permittivity of free space

m = mass of an electron

$\omega = 2\pi F_t$, the radian wave-frequency

ω_h = electron gyrofrequency.

Therefore,

$$N = \frac{\omega^2 \epsilon_m}{4\pi q^2} (1 - \mu^2) \left(1 - \frac{\omega}{h} \cos \theta \right) \quad (9.4.12)$$

where μ is obtained from Eq. (9.4.9) and θ from Eq. (9.4.10).

In applying this method, some approximate wave-normal path must be assumed in order to determine the initial angle of incidence, β . For these experiments, the wave direction was taken to be line-of-sight to a given altitude h_o , then vertically up to the rocket, to avoid iteration or involved path calculations. The boundary altitude h_o was set at 75 km for daytime and 90 km for nighttime, but neither this choice nor the assumption of vertical propagation through the ionosphere, rather than calculation of the true path, would have a large effect on the result, since β was greater than 60 degrees in any case. The use of the "QL" approximation to the refractive index equation is also justified, not only by the fact that this expression is valid even for large values of θ , but by the particular geometry in this case which resulted in the refracted wave normal coming close to the magnetic field direction.

It should be noted that this method of electron density measurement is particularly suited for operations in remote areas, since VLF propagates with such low loss that transmissions are available everywhere on earth. Relatively simple equipment is required, both in the rocket and on the ground, and use of a distant source eliminates the problem of estimating the initial angle of incidence. Furthermore, accuracies of tens of percent or better should be obtainable for electron densities above $10^3/\text{cm}^3$ through both the bottom and top sides of the ionosphere. While the results of this experiment justify the simplifying assumption of Snell's law for daytime bottomside wave-normal determination, at night and above some as yet undetermined altitude in daytime the measured wave-normal directions will have to be used.

9.4.2.2 Daytime Electron Density Profiles

In order to calculate electron density profiles by the method outlined in Sec. 9.4.2.1, the records were first scaled to determine the phase measured in the rocket, and the phase measured on the ground. The difference of these measurements minus the phase delay due to telemetry propagation has been plotted as a function of time and altitude, shown in Fig. 9.66. For reference, phase delay which should have been observed if the entire path were free space with a refractive index of 1 is shown on the same curve. The VLF phase delay measured on both the vertical loop and the horizontal loop are shown in this figure. Since the vertical loop is sensitive to the field transverse to the rocket axis, the frequency observed in this channel is the sum of the right-handed rocket spin rate and the left-handed polarization rotation. The measured rocket spin has been subtracted in preparing the phase delay data. The phase observed on the horizontal loop, which is sensitive to the field component in the direction of the rocket's axis, is independent of rocket spin and shows excellent agreement with the corrected phase from the vertical loop except below 90-km altitude on descent, which is where the rocket flipped over on re-entry. The phase observed on the horizontal electric antenna was essentially identical to the one observed on the vertical loop, and has not been used directly in this analysis. At some points in the flight, particularly in the reflecting region from 70 to 90 km, the phase patterns were ambiguous and continuity could be established only by comparing all three components. One unexplained feature of the measured phase that should be noted here is an advance of about one cycle with respect to the calculated free-space phase, which occurred well below the reflecting region during ascent. This advance was observed between about 20 and 40 km on all components of the wave, which eliminates the possibility that it was an error in correcting the spin frequency.

Refractive index was calculated by the method outlined in Sec. 9.4.2.1 and is shown in Fig. 9.67. The points used are derived from Doppler frequency measurements made over periods of one spin cycle, or about one-third of a second. The velocities used were obtained from

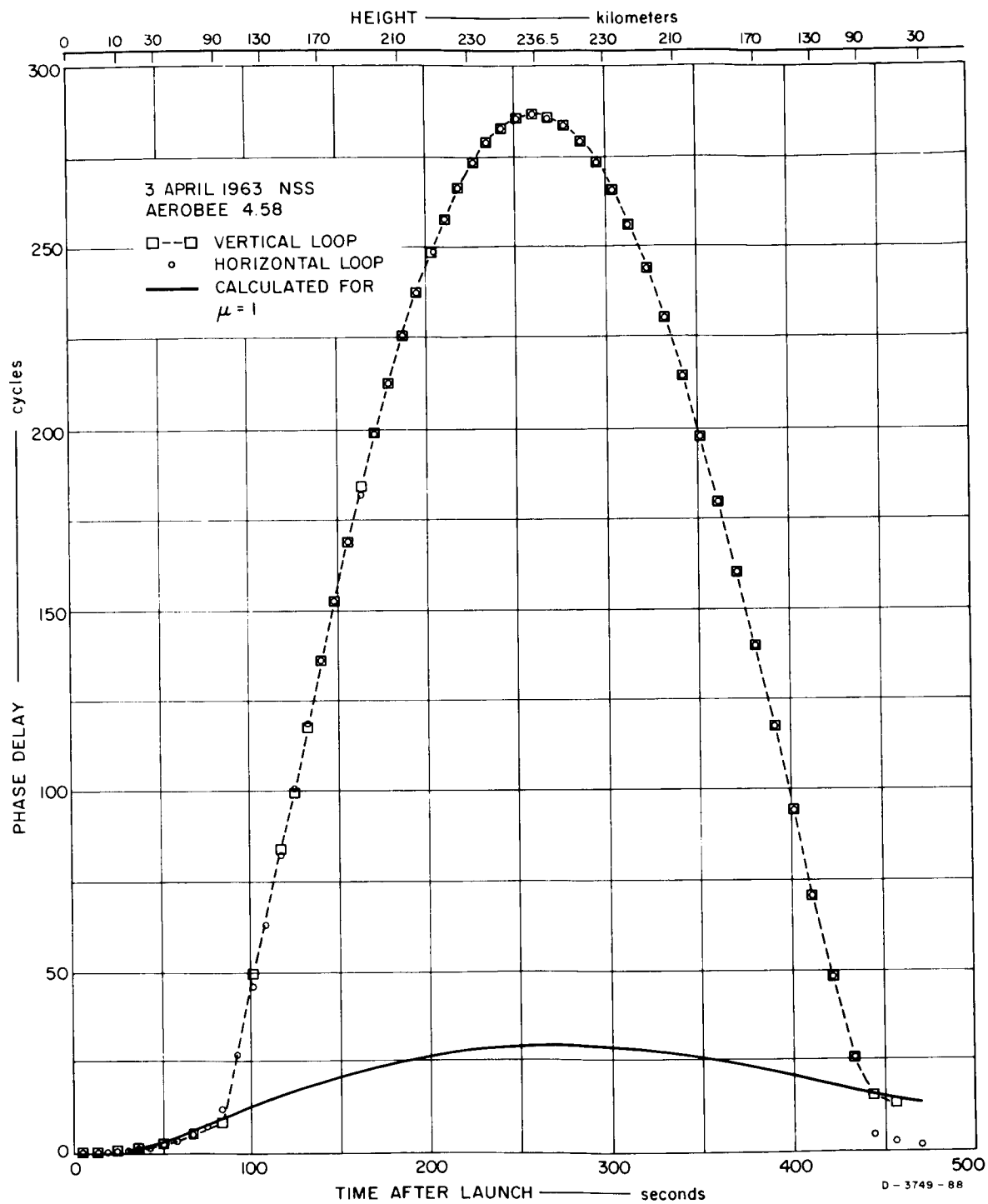


FIG. 9.66 DAYTIME PHASE DELAY AT 22.3 kc

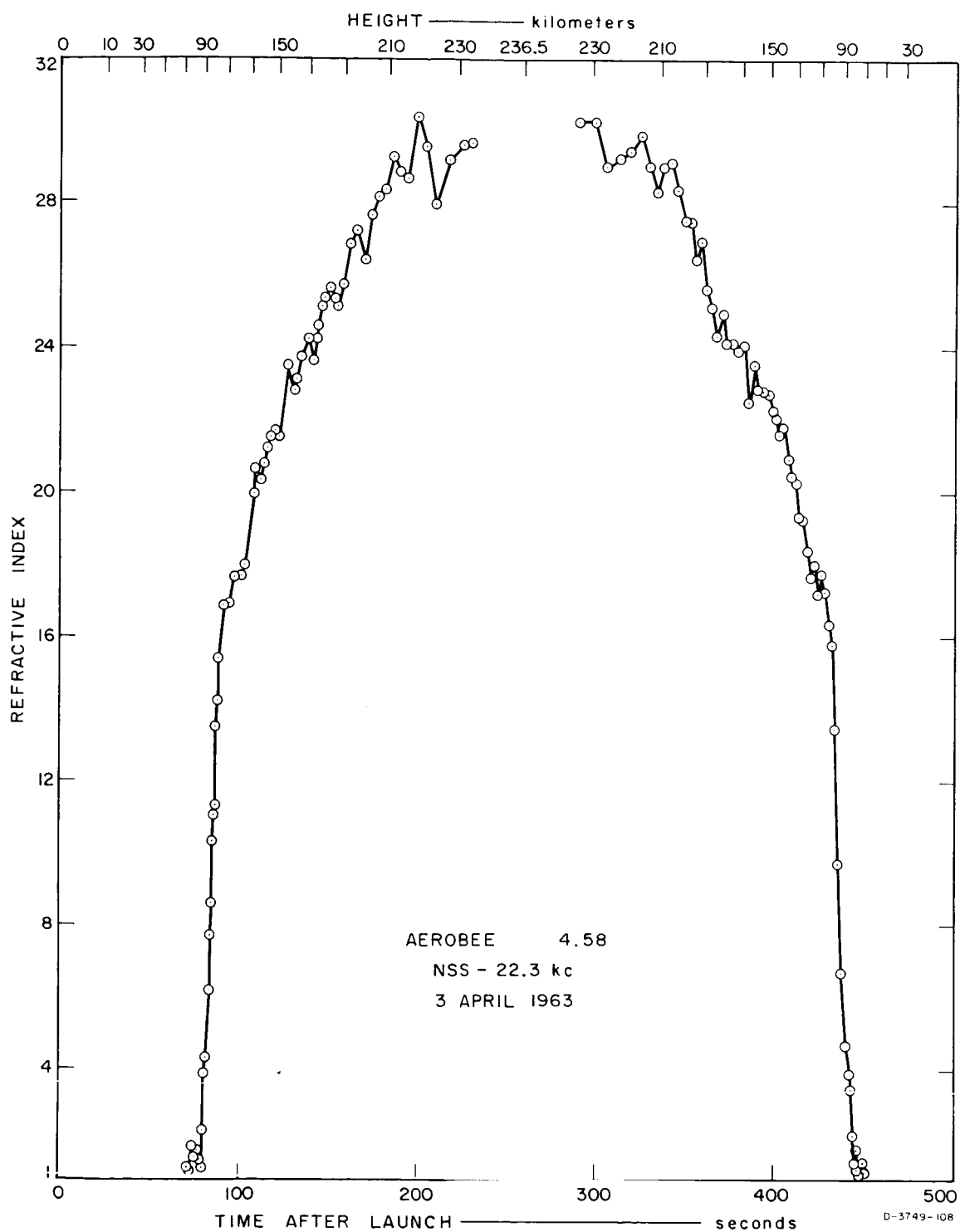


FIG. 9.67 DAYTIME REFRACTIVE INDEX AT 22.3 kc

an analytical expression for the trajectory to smooth the radar position data. The initial angle of incidence data were calculated as a function of rocket position, assuming the reflecting boundary to be at an altitude of 75 km. Most of the phase data used were from the vertical loop antenna, except in the reflecting regions, where the horizontal data appeared more stable. The apparent fluctuations in refractive index below 87 km are due to the phase interference of the reflected and evanescent waves with the propagating waves. On the other hand, the variations in the vicinity of 110 km are probably real, since the variations occur over a distance large compared to the wave length in the medium, which is about 0.7 km. Near apogee, the calculated refractive index is not reliable, since the vertical velocity goes through zero.

Electron density profiles derived from these data are shown in Fig. 9.68, along with the electron density versus true height derived from ionograms taken at Wallops Island during the flight. The maximum F-region density occurred at an altitude of 225 km, just below the rocket apogee. Although the ascent and descent profiles above 90 km agree to within about 10 percent, there is a consistent discrepancy of about 12 percent between the rocket and ionosonde data above 110 km. This difference is considerably larger than would be expected from errors in scaling and calculation, and may be evidence of small-scale irregularities in electron density. The ionosonde will obtain reflections from the maximum density at a given range within its area of illumination, while the propagation experiment responds to the local value. It should be noted that the maximum obtained by the rocket experiment agrees almost exactly with the ionogram.

Another region of disagreement between the propagation experiment and the ionogram is below 100 km, where the rocket shows a similar profile but about 3 km below the ionogram. It has been pointed out, however, that the program for calculating true height from the ionogram neglects the electron content below the lowest scalable reflection. An estimate of the delay due to the profile measured by the rocket below that point indicates that the ionogram should be lowered by about 4 km at its lowest frequency, bringing it into excellent agreement.

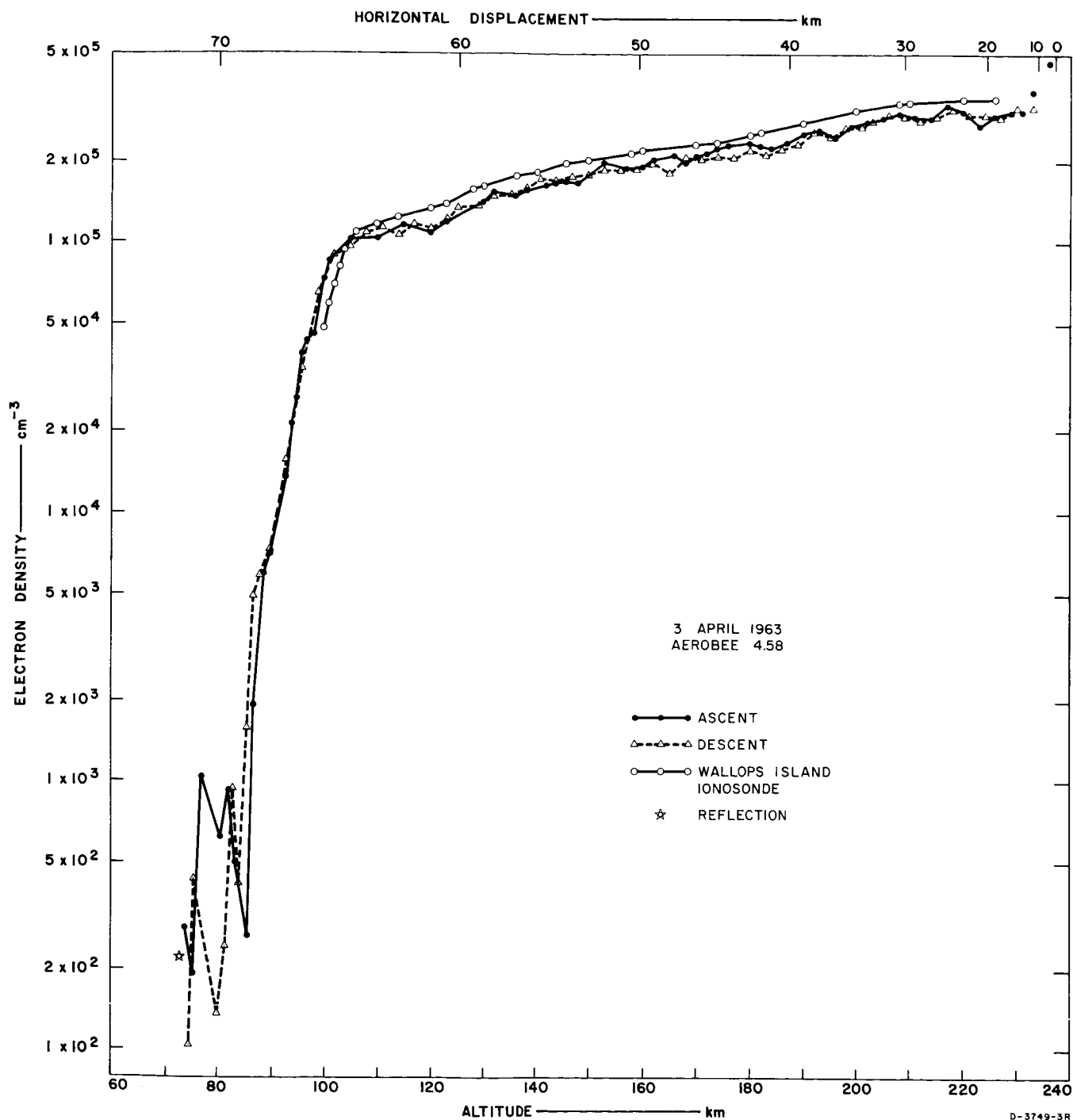


FIG. 9.68 DAYTIME ELECTRON DENSITY PROFILE

As in the refractive index curves, the fluctuations below 87 km are due to the interference of transmitted and reflected waves. In this region, the polarization changes from linear to left-handed circular, as the evanescent wave due to the reflection of the right-handed mode dies out. The star at 72 km indicates the best estimation of the reflection height of the right-handed mode on ascent, from both phase and amplitude data, and the corresponding electron density was calculated from the full Appleton-Hartree expression including collisions. Below this altitude, about 45 degrees of rotation of the linear polarization was observed, which is presumed to be simply Faraday rotation, although the presence of reflections have precluded any quantitative conclusions until a full-wave analysis can be undertaken.

Another feature worthy of note is the agreement in fine structure between the ascent and descent profiles above about 180 km. To indicate the region of correlation, a scale has been added to Fig. 9.68 which indicates the horizontal displacement between ascent and descent at a given altitude. At the higher altitudes, similar fluctuations are apparent over a distance of about 40 km.

9.4.2.3 Nighttime Electron Density Profiles

Records from the nighttime flight, Aerobee 4.59 UI, were scaled and the data processed by the same methods described above for the daytime flight. The result in phase delay is shown plotted in Fig. 9.69 for the vertical and horizontal loops, and the calculated value for a free-space path. Unlike the daytime flight, an extra delay rather than an advance in phase with respect to the free-space path was observed below the reflecting region. Another distinct difference was the penetration of dense sporadic-E clouds on both ascent and descent, and the relatively low electron densities observed on the remainder of the flight due to the 205-km apogee attained instead of the expected 230. As a result, there were several regions, particularly just above and below the sporadic-E, in which it was very difficult to determine phase unambiguously. It is apparent from the phase plot that two cycles have been lost somewhere, since the cumulative phase fails to return to the free space value on descent.

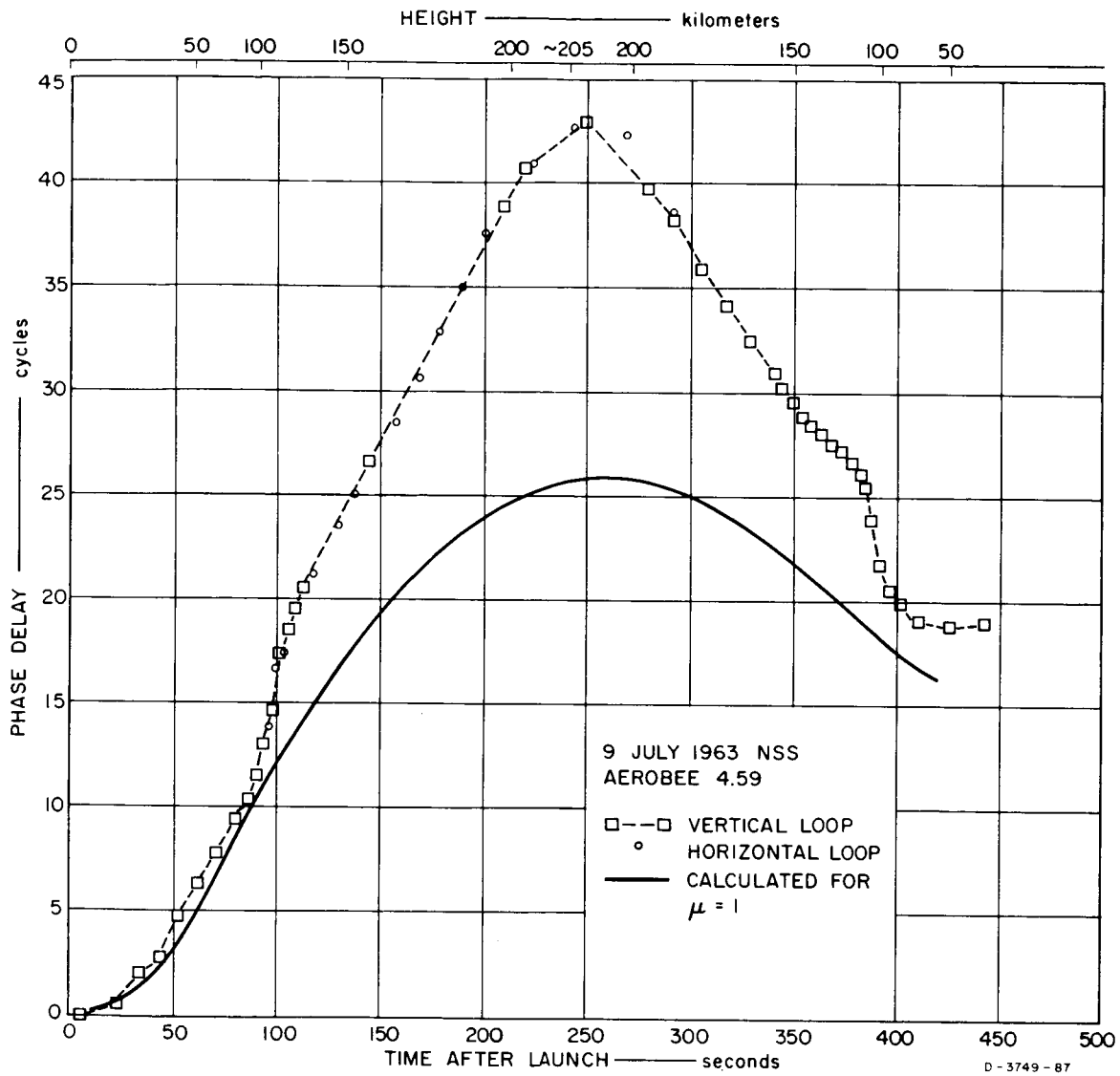


FIG. 9.69 NIGHTTIME PHASE DELAY AT 22.3 kc

In calculating the refractive index, shown in Fig. 9.70, it was necessary not only to switch back and forth between vertical and horizontal loop data several times, but also to use longer sample periods to determine Doppler frequency in the regions of severe phase interference. Samples of one spin period were used in the sporadic-E clouds, but over most of the rest of the flight samples of two to eight spin periods, or as much as 3 seconds, were used. As a result, only the data taken above 170 km on ascent are considered reliable. Nevertheless, the electron density profiles were calculated, and are probably within a factor of 2, excepting the obvious wild fluctuations, as shown in Fig. 9.71. The Wallops Island ionogram taken during the flight does not overlap the rocket data, nor would it appear to extrapolate to the same curve. However, the correction for the neglected electron content below the lowest point scaled must be considered as in the daytime flight. Although this calculation has not been carried out, because of the greater uncertainty in electron density and the more complicated profiles involved, a reduction of 10 km in the true height of the lowest point would provide excellent agreement.

One of the difficulties in devising a means to analyze data of this type is first determining whether the phase interference is due to reflections or multipath propagation. The magnitude of this task is beyond the hand-scaling methods employed in this experiment. It could be accomplished by running a full-wave solution on a computer, in which case the entire experiment should be designed for machine handling of data. The phase and amplitude of all six components of the wave could then be measured to minimize ambiguities.

9.4.3 Amplitude Measurements

During both flights, the amplitude of uninterrupted 22.3-kc transmissions from station NSS were measured on the vertical and horizontal loops, and on the plate antenna. The fields actually measured by the vertical loop and plate antennas were the magnetic and electric fields, respectively, transverse to the spin axis of the rocket. The horizontal loop measured the magnetic field component in the direction

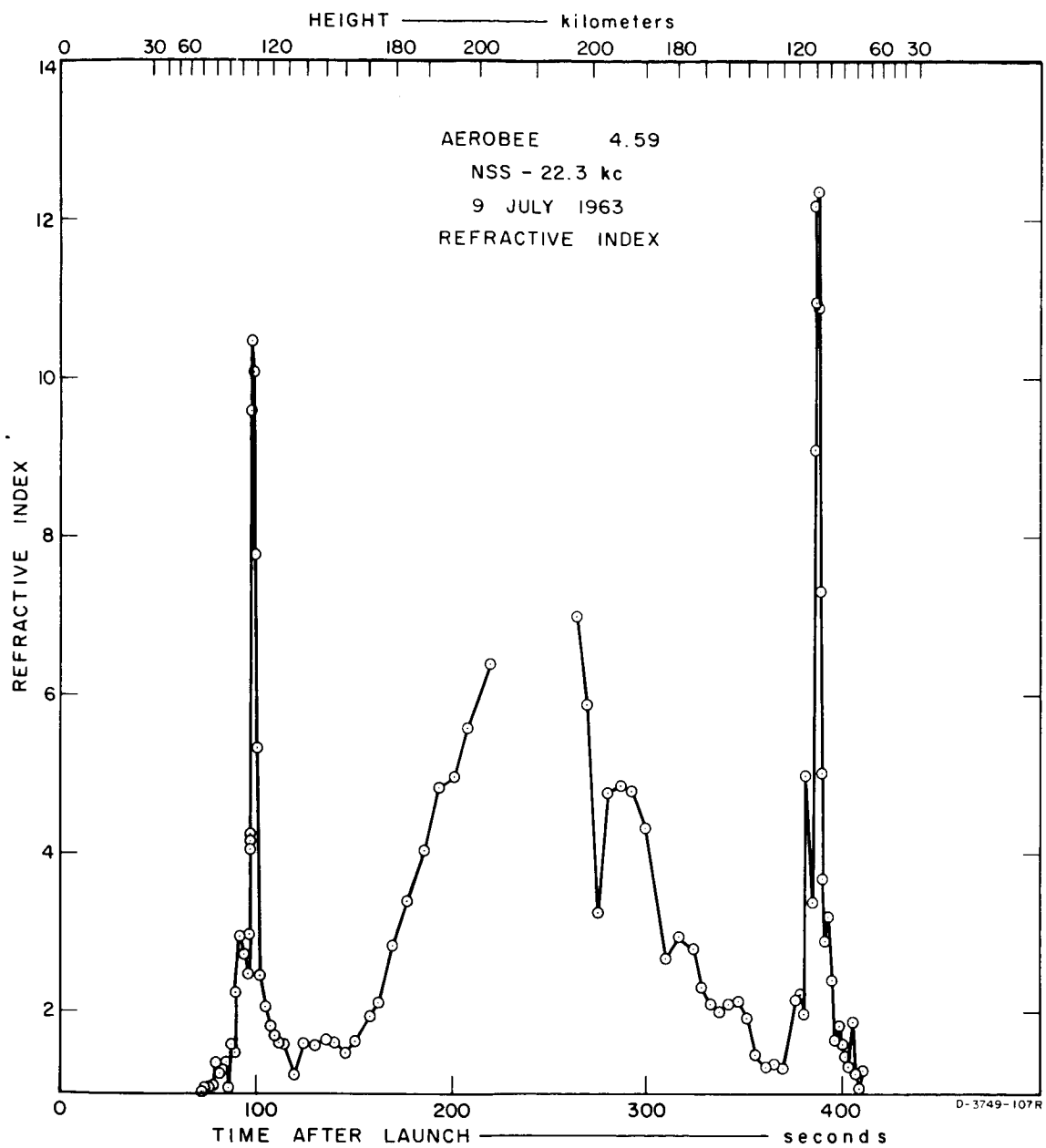


FIG. 9.70 NIGHTTIME REFRACTIVE INDEX AT 22.3 kc

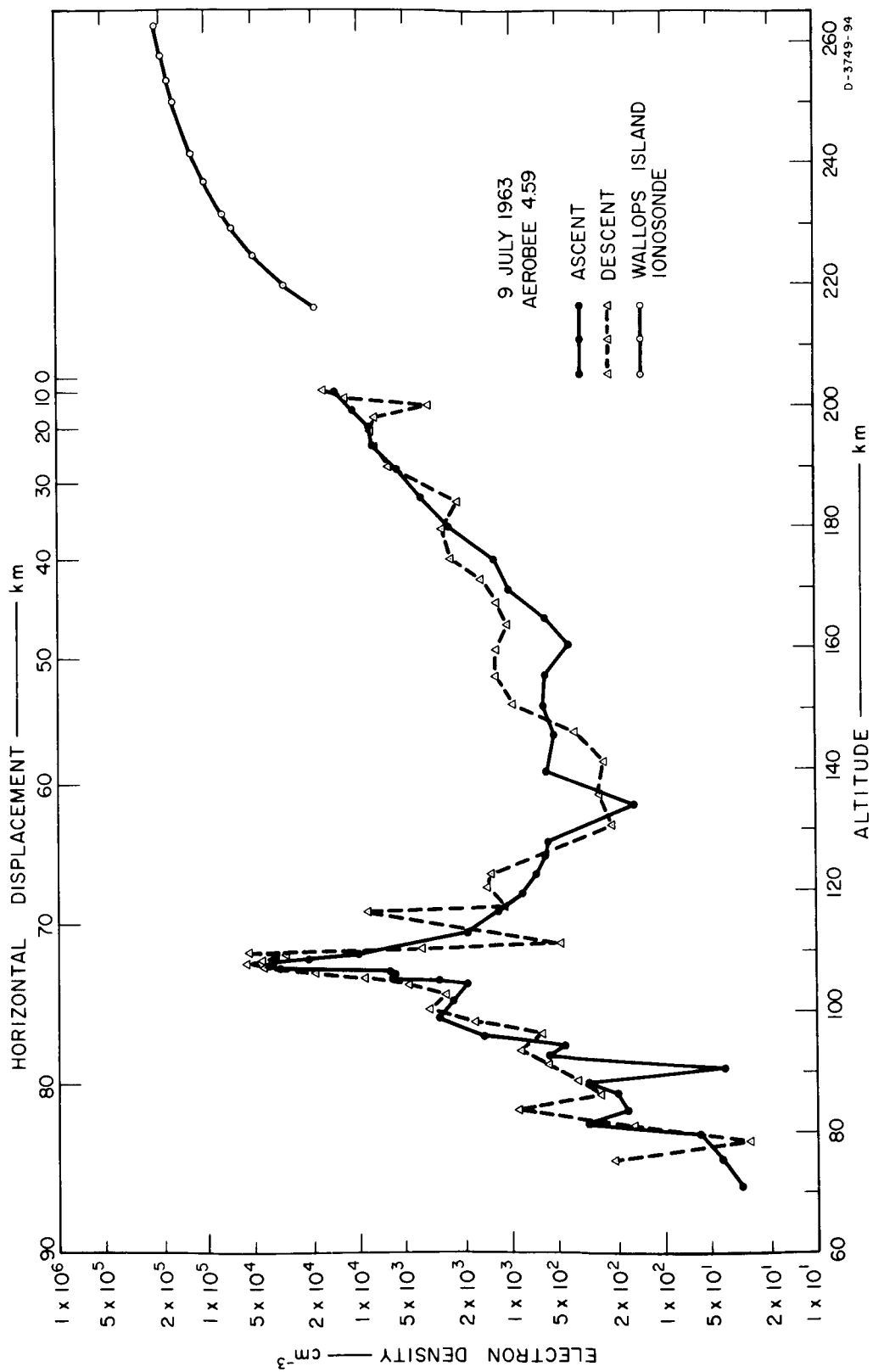


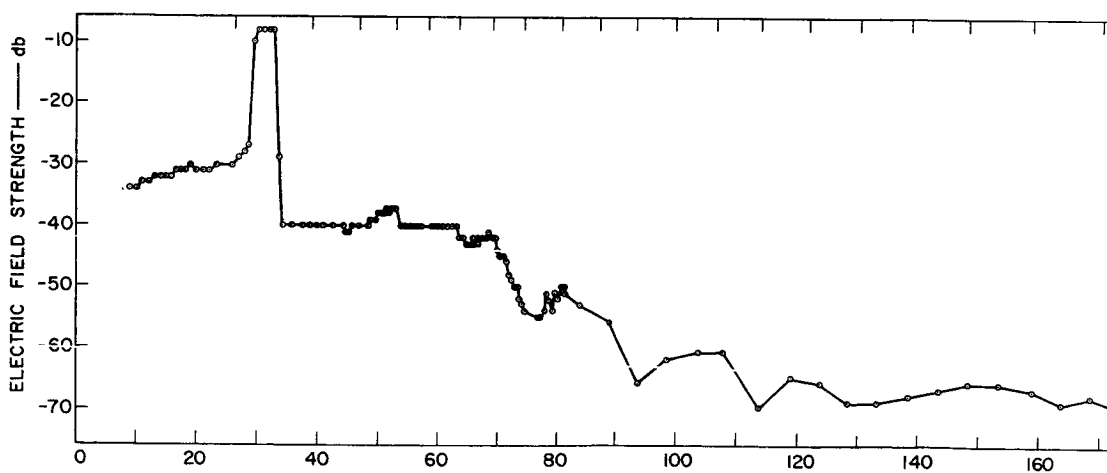
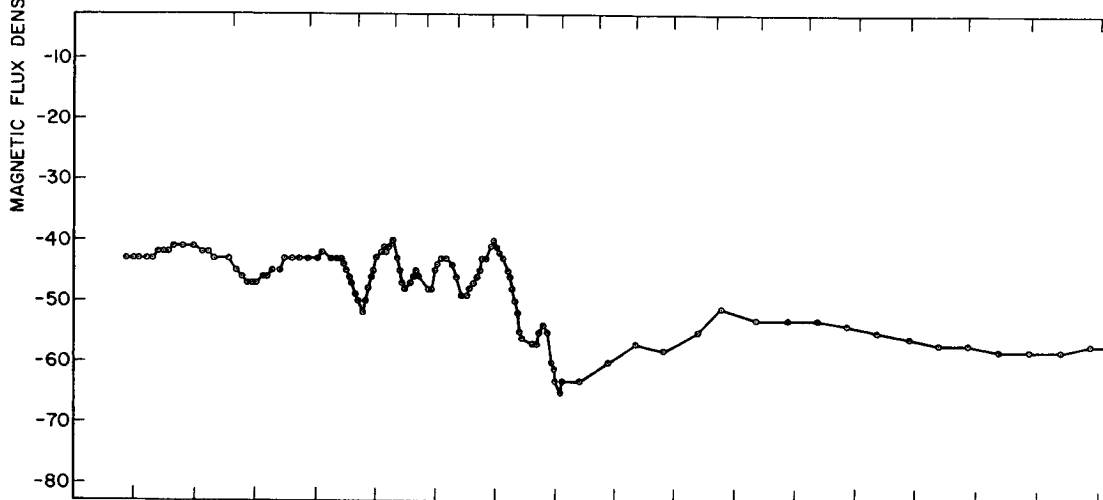
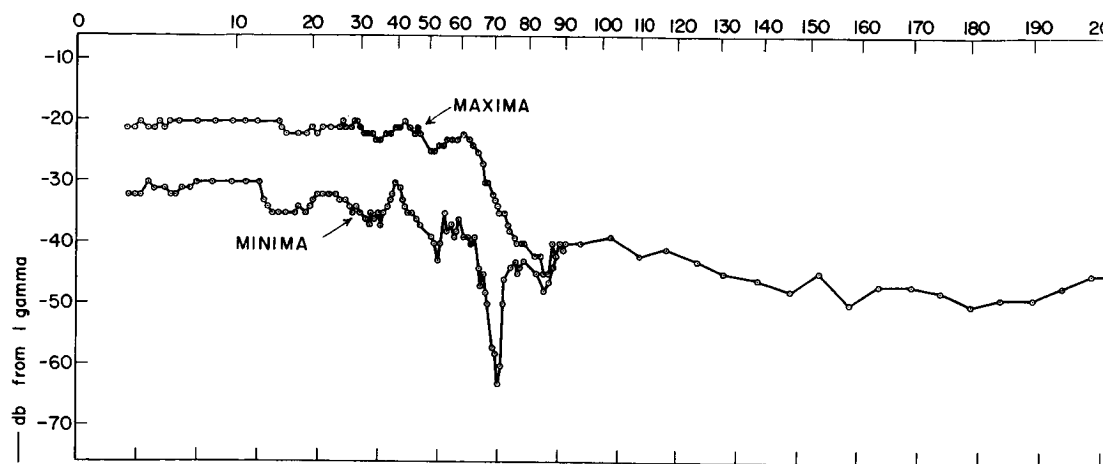
FIG. 9.71 NIGHTTIME ELECTRON DENSITY PROFILE

of the rocket axis. (Refer to Sec. 8 for spin axis direction.) The log-compressed amplitude data were scaled from the telemetry records with an estimated accuracy of ± 1 db within the 90-db dynamic range of the instrument, as described in Sec. 9.4.1. Magnetic field strengths will be given here in db with respect to 1 gamma rms, where the number of db is $20 \log_{10}$ of the ratio, and 1 gamma is 10^{-5} gauss. In a magneto-ionic plasma, the magnetic field strength H is presumed to be always equal to the flux density B divided by the permeability of free space. However, the ratio of electric to magnetic field strength, E/H , equals η , the local wave impedance. This impedance is the free-space impedance divided by the local refractive index, which is a function of the medium. As an example, an infinite plane wave propagating in free space with a magnetic flux density of 1 gamma would have an electric field strength of 0.30 v/m, and a magnetic field strength of 7.93×10^{-4} a/m.

In these experiments, the measurement of electric field strength was only partially successful during the daytime flight, because the plate antenna strips peeled off before burn-out. Although signals were received on the remaining leads throughout the flight, the effective length and orientation of this antenna can only be guessed at. During the nighttime flight, however, the redesigned antenna stayed on and reliable data were obtained throughout the flight. The effective length of the nighttime antenna, defined as the ratio of terminal voltage to field strength, was calculated from the electric to magnetic field strength ratio as 0.094 meter which was consistent with the refractive index measured by the Doppler method. This value of effective length was in agreement with the value estimated from the geometry and approximate measurements of the base and active capacitances of the antenna.

9.4.3.1 Daytime Results

The amplitudes measured at 22.3 kc during Aerobee 4.58 U1 are shown in Fig. 9.72. In this figure, the magnetic flux densities measured on the vertical and horizontal loop antennas are plotted in db with respect to 1 gamma rms as a function of time and altitude. The electric field strength is shown only in relative units, since it was not possible to calibrate the antenna after the plates stripped off.



17

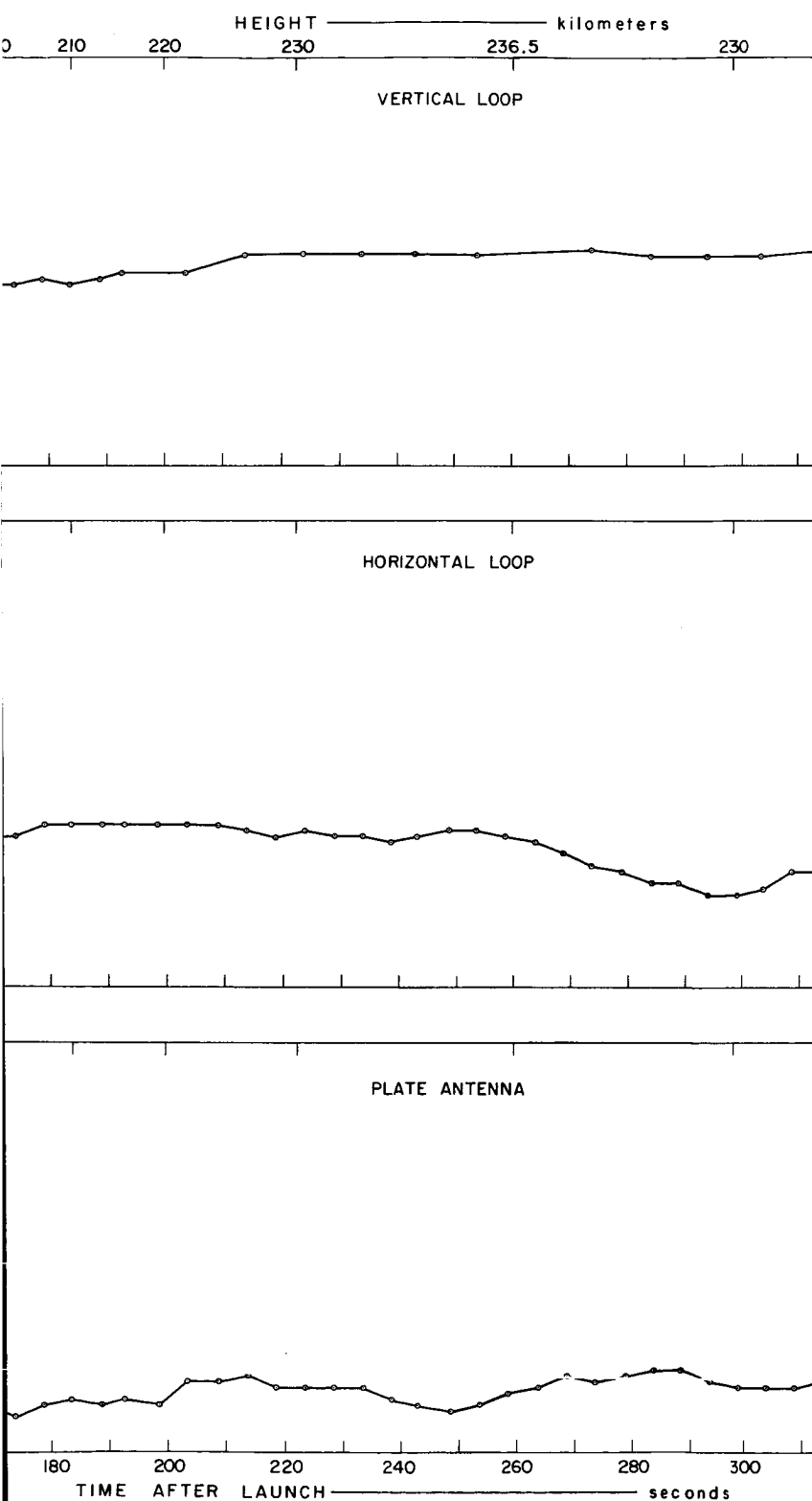
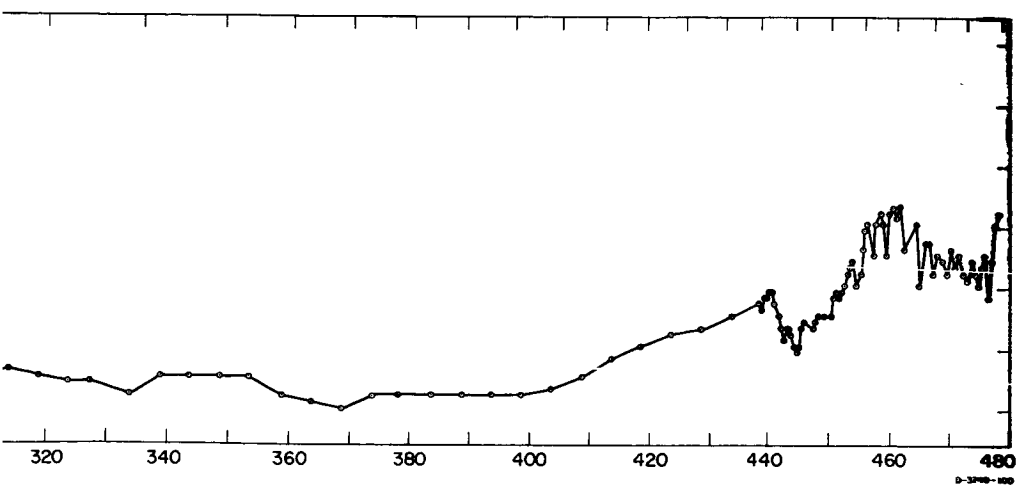
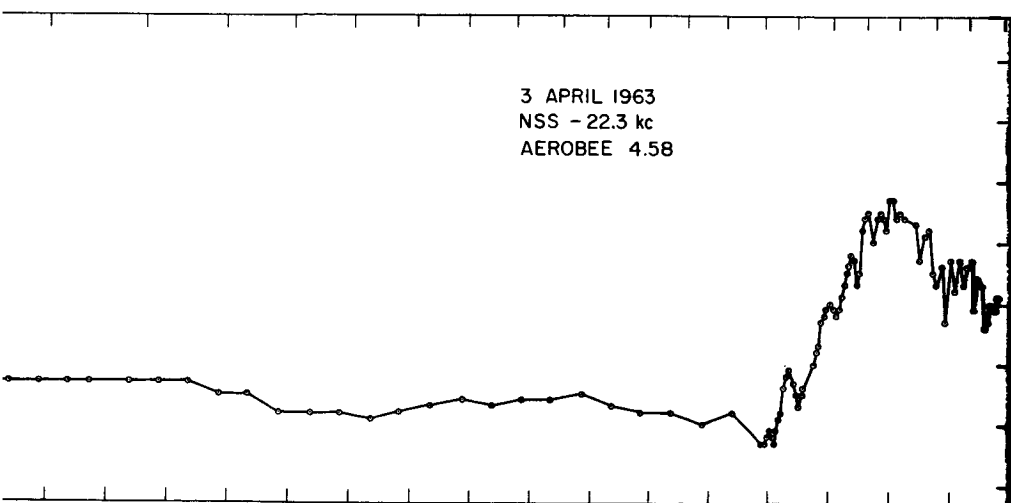
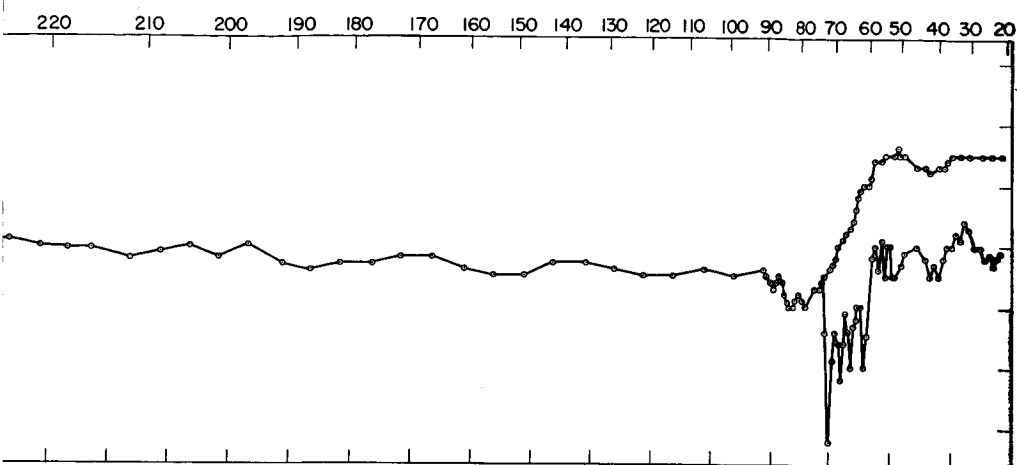


FIG. 9.72 DAYTIME AMPLITUDES AT 22.3 kc



57

The curves labeled "maxima" and "minima" on the vertical loop plot indicate the maximum and minimum amplitudes during a spin cycle. The disappearance of significant spin modulation between 72- and 87-km altitude during ascent indicates the reflection of the right-hand polarized wave, interference of the remaining evanescent wave with the propagating left-hand mode, and refraction of the propagating mode toward the vertical. This region appears quite different on descent, largely due to the fact that the rocket flipped over at 90 km. Below about 70 km, the expected four cycles of standing-wave pattern are observed as a result of the interference between the direct and reflected waves. The amplitude of this pattern indicates a reflection of about one-fourth the incident power. This is not an unreasonable value, although no detailed analysis has yet been made of the reflection, transmission, and absorption in this region for comparison. It is apparent, however, that the main reflection is taking place in the lower part of the absorbing region, which extends between 60 and 80 km.

The horizontal loop does not exhibit spin modulation, but it is much more sensitive to the angle of the wave normal, since the magnetic vector lies nearly in the plane of the loop. In spite of this, the amplitude observed above 90 km is remarkably free of fluctuations, as is that of the vertical loop. Below 90 km, however, the horizontal loop exhibits large variations due to the change in direction of the wave and of the rocket axis.

The electric field, on the other hand, shows considerably more variation above 90 km, particularly in the region between 90 and 170. Above that it also appears undisturbed. Between 90 and 150 km, the electric field also exhibits the expected decrease due to the increase in refractive index. Above 200 km, however, the field again increases, possibly due to the reduced ion sheath spacing which would increase the active capacitance to the antenna and therefore increase its effective length. The power density in the wave, which is the square of the magnetic field strength times the local wave impedance, is shown in Fig. 9.73. The wave impedance used is the free-space value divided by the refractive index determined from the Doppler experiment. Below

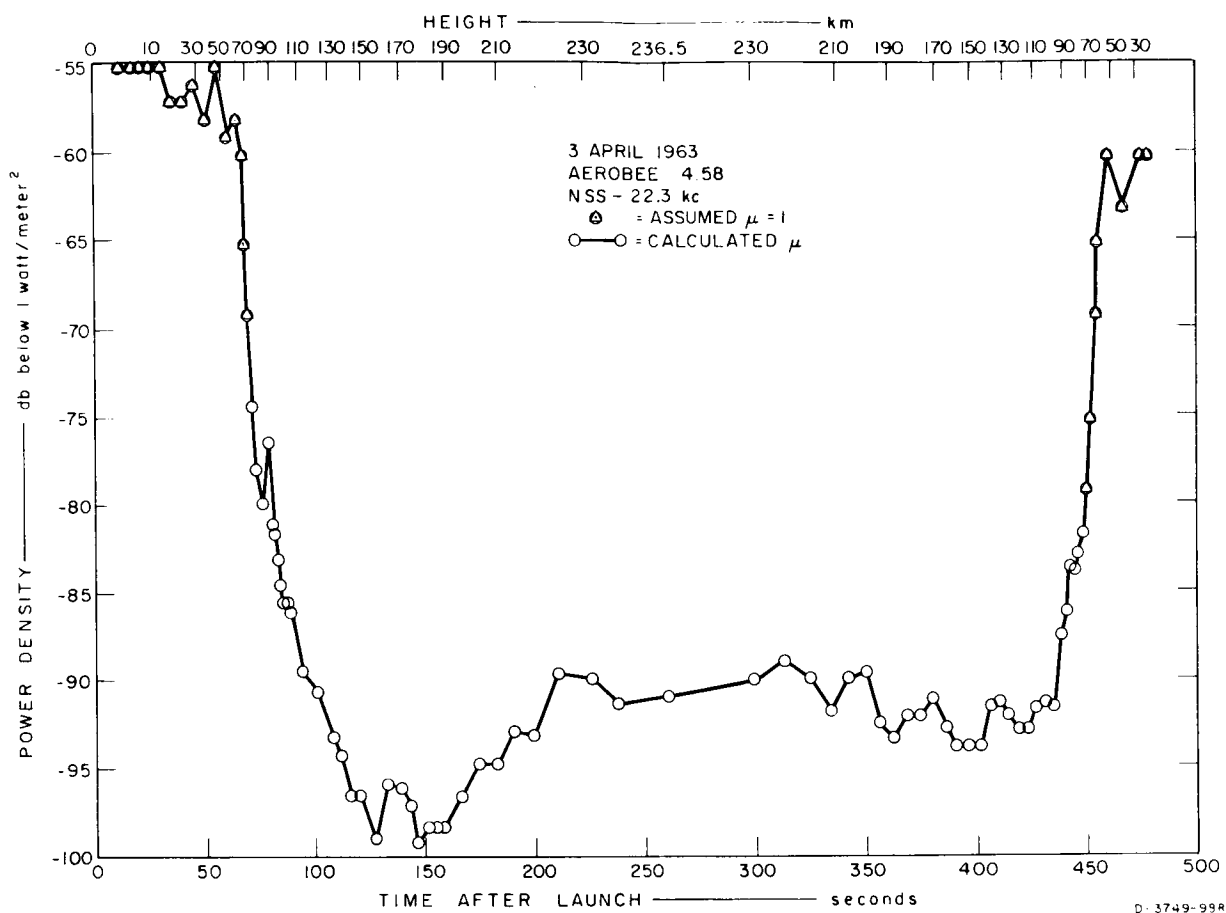


FIG. 9.73 DAYTIME POWER DENSITY AT 22.3 kc

50 km altitude, the observed power density is close to the expected standing wave pattern superimposed on the inverse square law of distance from the transmitter. Between about 50 and 70 km, both absorption and reflection are taking place. From 70 to 80 km, absorption seems to predominate, since power density drops smoothly by about 20 db on both ascent and descent. Above about 80 km, where the refractive index exceeds 1.5, the total attenuation at apogee is found to be about 35 db, of which at least 20 db are due to absorption and the rest to reflection. Spreading of the wave is expected to be negligible under these conditions. Between 120 and 200 km, the power density dips an additional 10 db during ascent. This is thought to be due to a multipath interference rather than a change in absorption with position of the ray path, since the wave normal deviates considerably from its expected direction in this region, as

explained below. The slow drop of power density after apogee is consistent with the increase in distance from the transmitter to the ray path's point of entry into the ionosphere. Before apogee, however, this distance did not increase rapidly, and in fact may even have decreased initially.

Although the electric field of the wave does not necessarily lie in the plane of the wavefront, the magnetic field does. This fact has been used to calculate the angle of the wave normal from the rocket axis, which is the arctangent of the ratio of amplitudes measured on the horizontal and vertical loops. This angle is shown in Fig. 9.74 as a function of time and altitude. The arrow labeled "vertical" marks the direction of vertical with respect to the principal spin axis of the rocket, neglecting precession. If the assumptions of Sec. 9.4.2 are correct, the wave normal angle should lie within about 6 degrees of the vertical everywhere above 100 km, or between about 3 and 10 degrees on this plot. The apparent deviations beyond this range are thought to be multipath effects, either below or above the ionosphere, rather than actual deviations of the wave normal. It should be pointed out that, even if the observed wave normal directions are correct, the errors introduced in the electron density calculations are not greater than about 7 percent. It is also apparent, however, that a simple stratified model will not be adequate for accurate calculations of the characteristics of propagation in this region.

9.4.3.2 Nighttime Results

The 22.3-kc amplitudes measured at night on Aerobee 4.59 UI are shown in Fig. 9.75. Unlike the daytime data, the electric field strength is given in db below 1 v/m rms, assuming the effective length of the antenna is 0.094 meter as discussed in Sec. 9.4.3. Considering the vertical loop amplitude, where the upper and lower traces are the maximum and minimum amplitudes due to spin modulation, little absorption is evident. The transition from linear to circular polarization now takes place between about 80 and 100 km, with spin modulation reappearing between 130 and 170 km on ascent. This recurrence of spin modulation above the sporadic E occurs in a region of low refractive

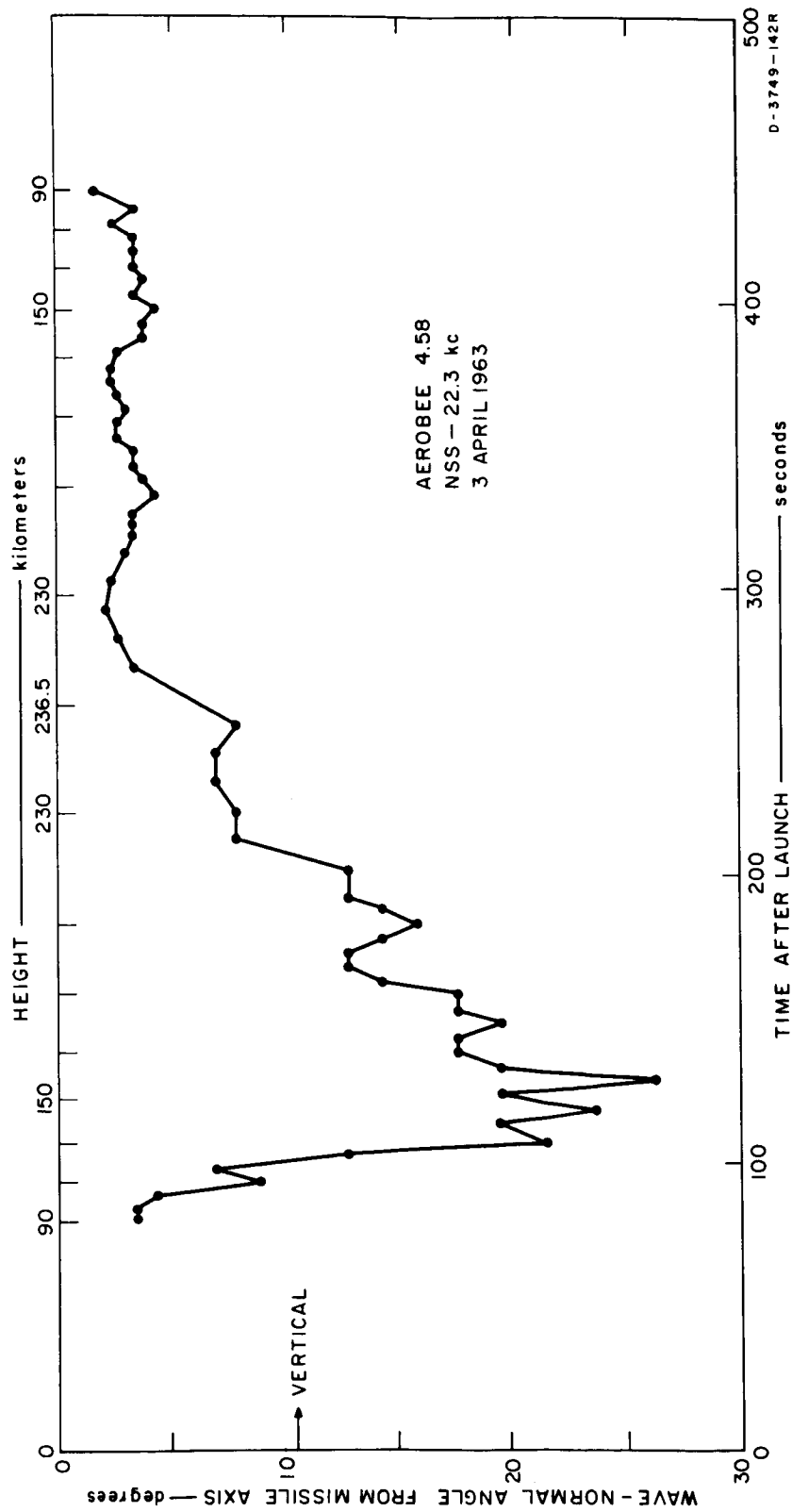
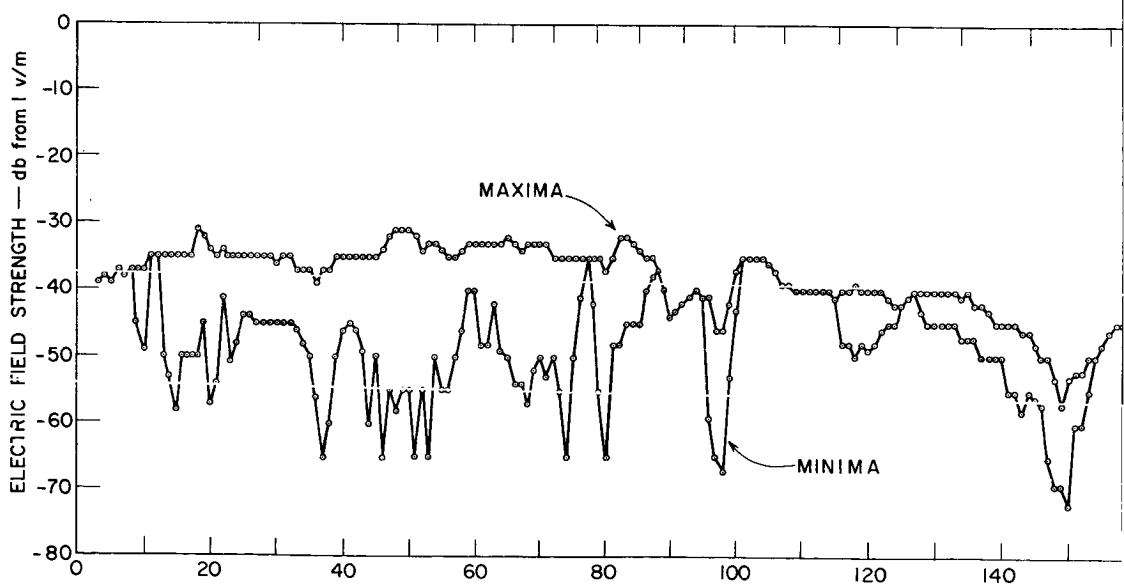
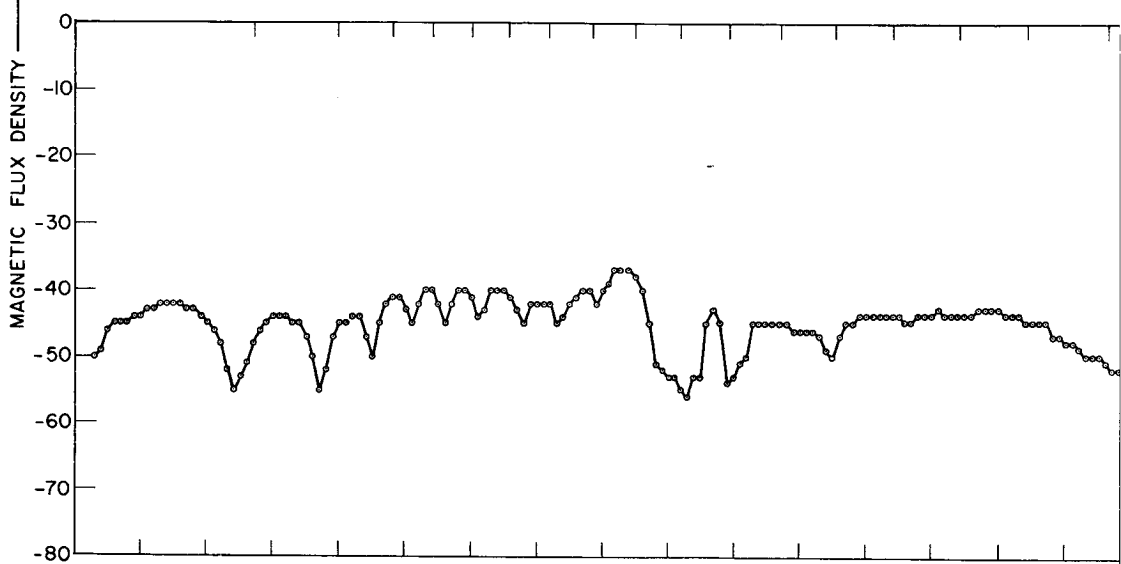
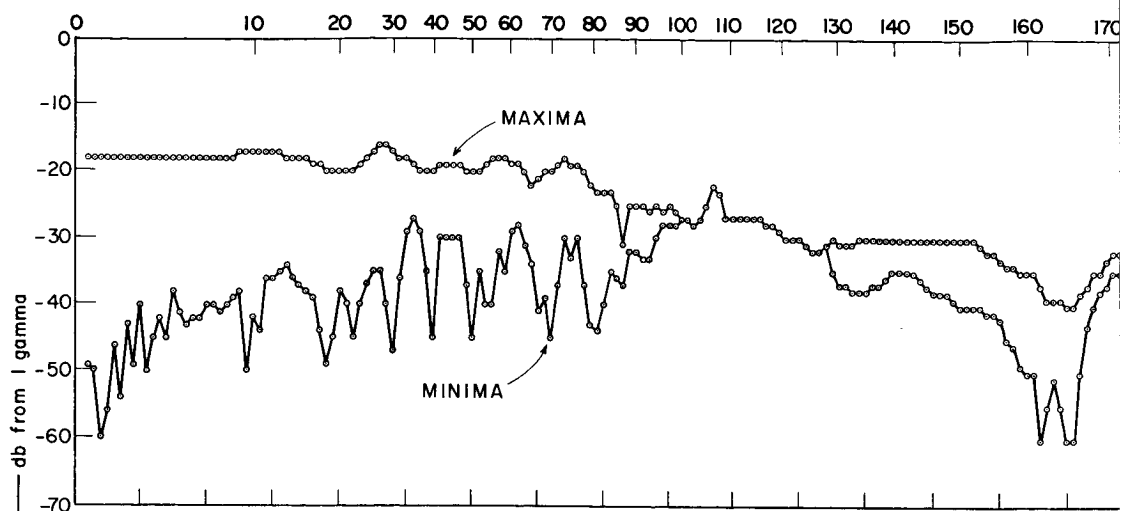


FIG. 9.74 DAYTIME WAVE-NORMAL ANGLES AT 22.3 kc



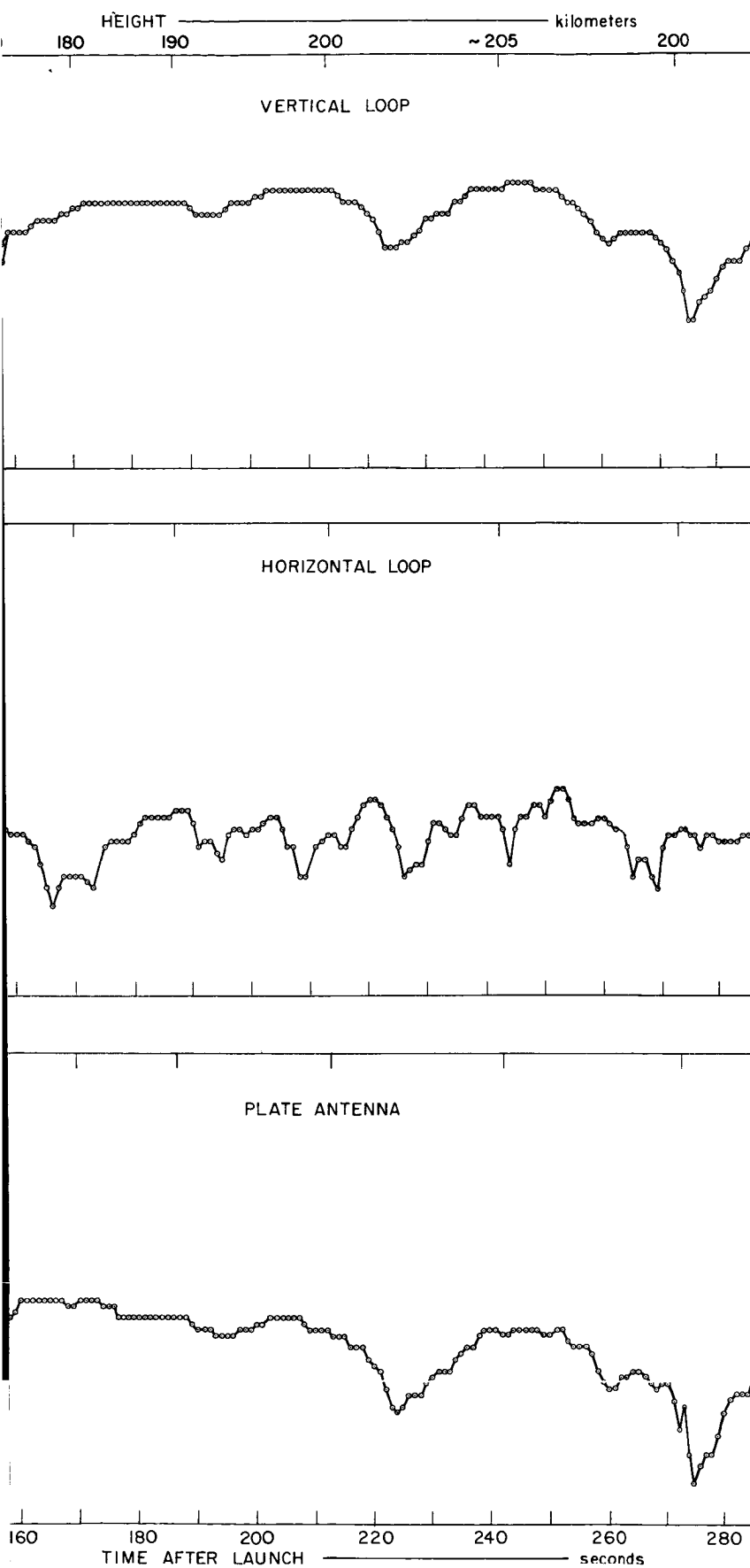
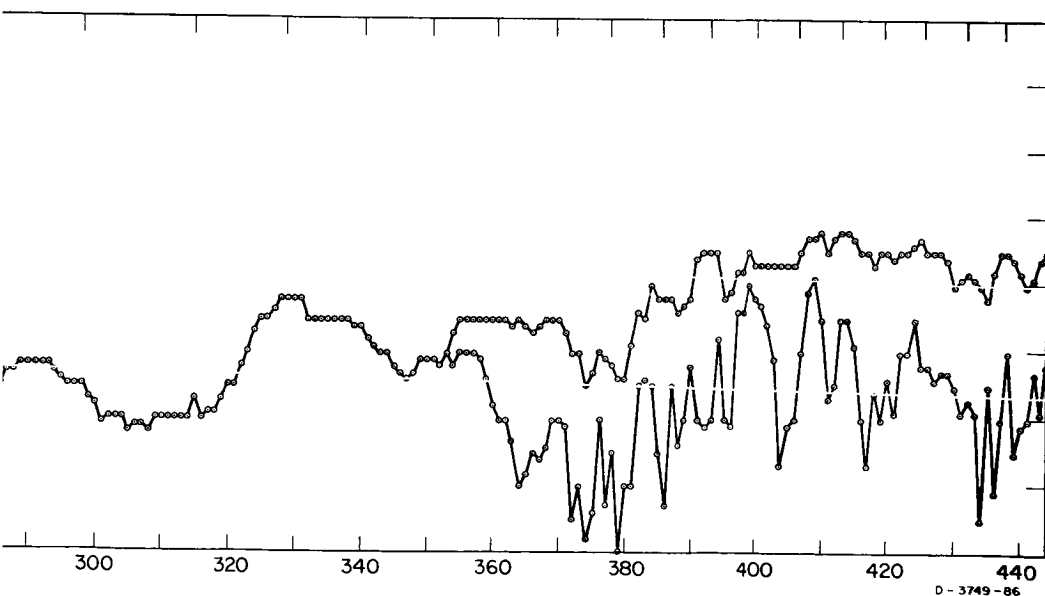
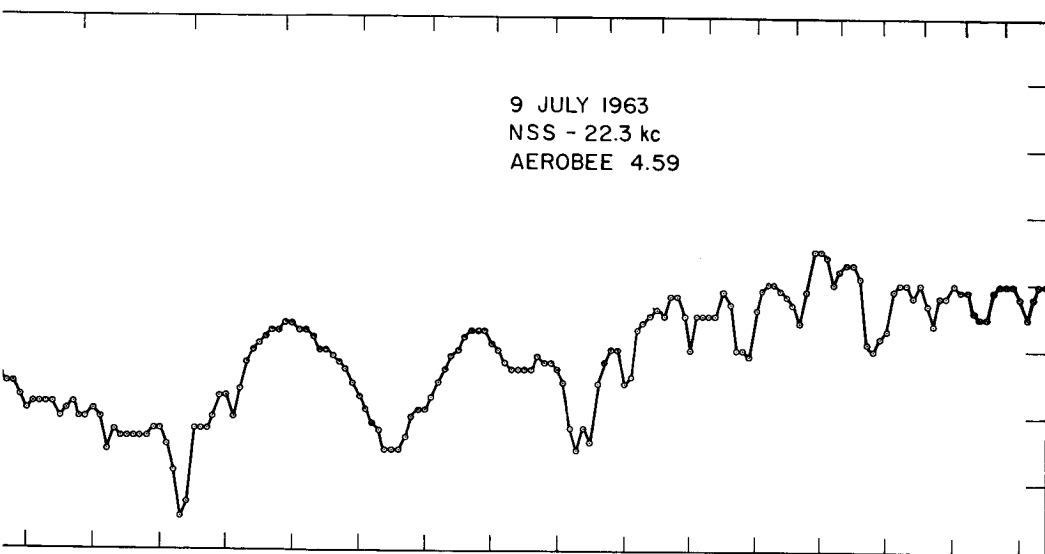
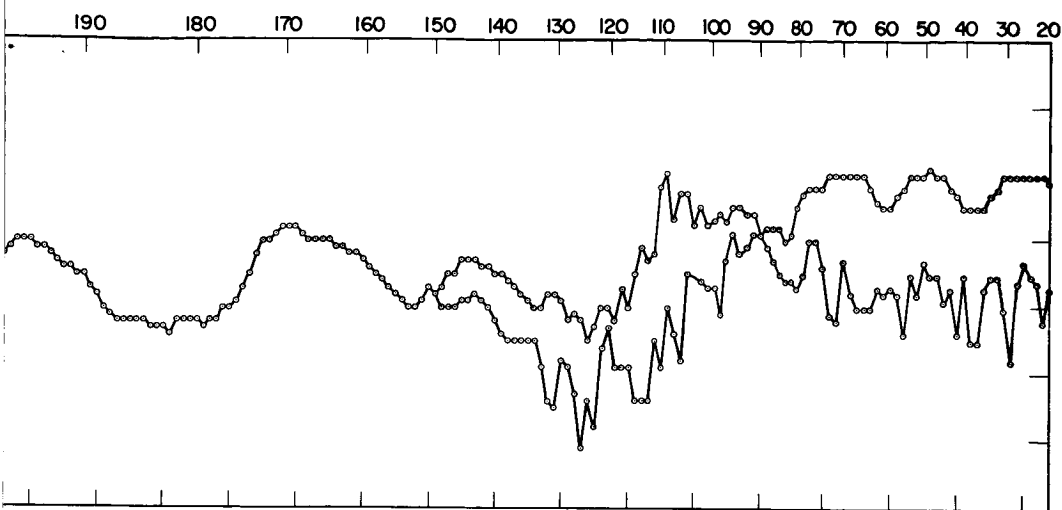


FIG. 9.75 NIGHTTIME AMPLITUDES AT 22.3 kc



9 JULY 1963
 NSS - 22.3 kc
 AEROBEE 4.59

D - 3749 - 86

index bounded by steep gradients, probably giving rise to numerous reflections. On descent the picture is even more confused, since spin modulation reappears at about 150 km and persists completely through the E region. In spite of its density, the sporadic-E cloud exhibits little effect on the amplitude of any component during either ascent or descent. In general, the nighttime amplitudes fluctuate considerably more than the daytime ones, which is also true of the power density, shown in Fig. 9.76. As expected, however, the total absorption and reflection loss is considerably less at night than in the day, being only about 15 db, including sporadic-E effects. The nighttime wave normal angles, shown in Fig. 9.77, are extremely erratic but still within about 15 degrees of their expected values above 90 km. Below 90 km, where the magnetic field is expected to be linearly polarized and horizontal, the angle calculated no longer represents the direction of the wave normal. Instead, it is the complement of the angle between the magnetic field and the rocket axis, and should be near zero. This appears to be the case on ascent; and descent must be discounted below 90 km since the rocket flipped over at that altitude.

In order to determine whether the effective length of the electric antenna remained constant, the ratio of magnetic to electric field strength was plotted in arbitrary units shown in Fig. 9.78. Since this ratio is proportional to the local refractive index, the latter as determined by the Doppler experiment has been plotted on the same chart on a suitable logarithmic scale. Only a few points were used to avoid cluttering the data, but it is apparent by referring to Fig. 9.70 that the general agreement will be good. In fact, this ratio exhibits remarkably little fluctuation compared to the direct amplitude measurements, supporting the contention that these fluctuations are due to irregularities in the medium rather than to interference of different modes. In the sporadic-E region, however, this situation is reversed and the H-to-E ratio exhibits stronger variation than the field strength measurements, although not as strong as the refractive index calculated from phase delay. The meaning for this is not clear, although it is probably due to the strong reflections in the sporadic-E region.

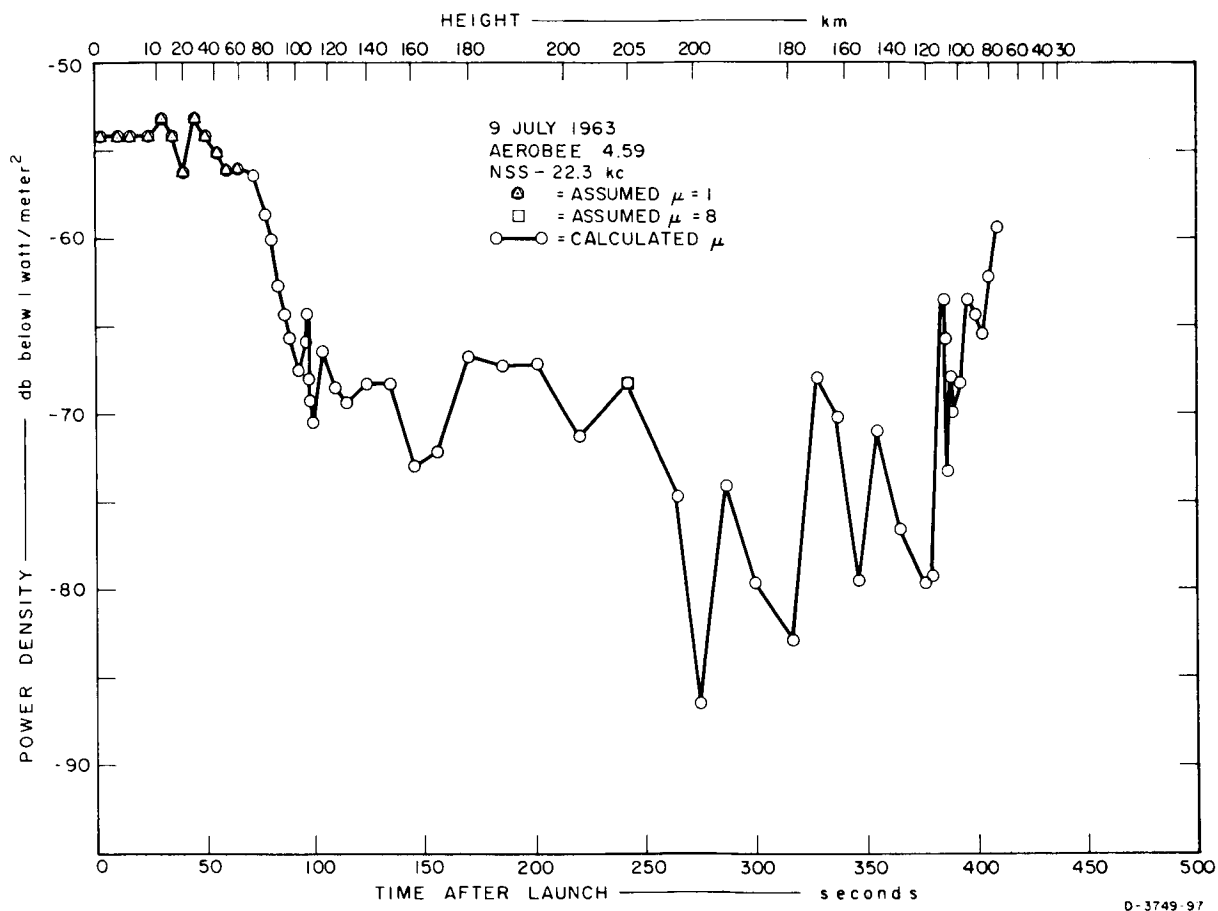


FIG. 9.76 NIGHTTIME POWER DENSITY AT 22.3 kc

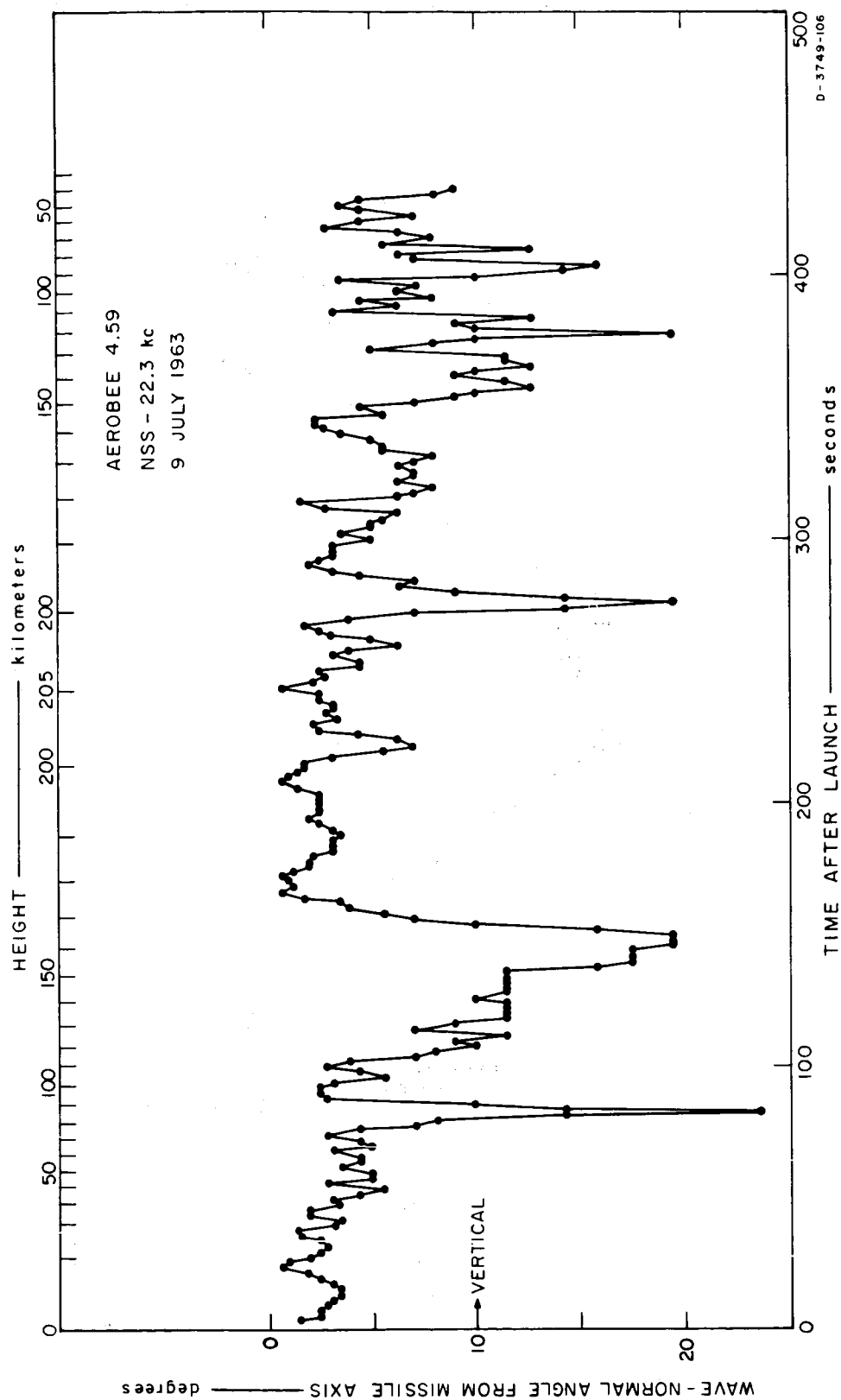


FIG. 9.77 NIGHTTIME WAVE-NORMAL ANGLES AT 22.3 kc

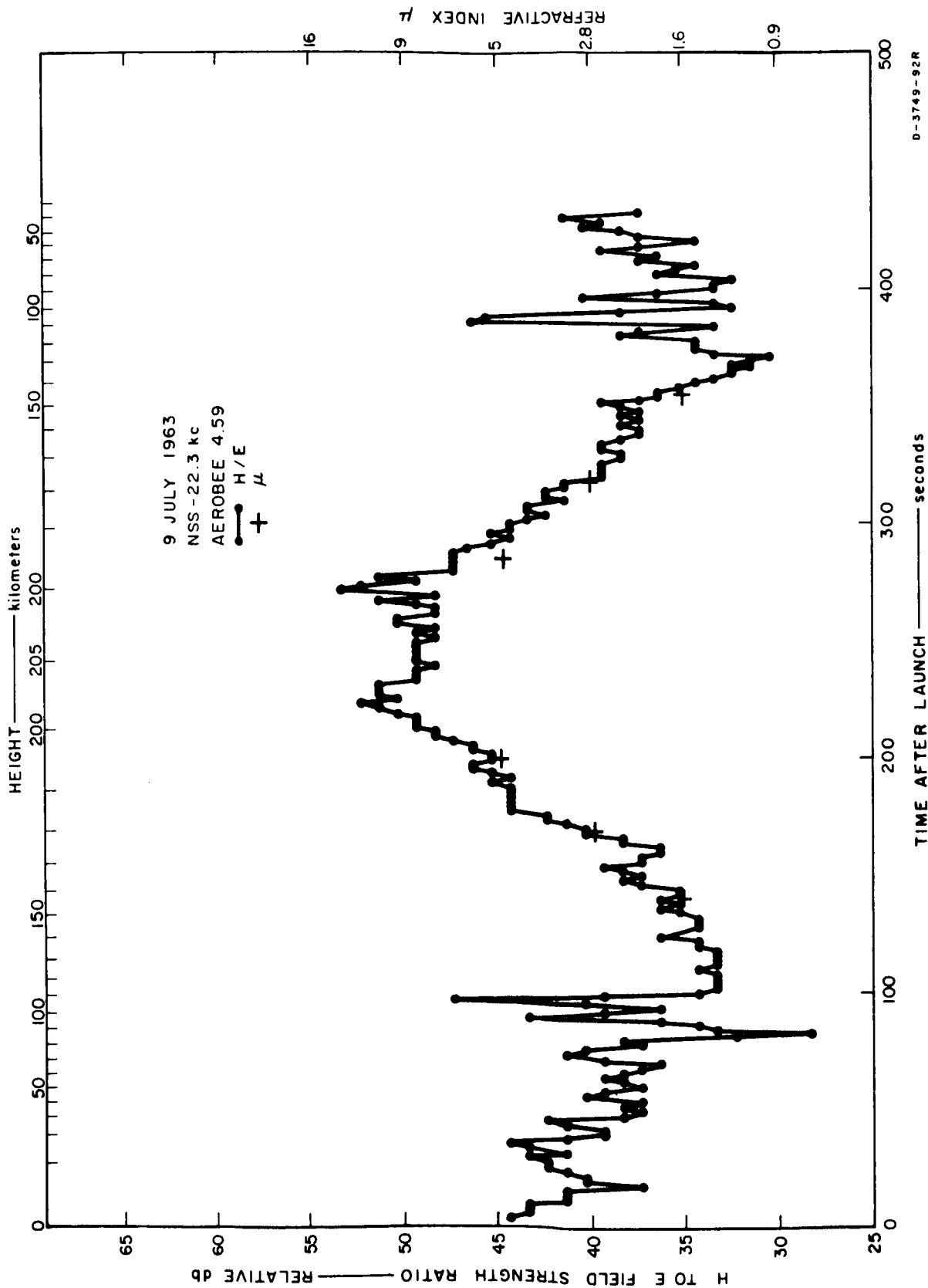


FIG. 9.78 RATIO OF MAGNETIC TO ELECTRIC FIELD STRENGTH AT 22.3 kc

9.5 Conductance Probe

9.5.1 Purpose

In order to determine electron temperature and vehicle potential, a plasma probe was included in the instrumentation for the night shot, Aerobee 4.59 UI. The direct benefit of these data is apparent, particularly since relatively few measurements of this type appear to have been made at night.

A second objective was to aid in the analysis of data from the impedance probe experiment, described in Sec. 9.3. Correlation of impedance probe data with known values of electron density and temperature and of vehicle potential are essential in developing an understanding of the various plasma effects on low-frequency antenna impedance.

The third objective, common to all instrumentation, was to evaluate the effectiveness of experimental technique and the performance of equipment. These results will be used in future experiments to correct design deficiencies and to improve instrument reliability and accuracy.

9.5.2 Instrumentation

The device flown was a form of dynamic Langmuir probe, as described by Mlodnosky and Crawford (1964). The probe structure, shown in Fig. 5.1, was a thin cylinder on the rocket axis extending 60 cm beyond the normal nose tip. The base 25 cm of the probe, which was 1.25 cm in diameter, was driven as a guard at probe potential. The remaining 35 cm of probe, 1 cm in diameter, was the active portion. Except for a stainless steel conical tip, 2.5 cm long, the entire structure was fabricated of aluminum, with Teflon and silicone rubber for internal insulation. All electronic components, except the input-matching transformer, which was in the conical base section of the probe, were attached to the loop support structure or in the instrument section of the payload. The probe itself was expected to reach a temperature over 400°C.

In operation, this device was a highly unsymmetrical Langmuir probe, where the entire rocket body was the second electrode. Since the ratio of the area of the rocket to that of the probe plus guard was over 400 to 1, greater than the ratio of electron-to-ion mobilities, the rocket body could be considered to maintain a floating potential essentially unaffected by the probe voltage over most of the bias range. The probe and guard were driven with respect to the rocket body by a known voltage, consisting of 10 mv rms at 112 cps superimposed on a slow bias sawtooth, which swept from -1 to +1 v every 1.4 sec. These levels were chosen to keep the ac excitation below the mean electron thermal potential. The 112-cps current flow resulting in the active probe was filtered out with a bandwidth of about 20 cps, amplified and log compressed, and detected. This output and the bias voltage were telemetered. Once every minute, both channels were calibrated at six points, and the probe voltage was then clamped to zero for 0.1 sec.

Under the conditions of the experiment, capacitive current contributed less than 2 percent of the total, so the data output has been considered as the log of the probe's conductance to simplify analysis. A capacitance correction would have been required at low densities if the original design goal, a measurement threshold of 10 elec/cc, had been met. This threshold was not achieved because of two factors. The first problem was stray coupling of the ac injection voltage directly into the preamplifier. Attempts to neutralize this coupling before launch were only partially successful, largely because it was sensitive to surrounding objects. Since time was short and the conductance probe was a secondary experiment, it was flown without knowing how much coupling would remain in free flight. From flight data, the theoretical threshold has been calculated as about 200 elec/cc. However, even this sensitivity was not realized, due to the second problem, which is the apparent lack of sufficient conducting area on the rocket body. The reasons for this conclusion, and its implications, are discussed in Sec. 9.5.3. It is sufficient to note here that the threshold actually realized was about 1000 elec/cc, as determined by comparison with electron densities measured by propagation phase delay (Sec. 9.4). By redesigning the probe coupling

system and establishing a reliable conducting surface on the rocket, the goal of 10 elec/cc resolution should be attainable. Further improvement of the technique should be possible by reducing the bias range to obtain better time resolution, and by using coherent detection to avoid the necessity of correcting for capacitive current. For additional sensitivity, a larger probe could be used if the excess electron current to the entire collecting surface were dumped by an electron gun. In fact, this last technique was considered for this shot, but appeared to require more effort than warranted for a secondary experiment.

9.5.3 Theory of Operation

The probe used in this experiment was operated as a dynamic probe similar to the "VLF" type by Crawford and Mlodnosky (1964), since the measuring frequency was low enough (112 cps) that heavy ions as well as electrons could be considered mobile. Analysis can be further simplified if the ratio of length to sheath radius was sufficiently large, for both the probe and the rocket, that both could be treated as segments of infinite cylinders. An effective sheath radius can be calculated by assuming a uniform ion density throughout the plasma, neutralized outside a sharply bounded sheath by an equivalent electron density, N . Inside the sheath, which lies at radius R about the center of an infinitely long cylindrical electrode of radius R_o , the electron density is zero. The net charge per unit length outside radius r is then

$$Q(r)/L = -\pi Nq(R^2 - r^2) , \quad (9.5.1)$$

where q is the (negative) charge of an electron, and the radial electric field at r is

$$E_r(r) = \frac{-Q(r)}{\epsilon 2\pi r L} = \frac{-Nq}{2\epsilon} \left(\frac{R^2}{r} - r \right) , \quad (9.5.2)$$

where ϵ is the permittivity of free space. The potential V on the electrode is then

$$\begin{aligned} V &= \int_R^{R_o} E_r dr \\ &= \frac{Nq}{4\epsilon} \left[2R^2 \ln(R/R_o) - R^2 + R_o^2 \right] . \end{aligned} \quad (9.5.3)$$

Although the assumption of a sharply-bounded sheath is not always a good approximation, it should be valid in cylindrical geometry if the mean free path is large compared to the sheath radius ($l_m > R$), the electrode potential is larger than the thermal potential ($|qV| > KT$), and the effective sheath distance is larger than the Debye length ($R - R_o > \lambda_d$), all of which are true in the calculations of Sec. 9.5.4, for an altitude of 200 km and an electron density of 10^4 elec/cc. At a potential of -0.5 v, the probe sheath radius R_p becomes 5.3 cm, and the rocket sheath radius R_r becomes 26 cm. Comparing these dimensions with the probe length of 35.5 cm (61 cm with guard) and the rocket length of about 8 m, treating the electrodes as segments of infinite cylinders should not introduce gross errors.

The total current to the probe and guard, assuming thermal equilibrium of electrons and ions, can now be written as

$$I_p + I_g = -Nq \left(\frac{KT}{2\pi m_e} \right)^{1/2} (A_p + A_g) \left[\exp \left(\frac{-qV_p}{KT} \right) - \left(\frac{m_e}{m_i} \right)^{1/2} \psi_p \sigma \right], \quad V_p < 0, \quad (9.5.4)$$

where

- I_p is probe current,
- I_g is guard current,
- K is Boltzmann's constant,
- T is plasma temperature,
- m_e is electron mass,
- A_p is probe surface area,
- A_g is guard surface area,
- V_p is probe (and guard) potential with respect to the plasma,
- m_i is ion mass (assumed singly ionized),
- ψ_p is an ion current factor due to the accelerating potential V_p (see Appendix A)
- σ is an ion current factor due to rocket velocity (see Appendix B).

The function ψ is shown in Fig. A.1 of Appendix A, where $\psi - 1$ is plotted against $\rho = R/R_0 - 1$ for several values of the parameter qV/KT . For large values of ρ , ψ can be approximated by

$$\psi_{\infty}(\rho = \infty) = \left(\frac{4qV}{\pi KT} \right)^{1/2} + \exp\left(\frac{qV}{KT} \right) \operatorname{erfc}\left(\frac{qV}{KT} \right)^{1/2}. \quad (9.5.5)$$

A simpler expression, within 3 percent of ψ_{∞} , is

$$\psi_{\infty} \approx \left(\frac{4qV}{\pi KT} + 1 \right)^{1/2}. \quad (9.5.6)$$

Denoting $-Nq[(KT)/(2\pi m_e)]^{1/2}$ by J_e and $\sigma[(m_e)/(m_i)]^{1/2}$ by η , and substituting Eq. (9.5.6) into Eq. (9.5.4),

$$I_p + I_g = J_e(A_p + A_g) \left\{ \exp\left(\frac{-qV_p}{KT} \right) - \eta \left[\left(\frac{4qV_p}{\pi KT} \right) + 1 \right]^{1/2} \right\}. \quad (9.5.7)$$

Similarly, the total current to the rocket is

$$I_r = J_e A_r \left[\exp\left(\frac{-qV_r}{KT} \right) - \eta \psi_r \right]. \quad (9.5.8)$$

In this case, however, ρ is much smaller than 1, and ψ_r reduces to

$$\psi_r = 1 + \rho. \quad (9.5.9)$$

But for small ρ , Eq. (9.5.3) becomes

$$V \approx \frac{Nq}{2\epsilon} (R - R_0)^2 = \frac{NqR_0^2 \rho^2}{2\epsilon}. \quad (9.5.10)$$

Combining,

$$I_r = J_e A_r \left\{ \exp\left(\frac{-qV_r}{KT} \right) - \eta \left[1 + \left(\frac{2\epsilon V_r}{NqR_0^2} \right)^{1/2} \right] \right\}. \quad (9.5.11)$$

For equilibrium, letting the probe bias voltage $V_b = V_p - V_r$ and dividing by $J_e (A_p + A_g)$,

$$0 = \exp \left[\frac{-q}{KT} (V_r + V_b) \right] - \eta \left[\frac{4q}{\pi KT} (V_r + V_b) + 1 \right]^{1/2} + \frac{A_r}{A_p + A_g} \left\{ \exp \left(\frac{-qV_r}{KT} \right) - \eta \left[1 + \left(\frac{2\epsilon V_r}{NqR_o^2} \right)^{1/2} \right] \right\}. \quad (9.5.12)$$

This equation can be solved, graphically or by other means, for V_r (and hence V_p) as a function of V_b , the known voltage applied from probe to rocket. Assuming that electrode geometry and rocket velocity are known, the ion mass, plasma temperature, and electron density must be estimated for the first calculation. The conductance vs. bias that would be measured by the instrument under these conditions can now be calculated and compared with actual measurements. Revised estimates can then be applied iteratively until agreement is obtained.

The conductance G measured by the instrument is given by

$$G = \frac{G_p G_r}{G_p + G_r}, \quad (9.5.13)$$

where

$$G_p = \frac{dI_p}{dV_p} = J_e A_p \left[\frac{-q}{KT} \exp \left(\frac{-qV_p}{KT} \right) - \frac{2\eta q}{\pi KT} \left(\frac{4qV_p}{\pi KT} + 1 \right)^{-1/2} \right], \quad V_p < 0 \quad (9.5.14)$$

is the probe conductance, and

$$G_r = \frac{dI_r}{dV_r} = J_e A_r \left[\frac{-q}{KT} \exp \left(\frac{-qV_r}{KT} \right) - \frac{\eta \epsilon}{NqR_o^2} \left(\frac{2\epsilon V_r}{NqR_o^2} \right)^{-1/2} \right], \quad V_r < 0 \quad (9.5.15)$$

is the rocket conductance.

G_p and G_r are fairly easily obtained by constructing log plots of their terms. The exponential terms then become linear, and a few points determine the square root terms. These terms, and consequently G , can then be evaluated at the appropriate V_p or V_r from the solution of Eq. (9.5.12) for a given V_b .

Initial estimates of T , η , and N can be obtained directly from the data by treating the rocket as an infinite plane conductor with plasma on one side, and the probe as an electrically isolated segment of the plane. Temperature would then be given by

$$T_1 = \frac{-qG}{K} \frac{dV_b}{dG} \quad V_b < -V_f, \quad (9.5.16)$$

which is proportional to the reciprocal slope of $\log G$ vs. V_b . The floating (or equilibrium) potential V_f is given by

$$V_f = \frac{KT}{-q} \ln \eta = \frac{KT}{2q} \ln \frac{m_i}{m_e} \quad (9.5.17)$$

Since the conductance has a maximum very close to $V_p = 0$, and $V_p = V_f + V_b$, the initial estimate of η is

$$\eta_1 = \exp \frac{q}{KT_1} V_b (G \text{ max}) \quad (9.5.18)$$

N can now be estimated as

$$N_1 = \frac{(2\pi m_e KT_1)^{1/2}}{q^2 A_p \eta_1} G_o (V_b = 0) \quad (9.5.19)$$

In the case of finite cylindrical electrodes, T_1 is actually the maximum possible value of T , so the initial estimate could be taken somewhat lower. Also, Eq. (9.5.18) will hold only if

$$\eta^2 A_r^2 \gg A_p (A_p + A_g) \quad (9.5.20)$$

but this is of little importance, since a good estimate of mass ratio is usually available a priori.

9.5.4 Results

In applying the procedures of Sec. 9.5.3 to the data from Aerobee 4.59 UI, a complete analysis has been made at only one altitude for several reasons. First, good data were obtained only in the upper 25 km of altitude because the peak altitude, 205 km, was considerably below the predicted 230-km apogee, and the electron density below 180 km was too low to obtain useful data except in the sporadic-E cloud, which was traversed too quickly. Second, the lengthy calculations required did not seem warranted until the difference between ascent and descent data is explained. Referring to Fig. 9.79, both the peak conductance observed during each bias sweep, G_m , and the bias voltage V_m at which this peak occurs, become erratic and rapidly decreasing during descent. These effects are tentatively ascribed to a turbulent wake of depleted ion density which begins to envelop the probe at apogee, but the mechanism is not yet understood. To minimize the difficulties noted above, the data sample chosen for analysis, shown in Fig. 9.80, is an average of five sweeps centered at about 200-km altitude on ascent. During this interval both G_m and V_m were essentially constant and large enough to provide a well-defined G vs. V_b characteristic. Since this was near apogee the rocket velocity was near its minimum, reducing the required drift correction, and good electron density measurements were available from the VLF Doppler experiment (Sec. 9.4). It should also be pointed out that G_m appeared proportional to N measured by Doppler during ascent, but behaved quite differently during descent. For comparison, N calculated from the Doppler data is shown in Fig. 9.80.

In the process of determining the plasma characteristics that would best match the probe data, it became apparent that the assumed geometry of the probe and rocket could not result in the observed G - V_b plot unless both η and N were far different than their assumed values. In fact, the ion current factor η would have to be about six times the value corresponding to atomic oxygen (16 AMU) as the ion species, which would reduce the floating potential to about 3.5 KT/q. The maximum conductance would then occur as the probe potential passed through the plasma potential, from which N could be calculated as about $2 \times 10^3 \text{ cm}^{-3}$.

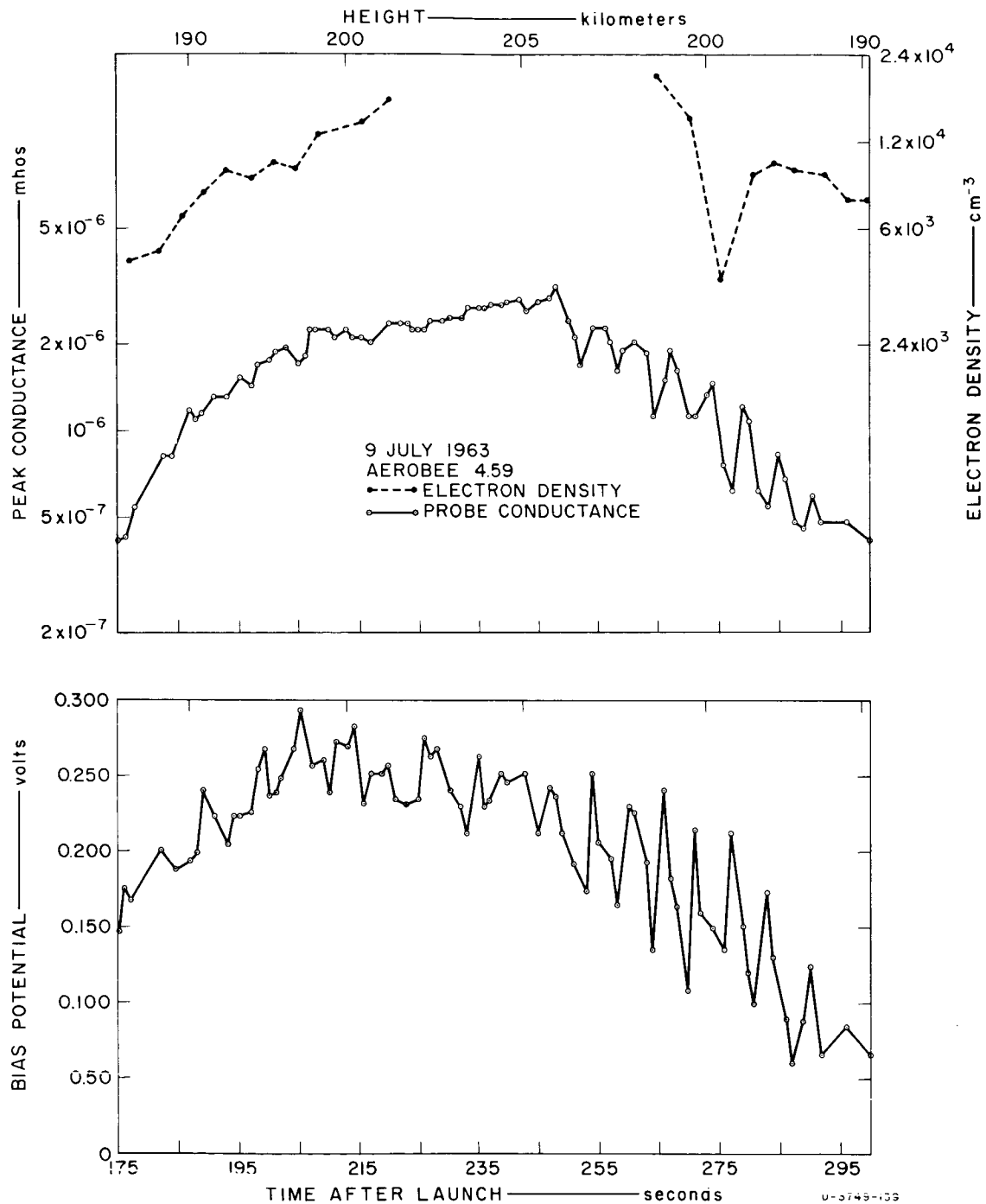


FIG. 9.79 PROBE PEAK CONDUCTANCE, ELECTRON DENSITY FROM DOPPLER DATA, AND PROBE BIAS RESULTING IN PEAK CONDUCTANCE

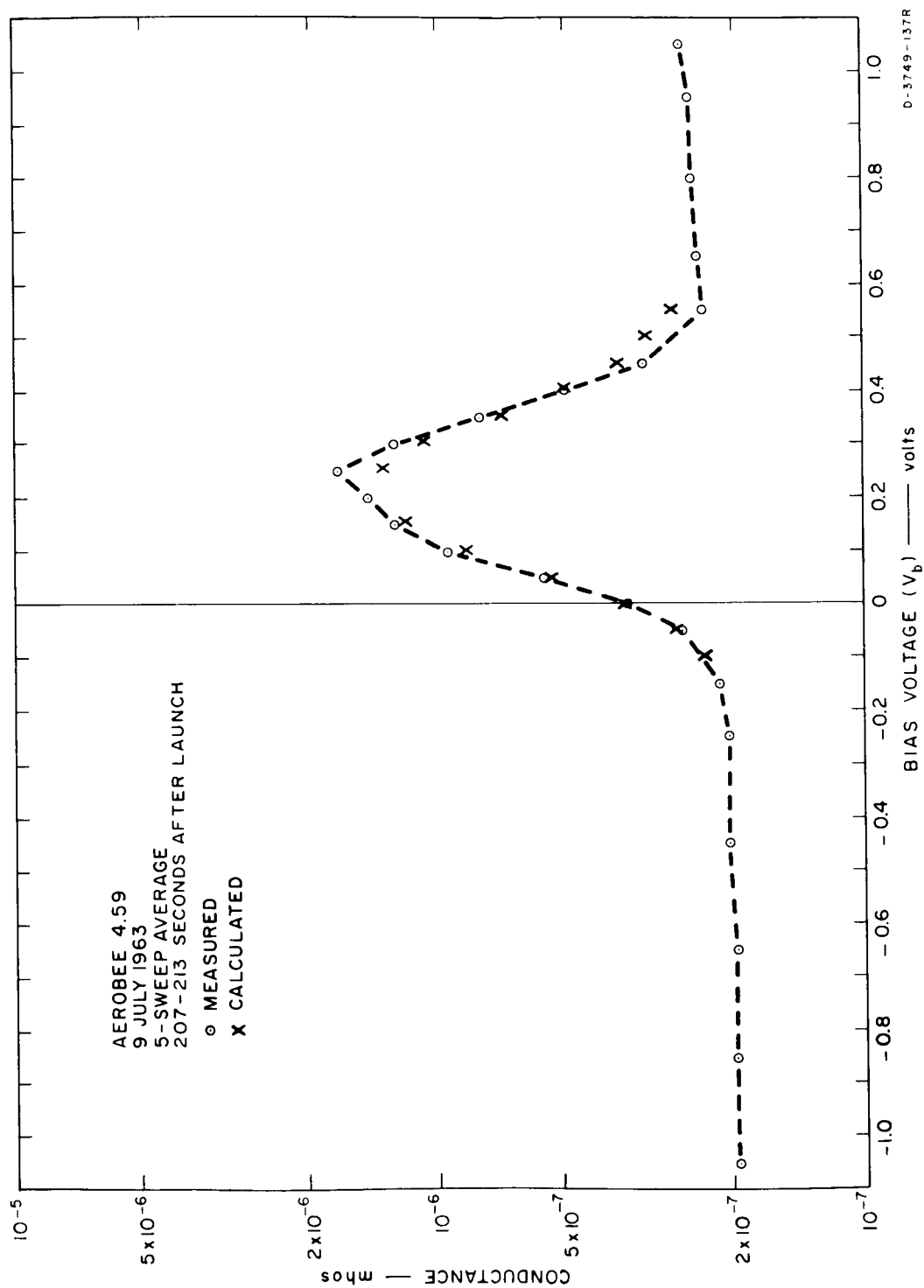


FIG. 9.80 CALCULATED AND MEASURED PROBE CONDUCTANCE vs. BIAS FOR 200-km ALTITUDE

This is a much lower value than the $1.0 \times 10^4 \text{ cm}^{-3}$ obtained from the Doppler experiment (Sec. 9.4) at this altitude. Since the Wallops Island ionograms extrapolate to good agreement with the Doppler results, and since such an extremely high value of η must result, it was felt that this interpretation of the probe results could not be accepted. The electron density was then taken as a known value of $1 \times 10^4 \text{ cm}^{-3}$ from the Doppler experiment, and the conducting surface area of the rocket was treated as an unknown, since the heat treatment of the steel skin could have resulted in a partially insulated surface. A set of parameters was then found which best match the data as shown in Fig. 9.80. The calculated conductance profile is also shown in this figure. The minimum measurable conductance was limited by the residual capacitance current (Sec. 9.5.2), added in phase quadrature in the calculations. For the best fit, $T = 800^\circ \text{K}$, $\eta = 1.75 \times 10^{-2}$, and $A_r = 0.307 \text{ m}^2$, using a velocity factor $\sigma = 1.11$ corresponding to $u = 423 \text{ m/sec}$ and $\alpha = 65.5$ degrees (App. B). The sheath geometry surrounding the rocket is presumed the same whether it is in the vicinity of insulated surface or a portion of the 4.8 percent that is conducting. The dichromate-coated magnesium fins are assumed to be completely insulated.

The value of η deduced is still rather high, and seems to require one of four explanations: the ion temperature is over six times the electron temperature, the effective ion mass is less than 1 AMU, about 1.5 secondary electrons are emitted for each impacting ion, or a bulk drift velocity several times the mean thermal velocity is superimposed on the ion distribution. The first three of these possibilities are clearly contrary to theory and experimental evidence, leaving the existence of an ion drift velocity on the order of kilometers per second as the only plausible explanation. McGill and Carlton (1964), in developing the hypothesis that electric fields excite certain auroral forms, particularly the "midlatitude red arcs," find drift velocities of this order (about 2 km/sec) would accompany strong emissions, and need be only slightly lower (possibly 1.5 km/sec) to reduce the intensity below a detectable level.

To estimate the drift velocity corresponding to the conductance probe measurements, without pursuing the subject in detail, we will adopt the "drift frame" of Megill and Carlton, which is a coordinate system moving at the average drift velocity, v_d . In this frame they show that the ions will tend toward a Maxwellian distribution with an effective temperature T^* of

$$T^* = T + \frac{m_i v_d^2}{3K} \quad (9.5.21)$$

Since this is different than the electron temperature T , the relative ion current factor η must be redefined as

$$\eta^* = \left(\frac{T^*}{T} \right)^{1/2} \eta(v_d, T^*) = \left(\frac{m_e T^*}{m_i T} \right)^{1/2} \sigma(v_d, T^*) \quad (9.5.22)$$

Assuming that the rocket velocity was small compared to v_d , and that v_d was perpendicular to the rocket axis, σ can be closely approximated by

$$\sigma \approx 1 + \frac{2m_i v_d^2}{\pi K T^*} \quad (9.5.23)$$

Substituting Eqs. (9.5.23) and (9.5.21) into Eq. (9.5.22) and solving for v_d^2 ,

$$v_d^2 = \frac{3\pi K T}{(\pi + 6)m_i} \left(\frac{m_i}{m_e} \eta^{*2} - 1 \right) \quad (2.5.24)$$

For $T = 800^\circ\text{K}$, $m_i = 16 \text{ AMU}$, and $\eta^* = 1.75 \times 10^{-2}$, we find $v_d = 1.86 \text{ km/sec}$, which is near the emission threshold predicted by Megill and Carlton.

It is not known whether detectable emissions were present. This value of v_d could be refined by iterating the entire process of matching the observed conductance characteristic, but it is unlikely that the results would be significantly changed. It seems more appropriate to direct

our future efforts toward improving the sheath model, including the effects of the expected drift velocities and collisions. In view of the initial results, it appears feasible to include probe experiments of this type on future shots, assuming the instrumental limitations due to lack of conducting surface and stray capacitive coupling will be removed. Independent measurements of electron temperature and density and ion drift velocity can then be made, and used to calibrate an impedance probe of the type discussed in Sec. 9.3 but possibly of different geometry. Since the impedance probe operates continuously at its floating potential, it is capable of millisecond time resolution; unlike a biased probe. At high altitudes, where ion mass may not be known, it should be possible to separate drift velocity and mass effects by measuring the static electric field. Since the cylindrical geometry is very easily extensible, it appears that threshold sensitivity on the order of 1 elec/cc would be practical, adequate for interplanetary space measurements if photoemission contamination can be suppressed.

9.6 Temperature and Voltage Monitor

On Aerobee 4.58 UI only, temperatures at three places on the payload and one instrument supply voltage were measured and subcommutated onto a single data channel. The supply voltage measurement indicated no measurable change during flight, which was expected. The temperature at the inside surface of the dielectric nosecone was measured in two places, namely, at 29 and 62 inches from the nose tip. A temperature inside the electronics package was measured to determine local heating effects. The temperature data are shown in Fig. 9.81. Although temperature changes were observed, the changes do not appear significant with respect to nosecone high-temperature performance or serious heating of electronics inside the nosecone.

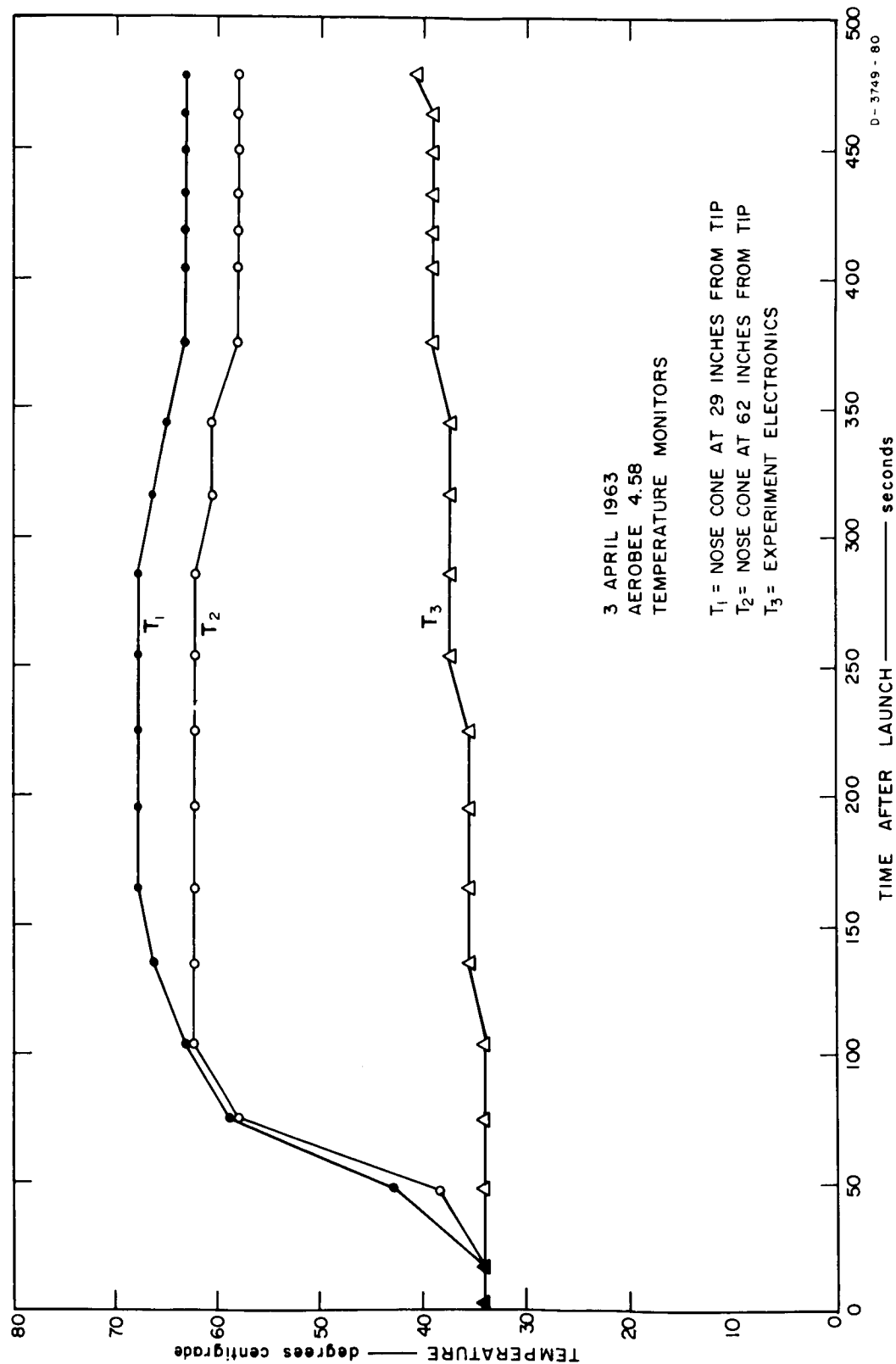


FIG. 9.81 PAYLOAD TEMPERATURE DATA

10. SUMMARY

Two payloads on Aerobee rockets were successfully launched from Wallops Island and a great deal of data was obtained on the numerous experiments flown. The first shot was at noon (LMT) and the second shot was at night two hours before midnight (LMT), providing samples of data representing the daytime and nighttime ionosphere and signal sources.

The daytime shot (Aerobee 4.58 UI) reached an altitude of 237 km and the nighttime shot (Aerobee 4.59 UI) reached an altitude of 205 km. Both flights were stable in attitude during the entire flight except for a slight precession which began well after burnout. This precession is attributed to a redistribution of liquid propellants remaining in the rocket.

The sweeping receivers covering the range 0.2 to 100 kc and the broad-band receiver (0.2 to 12.5 kc), which constituted the essential components of the experiment flown by Stanford University and Stanford Research Institute on the NASA EOGO satellite, performed completely satisfactorily thus validating the engineering and scientific design of the satellite experiment. The data obtained was a useful preview of the data expected on EOGO and was also useful in formulating the data display for EOGO data.

Attenuation profiles were obtained on both flights by narrow-band sweeping receivers for signals, man-made as well as natural, in the frequency ranges 0.2 to 100 kc and 1250 to 1600 kc. The following interesting features were observed on Aerobee 4.58 UI:

- (1) Except for rocket-associated signals, there were no signals above receiver threshold in the range 0.2 to 1.6 kc;
- (2) Above 85 km, a band of noise (hiss) appears in the band 2 to 8 kc, which varies somewhat in frequency range and develops some distinctive peaks as the rocket passes through the altitudes above 85 km;

- (3) A band of noise appearing between the times of rocket burnout and command cutoff in the frequency range 1 to 4 kc is apparently associated with the rocket exhaust plume;
- (4) Attenuation of man-made signals in the frequency range 17.8 to 100 kc showed total attenuations through the D layer of 20 to 50 db depending on frequency and penetration angle; and
- (5) Attenuation of signals in the 1250 to 1600 kc range through the D layer reduced signals below receiver threshold to indicate at least 50 db attenuation. The broad-band receiver exhibited the same 1 to 4 kc rocket noise and the 2 to 8 kc hiss band as did the sweeping receivers; in addition, as many as nine whistlers were observed in the rocket while none were observed by a nearby ground station.

The following features were observed by the sweeping receivers on Aerobee 4.59 UI:

- (1) Signals appeared above receiver threshold at all frequencies and altitudes;
- (2) Attenuation through a sporadic-E layer varied from less than 10 db to greater than 40 db as a function of frequency and penetration angle;
- (3) Above the E layer (110 km) the signals were essentially not attenuated to the peak of the flight (205 km);
- (4) A reduction in signals in the 1.3 to 3 kc band corresponding to the expected earth-ionosphere cutoff was observed; and
- (5) Reappearance of signals in the 1.3 to 3 kc band during the time the rocket was in the sporadic-E layer and the lower F layer indicates possible locally generated signals.

The most prominent feature of the broad-band data on Aerobee 4.59 UI is the presence of about 75 whistler signals and numerous sferics. The whistler signals included a new class called subprotonospheric.

Data on the impedance of an electric dipole were obtained on Aerobee 4.59 UI which showed significant variations in the sporadic-E layer and in the lower F layer (apogee). Greater change in impedance in the E layer than at the lower F layer were observed. Changes of capacitance from approximately 15 to 50 pf were observed at 1.54 kc

and from approximately 15 to 23 pf at 120 kc. Change of conductance from approximately 0 to 0.9 micromho was observed at 1.54 kc. The impedance data in the sporadic-E layer showed very sharp gradients and features of the layer which were less than 1 km in thickness. Different structure was observed on ascent than on descent indicating horizontal gradients. The impedance of the dipole was rocket-spin modulated, and it is presumed that this effect is an anisotropy of the sheath or the medium resulting from the rocket horizontal velocity or the earth's magnetic field.

On both flights, phase and amplitude of three wave components were measured at 22.3 kc, a frequency being transmitted continuously by U.S. Navy Station NSS at Annapolis. The effects of absorption, mode splitting and reflection, evanescent wave excitation, and refraction were observed in the D and E regions. Interference between direct and reflected waves was apparent below the reflecting region. The boundary attenuation due to absorption and reflection was on the order of 35 db during day, and 15 db at night. Unexplained variations of up to 10 db in power density, and 15 degrees in wave-normal angle, were observed during both flights. Electron density profiles were calculated from the observed Doppler shift. The daytime ascent and descent profiles are very similar, even to the fine structure, and in general agreement with ionograms. Very good results were obtained for $N > 10^3/\text{cm}^3$, with useful data down to 10^2 . At night, the data were much more difficult to interpret, but consistent results were again obtained for $N > 10^3/\text{cm}^3$.

The night flight carried a swept-biased cylindrical plasma probe to determine electron temperature and rocket potential. The first derivative of the probe characteristic was measured by recording the low-frequency conductance as a function of bias. A temperature of 800°K and potential of 0.258 were found at 200 km, as well as the unexpected result that an ion drift velocity of nearly 2 km/sec was required to explain the measurements.

REFERENCES

1. Barrington, R. E. and J. S. Belrose, "Preliminary Results from the Very-Low-Frequency Receiver aboard Canada's Alouette Satellite," Nature, 198(4881), pp. 651-656, (May 18, 1963)
2. Carpenter, D. L., N. Dunckel, and J. F. Walkup, "A New Very-Low-Frequency Phenomenon: Whistlers Trapped below the Protonosphere," J. Geophys. Res., Vol. 69 No. 23, pp. 5009-5017, (December 1, 1964)
3. Crawford, F. W., and R. F. Mlodnosky, "Langmuir Probe Response to Periodic Waveforms," J. Geophys. Res., Vol. 69, pp. 2765-2773 (July 1964)
4. Helliwell, R. A., J. H. Crary, J. P. Katsufakis, and M. L. Trimpi, "The Stanford University Real-Time Spectrum Analyzer," T.R. 10 Contract AF 18(603)-126, Stanford Electronics Laboratories, Stanford, California (10 November 1961)
5. Jöhler, J. R., and L. A. Berry, "On the Propagation of Long Wavelength Terrestrial Radio Waves--Two Theoretical Techniques," Proceedings of the Seventh Meeting of the AGARD Ionospheric Research Committee, Munich 1962, AGARDograph 74, pp. 101-129, Pergamon Press
6. McGill, L. R., and N. P. Carlton, "Excitation by Local Electric Fields in the Aurora and Airglow," J. Geophys. Res., Vol. 69, pp 101, 1964
7. Smith, R. L., "An Explanation of Subprotonospheric Whistlers," J. Geophys. Res., Vol. 69, No. 23, pp. 5019-5021, (December 1, 1964)

Appendix A

CURRENT TO AN INFINITELY LONG CYLINDER

Assume Maxwellian ion distribution outside the sheath of radius R , and no collisions inside the sheath (large mean free path). A conducting cylinder of radius R_0 is at potential V and cylindrical symmetry is assumed. Cylindrical coordinates r, θ, ℓ are used. An ion at the sheath boundary has velocity components u radially inward, v axial, and w tangential. The current that reaches the cylinder from the area element $Rd\theta d\ell$ on the sheath surface is

$$dI = Rd\theta d\ell Nq \int_{u=0}^{\infty} \int_{v=-\infty}^{\infty} \int_{-w_0(u)}^{w_0(u)} uf(u, v, w) dw dv du \quad (A.1)$$

where

$$f(u, v, w) = \left(\frac{m}{2\pi KT} \right)^{3/2} \exp \left[\frac{-m}{2KT} (u^2 + v^2 + w^2) \right] \quad (A.2)$$

Let u and $w_0(u)$ be the initial components of velocity of an ion that grazes the cylinder, and v_t is the θ component of velocity at tangency. By conservation of angular momentum,

$$mRw_0(u) = mR_0 v_t \quad (A.3)$$

By conservation of energy,

$$\frac{m}{2} \{ u^2 + [w_0(u)]^2 \} = \frac{m}{2} v_t^2 + qV \quad (A.4)$$

Combining,

$$[w_o(u)]^2 = \frac{R_o^2}{R^2 - R_o^2} \left(u^2 - \frac{2qV}{m} \right) \quad (A.5)$$

Integrating over θ , ℓ , and v , the current per unit length is

$$\frac{I}{\ell} = 2\pi RNq \left(\frac{m}{2\pi KT} \right) \int_{u_1}^{\infty} \int_{-w_o(u)}^{w_o(u)} u \exp \left[\frac{-m}{2KT} (u^2 + w^2) \right] dw du, \quad (A.6)$$

where

$$u_1 = 0 \text{ for accelerating potentials } (qV < 0)$$

$$\text{or } \left(\frac{2qV}{m} \right)^{1/2} \text{ for retarding potentials } (qV > 0)$$

Next integrate over w writing w_o for $w_o(u)$

$$\begin{aligned} \int_0^{w_o} \exp \left[\left(\frac{-m}{2KT} \right) w^2 \right] dw &= \left(\frac{2KT}{m} \right)^{1/2} \int_0^{w_o} \left(\frac{m}{2KT} \right)^{1/2} w_o \exp \left[\frac{-m}{2KT} w^2 \right] d \left[\left(\frac{m}{2KT} \right)^{1/2} w \right] \\ &= \left(\frac{2KT}{m} \right)^{1/2} \frac{\sqrt{\pi}}{2} \operatorname{erf} \left[\left(\frac{m}{2KT} \right)^{1/2} w_o \right] \end{aligned} \quad (A.7)$$

$$\therefore \frac{I}{\ell} = 2\pi RNq \left(\frac{m}{2\pi KT} \right)^{1/2} \int_{u_1}^{\infty} u \exp \left(\frac{-m}{2KT} u^2 \right) \operatorname{erf} \left[\left(\frac{m}{2KT} \right)^{1/2} w_o \right] du \quad (A.8)$$

Integrate by parts:

$$\int x dy = xy - \int y dx \quad (\text{A.9})$$

$$x = \text{erf} \left[\left(\frac{m}{2KT} \right)^{1/2} w_o \right] \quad (\text{A.10})$$

$$dx = \frac{2}{\sqrt{\pi}} \exp \left[\frac{-m}{2KT} w_o^2 \right] d \left[\left(\frac{m}{2KT} \right)^{1/2} w_o \right] \quad (\text{A.11})$$

$$dy = u \exp \left[\frac{-m}{2KT} u^2 \right] du \quad (\text{A.12})$$

$$y = -\frac{KT}{m} \exp \left[\frac{-m}{2KT} u^2 \right] \quad (\text{A.13})$$

$$\begin{aligned} xy &= \frac{KT}{m} \left\{ -\exp \left[\frac{-m}{2KT} u^2 \right] \text{erf} \left[\left(\frac{m}{2KT} \right)^{1/2} w_o \right] \right\}_{u_1}^{\infty} \\ &= \frac{KT}{m} \exp \left[\frac{-m}{2KT} u_1^2 \right] \text{erf} \left\{ \left(\frac{m}{2KT} \right)^{1/2} \left[\frac{R_o^2}{R^2 - R_o^2} \left(u_1^2 - \frac{2qV}{m} \right) \right]^{1/2} \right\} \end{aligned} \quad (\text{A.14})$$

$$xy = 0 \quad qV > 0 \quad (\text{A.15})$$

$$xy = \frac{KT}{m} \text{erf} \left[\frac{-R_o^2 qV}{\left(R^2 - R_o^2 \right) KT} \right]^{1/2} \quad qV < 0 \quad (\text{A.16})$$

$$-\int y dx = \frac{KT}{m} \frac{2}{\sqrt{\pi}} \int_{u_1}^{\infty} \exp \left[\frac{-m}{2KT} u^2 \right] \exp \left[\frac{-m}{2KT} w_o^2 \right] d \left[\left(\frac{m}{2KT} \right)^{1/2} w_o \right] \quad (\text{A.17})$$

Change variables to $\frac{R}{R_o} \left(\frac{m}{2KT} \right)^{1/2} w_o$:

$$u^2 = w_o^2 \left(\frac{R^2 - R_o^2}{R_o^2} \right) + \frac{2qV}{m} \quad (\text{A.18})$$

$$\frac{-m}{2KT} u^2 = \frac{-m}{2KT} w_o^2 \left(\frac{R^2}{R_o^2} - 1 \right) - \frac{qV}{KT} \quad (A.19)$$

$$\begin{aligned} - \int y dx &= \frac{2KT}{m\sqrt{\pi}} \exp \left(\frac{-qV}{KT} \right) \frac{R_o}{R} \int_x^\infty \exp \left[\frac{-mw_o^2}{2KT} \left(\frac{R^2}{R_o^2} \right) \right] d \left[\frac{R}{R_o} \left(\frac{m}{2KT} \right)^{1/2} w_o \right] \\ x &= \frac{R}{R_o} \left(\frac{m}{2KT} \right)^{1/2} w_o(u_1) \quad (A.20) \end{aligned}$$

$$\text{Note } \int_t^\infty e^{-s} ds = \int_0^\infty e^{-s} ds - \int_0^t e^{-s} ds = \frac{\sqrt{\pi}}{2} [1 - \text{erf}(t)]$$

$$\therefore - \int y dx = \frac{2KT}{m\sqrt{\pi}} \exp \left(\frac{-qV}{KT} \right) \frac{R_o}{R} \frac{\sqrt{\pi}}{2} \text{erfc} \left[\frac{R^2}{R^2 - R_o^2} \left(\frac{m}{2KT} u_1^2 - \frac{qV}{KT} \right) \right]^{1/2} \quad (A.21)$$

$$= \frac{KT}{m} \frac{R_o}{R} \exp \left(\frac{-qV}{KT} \right) \quad qV > 0 \quad (A.22)$$

$$= \frac{KT}{m} \frac{R_o}{R} \exp \left(\frac{-qV}{KT} \right) \text{erfc} \left[\frac{-R_o^2 qV}{(R^2 - R_o^2)KT} \right]^{1/2} \quad qV < 0 \quad (A.23)$$

$$\therefore \frac{I}{\ell} = 2\pi R_o Nq \left(\frac{KT}{2\pi m} \right)^{1/2} \exp \left(\frac{-qV}{KT} \right) \quad qV > 0 \quad (A.24)$$

$$\begin{aligned} \frac{I}{\ell} &= 2\pi R_o Nq \left(\frac{KT}{2\pi m} \right)^{1/2} \left\{ \frac{R}{R_o} \text{erf} \left[\frac{-R_o^2 qV}{(R^2 - R_o^2)KT} \right]^{1/2} \right. \\ &\quad \left. + \exp \left(\frac{-qV}{KT} \right) \text{erfc} \left[\frac{-R_o^2 qV}{(R^2 - R_o^2)KT} \right]^{1/2} \right\} \quad qV < 0 \quad (A.25) \end{aligned}$$

The function ψ used in Sec. 9.5 is a normalized current factor defined as

$$\begin{aligned}\psi &= \frac{I}{2\pi L R_o N q \left(\frac{KT}{2\pi m} \right)^{1/2}} \\ &= \frac{R}{R_o} \operatorname{erf} \left[\frac{-R_o^2 qV}{(R^2 - R_o^2)KT} \right]^{1/2} + \exp \left(\frac{-qV}{KT} \right) \operatorname{erfc} \left[\frac{-R_o^2 qV}{(R^2 - R_o^2)KT} \right]^{1/2}\end{aligned}$$

$qV < 0 \quad (A.26)$

This function is plotted vs. $\rho = R/R_o - 1$ for several values of qV/KT in Fig. A.1.

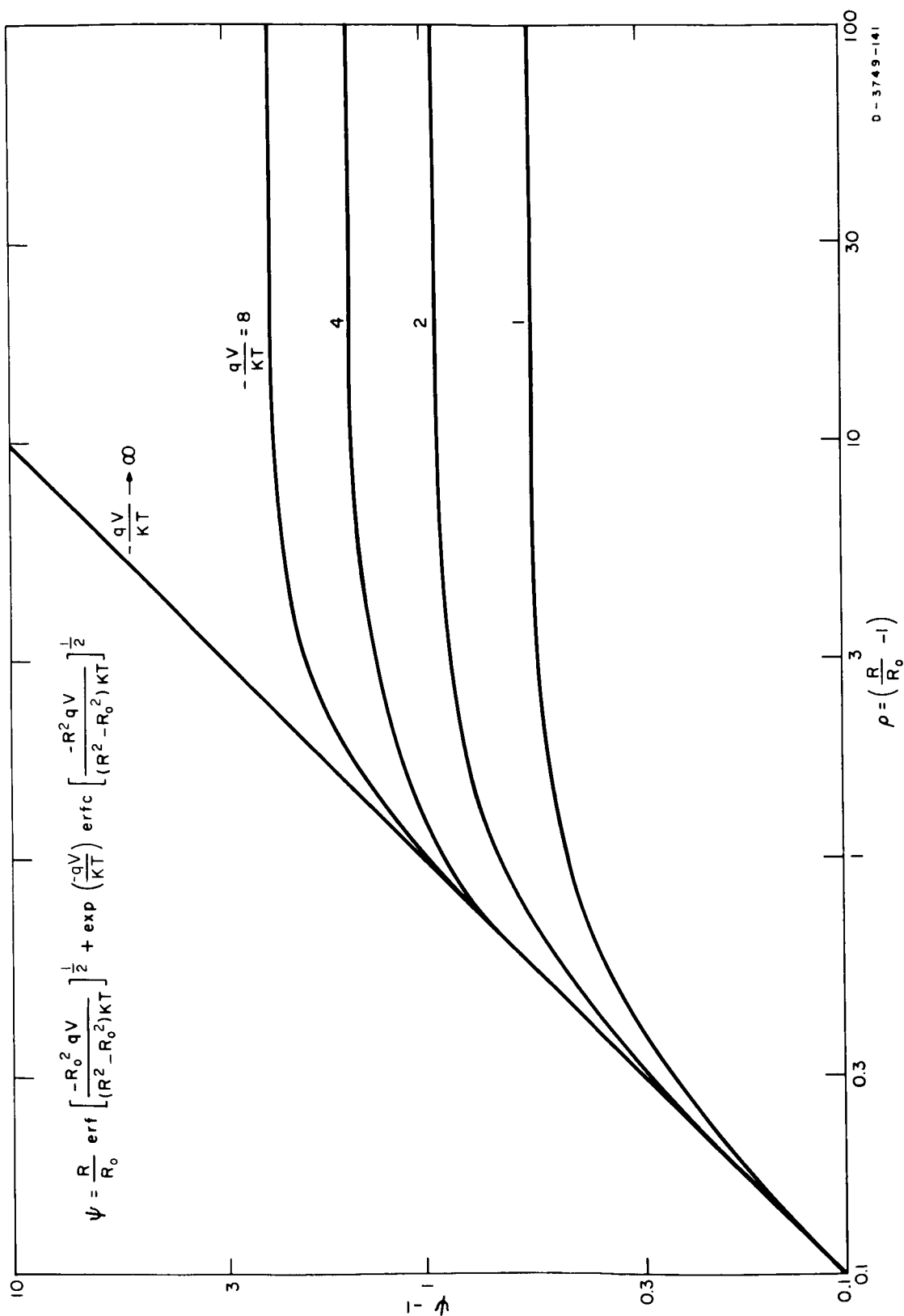


FIG. A.1 ION CURRENT FACTOR ψ AS A FUNCTION OF CYLINDER RADIUS FOR SEVERAL POTENTIALS

Appendix B

CURRENT TO A MOVING CYLINDER

Assuming a Maxwellian distribution of ion velocities, the density function of the velocity component in one direction (x) is

$$f(v_x) = \left(\frac{m_i}{2\pi KT}\right)^{1/2} \exp\left(-\frac{m_i v_x^2}{2KT}\right) \quad (\text{B.1})$$

The ion current density into both sides of a conducting plate normal to x and moving in the x direction with velocity u is

$$J_x(u) = N_i q_i \left[\int_{-\infty}^u (v_x - u) f(v_x) dv_x - \int_u^{\infty} (v_x - u) f(v_x) dv_x \right] \quad (\text{B.2})$$

where N_i is ion density
 q_i is ion charge

and the mean free path is assumed large compared to the dimensions of the body.

Carrying out the integrations and normalizing to $J_x(u=0)$ results in

$$v(u) = \frac{J_x(u)}{J_x(0)} = \exp\left(-\frac{x^2}{2}\right) + X\left(\frac{\pi}{2}\right)^{1/2} \left[2 \int_{-\infty}^x \Phi(x) dx - 1 \right] \quad (\text{B.3})$$

where $X = u \left(\frac{m_i}{KT}\right)^{1/2}$

and $\Phi(x) = (2\pi)^{-1/2} \exp\left(-\frac{x^2}{2}\right)$, the normal density function.

This form has been chosen to facilitate evaluation using the tabulated normal probability function.

The total ion current to the rocket can now be calculated by integrating current density over the surface area, where density normal to the direction of motion equals the density at rest. Integrating the normalized form yields the current factor σ :

$$\sigma = \frac{1}{A} \int_A [\nu^2(u) \cos^2 \theta + \sin^2 \theta]^{1/2} dA \quad (B.4)$$

where θ is the angle between the x axis (direction of motion) and the normal to the element of area. Since the derivation of ν is based on the current to both sides of an area, a symmetrical body is required, and the integration could be taken over only half the surface.

In this case, the rocket will be approximated by a right circular cylinder whose axis makes an angle α with the x axis. Let φ be the angle of longitude and α the colatitude of the x axis in spherical coordinates using the rocket axis as the pole.

$$\text{Then} \quad \cos \theta = \sin \alpha \cos \varphi \quad (B.5)$$

and equation B.4 becomes

$$\sigma = \frac{2}{\pi} \int_0^{\pi/2} [1 + (\nu^2 - 1) \sin^2 \alpha \cos^2 \varphi]^{1/2} d\varphi \quad (B.6)$$

$$= \frac{2}{\pi} [1 + (\nu^2 - 1) \sin^2 \alpha]^{1/2} \int_0^{\pi/2} \left[1 - \frac{(\nu^2 - 1) \sin^2 \alpha}{1 + (\nu^2 - 1) \sin^2 \alpha} \right]^{1/2} d\varphi$$

$$= \frac{2}{\pi} [1 + (\nu^2 - 1) \sin^2 \alpha]^{1/2} E(\nu, \alpha) \quad (B.7)$$

where E is a complete elliptic integral of the second kind.